UNIVERSITY OF SOUTHAMPTON

Faculty of Engineering and the Environment
Institute of Sound and Vibration Research

Self-tuning vibration absorbers

by

Michele Zilletti

Thesis for the degree of Doctor of Philosophy

August 2011

UNIVERSITY OF SOUTHAMPTON

ABSTRACT

FACULTY OF ENGINEERING AND THE ENVIRONMENT

INSTITUTE OF SOUND AND VIBRATION RESEARCH

Doctor of Philosophy

SELF-TUNING VIBRATION ABSORBERS

by Michele Zilletti

This thesis presents a theoretical and experimental study of self-tuning vibration control. Feedback design is often based on the assumption of time-invariance, which means that the controller has constant coefficients. Self-tuning control takes into account process changes in the response of the system under control by incorporating an adjusting mechanism which monitors the system, compares its status with the required one and adjusts the coefficients of the controller. In this thesis a self-tuning process is analysed for active and semi-active control of broadband vibration based on the maximisation of the power absorbed by the controller. The absorbed power can be locally estimated without using extra sensors to monitor the global response of the system under control. This is particularly advantageous in applications where many actuators are required, in which case each actuator and the collocated sensor can be treated as an independent self-tuneable unit.

A theoretical analysis of vibration control using this approach is presented for lumped parameter systems and also for distributed systems, such as beam and panels. Different tuning strategies are compared in terms of the reduction of the global response of the system under control. An algorithm is then discussed that tunes the feedback gains of independent control units to maximise their individual absorbed powers. Experimental studies are then presented of a self-tuning control system with two decentralised control units using velocity error signals and electromagnetic reactive actuators installed on an aluminium panel.

In the second part of the thesis the analysis is extended to the use of inertial actuators. In this case the implementation of the self-tuning control based on the maximisation of the power absorbed is investigated using simulations of velocity feedback control and shunted inertial actuators.

“You never know when you start a journey where you are going to end up…”

Steve Elliott

but it is always worth starting one

CONTENTS

List of figures

List of tables

Declaration of Authorship

I, Michele Zilletti

declare that the thesis entitled

Self-tuning vibration absorbers

and the work presented in the thesis are both my own, and have been generated by me as the result of my own original research. I confirm that:

- this work was done wholly or mainly while in candidature for a research degree at this University;
- where any part of this thesis has previously been submitted for a degree or any other qualification at this University or any other institution, this has been clearly stated;
- where I have consulted the published work of others, this is always clearly attributed;
- where I have quoted from the work of others, the source is always given. With the exception of such quotations, this thesis is entirely my own work;
- I have acknowledged all main sources of help;
- where the thesis is based on work done by myself jointly with others, I have made clear exactly what was done by others and what I have contributed myself;
- parts of this work have been published as:

1. Zilletti, M., Elliott, S.J. and Gardonio, P. (2009) "Self-tuning of local feedback loops for active vibration control", Proceedings of the 16th International Congress on Sound and Vibration: Recent Developments in Acoustics, Noise and Vibration (ICSV16), Krakow, Poland, 5-9 July 2009, Paper 507, CD-ROM, 8pp

2. Zilletti, M., Gardonio, P. and Elliott, S.J. (2009) "Self-tuning control algorithm for decentralised active damping control units", Proceedings of Active 2009 Conference, Ottawa, Canada, 20-22 August 2009, Paper 352, 11pp

3. Zilletti, M., Elliott, S.J. and Gardonio, P. (2010) "Self-tuning control systems of decentralised velocity feedback", Journal of Sound and Vibration, 329(14), 2738-2750

4. Elliott, S.J., Zilletti, M. and Gardonio, P. (2010) “Self-tuning of local velocity feedback controllers to maximise power absorption”, Proceedings of the Tenth International Conference on Recent Advances in Structural Dynamics (RASD2010), Southampton, UK, 12-14 July 2010, Paper 013, 12pp

5. Zilletti M., Elliott S. J., Rustighi E. (2011) ”Optimisation of dynamic vibration absorber to minimise kinetic energy and maximise internal power dissipation”, ISVR Technical Memorandum 992.

6. Elliott S. J., Zilletti M., Rustighi E., Teherani M. (2011) “Optimisation of dynamic vibration absorption in a system for self-tuning structural damping and energy harvesting”, Euromech Colloquium on Structural Control and Energy Harvesting, Bristol UK, 25-27 July 2011, Abstract

7. Elliott, S.J., Zilletti, M. and Gardonio, P. (2010) “Apparatus and method of vibration control”, UK Patent number GB2478790A

8. Zilletti, M., Elliott, S.J. and Gardonio, P. (2012) “Experimental implementation of a self-tuning control systems of decentralised velocity feedback”, Journal of Sound and Vibration, 331(1), 1-14

Signed: ……..

Date:……

Acknowledgments

This is without doubt the most difficult section of this thesis. My gratitude to those who supported me during this chapter of my life merits more than a few words but… I will give it a try.

The first person I want to thank is my supervisor Prof. Steve Elliott both on a professional and personal level. He has been an irreplaceable guidance thanks to his ability to approach complex problems with an extraordinary simplicity. He gave me the enthusiasm to carry on day by day. I really feel lucky to have had him as supervisor.

I would like to thank my co-supervisor Dr. Emiliano Rustighi, who spent many hours giving me indispensable help during these years. I have greatly benefited from his experience and advice.

A particular thank you goes to Prof. Paolo Gardonio who has always believed in me and has given me the opportunity to start my doctorate here at ISVR. He has been an excellent scientific guide thanks to his deep knowledge and experience. He has taught me that with determination and passion great results can be achieved. His sincerity and unconditional advice have been fundamental in taking important decisions in my career.

A special acknowledgment should be awarded to Dr. Jens Rohlfing and Dr. Neven Alujević for the constructive scientific discussions and of course for their profound friendship. Also a sincere thanks to Dr. Jens Rohlfing for having helped me during the long measurements sessions in the laboratory.

A great thanks goes to the ISVR technical support team. Thank you to Phil Oxborrow for building the experimental test rig and Antony Wood for his great help in constructing the controller and his immense patience.

The work done to produce this thesis was supported by “Smart structures”, ITN Marie Curie programme which was founded by the European Commission and is gratefully acknowledged. God bless Marie Curie!!! [Neven Alujević]

On a more personal level I would like to thank my family, in particular my father Franco and mum Rosalba for their encouragements and for having believed in me more than myself.

A special thank you to Pia who had the unique ability to make rainy Southampton look sunny!

Last but not least I would like to thank my friends in Southampton with whom I shared the best moments of this experience and of course, how could I forget my friends from home.

No matter what we achieve in life the most important thing is that we will always remain the same at our friends' eyes.

Thank you.

Nomenclature

Abbreviations

FRF	Frequency response function
DOF	Degree of freedom
SDOF	Single degree of freedom
B&K	Bruel & Kjaer
MEMS	Microelectromechanical systems
PSD	Power spectral density
ISVR	Institute of sound and vibration research
DVA	Dynamic vibration absorber

Symbol	**Description**	**Unit**
Latin letters		
a	Modal velocity	m/s
c or C	Damping	N/ms^{-1}
d	Width of a beam	m
f	Force	N
g	Control gain	various
h	Thickness	m
i	Current	A
j	Imaginary unit defined as $j = \sqrt{-1}$	
k or K	Stiffness	N/m
l	Length	m
m or M	Mass	Kg
q	Number of iteration of the algorithm	
t	Time	t
v	Velocity	m/s
s	Complex Laplace variable transform	
u	Voltage	V
x	x-coordinate	m
z	z-coordinate	m
y	y-coordinate	m
A	Magnet internal surface area	m^2
B	Magnetic flux	T
E	Young modulus	N/m^2
F	Modal force	N
$\boldsymbol{G}$	Diagonal matrix of the control gains	various
$\boldsymbol{H}$	Matrix of the open loop frequency response functions	various
I	Performance index	
KE	Frequency-integrated PSD of the kinetic energy	J/Pa^2
L	Electrical inductance	H
N	Total number of modes	
O	Origin of the Cartesian co-ordinate system	
P	Frequency-integrated PSD of the power	W/Pa^2
Q	Cross section of the coil's wire	m^2
R	Electrical resistance	Ω
T	Transduction coefficient of an electromagnetic actuator	N/A
Y	Mobility	ms^{-1}/N
S	Power Spectral Density	
$\boldsymbol{S}$	Dynamic stiffness matrix	m/N
Z	Impedance	Ns/m
Greek letters		
α	Step of the algorithm	
β	Angle	rad
Γ	Dimensionless mobility function	rad

ε	Real number $\ll 1$	rad
ζ	Damping ratio	
η	Loss factor	
θ	Zero of the open loop FRF	rad/s
Θ	Dimensionless mobility function	
λ	Forced frequency ratio	
λ_i	i-th Eigen value	
Λ	Dimensionless mobility function	
μ	Mass ratio	
ν	Natural frequency ratio	
ν_1	Poisson ratio	
π	Pi	
Π	Dimensionless mobility function	
ρ	Density	Kg/m^3
ρ_1	resistivity	Ω/m
ϕ	Mode shapes	
ω	Angular frequency	rad/s
Ω	Modal resonant term	

subscriptions

a	Referred to an inertial actuator
abs	Absorbed
b	blocked
c	Control
close	Close loop
d	Relative to a damper
eb	Electrical blocked
f	Relative to a force
H	Relative to the harvested power
k	Relative to the kinetic energy
L	Electric load
m	Mechanical
max	Maximum
mb	Mechanical blocked
min	Minimum
mo	Open loop mechanical
open	Open loop
opt	Optimum
p	Primary
P	Relative to the absorbed power
pr	Relative to the power absorbed by damper number r
r	Number of the control unit
R	relative
s	Structure
S	Shaker
w	Base mass

Mathematical terms

X	Real value *X*
$\tilde{X}$	Complex value *X*
$\mathrm{Re}\{\tilde{X}\}$	Real part of *X*
$\mathrm{Im}\{\tilde{X}\}$	Imaginary part of *X*
$\tilde{X}^*$	Complex conjugate of *X*
$\mathrm{E}[\tilde{X}^*\tilde{X}]$	Expectation value of *X*
X^n	*X* to the power of *n*
$\dot{X}$	First derivative of *X* with respect of time
$\ddot{X}$	Second derivative of *X* with respect of time
d	Differential operator
$\boldsymbol{X}$	Matrix
$\boldsymbol{X}^{-1}$	Inverse of $\boldsymbol{X}$
$\boldsymbol{X}^{T}$	Non conjugate transpose of matrix $\boldsymbol{X}$
$\boldsymbol{X}^{H}$	Complex conjugate transpose of matrix $\boldsymbol{X}$
$\boldsymbol{I}$	Identity matrix

XXX

$\exp\{X\}$	e to the power of X
$\text{sgn}[X]$	Sign of X
$\hat{X}$	Estimated complex value of X
$\bar{X}$	Time average of X

1. Introduction

1.1. The need to control structural vibration

Vibration occurs in most machines, structures and dynamic system and can be the cause of disturbance, damage or even destruction. At the extreme end of the vibration scale, an earthquake can have tragic consequences, being able to destroy entire cities. At the lowest end, vibrations produced by a vehicle or a home appliance can cause discomfort and reduce sales. Vibration control aims to reduce or modify the vibration of a mechanical system [1]. In the last few decades more and more attention has been devoted to vibration control and multi-million dollar industries have produced devices and materials for vibration control.

Vibrations can have different characteristics in terms of frequency and magnitude. For example the range of frequencies most often associated with the effects of the whole human body vibration on health, activities and comfort is approximately 0.5-100 Hz. Typically frequencies at about 0.5 Hz can causes motion sickness. Vibrations at around 20 Hz are typically transmitted through the seat of a vehicle while the frequency transmitted by vibrating tools is around 100 Hz. Depending on the magnitude of the vibration, the human body is generally more sensitive to low frequency vibrations [2].

Vibrations can have dangerous and destructive effects on mechanical systems. For example vibrations of high buildings and bridges due to the excitation produced by interaction with the wind or due to a strong earthquake can cause structural damage if the amplitude of the vibration excide a certain limit. In some cases, vibrations can also compromise the integrity of a component due to mechanical fatigue.

In many engineering systems a source of discomfort is represented by air-borne and structure-borne sound radiation. In particular, vibration of panels and shell structures may generate high levels of interior noise in transportation vehicles such as aircrafts, trains, helicopters, cars, etc. in the audio-frequency region, between about 0.02 and 20 kHz [1-3].

Because of this broad variety of vibrations problems it is difficult to find general solutions and each problem needs to be carefully considered to understand the nature of the vibration. It is important to understand the source of the vibration, its magnitude and frequency at receiving location and the path along which the vibration reaches the receiving location. The approaches to vibration control are typically classified into three types: passive, semi-active and active.

This thesis manly concerns with the active control of thin lightly damped structures such as panels. In cases where the controller is tuned to absorb power, however, the system may be classed as semi-active.

1.2. Passive vibration control

Passive vibration control aims to reduce the response of a system by passively modifying its characteristics. The modifications can involve structural changes or the addition of passive elements in order to change the stiffness, damping and mass of the system under control. These modifications reduce the response of the structure to the forces imposed by an external disturbance. Purely passive vibration control techniques do not require external power and are fixed at the time of implementation.

There are different approaches in designing passive vibration control systems. The first attempt in reducing structural vibration is made in the design process. The design of a mechanical component or of the entire system can be optimised in order to reduce the vibration level, either minimising the vibration input of the disturbance or shifting the structural resonance frequencies away from the disturbance frequencies. This method requires an accurate model to predict the structural response and can only be applied during the design process.

A second approach involves the use of localised devices placed in strategic locations on the structure in order to change a resonance frequency of the main system. A typical example of such a passive device consists of a single degree of freedom system, either tuned to a resonance frequency of the structure (vibration absorber) or at the disturbance frequency (vibration neutraliser) [3]. These systems can efficiently reduce the vibration level only at frequencies close to those it is tuned.

In the case where the vibration is characterised by many resonances of the structure, a passive control solution could be to increase the damping of the system. Damping dissipates some of the vibration energy of the structure by transforming it into heat. A preliminary estimate of the structural damping already existing in the structure is necessary before any attempt to add extra damping is made. The most common technique to add damping is to attach, at strategic locations on the structure, highly damped materials, such as polymeric, to dissipate vibration energy.

A fourth passive vibration control approach can be applied when one component of the system vibrates excessively due to high vibration level transmitted through a few connections points. The vibration of this part can then be efficiently reduced by isolating this path, for example by making the connections sufficient resilient. This technique is particularly suitable when delicate equipment have to be isolated from high vibration exposure.

In many applications passive vibration control can offer a satisfactory attenuation of the structural response, without excessive costs and with low maintenance requirements. The penalty for high levels of passive vibration control, however, can be a significant increase in weight and cost.

The effectiveness of localised passive devices is also generally limited to the narrow frequency band for which these systems are designed and in some cases can even increase the vibration of the main system if the operational conditions changes.

1.3. Semi-active vibration control

A resonant passive device may not work if there is a change in the operating or environmental conditions. Real mechanical systems can be subjected to changes of these conditions and a resonant device can lose its effectiveness, or in the worst cases, can enhance the vibration level of the system under control. A semi-active system is a passive system in which the parameters of the passive device (damping, stiffness, etc.) can be changed over time in order to tune the controller and allow good reduction for a wide range of operational conditions. The stability of a semi-active system is guaranteed as the passive system can only absorb power, although the tuning mechanism could give rise to modulations of the vibration if it fails to converge.

Many techniques to change the properties of passive systems have been developed, particularly to change the stiffness of a tuned device so that it can track changes in the excitation frequency. For example, the stiffness of pneumatic springs can be altered by changing the air pressure inside the device [4]. Another example using element of a shape memory alloy, whose Young modulus changes with temperature, and so can be controlled by adjusting the electrical current thorough it [5]. Other strategies of tuning the stiffness of a passive device involve changes in the geometric shape of the stiffness element, using piezoelectric actuators for example [6].

Electro/magneto rheological fluids are type of fluids that increase their viscosity when exposed to an electric or magnetic field. They are used in magnetorheological dampers in which the magnetic field is produced using an electro magnet. The viscous damping of the device can be therefore changed by varying the current across the coil that generates the magnetic field [7]. They have been used as adaptive dampers on vehicles, to allow less damping on smoother road surfaces, and on washing machines, to control the drum vibration as its speed runs up through a resonance.

Semi-active system can be implemented by shunting an electromechanical transducer with an electrical impedance that can be adapted. This approach has been used for both piezoelectric [8] and electromagnetic actuators [9, 10].

1.4. Active vibration control

Active vibration control can take many different forms, but the important components of any of them are a sensor, an electronic controller and an actuator. The sensor is used to detect the vibration, the controller manipulates the measured signal in a suitable way and the actuator applies a reacting force or moment to the system under control. Examples of actuators used in active control are: shakers, piezoelectric ceramics and magnetostrictive devices. A substantial advantage of an active control system is its adaptability to parameters changes of the system under control, which guarantees a better performance in a wider range of operating conditions compared with a passive one. Depending on the circumstances, active solutions may be cheaper or lighter then passive systems. In some applications active control systems can offer performances that no passive system can achieve, especially in controlling low frequency vibration. The drawback of an active system is that an external power supply is needed. Moreover active control is only effective in a given frequency band, generally at low frequencies, and can enhance the vibration level at other frequencies [7, 11].

Several control schemes have been proposed which can be broadly classified into two main families: feed-forward and feedback architectures.

Feed-forward control is generally the most suitable control strategy when a reference signal is available that is strongly correlated with the disturbance. Feed-forward control was first design for active noise control [12], but applications in vibration control can also be found in [11, 13]. The reference signal measured by a sensor, is passed to an adaptive filter and then used to drive an actuator, which influences the system's response. The coefficients of the adaptive system are adjusted in order to minimise the error signal measured by sensors placed in one or more strategic locations. The idea is to produce a secondary disturbance to cancel the effect of the primary disturbance at the locations of the error sensors. This type of control strategy does not guarantee global control unless the response is dominated by a limited number of modes that are detected by the sensors. The implementation of this type of control does not need a detailed model of the system under control. The performance of a feed-forward control system relies on the delicate balance between the interaction of the primary and secondary sources, therefore the amplitude and phase of a feed-forward controller must be carefully adjusted. Thus, to guarantee a good performance of the controller, it is of crucial importance to use an efficient adaptive algorithm that tunes the feed-forward controller in real time [14].

When a reference signal is not available, for example when a mechanical system is subjected to a broadband random disturbance from many sources, the most suitable control strategy is feedback control. In feedback control, the control signal measured by a sensor is influenced by both the primary and secondary source and fed back to the actuator. In principle feedback

control can be used to control tonal disturbances as well, although, in general, fixed feedback controllers underperform compared to feed-forward systems [14].

Multichannel vibration feedback control systems can be classified in two types. In the first one, all the actuators are driven by a single, centralised, controller, which uses the signals measured by all of the sensors. In general the number and type of actuators and sensor transducers is chosen in such a way as to measure and excite the vibration component of the structure to be controlled. Thus they do not need to be collocated and a different number of sensors and actuators may be used to selectively control different modes [7, 11, 15]. This arrangement is called centralised control; its design needs an accurate model of the plant responses in order to properly set the control functions and its implementation can be rather complicated. The plant responses are often derived from modal models, which are accurate only at low frequencies where the response of the structure is controlled by a small number of modes [15]. Thus the performance and stability of such a centralised control system can be affected by changes in the operation conditions of the structure (e.g. tensioning effects, temperature variations, etc.). Also failure of one control channel can disrupt the operation of the whole control system.

The second multichannel control arrangement uses an equal number of sensors and actuators, which are arranged in pairs. Each sensor–actuator pair is treated as an independent control unit so that the error signal measured by one sensor is only used to drive the collocated actuator. The advantage of this decentralised control architecture is the simplicity of the control loops, which can be simple gains for ideal force actuators and velocity sensors, whose design does not rely on a model of the plant response [7, 16, 17]. Since such loops are unconditionally stable [18], the failure of one control unit has no effect on the stability of the other units. Thus decentralised control systems offer a more robust but less selective approach to control, which can be based on modular control units that are evenly scattered on the system to be controlled [17]. In fact a whole range of possible control architectures exist between the fully centralised and fully decentralised, which are often described as distributed [19].

Conventional feedback design is usually based on the assumption of time-invariance, which means that the control system and the mechanism of generating the control signal have constant coefficients. In practice, however, systems parameters can change during time. The self-tuning controller philosophy takes into account process changes of the system with time by automatic adjustment of the controller’s parameters to optimise the control performance. In self-tuning control, the adaptation mechanism often consists of identifying the system by measuring input and output data, compare the status of the system with the desired one and tuning the controller to achieve this condition [20]. This approach makes the system self-adaptable to a wide range of operating conditions and different configurations of the system under control.

An example could be an active control system for reducing the vibrations of an aircraft panel, to reduce the noise transmitted inside the cabin. The fuselage is excited by a broadband disturbance due to turbulent boundary layer or jet engines for example [13]. The pressurisation of the cabin during the flight can produce a change of the lower resonance frequencies of the panels by a factor of three [21]. A self-tuning controller can adapt to changes of the system under control, guaranteeing an optimal reduction of the panels' vibration for different operating conditions. Another advantage is that a generic control system could be used in the same configuration to control different structures (panel with different thickness for example) without requiring a redesign process. If a fully decentralised arrangement is used, global information on the response of system is not available at each independent control unit, and thus it is not possible to automatically tune the control units in such a way that overall vibration of a structure is minimised. In this thesis the possibility of self-tuning independent control units to obtain a global effect of minimising the spatially averaged vibration of a structure is investigated.

1.5. Contributions of the thesis

The novel contributions of this thesis are:

- To demonstrate that for broadband excitation, tuning the damping of a dynamic vibration absorber to maximise its power absorption is exactly equivalent to tuning the damping to minimise the kinetic energy of a single degree of freedom host structure.
- To propose a self-tuning strategy of decentralised velocity feedback loops based on the maximisation of the absorbed power, in which the tuning process only relies on the local feedback signal.
- To assess the practical implementation of self-tuning decentralised velocity feedback control on a thin aluminium panel with multiple reactive actuators.
- To investigate the maximisation of absorbed power as self-tuning strategy of decentralised velocity feedback loops using inertial actuators.
- To provide a preliminary theoretical study to assess self-tuning broadband control of lightly damped structures using shunted electromagnetic inertial actuators.

1.6. Structure of the thesis

This thesis is organised in nine chapters.

Chapter 1 provides a brief introduction on the motivations and technical background for passive, semi-active and active vibration control of mechanical systems. Also the original contributions of this research are summarised and the structure of this dissertation is outlined.

Chapter 2 presents an analytical analysis of vibration control of lumped parameter systems subjected to a broadband disturbance and controlled by a tuneable damper. Two tuning

strategies are compared: the minimisation of the kinetic energy of the system and the maximisation of the power absorbed by the tuneable damper. Firstly, the simple case of a single degree of freedom system with a tuneable damper is considered. The analysis is then extended to a two degrees of freedom system consisting of two coupled oscillators. One of the two masses is subjected to a broadband disturbance and the vibration is controlled using a single end grounded damper acting on the other mass. An analytical expression of the optimal damping coefficient is found for the case where the two oscillators are connected by a spring and is presented in Appendix A. For the general case in which the two masses are connected by a spring and a damper, numerical simulations are carried out to compare the different tuning strategies.

Chapter 3 considers the vibration control of distributed structures subjected to a broadband disturbance using decentralised velocity feedback loops consisting in ideal collocated sensor-actuator pairs. This type of control approach corresponds on having a single end grounded damper attached to the structure at control positions. Different strategies of tuning the control gains of multiple feedback loops are compared. A self-tuning algorithm based on the maximisation of the individual power absorbed by each feedback loop is presented. The advantage of using the absorbed power as cost function to tune the control gain is that its estimation can be accomplished using the feedback signal only without requiring extra sensors to monitor the global response of the system. The formulation used to derive the mathematical model of lightly damped beams and panels controlled by a multichannel controller for deterministic and stochastic excitations is derived in Appendix B.

Chapter 4 describes the experimental test rig built for the implementation of multichannel control of a clamped aluminium panel excited by a shaker fed with white noise. Nine control units are mounted on the panel each consisting in a voice coil actuator closely collocated with an accelerometer. Particular care is taken in the design of the controller in order to guarantee the stability of the control system for values of control gains higher than the one producing the transition in the control action between optimum damping and pinning of the structure. Simulations results of the closed loop response of the system based on measured open loop responses are presented in order to predict the performance of the control system. A complete set of measurement for nine single control channels of the measured open loop and simulated close loop responses is presented in Appendix C.

Chapter 5 presents the experimental results for the implementation of the self-tuning control based of the maximisation of the power absorbed by the controller for single and two channels control system. The experimental results of the single channel control using one of the two control unit can be found in Appendix D.

Chapter 6 discusses simulations results of lightly damped panel controlled by a single velocity feedback loop which uses an inertial electromagnetic actuator when the structure is subject to a broadband disturbance. The need of using such inertial devices in vibration control arises from the fact that it is often not possible to use reactive actuator in practice, since there may be a solid structure to react the force against. It is illustrated that maximising the mechanical absorbed power provides a reasonable approximation to minimising the kinetic energy of the host structure. The problems arising from the instability caused by these devices are also discussed. The mechanical and electrical impedances of an inertial electromagnetic actuator are derived in Appendix E.

Chapter 7 introduces the use of the dynamic vibration absorbers to control broadband vibration. The DVA is used here to control the vibration of a single degree of freedom system subject to broadband disturbance. The maximisation of the power absorbed by the DVA is compared to the minimisation of the kinetic energy of the host structure. The parameters involved in the optimisation are the frequency ratio of the natural frequencies of the decoupled SDOF systems and their damping ratios. It is demonstrated that the two tuning strategies are exactly the same.

Chapter 8 presents preliminary studies of a self-tuning semi-active controller using electromechanical inertial actuator. The system consists of an electromechanical inertial actuator with an adaptable electrical shunt that acted as a passive damper and also as a source of electrical energy to drive the self-tuning circuit.

Chapter 9 summarises the findings of this thesis and presents suggestions for further work.

2. Comparison of tuning strategies for broadband control of lumped parameter systems

In this chapter the broadband vibration control of lumped parameter systems using a tuneable damper is investigated. The aim is to compare two different control strategies: the minimisation of the total kinetic energy of the system and the maximisation of the total power absorbed by the tuneable damper. A single degree of freedom (SDOF) system excited by a broadband disturbance is initially considered. A two degree of freedom system is then considered, consisting of two coupled oscillators, one of which is subjected to a white noise disturbance and controlled by a tuneable damper acting on the other mass. Firstly, a simplified model is considered in which the two vibrating masses are connected by a spring. Secondly, a damper is added between the two masses.

2.1. Broadband control of a single degree of freedom system

In this section the broadband vibration control of a single degree of freedom system is considered. The system is composed by a vibrating mass *m*, a spring *k* and a viscous damper *c* as shown in Figure 2.1. The mechanical damping constant *c* can be varied.

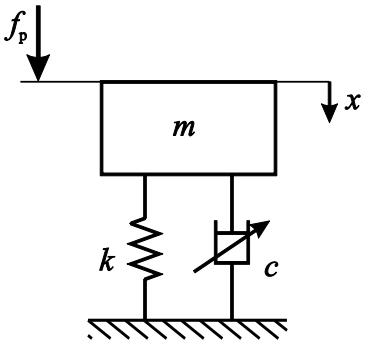

Figure 2.1: scheme of the single degree of freedom system with a tuneable damper.

The mass is excited by a white noise external force f_p. The equation of motion of the system can be written as:

$$m\ddot{x}(t) + c\dot{x}(t) + kx(t) = f_p(t) \tag{2.1}$$

where $x(t)$ is the displacement of the mass. The steady-state response of the oscillator is expressed assuming time-harmonic excitation for the time being of the form $\mathrm{Re}\{\exp(j\omega t)\}$ where ω is the angular frequency and $j = \sqrt{-1}$. For brevity the time harmonic term $\exp(j\omega t)$ will be omitted in the formulation which will be given in complex form. Therefore the time

harmonic displacement $x(t) = \mathrm{Re}\{\tilde{x}(\omega)\exp(j\omega t)\}$ and the force $f_p(t) = \mathrm{Re}\{\tilde{f}_p(\omega)\exp(j\omega t)\}$ will be replaced by the frequency dependent complex displacement and the force phasors $\tilde{x}$ and $\tilde{f}_p$. Throughout the thesis ~ will be used to identify complex, frequency-dependant functions. The displacement $\tilde{x}$ is then given by:

$$\tilde{x} = \frac{\tilde{f}_\mathrm{p}}{-\omega^2 m + j\omega c + k} \tag{2.2}$$

Deriving equation (2.2) the velocity of the mass per unit input force can be written as:

$$\tilde{\mathrm{Y}} = \frac{\tilde{v}}{\tilde{f}_\mathrm{p}} = \frac{j\omega}{-\omega^2 m + j\omega c + k} \tag{2.3}$$

Assuming that the excitation force $\tilde{f}_\mathrm{p}$ is random with a power spectral density, PSD, of $S_\mathrm{f}(\omega)$ (with the unit of N^2s/rad) the PSD of the kinetic energy of the moving mass is given by:

$$S_\mathrm{k}(\omega) = \frac{1}{2} m \left|\tilde{\mathrm{Y}}\right|^2 S_\mathrm{f}(\omega) \tag{2.4}$$

and substituting equation (2.3) in (2.4) yields:

$$S_\mathrm{k}(\omega) = \frac{1}{2} m \left|\frac{j\omega}{-\omega^2 m + j\omega c + k}\right|^2 S_\mathrm{f}. \tag{2.5}$$

where $S_\mathrm{f}(\omega)$ is now assumed to be a constant, S_f, independent of frequency, corresponding to white noise force excitation. If the aim of the tuneable damper is to minimise the integral of the kinetic energy of the mass *m* for frequencies between $\pm\infty$, so that the quantity to be minimised is given by:

$$KE = \int_{-\infty}^{\infty} S_\mathrm{k}(\omega) d\omega \tag{2.6}$$

Substituting equation (2.5) in (2.6) and using the integral tables given in reference [22] *KE* is given by:

$$KE = \frac{\pi}{2c} S_\mathrm{f} \tag{2.7}$$

Figure 2.2 shows the total kinetic energy as function of the damping constant *c*. It is interesting to notice that the total kinetic energy of the mass does not depend on the value of *m*. As expected the total kinetic energy of the mass decreases as the mechanical damping increases.

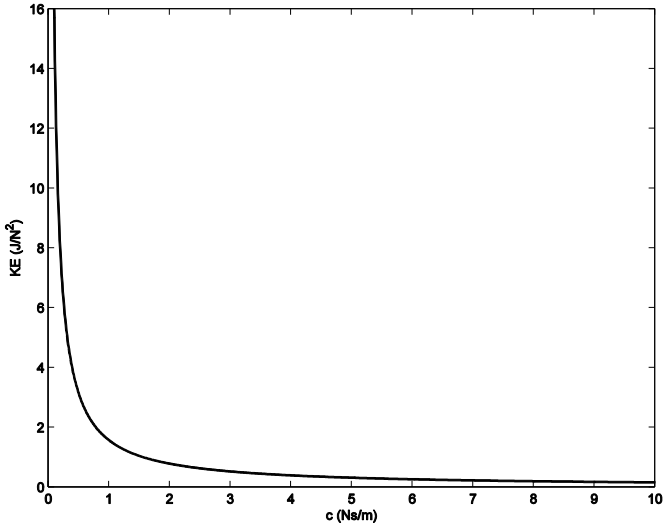

Figure 2.2: Total kinetic energy of the vibrating mass as function of the mechanical damping *c*.

For *c* equal zero the total kinetic energy tends to infinity since the system is undamped. For very high values of the control gain the effect of the controller is to stop the vibration of the mass so that its total kinetic energy tends to zero. This means that the overall response of the system is minimised when the value of *c* tends to infinity.

An alternative strategy of tuning the damper to obtain broadband control of the mass *m* is to maximise the power absorbed by the tuneable damper given by:

$$S_{\mathrm{P}}(\omega) = \frac{1}{2}\mathrm{Re}\{\tilde{f}_{\mathrm{d}}^{*}\tilde{v}\} \tag{2.8}$$

where * denotes the conjugate value of a complex number and $\tilde{f}_d$ is the force produced by the damper given by:

$$\tilde{f}_d = c\tilde{v} \tag{2.9}$$

Substituting equation (2.9) in (2.8) and assuming the primary disturbance to have a constant spectrum equal to unity, the PSD of the absorbed power is given by:

$$S_{\mathrm{P}}(\omega) = \frac{1}{2}c|\tilde{\mathrm{Y}}|^{2}S_{\mathrm{f}} \tag{2.10}$$

If the aim of the tuneable damper is to maximise the integral of the absorbed power between $\pm\infty$, the quantity to be maximised is equal to:

$$P = \int_{-\infty}^{\infty} S_{\mathrm{P}}(\omega)d\omega \tag{2.11}$$

Substituting equation (2.10) in (2.11) and using the integral tables given in reference [22] *P* is given by:

$$P = \frac{\pi}{2m} S_{\mathrm{f}} \tag{2.12}$$

Equation (2.12) shows that for this simple system the absorbed power does not depend on the value of the mechanical damping *c* and so this cannot be used as strategy of tuning the damping in the system. In this case the mathematical solution seems to be in contrast with the physical explanation, that if *c* tends to infinity the velocity of the mass tends to zero and no power should be dissipated by the damper. If the power absorbed is numerically integrated over a finite frequency band, *P* can be expressed as:

$$P = \frac{1}{2} c S_{\mathrm{f}} \int_0^{\omega_{\max}} |\tilde{Y}|^2 d\omega = c S_{\mathrm{f}} \sum_{i=1}^{N} |\tilde{Y}|^2 \Delta\omega_i \tag{2.13}$$

where $\Delta\omega_i$ is the sampling circular frequency and $\omega_{\max}$ is the maximum frequency considered. The integration band can include only positive frequency value because $\tilde{Y}(-\omega) = \tilde{Y}^*(\omega)$. Figure 2.3 shows the power absorbed integrated between 1 Hz-1 kHz (solid line), between 1 Hz-10 kHz (dashed line), 1 Hz-100 kHz (dotted line) and 0-infinity when *m* is 1 Kg and *k* is 40 N/m. The power absorbed is equal to $\pi/(4m)$ for low values of *c*. The plot also shows that for high value of *c* the absorbed power tends to zero if the integration frequency band is finite and it goes more rapidly to zero for smaller integration frequency bands.

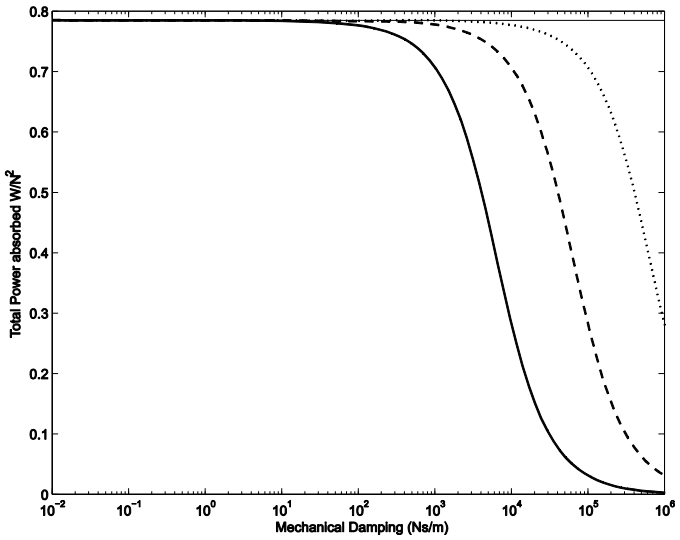

Figure 2.3: power absorbed by the damper as function of the mechanical damping *c* integrated between 0-1kHz (solid line), 0-10 kHz (dashed line), 0-100 kHz (dotted line) and 0-infinity (faint line).

The paradox between the mathematical and physically intuitive result is thus due to the infinite bandwidth assumed for the PSD of the applied force. This makes the single degree of freedom system a poor choice of model problem in this case.

2.2. Broadband control of a two degrees of freedom system

In this section the broadband control of the two degrees of freedom system shown in Figure 2.4 is analysed. The scheme shows a system comprising two coupled oscillators where $m_{1,2}$ are the masses, $k_{1,2,3}$ the stiffness of the springs and $c_{1,2,3}$ are the damping constants. The external force f_p is applied on mass 1.

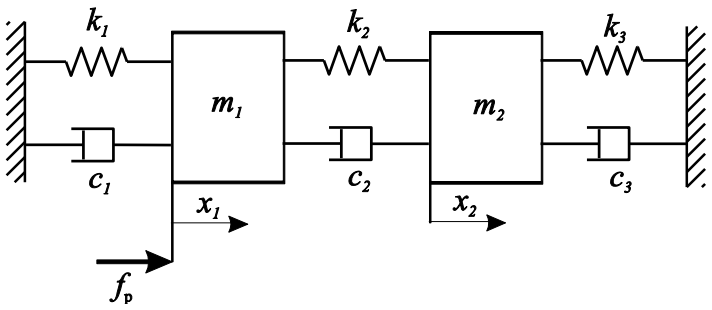

Figure 2.4: Two degrees of freedom system excited by a force f_p.

The equation of motion of the system shown in Figure 2.4 can be written in the matrix form as:

$$\mathbf{M}\ddot{\boldsymbol{x}}(t) + \mathbf{C}\dot{\boldsymbol{x}}(t) + \mathbf{K}\boldsymbol{x}(t) = \boldsymbol{f}(t) \tag{2.14}$$

Where **M** is the mass matrix, **K** is the stiffness matrix and **C** is the damping matrix given by:

$$\mathbf{M} = \begin{bmatrix} m_1 & 0 \\ 0 & m_2 \end{bmatrix},\ \mathbf{K} = \begin{bmatrix} k_1 + k_2 & -k_2 \\ -k_2 & k_2 + k_3 \end{bmatrix},\ \mathbf{C} = \begin{bmatrix} c_1 + c_2 & -c_2 \\ -c_2 & c_2 + c_3 \end{bmatrix}, \tag{2.15}$$

$\boldsymbol{x}(t) = [x_1(t) \quad x_2(t)]^T$ is the column vector containing the displacements of the two masses x_1 and x_2 and $\boldsymbol{f}(t) = [f(t) \quad 0]^T$ is the column vector of primary excitation.

Assuming the excitation to be harmonic for the time being and expressing the force and the steady-state response in exponential form, equation (2.14) becomes:

$$\tilde{\mathbf{S}}\tilde{\mathbf{x}} = \tilde{\mathbf{f}} \tag{2.16}$$

where

$$\tilde{\mathbf{S}} = -\omega^2\mathbf{M} + j\omega\mathbf{C} + \mathbf{K} \tag{2.17}$$

is the dynamic stiffness matrix. The solution of equation (2.16) can be obtained as:

$$\tilde{\mathbf{x}} = \tilde{\mathbf{S}}^{-1}\tilde{\mathbf{f}} \tag{2.18}$$

Integrating equation (2.18) to obtain the velocities yields:

$$\tilde{\mathbf{v}} = \tilde{\mathbf{Y}}\tilde{\mathbf{f}} \tag{2.19}$$

where $\tilde{\mathbf{v}} = j\omega\tilde{\mathbf{x}}$ and $\widetilde{\mathbf{Y}} = j\omega\tilde{\mathbf{S}}^{-1}$ is the mobility matrix. Using the expression of **M**, **K** and **C** of equations (2.15) the velocities per unit input force of the two masses are given by:

$$\tilde{Y}_{11} = \frac{B_0 + (j\omega)B_1 + (j\omega)^2 B_2 + (j\omega)^3 B_3}{A_0 + (j\omega)A_1 + (j\omega)^2 A_2 + (j\omega)^3 A_3 + (j\omega)^4 A_4} \tag{2.20}$$

$$\tilde{Y}_{12} = \frac{C_0 + (j\omega)C_1 + (j\omega)^2 C_2 + (j\omega)^3 C_3}{A_0 + (j\omega)A_1 + (j\omega)^2 A_2 + (j\omega)^3 A_3 + (j\omega)^4 A_4} \tag{2.21}$$

where

$A_0 = k_1k_3 + k_2k_3 + k_1k_2$	$B_0 = 0$	$C_0 = 0$
$A_1 = c_2k_1 + c_3k_1 + c_1k_2 + c_3k_2 + c_1k_3 + c_2k_3$	$B_1 = k_2 + k_3$	$C_1 = k_2$
$A_2 = c_1c_2 + c_1c_3 + c_2c_3 + k_2m_1 + k_3m_1 + k_1m_2 + k_2m_2$	$B_2 = c_2 + c_3$	$C_2 = c_2$
$A_3 = c_2m_1 + c_3m_1 + c_1m_2 + c_2m_2$	$B_3 = m_2$	$C_3 = 0$
$A_4 = m_1m_2$		

Two different configurations of the two degrees of freedom system of Figure 2.4 are considered in this section. In the first configuration the damper c_2 is assumed to be zero, while in the second configuration all the parameters are different from zero. In both configurations the primary force, which is assumed to be white noise with a PSD of unity at all frequencies and the tuneable damper is the damper c_3. Table 2.1 shows a summary of all the optimisation implemented on different configurations with the respective sections.

Table 2.1: summary of the different configurations of the two degrees of freedom considered in this section

N.	System's Configurations	Scheme	Optimisation	Subsection
1.	Two DOF system controlled by a grounded damper	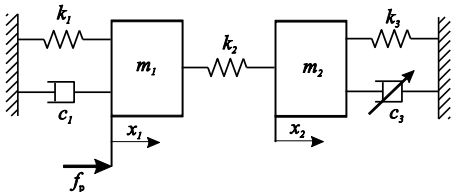	Minimisation of kinetic energy of m_1 Maximisation of power absorbed by c_3	2.2.1
2.	Case of a general two DOF system controlled by a grounded damper	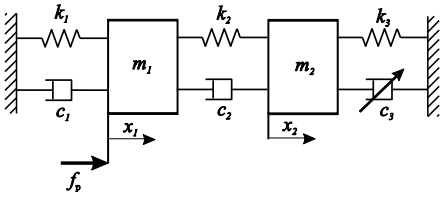	Minimisation of kinetic energy of m_1 Minimisation of kinetic energy of the entire system Maximisation of power absorbed by c_3	2.2.2

2.2.1. Case of a simplify two DOF system controlled by a grounded damper

The simplified two degrees of freedom system shown in Figure 2.5 is considered in this subsection.

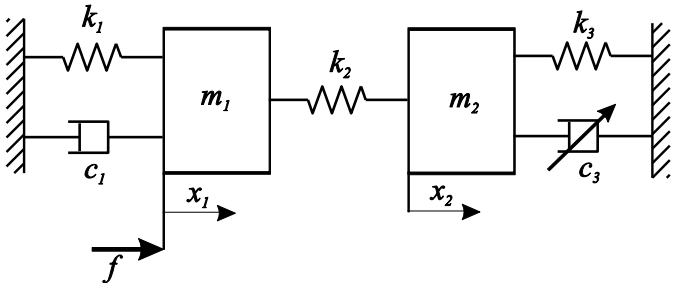

Figure 2.5: Two DOF system controlled by a single end grounded damper and c_2=0

For this configuration, with white noise force excitation, the $\pm\infty$ frequency integrated power input, P_{in}, to the system is independent of c_3 [23]. The balance between the power input and out to the system is thus equal to:

$$P_{\text{in}} = P_{\text{abs1}} + P_{\text{abs3}} \tag{2.22}$$

where P_{abs1} is the power dissipated by damper 1 and P_{abs3} is the power dissipated by damper 3. Differentiating equation (2.22) with respect of c_3 yields:

$$\frac{\partial P_{\text{abs1}}}{\partial c_3} + \frac{\partial P_{\text{abs3}}}{\partial c_3} = 0 \tag{2.23}$$

The PSD of the power absorbed by the damper 1 is given by:

$$S_{\text{P1}}(\omega) = \frac{1}{2}\text{Re}\{\tilde{f}_{\text{d}}^{*}\tilde{v}_1\} \tag{2.24}$$

where $\tilde{f}_{\text{d}}$ is the force produced by the damper 1 given by:

$$\tilde{f}_{\text{d}} = c_1\tilde{v}_1 \tag{2.25}$$

Substituting equation (2.25) in (2.24) and assuming white noise excitation, the PSD of the power absorbed by damper 1 can be written as:

$$S_{\text{P1}}(\omega) = \frac{1}{2}c_1|\tilde{Y}_{11}|^2 S_{\text{f}}(\omega), \tag{2.26}$$

and the PSD of the kinetic energy of mass 1 is given by:

$$S_{\text{K1}}(\omega) = \frac{1}{2}m_1|\tilde{Y}_{11}|^2 S_{\text{f}}(\omega). \tag{2.27}$$

where $S_{\text{f}}(\omega)$ is the PSD of the excitation force $\tilde{f}_{\text{p}}$. From equations (2.26) and (2.27), the frequency averaged power absorbed by damper 1 and the total kinetic energy of mass m_1 are given by:

$$P_{abs1} = \frac{1}{2}c_1\int_{-\infty}^{+\infty}|\tilde{Y}_{11}|^2\,d\omega \tag{2.28}$$

$$KE_1 = \frac{1}{2}m_1\int_{-\infty}^{+\infty}|\tilde{Y}_{11}|^2\,d\omega \tag{2.29}$$

where $S_{\text{f}}(\omega)$ is now assumed to be unity. Equations (2.28) and (2.29) indicate that the power absorbed by damper 1 is proportional to the kinetic energy of mass 1 and thus also the derivative with respect of c_3 of equation (2.28) is proportional to the derivative with the respect of c_3 of the kinetic energy of mass 1. Thus equation (2.23) yields to

$$\frac{\partial P_{\text{abs3}}}{\partial c_3} \propto -\frac{\partial KE_1}{\partial c_3} \tag{2.30}$$

Equation (2.30) shows that setting the value of c_3 to maximise the power dissipated by the damper 3, corresponds to minimise the kinetic energy of the mass m_1.

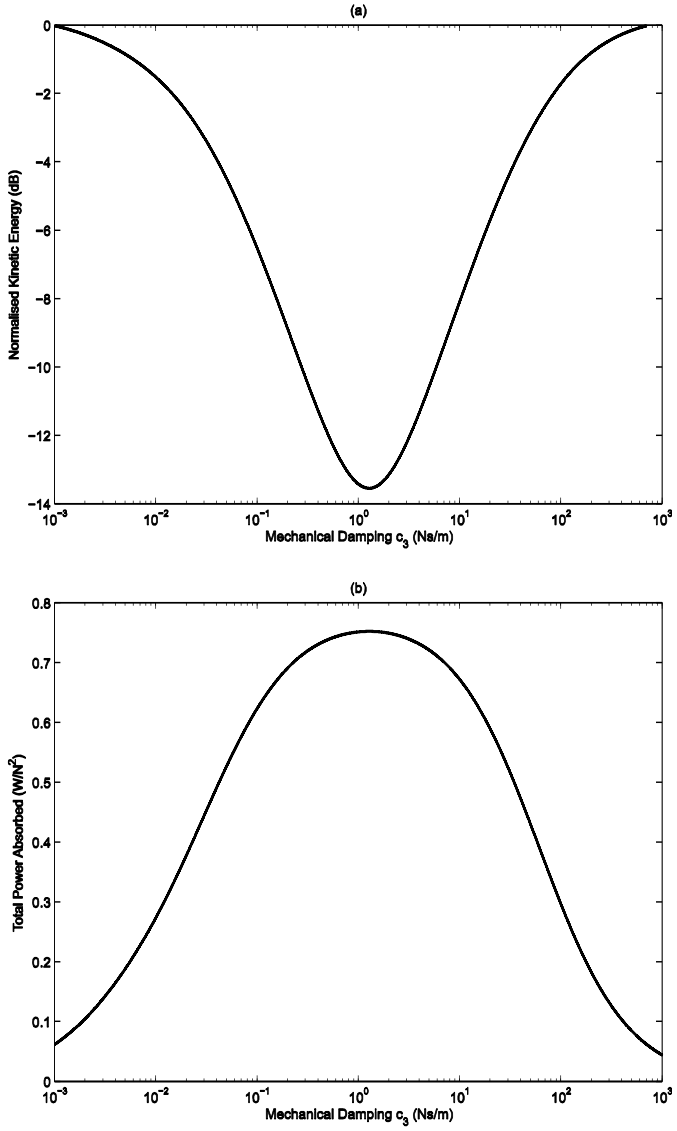

Figure 2.6: $\pm\infty$ frequency integrated (a) kinetic energy of a two DOF system consisting in two coupled oscillators connected by a spring and (b) power absorbed by damper 3 as function of the mechanical damping c_3.

Figure 2.6(a) and (b) shows the simulated $\pm\infty$ frequency integrated kinetic energy of the system and power absorbed by the damper 3 as function of the mechanical damping c_3. The parameters used in these simulations are listed in Table 2.2. The kinetic energy of the mass m_1 is minimised for the same value of c_3 (1.27 Ns/m) that maximises the power absorbed by damper 3. Analytical expressions for the optimal damping c_3 are derived in Appendix A in the case of c_2 and k_3 equal zero.

Table 2.2: physical parameters of the two degrees of freedom system

$m_1 = 1$ Kg	$k_1 = 1.3$ N/m	$c_1 = 0.02$ Ns/m
$m_2 = 0.5$ Kg	$k_2 = 2$ N/m	$c_2 = 0$ Ns/m
	$k_3 = 1.5$ N/m	

2.2.2. Case of a general two DOF system controlled by a grounded damper

The two degrees of freedom system considered in this subsection is shown in Figure 2.7. The integral of the total kinetic energy of the mass m_1, the total kinetic energy of the entire system and the power absorbed by the tuneable damper are compared as tuning strategy of the mechanical damping c_3.

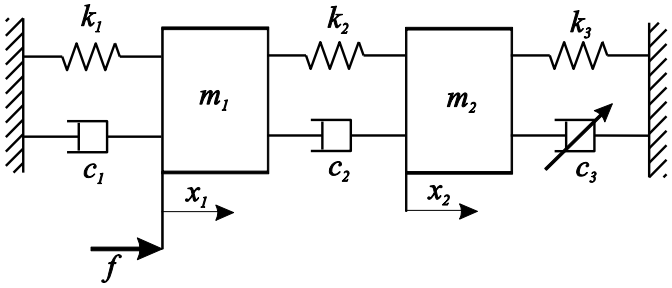

Figure 2.7: general two degrees of freedom system controlled by a single end grounded damper.

Assuming the excitation being white noise, the kinetic energy of mass two, KE_2 is given by:

$$KE_2 = \frac{1}{2} m_2 \int_{-\infty}^{+\infty} |\tilde{Y}_{12}|^2 \, d\omega \tag{2.31}$$

In this general case the frequency integrated power input is not constant, therefore it is not guaranteed that the maximisation of the power absorbed correspond to the minimisation of the kinetic energy of the mass m_1. Substituting the expression of the mobilities given in equations (2.20) and (2.21), when all the parameter of the system are different from zero, in equation (2.28), (2.29) and (2.31), KE_1, KE_2 and P_{abs3} can be written as:

$$KE_1 = \frac{\begin{array}{c}(\pi(-(k_2+k_3)^2 m_1((c_2+c_3)m_1+(c_1+c_2)m_2)+ \\ \big(c_3(k_1+k_2)+c_2(k_1+k_3)+c_1(k_2+k_3)\big)m_1(-(c_2+c_3)^2+2(k_2+k_3)m_2)+ \\ m_2((k_2k_3+k_1(k_2+k_3))((c_2+c_3)m_1+(c_1+c_2)m_2)-(c_3(k_1+k_2)+c_2(k_1+k_3)+ \\ c_1(k_2+k_3))(c_2c_3+c_1(c_2+c_3)+(k_2+k_3)m_1+(k_1+k_2)m_2))))\end{array}}{\begin{array}{c}(4(\big(c_3(k_1+k_2)+c_2(k_1+k_3)+c_1(k_2+k_3)\big)^2 m_1m_2+ \\ \big(k_2k_3+k_1(k_2+k_3)\big)\big((c_2+c_3)m_1+(c_1+c_2)m_2\big)^2- \\ (c_3(k_1+k_2)+c_2(k_1+k_3)+ \\ c_1(k_2+k_3))((c_2+c_3)m_1+(c_1+c_2)m_2) \\ (c_2c_3+c_1(c_2+c_3)+(k_2+k_3)m_1+(k_1+k_2)m_2)))\end{array}} \tag{2.32}$$

$$KE_2 = \frac{(\pi m_2(-c_2^2(c_3(k_1+k_2)+c_2(k_1+k_3)+c_1(k_2+k_3))-k_2^2(c_3m_1+c_1m_2+c_2(m_1+m_2)}{\begin{array}{c}(4(\big(c_3(k_1+k_2)+c_2(k_1+k_3)+c_1(k_2+k_3)\big)^2 m_1m_2+\\ \big(k_2k_3+k_1(k_2+k_3)\big)\big((c_2+c_3)m_1+(c_1+c_2)m_2\big)^2-\\ (c_3(k_1+k_2)+c_2(k_1+k_3)+\\ c_1(k_2+k_3))((c_2+c_3)m_1+(c_1+c_2)m_2)\\ (c_2c_3+c_1(c_2+c_3)+(k_2+k_3)m_1+(k_1+k_2)m_2)))\end{array}} \quad (2.33)$$

$$P_{\text{abs3}} = \frac{\begin{array}{c}(\pi c_3(-c_2^2(c_3(k_1+k_2)+c_2(k_1+k_3)+c_1(k_2+k_3))\\ -k_2^2(c_3m_1+c_1m_2+c_2(m_1+m_2))))\end{array}}{\begin{array}{c}(4(\big(c_3(k_1+k_2)+c_2(k_1+k_3)+c_1(k_2+k_3)\big)^2 m_1m_2+\\ \big(k_2k_3+k_1(k_2+k_3)\big)\big((c_2+c_3)m_1+(c_1+c_2)m_2\big)^2-\\ (c_3(k_1+k_2)+c_2(k_1+k_3)+\\ c_1(k_2+k_3))((c_2+c_3)m_1+(c_1+c_2)m_2)\\ (c_2c_3+c_1(c_2+c_3)+(k_2+k_3)m_1+(k_1+k_2)m_2)))\end{array}} \quad (2.34)$$

The total kinetic energy of the system is given by the sum of the individual kinetic energy of the two masses leading to:

$$KE = \frac{\begin{array}{c}(\pi(-(k_2+k_3)^2m_1((c_2+c_3)m_1+(c_1+c_2)m_2)+(c_3(k_1+k_2)+c_2(k_1+k_3)+c_1(k_2+k_3))m_1\\ (-(c_2+c_3)^2+2(k_2+k_3)m_2)+m_2(-c_2^2(c_3(k_1+k_2)+c_2(k_1+k_3)+c_1(k_2+k_3))-\\ k_2^2((c_2+c_3)m_1+(c_1+c_2)m_2))+m_2((k_2k_3+k_1(k_2+k_3))((c_2+c_3)m_1+(c_1+c_2)m_2)-\\ (c_3(k_1+k_2)+c_2(k_1+k_3)+c_1(k_2+k_3))(c_2c_3+c_1(c_2+c_3)+(k_2+k_3)m_1+(k_1+k_2)m_2))))\end{array}}{\begin{array}{c}(4(\big(c_3(k_1+k_2)+c_2(k_1+k_3)+c_1(k_2+k_3)\big)^2 m_1m_2\\ -\big(c_3(k_1+k_2)+c_2(k_1+k_3)+c_1(k_2+k_3)\big)\\ (c_2c_3+c_1(c_2+c_3)+k_2m_1+k_3m_1+k_1m_2+k_2m_2)\\ (c_3m_1+c_1m_2+c_2(m_1+m_2))+(k_2k_3+k_1(k_2+k_3))(c_3m_1+c_1m_2+c_2(m_1+m_2))^2))\end{array}}$$

(2.35)

Because of the complexity of these expressions it has not been possible to find analytical solutions for the various optimisations but to gain a better understanding of the physical behaviour of the system a specific case has been taken into account. The physical parameter of the system are summarised in Table 2.3.

Table 2.3: physical parameters of the two degrees of freedom system

$m_1 = 1$ Kg	$k_1 = 1.3$ N/m	$c_1 = 0.02$ Ns/m
$m_2 = 0.5$ Kg	$k_2 = 2$ N/m	$c_2 = 0.03$ Ns/m
	$k_3 = 1.5$ N/m	

Figure 2.8 shows the PSD of the kinetic energy of the system for different values of c_3. When c_3 is equal zero the response is characterised by two resonances (solid line). When c_3 is increased the two resonances are gradually damped. The dashed and dash-dotted line in Figure 2.8 represent the response of the system when the total kinetic energy is minimised and when the power absorbed by the tuneable damper is maximised respectively, while the dotted line shows the response when only the kinetic energy of the mass m_1 is minimised. The plot shows that there is no much difference in the three optimisations in term of the total response of the system. For very high values of c_3 the response is characterised by a single resonance. In this case the effect of the damper is to pin the mass m_1 so that the system behaves like a single degree of freedom system.

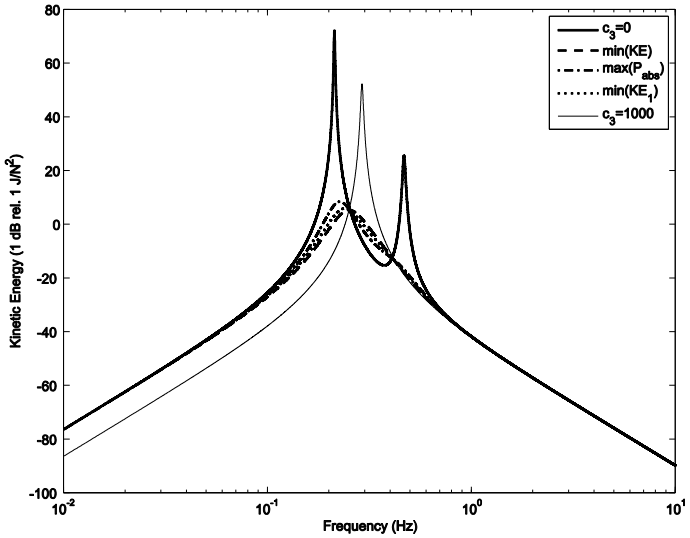

Figure 2.8: PSD of the total kinetic energy of the system when: c_3=0 (solid line), KE in minimised (dashed line), P_{abs3} is maximised (dash-dotted line), KE_1 in minimised (dotted line) and c_3=1000 Ns/m (faint line)

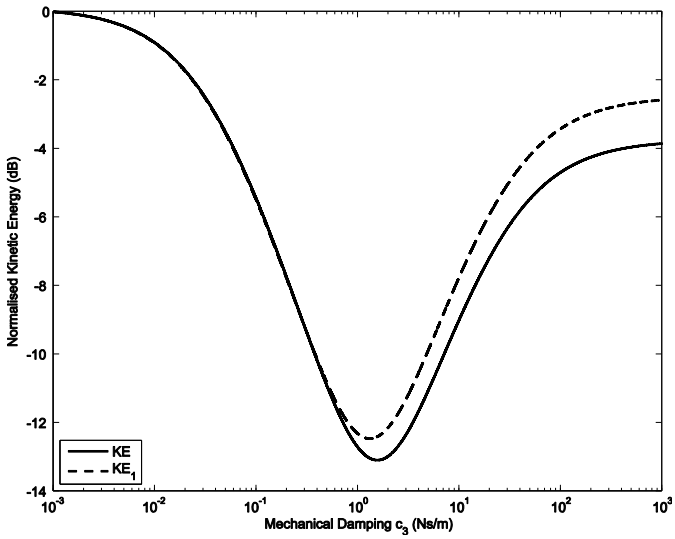

Figure 2.9: total kinetic energy of the system (solid line) and kinetic energy of the mass m_1 as function of the mechanical damping c_3.

Figure 2.9 shows the total kinetic energy of the system (solid line) and the kinetic energy of the mass 1 (dashed line) normalised to the value of the kinetic energy for c_3 equal zero as function of c_3. The plot shows that both curves decrease when c_3 is increased until they reach a minimum and start to increase again when c_3 is further increased. The two curves are minimised for about the same value of c_3.

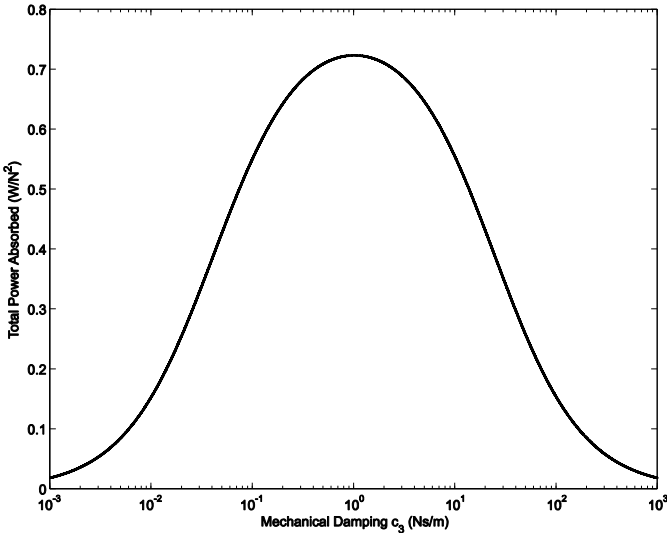

Figure 2.10: Total power absorbed by the tuneable damper as function of the mechanical damping c_3.

Figure 2.10 shows the power absorbed by the damper 3 as function of the mechanical damping c_3. The plot shows that the power absorbed is zero when c_3 is zero and increases when c_3 is increased until it reaches a maximum. For very high values of c_3 the power tends to zero. In this case the effect of the damper is to pin the second mass such that its velocity goes to zero and no power is absorbed. The maximum of the power absorbed by the tuneable damper roughly corresponds to the minimum of the total kinetic energy of the system and the kinetic energy of the mass m_1.

Table 2.4: optimal values of c_3 and the corresponding attenuation in the total kinetic energy of the system.

	Optimal values of c_3 (Ns/m)	Attenuation in the total kinetic energy of the system (KE) in dB
Minimising *KE*	1.556	-13.1
Maximising P_{abs3}	1.010	-12.7
Minimising KE_1	1.313	-13.0

A summary of the optimal damping values together with the corresponding attenuation in the total kinetic energy of the system in dB are summarised in Table 2.4. Although the optimum values of c_3 are slightly different, the attenuation in the total kinetic energy of the system is only

0.1 dB higher when the kinetic energy of the mass m_1 is minimised and about 0.4 dB higher when the absorbed power is maximised. In the case of a general two degree of freedom system the maximisation of power absorbed as strategy of tuning a single-end grounded damper seems to be a good approximation for the minimisation of the kinetic energy of the entire system.

2.3. Summary and Conclusions

This chapter has presented a theoretical study of broadband vibration control of lumped parameter systems. Two control strategies have been compared: the minimisation of the total kinetic energy of the system under control and the maximisation of the power absorbed by a tuneable damper integrated over $\pm\infty$ frequency band. For a single degree of freedom system with a tuneable damper, the kinetic energy of the mass monotonically decreases when the damping increases, while the power absorbed by the damper tends to a finite value when the damping tends to infinity. This is in contrast with the more intuitive and physical explanation of zero absorbed power when the motion of the mass is constrained by the very high value of damping. This is due to the infinite bandwidth assumed for the PSD of the applied force, which makes the single degree of freedom system a poor choice of model problem in this case.

A two degree of freedom system has also been considered, consisting of two coupled oscillators, one of which is subjected by a white noise disturbance and which is controlled by a tuneable damper acting on the other mass. A simplified model in which the two oscillators are connected by a spring has been analysed first. In this case it has been demonstrated that the maximisation of the power absorbed by the tuneable damper corresponds exactly with the minimisation of the kinetic energy of the excited mass.

Finally a general two degree of freedom system in which the two masses are connected by a spring and a damper has been analysed. In this case no analytical expression of the optimal damping have been found but numerical simulation have shown that the values of damping that minimises the kinetic energy of the entire system, are very similar to those that minimises the kinetic energy of the excited mass and that maximises the power absorbed by the damper. In the next chapter the analysis will be extended to distributed multi-degree of freedom systems.

3. Tuning strategies of decentralised velocity feedbacks for broadband control of distributed structures

This chapter considers various tuning strategies for feedback control on distributed structures such as beams and panels. A model is first introduced for lightly damped flexible structures excited by a primary disturbance and controlled by multichannel decentralised velocity feedback loops. Different control strategies of tuning the control gains of each independent feedback loop are implemented with the aim of obtaining broadband control. The first strategy considered tunes the feedback control gains in order to minimise the frequency-averaged total kinetic energy of the structure. The overall kinetic energy is a global property, however, and its measurement would require a dense array of sensors over the whole structure. Tuning the feedback gains on this criterion thus defeats the idea of having entirely locally-acting control loops. A parameter that can be measured entirely locally, however, is the mechanical power absorbed by the control loop. The background in using the absorbed power as a tuning strategy is reviewed in the first section. In this application the force is generated by the ideal actuator and is made proportional to the measured velocity. The absorbed power can thus be readily estimated from the mean square value of the measured velocity and the feedback gain, thus providing a simple measurement of an entirely local parameter that could be used to tune the gains. These two tuning methods are compared when the structure is subject to broadband, narrow band and single frequency disturbance.

A third tuning strategy considered is the maximisation of the control stability, which sets the control gains to maximise the damping ratio of a selected mode of the vibrating structure. In the last part of this chapter the performance of three tuning strategies are compered in controlling structural vibration of both a panel and a cantilever beam.

3.1. Background in self-tuning control using power absorption

In the last few years there has been much interest in developing strategies of self-tuning decentralised feedback loops.

Elliott *et al.* [24] used a model of a thin aluminium plate controlled by an array of 4x4 direct velocity feedback loops to study the performance of the controller. The feedback gains were set to constant equal values while the total kinetic energy of the plate was monitored. It was found that as the control gain increases the total kinetic energy is attenuated providing active damping on the excited modes. As the control gain becomes very large, the action of the feedback loops

is to pin the plate at the control positions, so that the structure has a new set of lightly damped modes. As result the kinetic energy of the plate started to rise again as the feedback gain is increased.

Another important finding of Elliott *et al.* [24] was that the optimum gain is approximately equal to the mobility of the infinite structure. It is interesting to note that this is a real, frequency independent quantity for a plate, but for a beam, it is frequency dependent and has real and imaginary components [25]. On the basis of this idea Engels *et al.* [26] estimated the optimum gain value from the frequency average of the real part of the control point mobility to self-tune the gain of the feedback control loop.

However, in a totally decentralized architecture the optimum gain cannot be deduced from global quantity such as, for example, the total kinetic energy of the plate. Another proposed strategy to tune the gains of decentralized feedback loops is the maximisation of the power absorbed by the control system. The power absorbed is a local quantity since is calculated on the base of the velocity at control position, measured by the error sensor, and the actuation force.

Experiments on active control of flexural wave power flow in structures were carried out by Redman - White *et al.* [27] who investigated active methods for reducing the magnitude of the vibrational power flow associated with the propagation of flexural waves in a beam. The two ends of the beam were terminated in sand boxes, which absorbed the vibrations, in order to simulate an infinite structure by avoiding reflection effects at the two ends of the beam. The beam was excited by a single frequency primary source located in the centre of the beam and controlled by a pair of closely spaced secondary control forces placed halfway between the primary excitation and the termination of a beam. The single frequency excitation signal was used as a reference for the secondary control sources in a feedforward control arrangement. The goal of the control system was to reduce the power flowing from the primary excitation into the section between the secondary source and the end of the beam. 36 dB of reduction in the power flowing between the control source and the end of the beam was achieved by maximising the power absorbed by the controller. This had the effect of simulating a perfectly absorbing termination such that the total power flowing downstream from the secondary source is controlled, while the power flowing from the primary source remains substantially unchanged.

Guicking et al. [28] used an analog feedback using an accelerometer and an electromagnetic shaker to control the vibration of a cantilever beam. The clamped edge of the beam included an absorbing material to reduce reflections simulating a semi-infinite structure. The aim of the analog controller was to maximise the absorbed power when the structure is excited at a single frequency by matching the control point structural impedance. The secondary source was placed at the free edge of the beam and was able to absorb all the power flowing

from the primary source, avoiding reflections. The power was estimated by measuring both the velocity at the control position and the control force.

Bardou *et al.* [29] further developed this approach by considering the two-dimensional vibration field on a plate using feedforward control. They compared two active control strategies in order to reduce the vibration of an infinite and a finite plate. The aim of the first one was to minimize the total power supplied to a plate while the aim of the second was to maximize the power absorbed by the secondary source. The work was focussed in the understanding of the physical limitations of using the two different strategies at single frequencies. A model of a plate excited by an array of single frequency primary forces and moments and controlled by an array of secondary forces and moments was considered. A general method was used for the calculation of the effect of minimizing the total power into the plate and the analytic results were obtained for different configurations of primary and secondary sources using combinations of moments and forces. In general the strategy where the total power produced by the primary and secondary sources is minimised provided the best control results. The other strategy where the power absorbed by the secondary sources is maximised produces rather different results for single frequency control, since the action of the control source tends to enhance the power input by the primary source and thus the total power in the structure tends to increase rather than decrease.

Hirami [30] used the maximization of power absorbed to actively control the vibration of finite structure. The first analysis was conducted on a single degree of freedom (SDOF) mass-spring-damping excited by a harmonic force. The vibration of the system was controlled using a velocity feedback loop with a complex control gain. It was shown that, in this case, the condition of maximum power absorption is not the same as that of the minimization of energy. For a real control feedback gain, it was shown that by maximizing the absorbed power the control gain converges to the magnitude of the mechanical input impedance of the system but the energy of the system is not minimized. The second example considered by Hirami [30] was a finite string in a steady state vibration condition when excited by a harmonic displacement at one end and controlled by a transversal force at the other end. The control force was set to be equal to the product of the velocity at that point and complex control function. The condition of maximum power absorption again tends to increase the total energy in the string, as it was found for SDOF system. Some attenuation was achieved when the excitation is close to a resonance frequency of the string. However, Hirami [30] showed that if the string is semi-infinite and the controller is placed at the end of it, the implementation of maximum power absorption is identical to adjust the control gain to equal the system's infinite impedance, avoiding reflection from the control end, as already found by other authors. In the case of a finite string excited at its resonance frequency, if the control gain is increased the energy of the system increases as

soon as the primary source is subjected to reflected wave. Instead, when the control gain is set on the value that absorbs as much power as possible from the incident wave, the energy of the system results bounded. In practice, the best performance in the control of a finite system excited at a single frequency excitation appears to be achieved when the control gain is set on the optimum value of power absorption estimated for the infinite system. Since the power absorbed is a local quantity, an algorithm that self-tune the control feedback gain can be used to make the system adaptive. Experiments in this direction have been carried out by Hirami [31]. The control system undertakes two tasks at the same time. One is the measurement of the power absorbed by the controller using both, a force and velocity sensor and the other is to feed back the velocity signal to the actuator with a certain gain. The controller proposed used a gradient based algorithm that converges to the optimal feedback gain, which maximises the measured absorbed power. The algorithm was designed to adapt in a short time before the reflected wave reached the controller. The power absorbed is estimated by measuring both the control force and the velocity at control position. Experiments were carried out by Hirami [31] on a string excited at resonance and controlled by a shaker. The initial vibration level is reduced by 15dB after placement of the shaker which changes the modal response of the string and introduces passive damping. The active control produces a further 10 dB reduction. It was found that the optimum gain increases with the frequency and the peak of power absorbed becomes smoother. Also in the case of broadband excitation when a wide range of frequencies are excited, the algorithm converges to the optimal value of gain that maximise the power absorbed, giving good results.

Sharp *et al.* [32] presented a method of reducing the sound power radiated by a vibrating structure using a feedback control system based on optimal power absorption, focusing on broadband frequency excitation. The optimal controller provides a casually constrained impedance match between the control system and structure, maximising the power flow between two systems. The structure used in this study was a simply supported beam. This control method gave a reduction of radiated sound power at all resonance frequency of the beam. The total kinetic energy of the beam was also reduced, demonstrating that the control system does not reduce only the vibration at control position but provide global vibration attenuation.

Sharp et al. [32] also investigated the conditions under which the maximization of power absorption could lead to an increase in the energy in the system. The occurrence of this phenomenon is due to the secondary source driving the primary source to generate additional power in order to achieve greater power dissipation. Sharp et al. [32] however argues that as the predictability of the disturbance decreases, as the excitation bandwidth increases, it becomes less likely that the secondary source will influence the primary source and increase the total power input.

3.2. Broadband vibration control of a panel

In this section the model of a simply supported panel subject to an external primary excitation is used to predict the structural response when controlled by direct velocity feedback loops. Different types of excitations are considered. The first one is a white noise force acting at a point of the panel. In this case the relative distance between the control location and the point of the application of the primary force will influence the performance of the controller. To overcome this effect, 'rain-on-the-roof" primary excitation, consisting of a random distribution of pressure in time and space, is considered. The effect of more than one channel control system is considered and in the last subsection the implementation of a self-tuning algorithm to maximise the power absorbed by each control loop is discussed.

3.2.1. Fixed gain for broad frequency band control

In this section, the implementation of a single direct velocity feedback control loop on a simply supported panel is considered. The feedback gain is fixed at a single, frequency independent, value. The feedback loop uses an ideal velocity sensor collocated with an ideal point force actuator. Since the sensor and actuator pair is dual and collocated the velocity feedback loop is unconditionally stable [18].

As shown in Figure 3.1, the origin O of the Cartesian co-ordinate system of reference (O, x, y, z) is assumed to be located at the top left corner of the panel with the z axis orthogonal to the surface of the panel.

The primary harmonic force f_p, which excited the panel, is located at point of coordinate (x_p, y_p), while the control force f_c, is located at point of coordinate (x_1, y_1). The geometric and physical parameters of the panel are summarized in Table 3.1 and the modal response of the panel is derived in Appendix B.

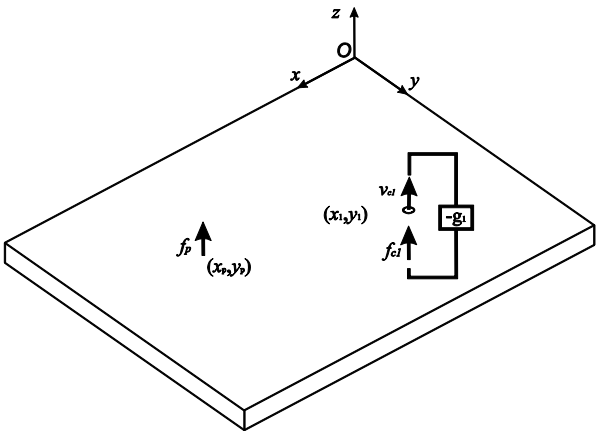

Figure 3.1: Schema of simply supported panel excited by a primary force f_p with a collocated ideal velocity sensor and force actuator feedback control system.

Table 3.1: Geometric and physical parameters for the panel

Parameter	Value
Dimensions	$l_x \times l_y = 0.414 \times 0.314$ m^2
Thickness	h=0.001 m
Position of the primary excitation	$(x_p, y_p) = (0.6\, l_x , 0.4\, l_y)$
Position of the control point	$(x_1, y_1) = (0.3\, l_x , 0.7\, l_y)$
Mass density	ρ =2700 kg/m^3
Young's modulus	E =7×10^{10} N/m^2
Poisson ratio	$\nu_1 = 0.33$
Loss factor	$\eta = 1\%$

Figure 3.2 shows the total flexural kinetic energy in the 10 Hz-1 kHz frequency range with no control (thick line) when the optimal control gain ($g = 36$ dB) that minimises the kinetic energy averaged between 1 Hz and 1000 Hz (dashed line) and when very high control gain (dotted line) are implemented. Figure 3.3 shows the normalised[†] total flexural kinetic energy integrated between 10 Hz and 1kHz, for a range control gains between -25 dB and 100 dB (relative to 1 Nsm^{-1} i.e. between $10^{-1.5}$ and 10^5 Nsm^{-1}). Figure 3.2 shows that for a moderate gain, g, the feedback loop effectively reduces the response at resonance frequencies. However, when a large feedback gain is implemented the response of the plate is no longer actively damped, but is characterised by a shifted set of resonances [33-35] due to the pinning of the structure at the control point.

[†] Normalized to the total kinetic energy when the feedback control loop is left open

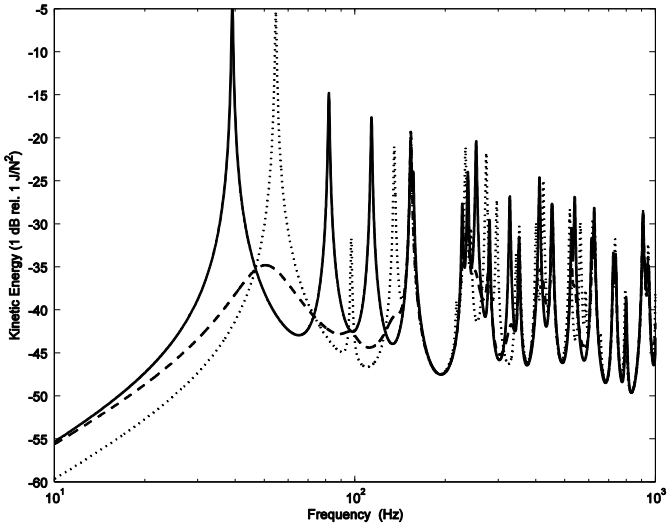

Figure 3.2: PSD of the total flexural kinetic energy of the panel when it is excited by a unit primary force and the control gains of the feedback control system using a force actuator are set to be 0 Nsm^{-1} (solid line) 36 Nsm^{-1} (dashed line) and 10^5 Nsm^{-1} (dotted line).

As Figure 3.3 shows, there is an optimal value of the gain, between these two extremes, that reduces the kinetic energy substantially.

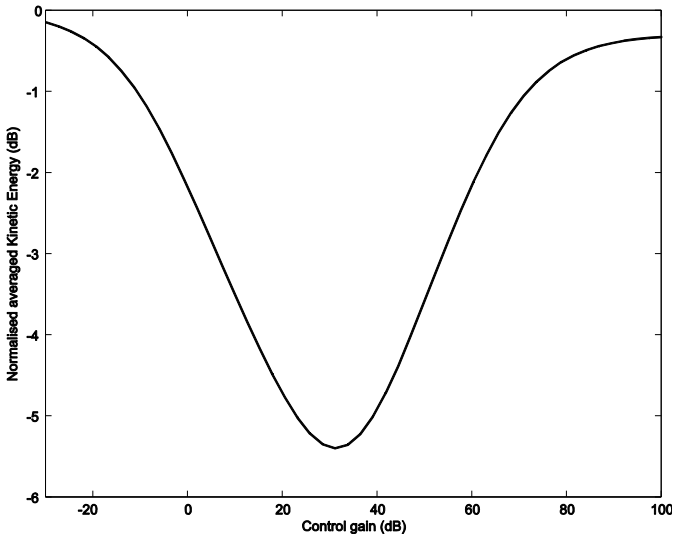

Figure 3.3: averaged PSD of total kinetic energy in the frequency range 0-1 KHz of the panel with and without feedback control plotted against the control gain. The total kinetic energy is minimised for $g = 36$ Nms^{-1}.

The velocity feedback control loop with a collocated velocity sensor and force actuator pair provides sky-hook active damping, which absorbs power from the structure under control. Thus, it would be interesting to consider the optimal value of the control gain which maximises the power absorbed by the velocity feedback control loop and then to contrast the reduction of total flexural energy it produces with reference to the optimal case described above. The PSD of the power absorbed by the feedback loop is given by:

$$S_{\mathrm{P}}(\omega) = \frac{1}{2}\mathrm{Re}\{\tilde{f}_c \tilde{v}_c^*\}. \tag{3.1}$$

Since the control force is proportional to the control velocity via the control gain g, the power absorbed can be written as:

$$S_{\mathrm{P}}(\omega) = \frac{1}{2} g |\tilde{v}_c|^2. \tag{3.2}$$

An advantage of this strategy is that the power absorbed is a local quantity because, as shown by equation (3.2), it only depends on the control gain and the mean squared value of the velocity at control position and thus it would be rather easy to implement a control algorithm that sets the optimal gain that maximises the power absorbed by the controller.

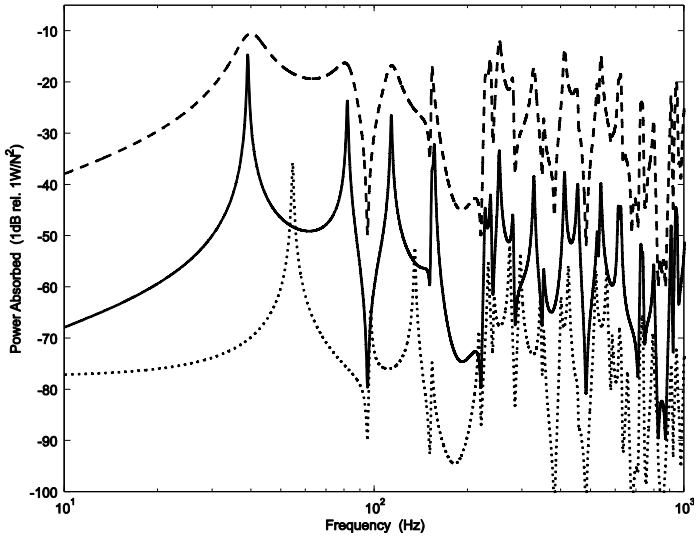

Figure 3.4: PSD of the power absorbed by the control feedback loop when it is excited by a unit primary force and the control gains of the feedback control system using a force actuator are set to be 0.001 $\mathrm{Nsm^{-1}}$ (solid line) 36 $\mathrm{Nsm^{-1}}$ (dashed line) and 10^5 $\mathrm{Nsm^{-1}}$ (dotted line).

Figure 3.4 shows the spectrum of the power absorbed by the control loop for three control gains. The thick line provides a benchmark reference of the power absorption produced by a very small gain of 0.001 $\mathrm{Nsm^{-1}}$. The dashed and dotted lines show the power absorbed when control gains are implemented that produce the spectra in Figure 3.2, plotted with the corresponding type of lines.

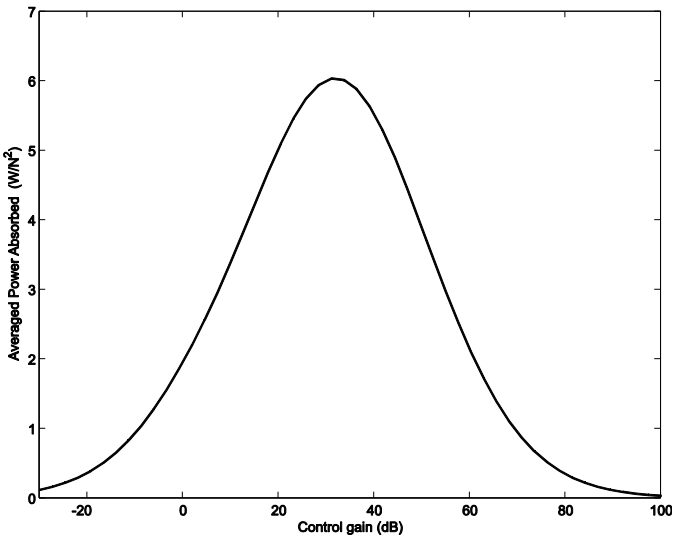

Figure 3.5: PSD of power absorbed averaged in the frequency range 1-0 kHz by the feedback control loop plotted against the control gain. The power absorbed is maximised for $g = 39$ Nsm^{-1}.

Figure 3.5 shows the total power absorbed, integrated between 10 and 1000 Hz, for a range control gains between -25 and 100 dB. Comparing Figure 3.3 and Figure 3.5 it is found that the maximum power absorbed by the control unit is produced by a similar gain that minimises the total kinetic energy of the plate. Thus the plots show a very interesting result: the control performance produced when the average power absorbed by the feedback loop is maximised is about the same as the one obtained minimising the averaged kinetic energy of the system. In other words, if a frequency-independent control gain is implemented, then the response of the panel is approximately minimised over a broad-frequency band when the control loop is set to maximise the power it absorbs.

It also interesting to notice that the impedance of an infinite panel of the same thickness is about 33.8 Nsm^{-1} which is approximately the same gain that minimises the total kinetic energy of the panel as shown in reference [24].

The plots in Figure 3.6(a) and (b) show the normalised total kinetic energy and the total power absorbed by the feedback control loop integrated between 1 Hz and 1 kHz as function of the control gain when the controller is placed near the primary excitation. From these plots, it can be noted that if the distance between the control and the primary excitation points is reduced, the optimum value of control gain, which minimises the total kinetic energy, increases and produces much higher reduction in terms of the panel's response (about 16.5 dB).

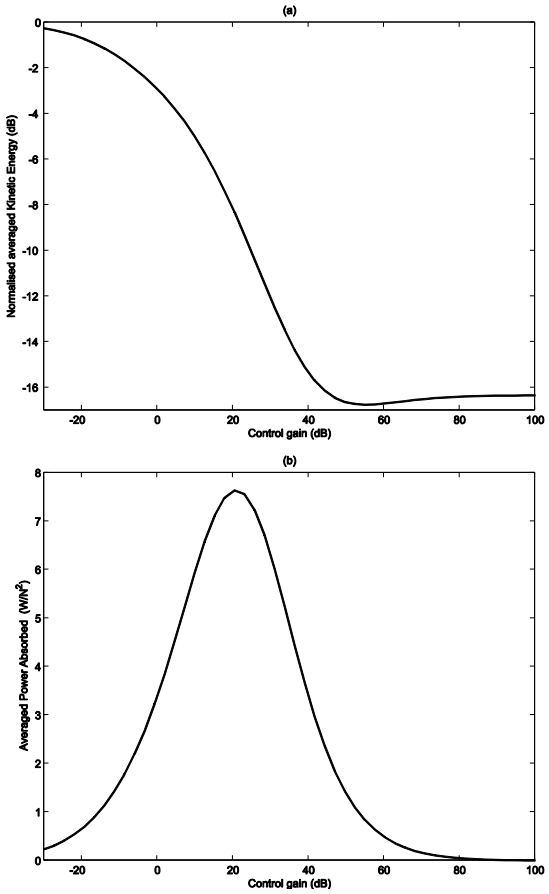

Figure 3.6: Total kinetic energy and total power absorbed plotted against the control gain when the primary force is acted on ($0.6l_x$,$0.4l_y$) and the control point is a) ($0.58l_x$,$0.41l_y$). Total kinetic energy is minimised for $g = 555$ Nsm^{-1} and the total power absorbed is maximise for $g = 10$ Nsm^{-1}.

Figure 3.6(a) shows that when the control gain is greater than the optimal value, the total kinetic energy of the panel is about the same as that for the optimal control gain. This is due to the fact that as the control loop gets closer to the primary excitation, the best way to reduce the overall vibration of the plate is by pinning the excitation point so that very little residual vibration is allowed at the excitation point and thus very little energy is injected by the primary force to the plate. If, in an ideal condition, the control point and primary force are assumed to be at the same position on the plate, the optimum gain, which minimises the total kinetic energy, would tend to infinity, since the velocity at the control position would tend to zero. Thus no energy would be input to the plate and the total energy of the plate would go to zero.

Comparing Figure 3.6(b) with Figure 3.5, the value of the control gain which maximises the power absorbed decreases when the distance between the primary force and control point is reduced. But, if the control system is tuned with the value of gain that maximises the power absorbed it still gives about 11 dB of reduction in terms of the total kinetic energy of the panel. This result demonstrates that the maximisation of the absorbed power gives acceptable level of performance even in the case where the primary and control points are close to each other, but

the difference in optimised gains larger as the control point approaches the single excitation point in this case.

To make the control system insensitive to the distance between the primary and secondary force, a random distribution of pressure (i.e. 'rain-on-the-roof') acting on the panel's surface has been considered. The primary forces are spatially uncorrelated and have a power spectrum density that is constant in frequency (white noise) and in space (uniformity). The formulation for multichannel control of a panel subject to 'rain-on-the-roof' excitation is derived in Appendix B. Figure 3.7 shows a scheme of the simply supported panel. The geometric and physical parameters for the plate and the position of the control point are summarized in Table 3.1.

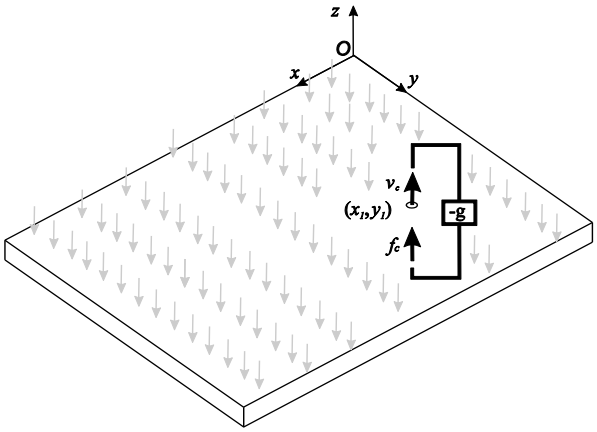

Figure 3.7: Schema of the simply supported plate subject to a random excitation "rain-on-the-roof" with a collocated ideal velocity sensor and force actuator feedback control system.

Figure 3.8 shows the PSD of the kinetic energy of the panel without control (solid line) and when the frequency independent gain of the control loop is increased from a very small value to higher values (dashed line, faint line and dotted line, respectively). As already seen in the case of point force excitation, for small gains, the control loop produces active damping which reduces the response of the plate up to the third resonance frequency at about 120 Hz. The dashed line represents the response of the panel for the control gain that minimises the frequency averaged response of the panel. If the control gain exceeds this value, the response of the panel increases again, at other frequencies, eventually creating a new set of resonance frequencies due to active pinning [33-35].

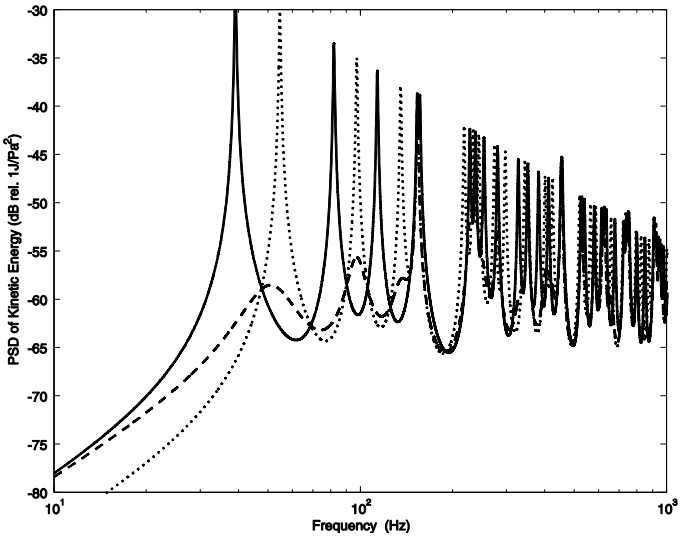

Figure 3.8: PSD of the flexural kinetic energy of the plate when it is subject to a random excitation and the control gains of the feedback control system using a force actuator are set to be 0 Nsm^{-1} (solid line) 38 Nsm^{-1} (dashed line) and 10^6 Nsm^{-1} (dotted line).

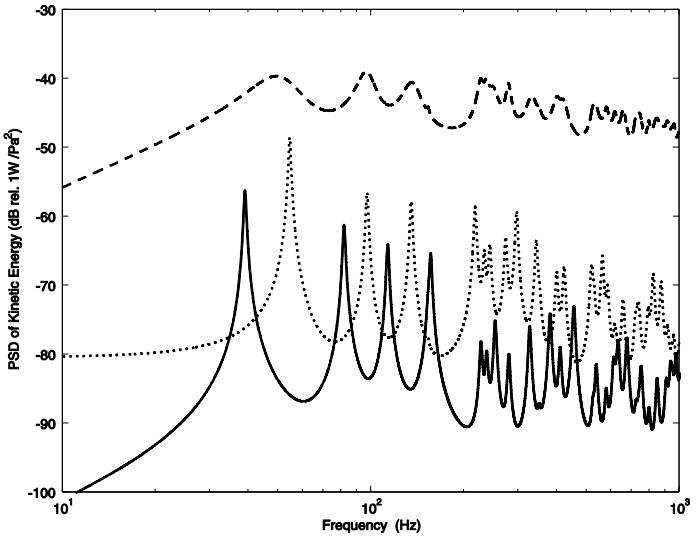

Figure 3.9: PSD of the power absorbed by the control feedback loop when the plate is subjected to a broadband random excitation and the control gains of the feedback control system using a force actuator are set to be 0.001 Nsm^{-1} (solid line) 38 Nsm^{-1} (dashed line) and 10^5 Nsm^{-1} (dotted line).

Figure 3.9 shows the PSD of power absorbed by the feedback loop when the control gain g is increased. The solid line provides a benchmark reference of the power absorbed for a very low value of feedback gain (0.001 Nsm^{-1}). When the control gain is increased with the same values considered in Figure 3.8, the spectrum of the power absorbed increases until an optimum value of control gain (dashed line) is reached.

When the gain is further increased, the power absorbed decreases again as the new set of resonances emerge (dotted line). This interesting result suggests that a good level of performance can be achieved by maximising the total power absorbed by the feedback loop over a wide frequency band.

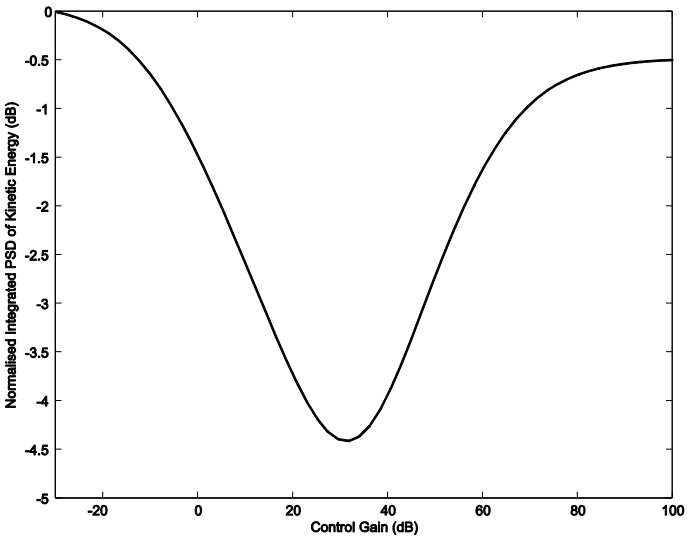

Figure 3.10: PSD of average total kinetic energy in the frequency range 1Hk-1 KHz of the plate plotted against the control gain. The total kinetic energy in minimised for $g = 38$ Nsm^{-1}.

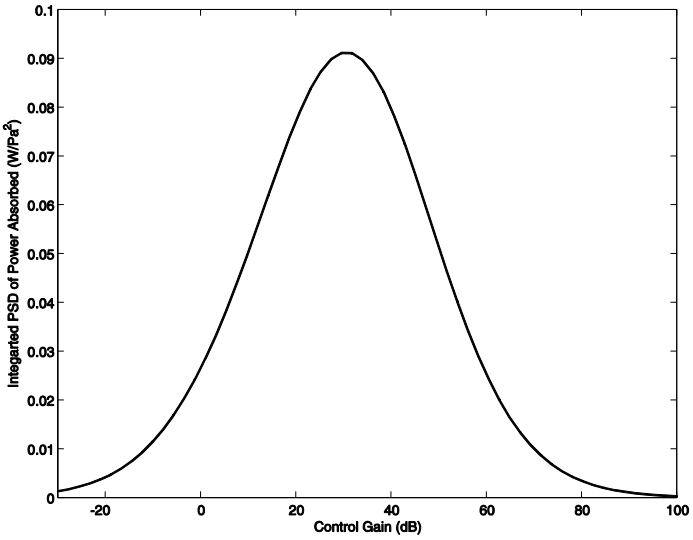

Figure 3.11: PSD of power absorbed in the frequency range 1Hk-1kHz by the feedback control loop plotted against the control gain. The total power absorbed is maximised for $g = 29$ Nsm^{-1}.

This observation is confirmed by the plots in Figure 3.10 and 11, which show the 1 Hz to 1 kHz frequency-integrated PSD of the total kinetic energy, normalised to the reference level without control, and the 1 Hz to 1 kHz frequency-integrated PSD of the total power absorbed, as a function of the control gain.

The two plots show that as the feedback control gain g is raised, the frequency integrated kinetic energy initially decreases while the frequency integrated power absorbed initially increases. The minimum of the kinetic energy and the maximum of power absorbed are achieved at about the same control gain. At higher gains, the kinetic energy increases again and the power absorbed drops off.

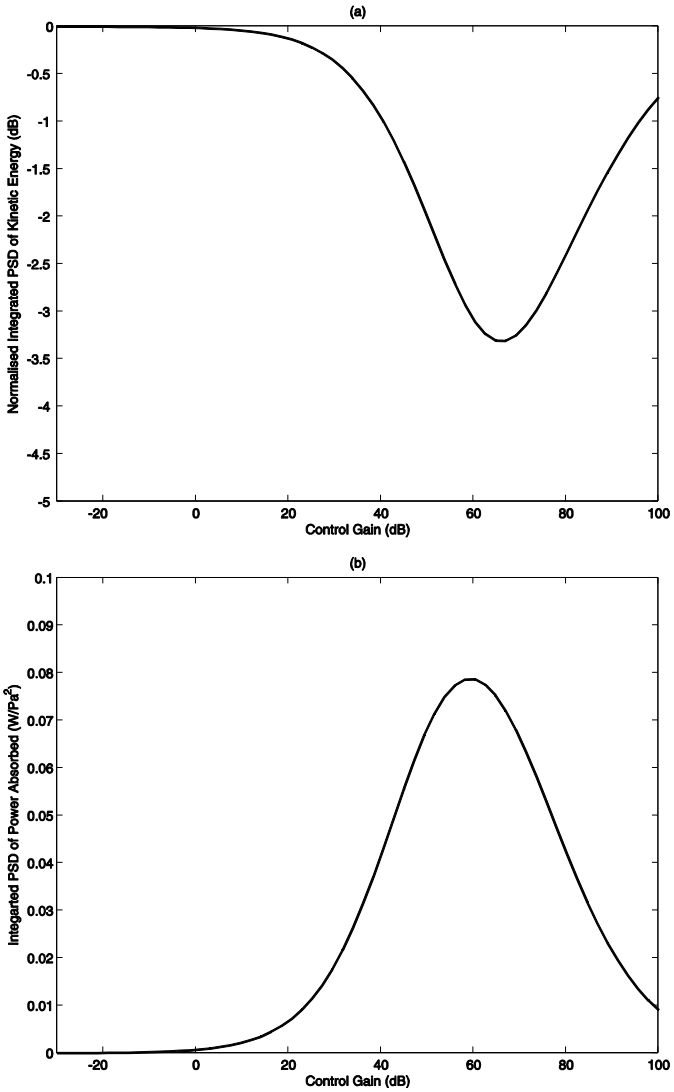

Figure 3.12: PSD of kinetic energy and power absorbed plotted against the control gain when the plate is subject to a random excitation and the control point is (0.8 l_x, 0.01 l_y). Total kinetic energy is minimised for $g = 67$ Nsm^{-1} and the total power absorbed is maximise for $g = 60$ Nsm^{-1}.

Figure 3.12 (a), (b) shows the PSD of the normalised total kinetic energy and the PSD of the power absorbed integrated between 1 and 1000 Hz plotted against the control gain when the controller is located near the edge of the panel. It can be noted that the optimum values of control gain, which minimise the PSD of the total kinetic energy and maximise the PSD of the power absorbed are still similar, but are higher than in the previous case. This is due to the fact that the control force is no longer able to excite the plate efficiently and that the plate's impedance is larger close to the edge. In the case of deterministic excitation there is a strong dependence of the optimum gain on the distance between the primary and control force. In the case of random excitation, the controlled response of the panel is relatively independent of the position of the control force, except when it gets close to the edge of the plate [26].

3.2.2. Fixed gain for narrowband control

This section investigates how the frequency band-width of the random excitations influences the optimal value of control gain.

Figure 3.13 shows the difference between the control gains that would produce maximum reduction of kinetic energy and maximum power absorption integrated over increasingly wider frequency bands between 1 Hz and 1 kHz, starting at lower frequency of 1 Hz.

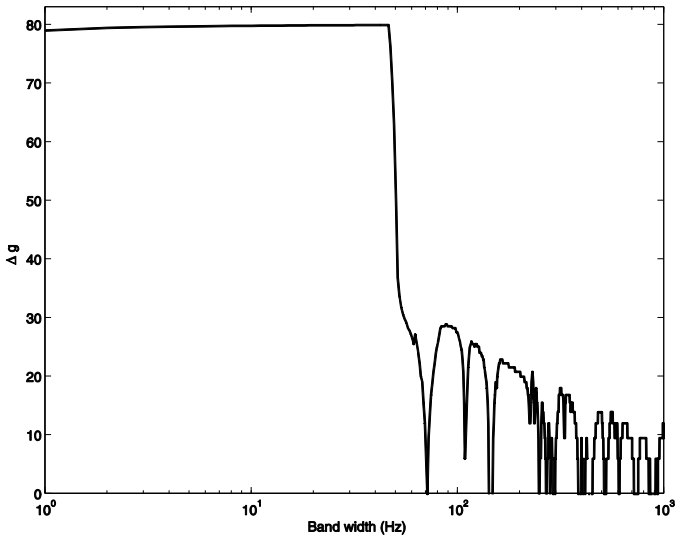

Figure 3.13: difference between the control gains minimising the kinetic energy and maximising the power absorption averaged over increasingly wider frequency bands between 1 and 1000 Hz.

For small bandwidths the two control gains differ by about four orders of magnitude since the panel is stiffness controlled in this region and minimising the kinetic energy can be achieved by almost pinning the panel, whereas the absorbed power is maximised at much lower gains. However, when the bandwidth exceeds about 60 Hz, the difference between the two gains abruptly drops down to values between 0 and 20 dB. Figure 3.14 shows a similar graph for the difference between the reductions of kinetic energy that are produced with the two control gains and shows a similar transition at 60 Hz.

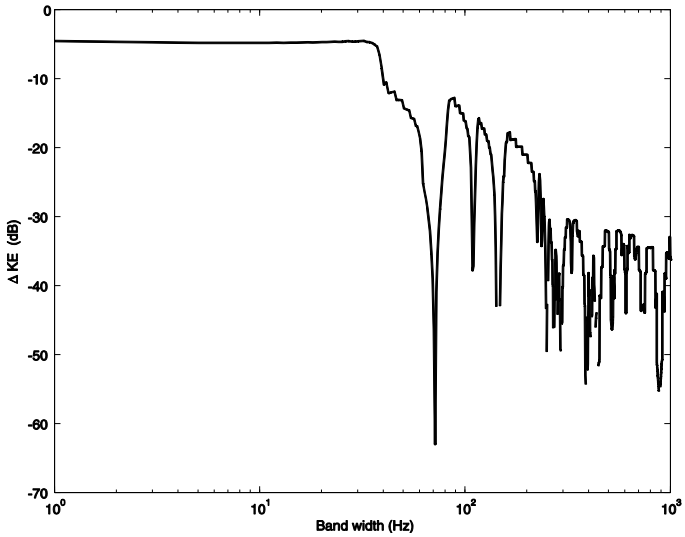

Figure 3.14: difference between the kinetic energy maximising the power absorption and the minimum of kinetic energy achievable

The 60 Hz cut-off frequency corresponds to the fundamental resonance frequency of the simply supported panel with the additional pinning constraint at the control position (the first peak of the dotted spectrum in Figure 3.8). This suggest that maximising the total power absorbed also minimises the kinetic energy provided the frequency range over which the two quantities are integrated includes at least the fundamental resonance of the plate response when the control unit pins the panel. In this case, the typical $\cup$ and $\cap$ shapes for the variations of kinetic energy and power absorbed as function of the control gain shown in Figure 3.10 and Figure 3.11 can be found. Figure 3.15 and Figure 3.16 show the total kinetic energy and total power absorbed as function of the control gain respectively averaged between 1-40 Hz. Figure 3.15 shows that the kinetic energy remains low at high gain, since the new resonance is outside this frequency band of integration, and the absorption peak does not occur at the same gain as the minimum kinetic energy.

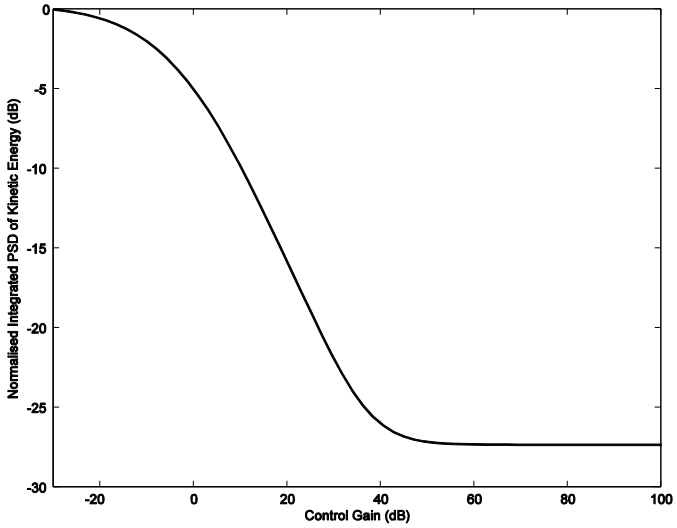

Figure 3.15: Frequency averaged PSD of the kinetic energy plotted against the control gain, averaged from 1 to 40 Hz.

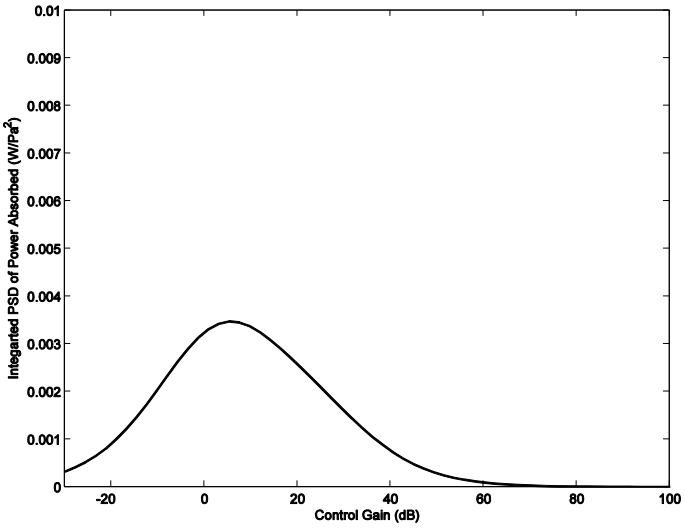

Figure 3.16: Frequency averaged PSD of the power absorbed plotted against the control gain, averaged from 0 to 40 Hz. The absorbed power is maximised for for $g = 1.8$ dB

3.2.3. Single frequency excitation

All the results presented so far are related to broadband excitation, so that the total kinetic energy and power absorbed have been averaged over range of frequencies. In this section the two strategies of tuning the control gain are compared in the case of a single frequency excitation. Figure 3.17 shows the spectrum of the plate kinetic energy when excited one frequency at a time and there is no control (thick line) and when the control gain is set to either minimise the panel kinetic energy (dotted line) or maximise the power absorbed (dashed line) independently at each frequency.

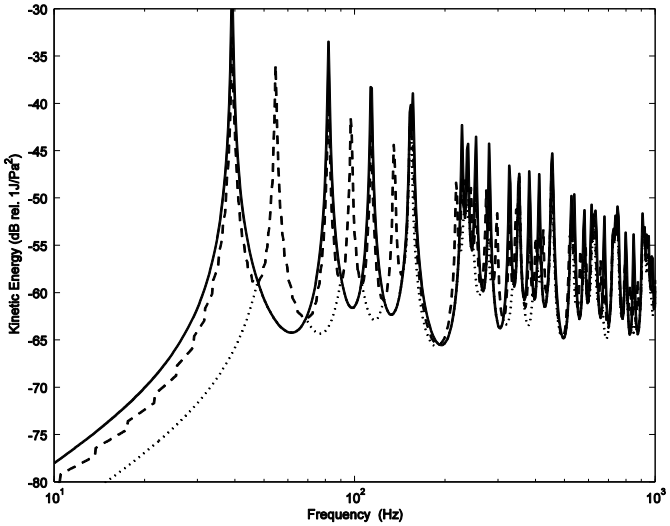

Figure 3.17: Kinetic energy for single frequency excitation without control, as function of excitation frequency (solid line), with the gain adjusted at each excitation frequency to minimise the kinetic energy (dotted line) and with the gain adjusted at each excitation frequency to maximise the power absorbed (dashed line).

The resulting frequency-dependent control gains for the two cases are shown in Figure 3.18. However it would not be possible to implement a broadband controller with frequency responses corresponding to either of these curves, since their phase response is zero and so their impulse responses would be symmetrical in the time domain and hence non-causal. Figure 3.17 indicates that, as one would expect, the best control approach is produced when the feedback gain is adjusted to minimise the kinetic energy.

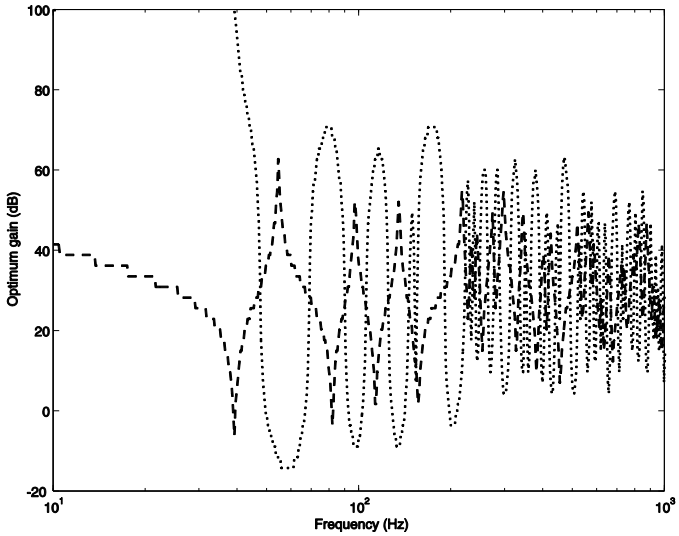

Figure 3.18: optimum gain minimizing the total kinetic energy (dotted line) and maximizing the power absorbed (dashed line) for single frequency excitation

The other approach, where the power absorbed by the control loop is maximised at each frequency independently, produces reductions of the kinetic energy only over small frequency bands. The resulting kinetic energy spectrum is characterised by resonance peaks and also new

peaks that occur in between two resonances. A detailed analysis of the response of the plate at the new peak at around 55 Hz, shows that the feedback loop reduces the error velocity to very low values by implementing the very large feedback gain seen in Figure 3.18 at this frequency, so that a new resonant mode is generated [33]. These single frequency simulations reinforce the requirement for a significant excitation bandwidth if minimisation of power absorbed is to be used to minimise kinetic energy.

3.2.4. Broadband control using two feedback loops

In this section the control effects of two feedback loops, with frequency independent gains, are investigated when the panel is subject to broadband 'rain-on-the-roof' excitation. The positions of the two control points are given in Table 3.2 and they are a distance of about 0.3 m apart.

Table 3.2: position of the two feedback loops

Control position 1	$x_1, y_1 = 0.3\ l_x, 0.7\ l_y$
Control position 2	$x_2, y_2 = 0.43\ l_x, 0.4\ l_y$

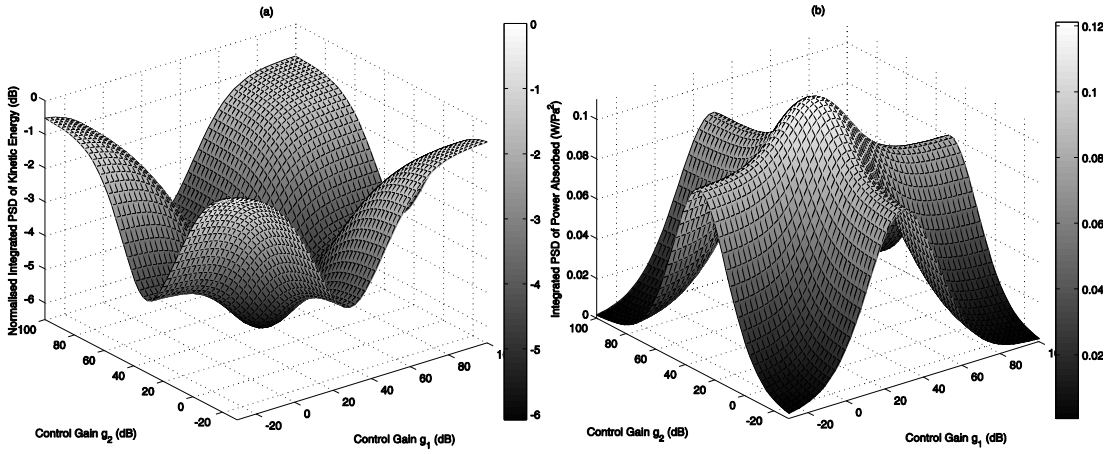

Figure 3.19: 1Hz to 1 kHz frequency integrated a) PSD of total kinetic energy and b) PSD of total power absorbed by the two feedback loops as a function of the control gains g_1 and g_2.

Figure 3.19 shows, as a function of the two feedback gains g_1 and g_2, the 1 Hz to 1 kHz integrated PSD of the total kinetic energy of the panel normalised to the reference PSD of kinetic energy without control and the 1 Hz to 1 kHz integrated PSD of the total power absorbed by the two control feedback loops. The plots show that the minimum total kinetic energy and the maximum power absorbed are given when the two feedback gains are similar to the values that they would have if they were controlling the vibration of the panel independently. Moreover, the minimum total kinetic energy and the maximum total power absorbed occur for a very similar pair of control gains. This suggests that controlling the response of the panel by

locally tuning each control loop to maximise its power absorbed in a wide range of frequencies can be extended to multiple feedback loops. Comparing Figure 3.10 with Figure 3.19(a) and Figure 3.11 with Figure 3.19(b), shows that using two feedback loops instead of one further reduces the total kinetic energy by about 1.5 dB and further increases the total power absorbed by about 1.5 dB.

Figure 3.20 show the PSD, integrated between 1 Hz and 1 kHz, of the power absorbed by the individual feedback loops as functions of the feedback gains g_1 and g_2. The two plots show that the power absorbed by each control unit is reduced when the other control unit is tuned close to its optimal value, and the control gain that maximises the power absorbed by one control unit is influenced by the control gain in the other loop.

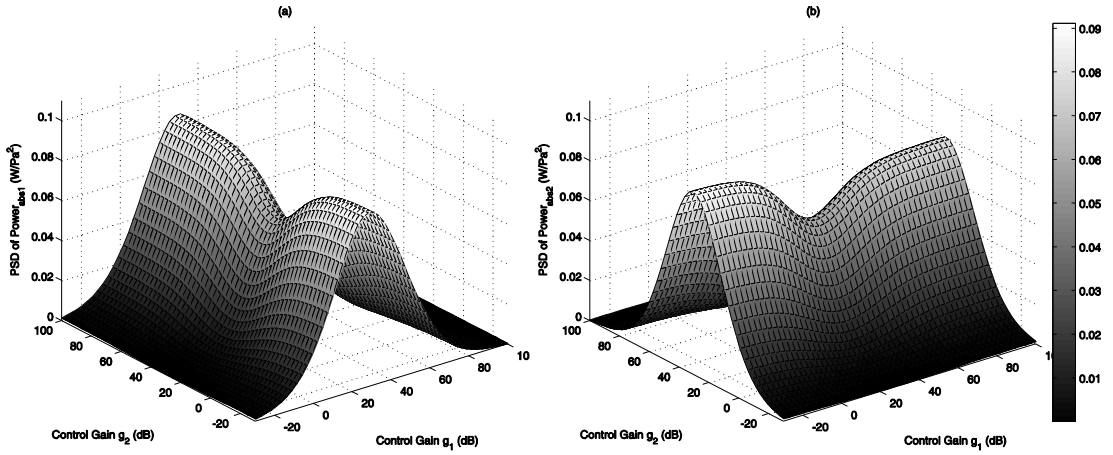

Figure 3.20: 1 Hz to 1 kHz PSD of power absorbed by (a) control unit number 1 and (b) number 2 as a function of the control gains g_1 and g_2.

The simultaneous maximisation of the local power in both control units, however, converges to the maximisation of the total absorbed power shown in Figure 3.19. The important aspect of the curves in Figure 3.20, as far as a practical adaptation algorithm is concerned, is that if one control gain is fixed, the local power absorbed by the other loop is still maximised by a single value of its control gain. It is thus possible to use gradient-based algorithms to adjust the individual control gains.

3.2.5. Self-tuning algorithm to maximise the power absorbed by the controller

The simulation study presented in the previous subsections has shown that, assuming broadband excitation, a similar control performance is achievable minimising the total kinetic energy of the plate or maximising the power absorbed by each of the feedback loops. This suggests that reductions in the overall vibration can be obtained by adapting the local feedback gains of the control units to maximise the total power absorbed by each control unit.

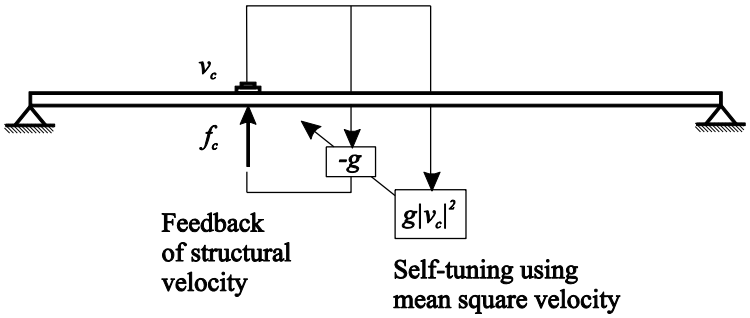

Figure 3.21: Scheme of a single self-tuning velocity feedback loop.

Figure 3.21 shows a potential self-tuning scheme for a local feedback loop. Since the control force produced by the *r*-th feedback loop, f_{cr}, is proportional to the velocity measured at the *r*-th control position, v_{cr} via the control gain g_r then the power absorbed by the controller at a given frequency is proportional to the mean squared value of the control velocity via the control gain, as previously shown in equation (3.2) for a single channel. Thus an algorithm that adjusts the control gain to maximise the total power absorbed can be implemented using only the local velocity measured by the feedback sensor, the instantaneous value of which is used as the feedback signal.

In this study, a simple algorithm that adjusts the control gain to maximise the total power absorbed by each loop has been investigated. The algorithm increases the control gain in each loop gradually from zero in fixed steps, then uses the calculated power absorbed to adapt the control gain. The algorithm at the *q*-th iteration can be written as:

$$g_r(q+1) = g_r(q) + \alpha(q)\{\text{sgn}[\Delta P_r(q)]\text{sgn}[\Delta g_r(q)]\} \tag{3.3}$$

where sgn[ ] signifies the sign of the parameter in brackets, ΔP and are Δg the differences in power absorbed and control gain between two consecutive iterations with all other control gains in the other feedback controllers fixed. The parameter $\alpha(q)$ is the step by which the gain is increased at the *q*-th iteration. When the power absorbed starts to decrease, the algorithm reduces the control gain by half a step and so $\alpha(q)$ is given by:

$$\alpha(q+1) = \alpha(q) - \frac{\alpha(q)}{4}\{1 - \text{sgn}[\Delta P_r(q)]\} \tag{3.4}$$

where the initial value of α for $q = 0$ must be specified. The error in the estimation of g_r after q iterations is $\pm 2\alpha(q)$ and since $\alpha(q)$ decreases in size with *q*, the algorithm converges to the optimum. If the conditions on the plate change, it is assumed that this can be detected and the value of $\alpha(q)$ re-initialised so that the algorithm can adapt the gain to its new optimum value. When multiple feedback loops are tuned simultaneously, the power absorbed by one feedback loop is influenced by all the others, as shown in Subsection 3.2.4. Therefore, the individual

power absorbed by the *r*-th control loop must be re-estimated, keeping all the other gains constant, before the *r*-th control gain is varied. A limitation of this tuning algorithm is thus that global synchronization is required to ensure sequential tuning, even though each control loop is still tuned using only the signal of the collocated sensor in decentralised manner. It is not clear whether other control algorithms, which allow simultaneous adaptation of each control loop, could be used and thus avoids the need for global synchronisation of the tuning. It is also important to highlight that the broadband disturbance is assumed to be stationary during the adaptation so that a change in the absorbed power is only due to change in the control gain.

3.2.6. 16 Self-tuning feedback loops

In this section the effects of implementing 16 self-tuning feedback loops on the panel are investigated. Figure 3.22(a) shows the positions of the control points on the panel. Figure 3.22(b) shows the value of the control gains of each feedback loop after the self-tuning algorithm given in equations (3.3) and (3.4) has been used to tune all the feedback loops sequentially to maximise their power absorbed. The way this is achieved is that the gain on the first control loop is adjusted using equation (3.3), and then each of the other loops are adjusted, after which this sequence is repeated until the gains have converged. The gain distribution is symmetric, as expected, but within the range 27.5 to 33.8 Nms^{-1}.

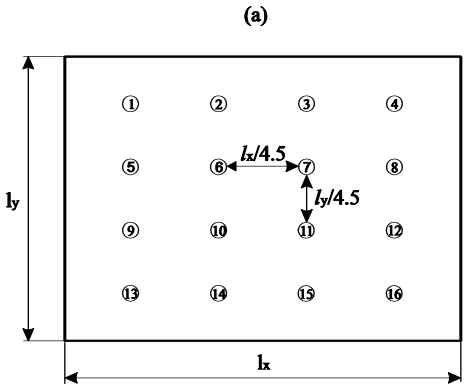

(b)

31.7	33.8	33.8	31.7
27.5	31.1	31.1	27.5
27.5	31.1	31.1	27.5
31.7	33.8	33.8	31.7

Figure 3.22: a) Scheme of a plate with the control points disposition and (b) values of control gain, in Nsm^{-1}, maximising the power absorbed of each control feedback loop, found using the self-tuning algorithm.

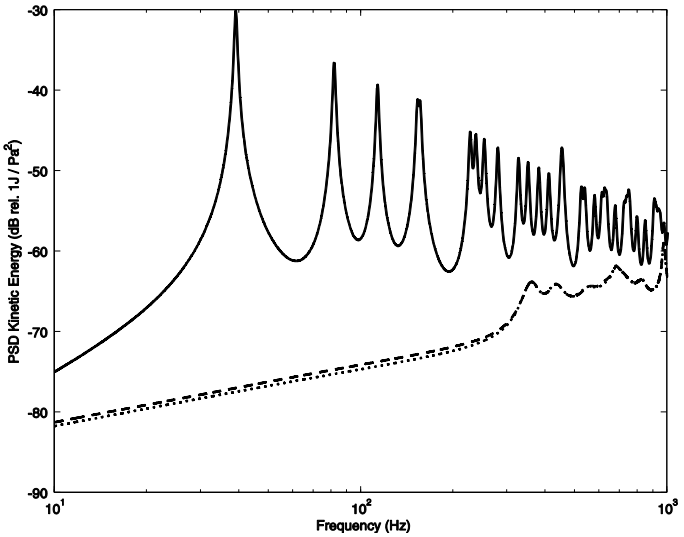

Figure 3.23: PSD of the total kinetic energy when $g_{1\text{-}16}= 0$ (solid line), the self-tuning algorithm is implemented (dashed line) and $g_{1\text{-}16} = 32.7$ Nsm^{-1} (dotted line).

Figure 3.23 shows the PSD of the panel's kinetic energy without control (solid line), after the self-tuning algorithm has been used to adapt the gain of each feedback loop (dashed line) and when the total kinetic energy is minimised off line using the same value of gain for each feedback loop (dotted line). Although the kinetic energy PSD is only shown up to an excitation frequency of 1 kHz in Figure 3.23, the simulations were performed with an excitation bandwidth up to 10 kHz. This is to include the new resonance frequencies that would be created with high gains in each of these 16 feedback loops, which may interfere with the adaptation process. The plot demonstrates that the self-tuning algorithm provides an overall reduction very close to the minimum that would be achieved if the total kinetic energy is minimised using equal control gains, yet only uses information local to the control loops.

Figure 3.24 shows the convergence of the control gains g_1, g_2, g_5 and g_6 when adapted using the self-tuning algorithm (a) when their initial value is set on 0 and (b) when they are set to random values. In the simulations the initial value of alpha is set on 10 and the error on the estimation of g which is twice the minimum alpha is ± 0.02. Figure 3.24 illustrates that the algorithm reliably converges to the correct optimum values, within these limits, whatever the initial conditions.

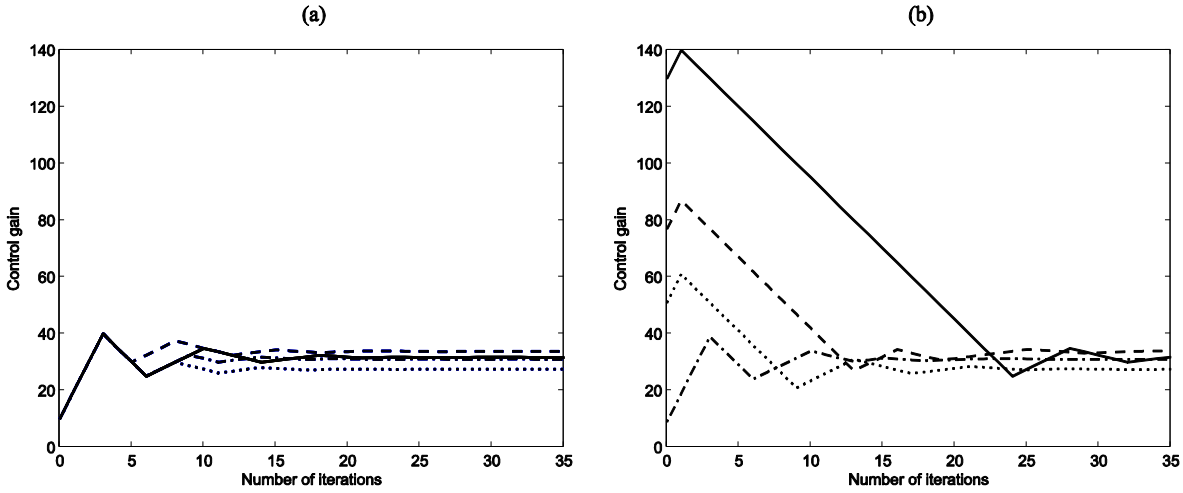

Figure 3.24: Convergence of control gains g_1 solid line), g_2 (dashed line) g_5 (dotted line) and g_6 (dash-dot line) (a) starting from 0 and (b) random values.

Figure 3.25 shows the simulation results when the control unit 6, 10 and 12 fail after 5 iterations and the corresponding values of g are then set to zero. Comparing Figure 3.22(b) and Figure 3.25(a), the converged values of the control gains vary slightly from those above, but still maximise the power absorbed in the remaining units.

(a)

31.4	35.1	35.1	32.0
27.1	✕	31.5	25.9
28.1	✕	31.5	✕
31.5	34.5	34.6	29.7

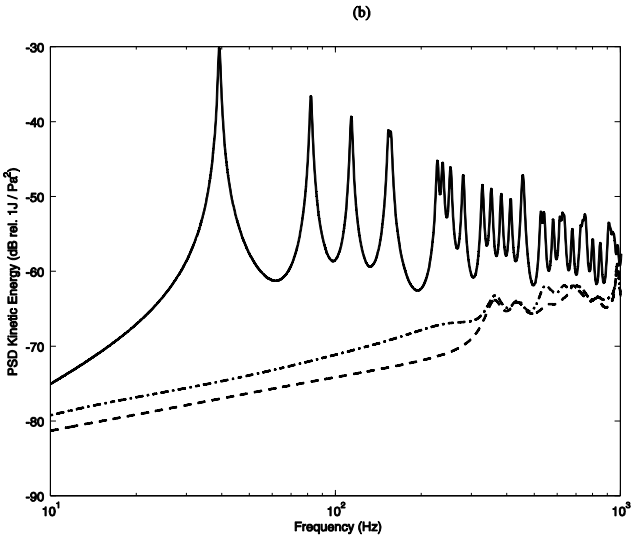

Figure 3.25: (a) Control gains after convergence when the control unit 6, 10, and 12 fail after 5 iterations; (b) PSD of the total kinetic energy of the panel without control (solid line), using 16 self-tuning control loops (dashed line) and after failure of three control units (dot-dashed line).

Figure 3.25(b) shows the PSD of the kinetic energy of the panel without control (solid line), using 16 self-tuning control units (dashed line) and after the convergence of the algorithm when the three control units fail (dot-dashed line). The plot shows that after the failure, the remaining feedback gains have been slightly adjusted, but a good reduction of vibration is still achieved over this frequency range.

3.3. Vibration control of a beam to maximise control stability

This section considers the maximisation of control stability as a strategy of tuning the gain of an ideal single velocity feedback loop. The objective of stability maximisation criterion is to minimise the transient vibration of the system, and has been suggested as a tuning strategies by Preumont [7] and Engelen [36] for example.

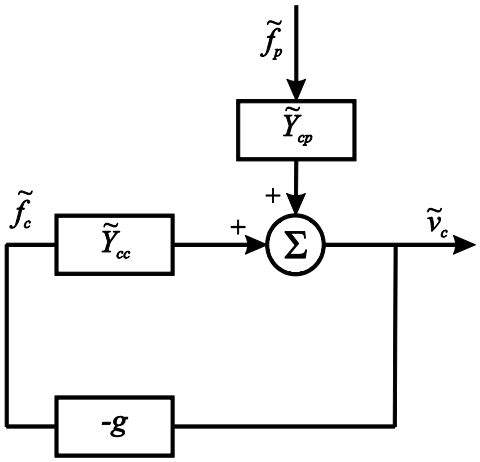

Figure 3.26: Block diagram of a single direct velocity feedback loop control implemented on the plate.

The optimisation is achieved when the pole of a chosen mode of the closed loop frequency response function (FRF) of the control system is located as far as possible from the imaginary axis in the left-half of the *s*-plane so that the modal damping of that particular mode is maximised.

Figure 3.26 shows the block diagram of the velocity feedback loop. $\tilde{Y}_{cc}$ is the FRF between the control force, $\tilde{f}_c$ and control velocity $\tilde{v}_c$, $\tilde{Y}_{cp}$ is FRF between the primary excitation $\tilde{f}_p$ and control velocity and g is the control gain. A beam, with the characteristic listed in Table 3.3, is initially used as an example of a distributed structure in this section since it has more widely spaced resonances and the behaviour of the poles is easier to visualise. The expression of the FRFs can be found in reference [25]. The closed loop FRF is given by:

$$\frac{\tilde{v}_c(s)}{\tilde{f}_p(s)} = \frac{\tilde{Y}_{cp}(s)}{1 + g\tilde{Y}_{cc}(s)}, \tag{3.5}$$

and thus, the characteristic equation is given by:

$$1 + g\tilde{Y}_{cc}(s) = 0. \tag{3.6}$$

The root locus is a plot of the solution of the characteristic equation of the closed loop system when the control gain is varied between zero and infinity. The root locus is constructed knowing

the poles and zeros of the open loop FRF $\tilde{Y}_{cc}$ which, for a lightly damped structure, can be written as [36]:

$$\tilde{Y}_{cc}(s) = \frac{s}{k}\frac{\prod_{i=1}^{N}\omega_i^2}{\prod_{i=1}^{N}\theta_i^2}\frac{\prod_{i=1}^{N}(s^2+\theta_i^2)}{\prod_{i=1}^{N}(s^2+\omega_i^2)} \tag{3.7}$$

where s is the complex Laplace transform variable, k is the static stiffness of the structure at control position, ω_i is the i-th complex resonance frequency, θ_i is the i-th complex zero or anti-resonance of the open loop FRF. As an example the cantilever beam of Figure 3.27 controlled by a single ideal velocity feedback loop is considered when the response of the beam is calculated, rain-on-the-roof excitation is assumed.

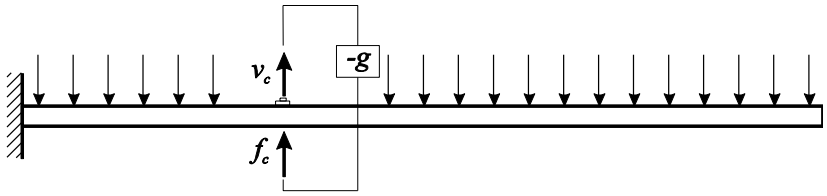

Figure 3.27: Scheme of a cantilever beam subjected to 'rain-on-the-roof' excitation and controlled by a single ideal velocity feedback

Table 3.3: geometrical and physical characteristic of the beam:

Parameter	Value
Dimensions	l =0.31m
Thickness	0.001 m
Width	d=0.025
Mass density	$\rho = 2700$ kg/m^3
Young's modulus	$E = 7 \times 10^{10}$ N/m^2
Poisson ratio	$\nu_1 = 0.33$
Loss factor	$\eta = 1\%$

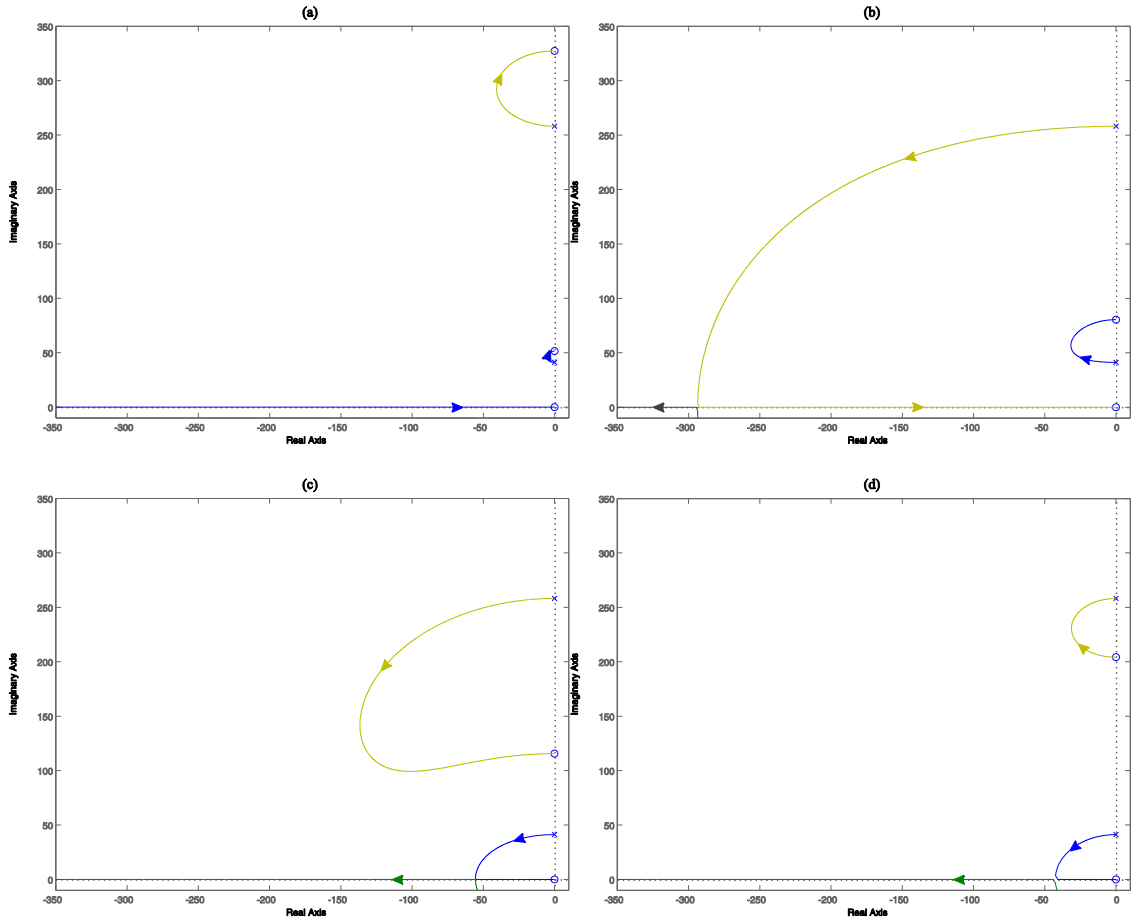

Figure 3.28: root loci of characteristic equation for different position along the beam: a) 0.07 mm b) 0.18 mm c) 0.25 mm d) 0.47 mm

Figure 3.28 shows the root loci plot of the closed loop FRF for four different locations of the controller along the beam. The roots start at the poles of the open loop system when the feedback gain is zero and end up at the zeros of the open loop as the feedback gain tends to infinity [37]. All plots are characterised by an alternating succession of open loop poles and zeros near the imaginary axis. This is due to collocation of the actuator and sensor. The root-locus plot is entirely located on the left hand side of the *s*-plane, since the system is unconditionally stable. Although only the root loci relative to the first two modes are shown, the first five modes in equation (3.7) have been taken into account in the simulations. The open loop poles of the system are independent of the location of the control loop but the open loop zeros change with this location.

Figure 3.28(a) shows the root locus plot when the control position is located at x=0.07 m. The two poles move to the nearest zeros, which are closely spaced in this case, when the control gain is increased and they coincide with the zeros when the control gain tends to infinity. The zeros represent the natural frequency of the structure when pinned at the control position. Figure 3.28(b) shows the root locus plot when the controller is located at x=0.18 m. In this case the second pole does not move to the next zero but towards the origin of the *s*-plane when the

gain is increased. When the second pole is real, the second mode becomes critically damped. When the controller is located at x=0.25mm (Figure 3.28(c)), the distance between the first zero and the second pole becomes smaller than the distance between the first pole and origin, therefore the first pole moves towards the origin and the second pole moves to the first zero as the control gain is increased. Figure 3.28(d) shows the root locus plot when the control position is located near the tip of the beam. The root locus does not show substantial difference with the previous case.

The uncontrolled response of a cantilever beam is characterised by well separated modes at low frequency, which have a magnitude that rapidly decreases with the frequency for a fixed loss factor. Therefore a good broadband attenuation of the beam's response can be obtained by controlling only the first mode. The modal damping for a given control gain can be obtained from the root locus plot as the sine of the angle formed by the imaginary axis and the line connecting the origin of the s-plane to the point of the root locus corresponding to that particular gain. Figure 3.29 shows the root locus plot of the closed loop FRF relative to the first mode only when the controller is placed at x=0.18 m. The maximum damping achievable for the first mode is given by the sine of the angle β.

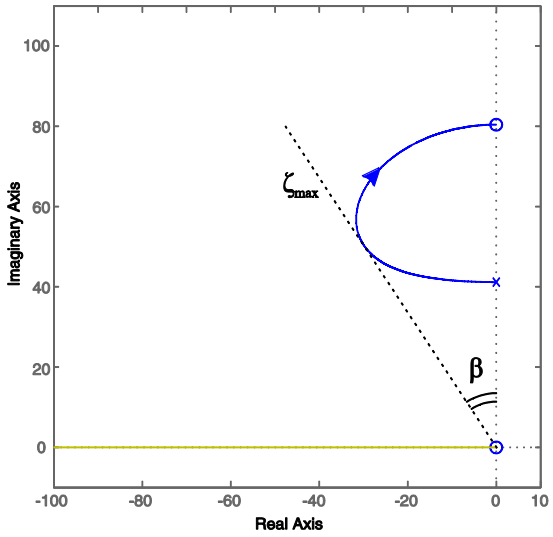

Figure 3.29: root locus of the direct velocity feedback loop for the first mode at control position 0.18 m

The root locus plot of Figure 3.28 shows that it is not a simple matter to predict the trend of the root locus plot just knowing the position of the open loop zeros and poles. To compute the optimal value of the control gain, it is necessary to calculate the entire root locus. Therefore, the implementation of this strategy as a self-tuning control would first require the measurement of the open loop poles and zero of the structure from its measured frequency response, the computation of the root locus of the characteristic equation and, finally, the estimation of the optimal control gain.

Approximate values of the control gain that maximises the modal damping of the first mode can, however, be found in literature [7, 36]. Considering the root locus of the first mode in Figure 3.28, two distinct situations can be highlighted: in the first one the pole moves to the next highest zero (plot (a) and (b)) and in the second one the first pole moves to the origin of the *s*-plane (plot (c) and (d)). In plots (a) and (b) the distance of the first pole to the first zero can be considered small compared to all the other poles and zeros. Therefore, equation (3.7) can be approximated, in the vicinity of the first pole, by only considering the contribution of the first mode, as:

$$\tilde{Y}_{cc}(s) = \frac{1}{k_1}\frac{s(s^2 + Z_1^2)}{s^2 + \omega_1^2} \tag{3.8}$$

where

$$k_1 = \frac{1}{k}\frac{Z_1^2}{\omega_1^2} \tag{3.9}$$

Under this assumption, Engelen et al. [36] found an approximate solution of the maximum value of modal damping by solving equation (3.6) using a perturbation method, giving:

$$\zeta_{1max} = \frac{\omega_1 - Z_1}{2\omega_1} \tag{3.10}$$

which correspond to an optimal gain of:

$$g_{opt} = \frac{1}{k}\frac{Z_1^2}{\omega_1^2}\frac{\sqrt{\omega_1/Z_1}}{Z_1} \tag{3.11}$$

In the second case, when the pole moves towards the origin of the *s*-plane, the optimal gain is the smallest values that critically damp the first mode. No expressions for the optimal control gain have been found in literature for this specific case. However, Engelen *et al.* [36] have shown that setting the control gain using equation (3.11) gives a good approximation for the optimal gain, even if the controlled mode can be critically damped. Figure 3.30 shows a comparison of the optimal control gains for different location of the feedback loop along the beam obtained from equation (3.11) (solid line) and numerical simulations (dashed line). In the simulation the optimal control gain has been tuned to maximise the modal damping of the first mode or, in case the first mode can be critically damped, has been tuned to the minimum control gain for which critical damping is achieved. The plot show that the maximum difference in control gain using equation (3.11) and the numerical values is about 7 dB.

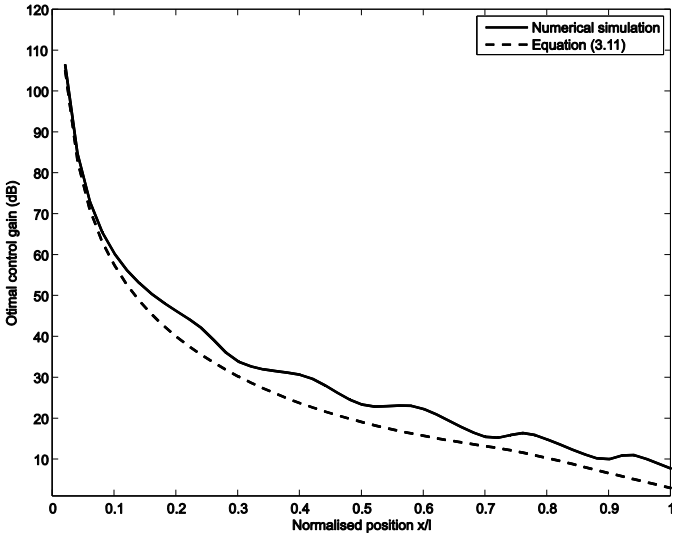

Figure 3.30: optimal control gains for different position of the controller along the beam calculated with numerical simulations (solid line) and using equation (3.11) (dashed line).

Similar strategy can be used to optimise the gain of a feedback controller on a panel, although the root locus diagram becomes more complicated due to the closer spacing between the modes. This makes the root loci very dependent on the position of the controller on the panel and requires some care in the selection of the locus whose real part is to be minimised.

3.4. Comparison of different strategies of tuning single feedback loop

In order to compare the three tuning strategies discussed in the previous sections, simulations have been carried out for different control loop locations on a cantilever beam subjected to rain-on-the-roof excitation. In the simulations the first eleven modes of the beam have been taken in to account and the kinetic energy of the structure and the power absorbed by the controller have been averaged between 1Hz-1kHz. The optimal values of the control gains which maximise the control stability have been found numerically. For control location where the first mode can be critically damped, the minimum value of control gain for which critical damping is achieved is assigned. Figure 3.31 and Figure 3.32 shows the three values of the control gains and the corresponding reduction in the total kinetic energy found using the three optimisation strategies for different controller position along the beam. Although the optimal gains using the three optimisation methods can be quite different, the reductions in the total kinetic energy are very similar. The major differences can be observed near the clamped side of the beam where the maximisation of the power absorbed seems to underestimate the control gain compared with the other two. This is also the area where the smallest reduction in the total kinetic energy of the beam can be achieved because the modal amplitude of all the structural modes is small.

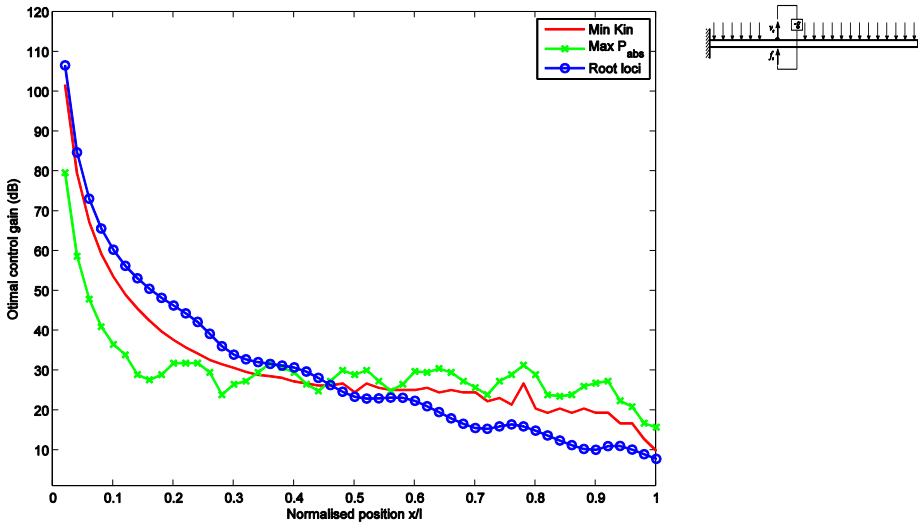

Figure 3.31: Values of the control feedback gain found using the three tuning strategies as function of the control point along a cantilever beam

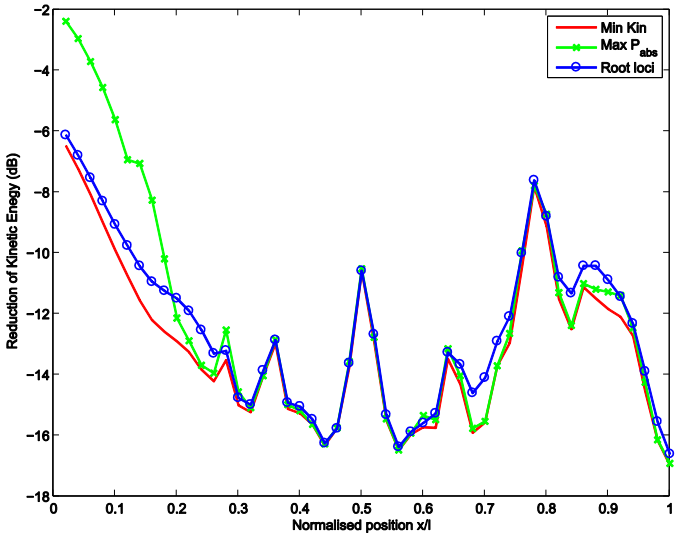

Figure 3.32: Reduction of total kinetic energy achieved using the three strategies as function of the control point along a cantilever beam

Simulations have also been carried out to compare these three tuning strategies for control of a simply supported panel subject to 'rain-on-the-roof' excitation. Two cases have been considered: when the controller is moved along the x-axis at y=0.5l_y and at y=0.25l_y.

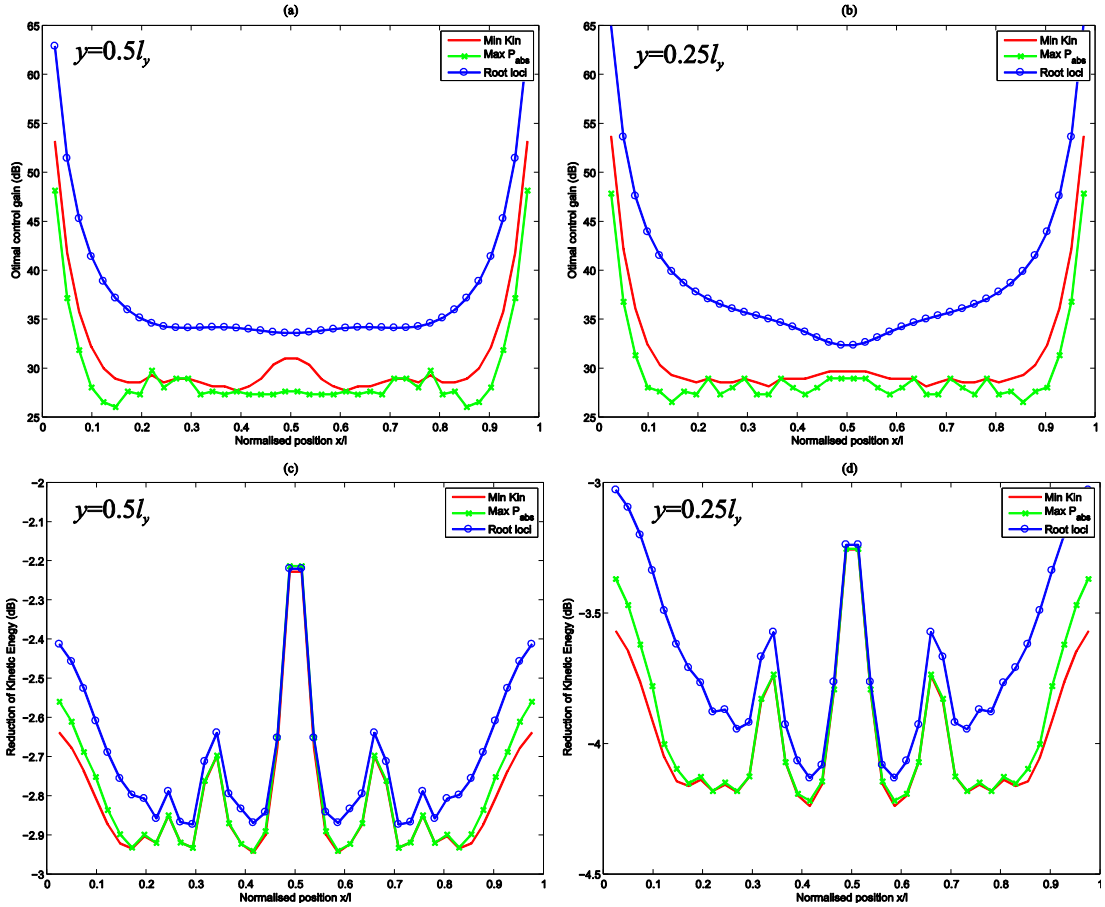

Figure 3.33: (a) and (b) optimal control gains and (c) and (d) reduction in the kinetic energy for the three tuning strategies on a panel when the controller moves along the x-axis at y=0.5l_y and 0.25l_y

The optimal control values and corresponding reduction in terms of kinetic energy of the panel are shown in Figure 3.33 for the two cases.

The plots show that although the optimal feedback gains are relatively independent on the position except near the boundaries, as observed by [26], the attenuation varies depending on which modes can be easily control by the actuator. A controller at the centre, for example, cannot control any even-even order modes.

In the control of a panel the maximisation of control stability method seems to performance worse than in the case of a cantilever beam if compared with the minimisation of the kinetic energy of the structure. This is due to the fact that the uncontrolled panel's response is dominated by more modes at low frequency than the beam and this tuning method is optimised to control only the first structural mode. However the three methods give similar performance in terms of the total kinetic energy of the panel, as shown in the two bottom plots of Figure 3.33, provided the controller is not positioned to close to the edge of the panel.

3.5. Summary and conclusions

This chapter has discussed the vibration control of flexible structures using self-tuning ideal velocity feedback loops. The total kinetic energy of the structure has been taken as a benchmark to compare two tuning strategies: the maximisation of the power absorbed by the controller and the maximisation of the control stability.

The background in using the absorbed power as a tuning strategy has been reviewed in the first section. In the application considered here, the force is generated by the ideal actuator and is made proportional to the measured velocity. The absorbed power could thus be readily estimated from the mean square value of the measured velocity and the feedback gain, thus providing a simple measurement of an entirely local parameter that has been used to tune the gains. It has been shown that, for broadband disturbance, maximising the absorbed power approximately minimises the kinetic energy of the structure. For narrow-band and single frequency excitations, however, the maximisation of the power absorbed could increase the structural response. Simulations on the convergence of an algorithm to adjust the control gains of independent feedback loops have been carried out.

The maximisation of the control stability as a further tuning strategy of the control gain of a single feedback loop has been considered in this chapter. A cantilever beam subjected to broadband excitation has been considered for this application. This control strategy aims to maximise the damping ratio of the first structural mode. The estimation of the optimal control gain has been made using the root locus plot of the closed loop response. It has been shown that the root locus plot changes depending on the position of the controller along the beam. Therefore the optimisation can be done after the entire root locus has been computed. To avoid this, approximate expression of the optimal control gain could be used instead. In this case the self-tuning procedure would require the measurement of the poles and zeros of the open loop structure and the estimation of the control gain.

In the last section the two tuning strategies have been compared with the minimisation of the kinetic energy of the entire structure under control giving similar level of performance.

The next two chapters will discuss the experimental implementation of self-tuning decentralised velocity feedback based on the maximisation of the power absorbed by the controller using reactive actuators.

4. Design and testing of the experimental panel and the controller

In this chapter the panel used for the experiments on decentralised velocity feedback using reactive actuators is described. The experimental panel is equipped with nine reactive electromagnetic actuators collocated with nine sensors. Two different types of sensors were used: B&K piezoelectric accelerometers and low cost MEMS accelerometers. All the components in the control loop are first described for each of the two configurations, including sensor-actuator pairs and control electronics.

In the theoretical analysis in Chapter 3 it was possible to assume that the control loops were unconditionally stable, since ideal force actuators and velocity sensors were used. The dynamic response of the actuator and sensor in the experimental system can lead to instability for high feedback gains i. e. conditional stability. Particular care must thus be taken to assess the stability of the controller from the open loop frequency response before the closed loop frequency response is calculated. Simulations are then performed to predict the closed loop behaviour of the control system. The experimental results of closed loop control are left until Chapter 5.

4.1. The experimental panel design

The experimental panel demonstrator built for this study consists of a 1 mm thick rectangular aluminium panel with dimensions 0.412×0.312 m^2. The panel is equipped with 9 miniature voice coils actuators, consisting of a coil and a permanent magnet. As shown in Figure 4.1 the actuators are placed between the panel and a frame which is used to react the force off. Since the coils are lighter than the magnets, they were attached to the panel, whereas the permanent magnets were attached to the relatively rigid frame. In this way the passive effect of the actuator on the panel is minimised. The reactive actuators were commercial coil and magnet device (H2W technologies, NCC01-04-001) and one is shown in Figure 4.2.

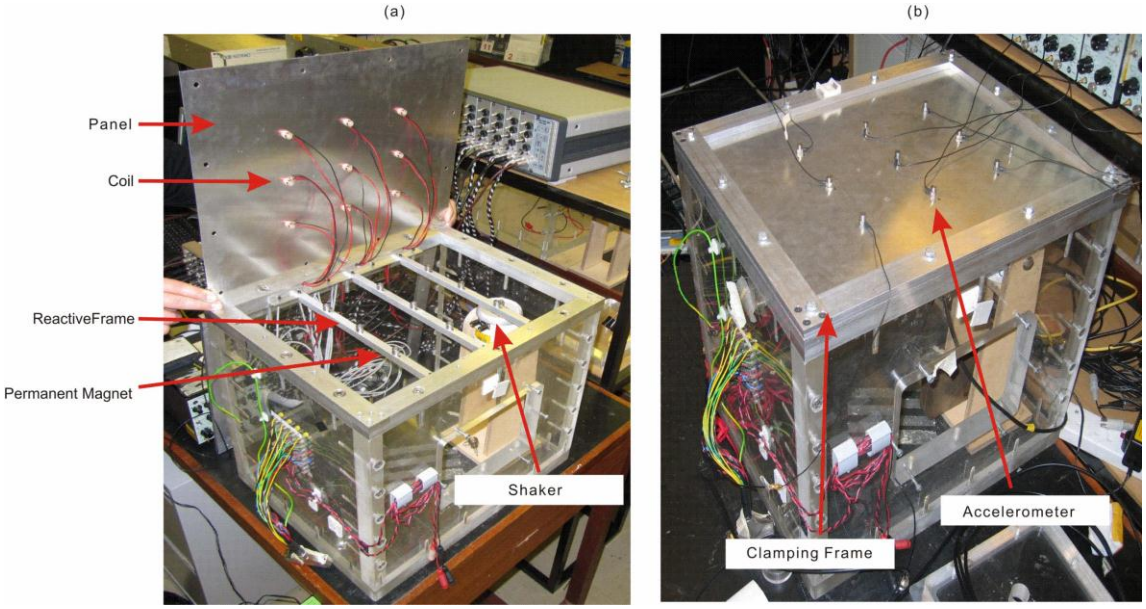

Figure 4.1: The prototype experimental panel; a) the lower clamping frame with the reactive frame mounted on top of the thick-walled Perspex box, b) aluminium panel with 9 B&K accelerometers.

Figure 4.2: a) the miniature voice-coil actuator (H2W, NCC01-04-001) shown in comparison to a US$ quarter coin.

Each of the nine coil and magnet pairs is equipped with an accelerometer closely located with the coil. Two configurations are analysed: in the first one the feedback sensor is a high-performance piezoelectric accelerometer (B&K type 4375) shown in Figure 4.3(a), in the second one the feedback sensor is a MEMS accelerometer (Analog Devices ADXL103) shown in Figure 4.3(b).

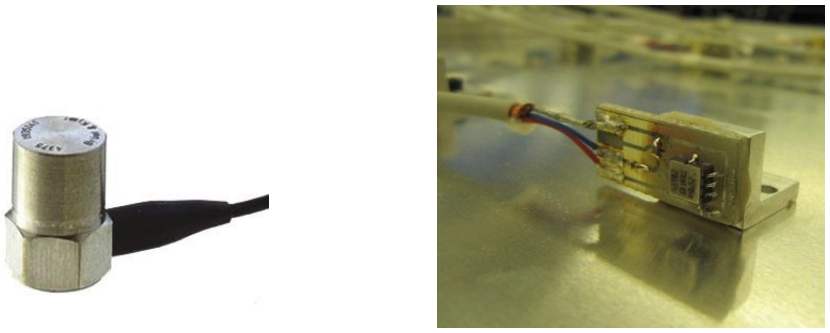

Figure 4.3: a) the B&K accelerometer type 4375, b) the MEMS accelerometer chip connected to a 10×20 mm^2 board.

As shown in Figure 4.1(b), the panel is clamped between two aluminium frames. The frames have a width of 32 mm, but they have different thicknesses: 25mm for the bottom frame and 10 mm for the top one. The clamping frame and the panel are mounted on one side of a Perspex box, which was left open during the experiments to avoid strong coupling between the panel and the volumetric mode of the cavity.

Table 4.1: Physical properties of the smart panel and transducers

	Parameter	Value
Aluminium Panel	Dimension (mm)	412×312
	Thickness(mm)	1
	Density (kg/m3)	2700
	Young's modulus (GPa)	70
	Poisson's ratio	0.33
Perspex Box	Box wall thickness (mm)	30
	Shaker position (x, y) (mm)	(65, 93)
	Box inner dimension (mm)	412×312×400
Accelerometer B&K	Resonant frequency (KHz)	35
	Frequency bandwidth (Hz)	0.1 - 16500
	Model	4375
Accelerometer MEMS	Resonant frequency (KHz)	5.5
	Frequency bandwidth (Hz)	0.1 - 2500
	Model	Analog Devices ADXL103
Voice-coil actuator **H2W Technologies**	Peak force (N)	0.9
	Outside Diameter (mm)	9.5
	Total length (mm)	12.7
	Coil mass (g)	1.2
	Resistance (Ω)	1.5
	Model	NCC01-04-001
EDVECO Force sensor	Model	2312
B&K charge amplifier	Model	2635
LDS Shaker	Model	V200
LDS Power amplifier	Model	PA25E-CE

The panel was excited by a shaker placed in the box. A force sensor was placed between the shaker and the panel to measure the primary force produced by the shaker. The physical

properties and geometry of the smart panel and the main characteristics of the transducers are summarised in Table 4.1.

An initial set of measurements have been taken using B&K piezoelectric accelerometers as feedback sensors. The charge output of each B&K accelerometer was amplified using a charge amplifier (B&K type 2635). The charge amplifiers are equipped with a high pass filter with cut off frequency of 10 Hz and an electrical integrator in order to obtain a measurement of the velocity. An second set of measurements have been taken using nine low cost MEMS accelerometers mounted on an aluminium L support. The aim of these measurements is to test the possibility of using cheap and low performance accelerometers without compromising the control stability. The MEMS accelerometer is designed to measure vibration up to 2.5 kHz and has a resonant frequency of the seismic vibrating mass at 5.5 kHz. These sensors need external power supply of 5 V and do not have a circuit to integrate the signal output to get a measurement of the velocity. An existing control box, designed in ISVR and manufactured for similar applications, has been used to supply power to the MEMS accelerometer, integrate and amplify the signal output.

In both configurations, in order to measure the open loop frequency response functions (FRFs) using a twenty channels analyser (Data Physics Mobilyzer II), the actuators have been driven with a reference white noise signal, amplified by a LDS PA25E voltage amplifier.

4.2. Response of the open loop system

In this section the response of the controller for the configurations using B&K and MEMS accelerometers is described in detail. If the control-sensor pairs are dual and collocated, constant gain feedback loops are in theory unconditionally stable [18], since the phase of the open loop frequency response function, FRF, is confined between ±90º at all frequencies.

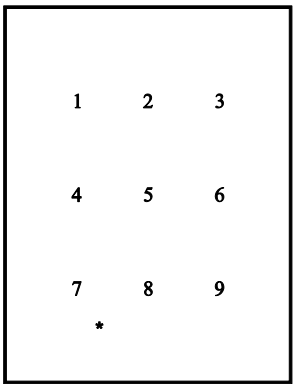

Figure 4.4: Scheme of the panel with the positions of the 9 control units and position of the primary source, *.

Unfortunately in a real system the actuators and sensors approximate ideal force and velocity transducers only for a certain frequency band. Moreover the presence of filters in feedback loop

may introduce phase shift which can limit the control gain before instability [38]. All the results shown in this section for the stability studies of the single channel system refer to the control unit number 5 of Figure 4.4.

4.2.1. Response of the controller using B&K accelerometers

In this section B&K accelerometers were used as sensors, since these have a good frequency response below resonance. In order to analyse the stability of the feedback loop when B&K accelerometers are used as feedback sensors, the control system has been notionally divided into the blocks shown in Figure 4.5 and the FRF of each component of the system has been measured. In this way it is easier to identify the effect of each element on the overall stability of the control loop. The reactive force actuators are made of miniature coil and magnet pairs, which have their own dynamics. The electrical admittance of the actuator, represented in Figure 4.5 by the first block, has been measured taking the voltage input signal *U* as reference and measuring the current *I* which is proportional to the force generated by the actuator [7].

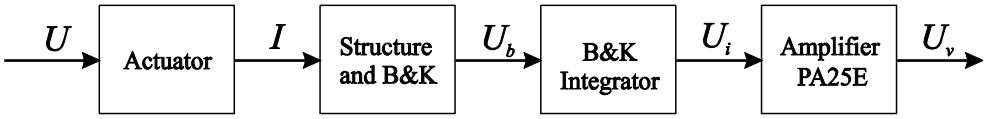

Figure 4.5: Schematic representation of all the components of each feedback loop using B&K accelerometers.

The FRF in Figure 4.6 shows that the coil behaves like a low pass filter with a cut-off frequency of 7.3 kHz. The phase is about zero up to 200 Hz above which it starts to drop due to the inductance of the coil. The small peaks visible in the plot are due to the response of the panel which affect the electrical impedance of the actuator through the transduction coefficient [39]. The maximum phase lag, of about -70°, occurs at around 8 kHz.

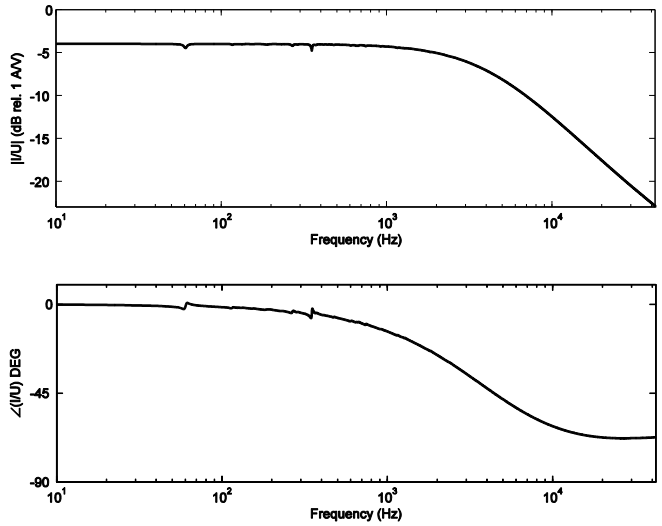

Figure 4.6: Measured admittance of the actuator

The structural response is represented by the second block in Figure 4.5. Since the applied force is proportional to the current, the main part of the FRF curve in Figure 4.7 is what one would expect from the point excitation of a structure, with a phase between 0° and -180°. The response is characterised by resonances followed by anti-resonances. An additional phase lag of 180º appears at around 35 kHz due to the natural frequency of the B&K accelerometer.

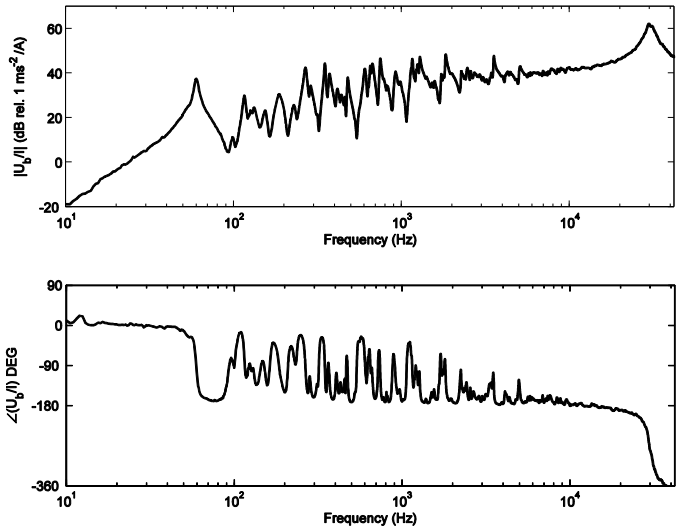

Figure 4.7: Measured structural response at position 5.

The output signal of the accelerometer is integrated to get a measurement of the velocity of the structure using the electrical integrator of the B&K charge amplifier. The measured FRF of the integrator in the charge amplifier is plotted in Figure 4.8 when the cut-off frequency of the high pass filter is set to 10 Hz. The plot shows that the integrator behaves almost like an ideal integrator over the frequency band of interest, producing the desired 90º phase shift.

The amplifier used to amplify the sensors signal is the LDS PA25E voltage amplifier, its FRF is shown in Figure 4.9 when the amplification gain is set on the maximum value. The response of this amplifier is almost constant at all the frequencies except for the offset of a high pass filter with a cut-off frequency of 4 Hz.

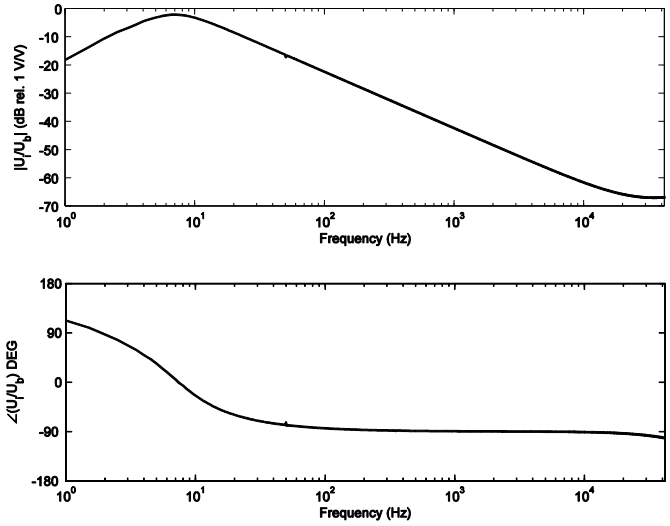

Figure 4.8: Measured FRF of the B&K integrator

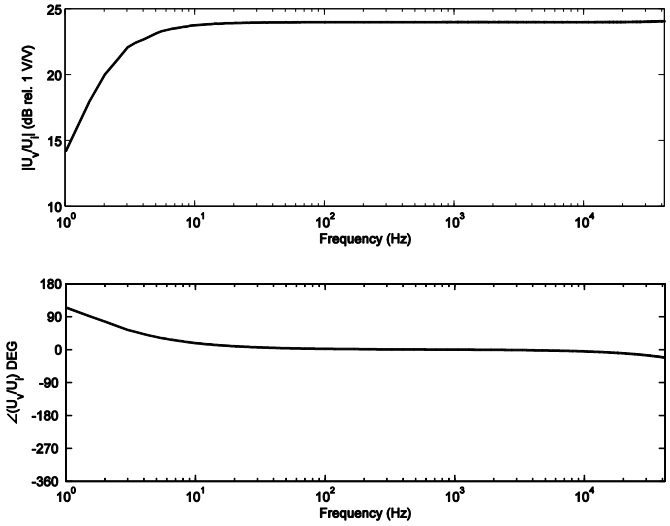

Figure 4.9: Measured FRF of the LDS PA25E voltage amplifier

Figure 4.10 shows the directly measured open loop FRF (solid line) and the one predicted using the individual measured responses of each element of Figure 4.5 (dashed line). The plot shows that the prediction is in reasonable experimental agreement with the measurement. The phase of the open loop FRF is confined between ±90º up 2.5 kHz. From about 2.5 kHz the phase excited -90º and starts to drop because of the phase lag introduced by all the component of controller. At 35 kHz a phase lag of -180º occurs due to the natural frequency of the sensor.

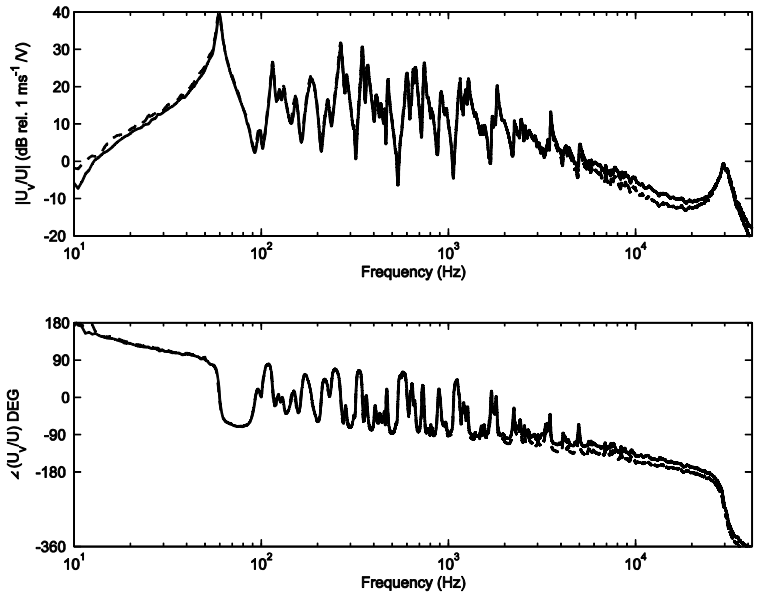

Figure 4.10: Measured open loop FRF of channel 5 (solid line) and predicted using the individual measured responses of each element of the feedback loop (dashed line).

4.2.2. Response of the controller using MEMS accelerometers

This section is focussed on the description of the controller using MEMS accelerometers following the same procedure of subsection 4.2.1. Figure 4.11 shows the block diagram of the second configuration of the controller. Each FRF of the components represents by the blocks in Figure 4.11 have been measured. The first and second blocks represent the electrical admittance of the actuator and the structural response already discussed in the previous section and plotted in Figure 4.6 and Figure 4.7.

Figure 4.11: Schematic representation of all the components of each feedback loop using MEMS accelerometers

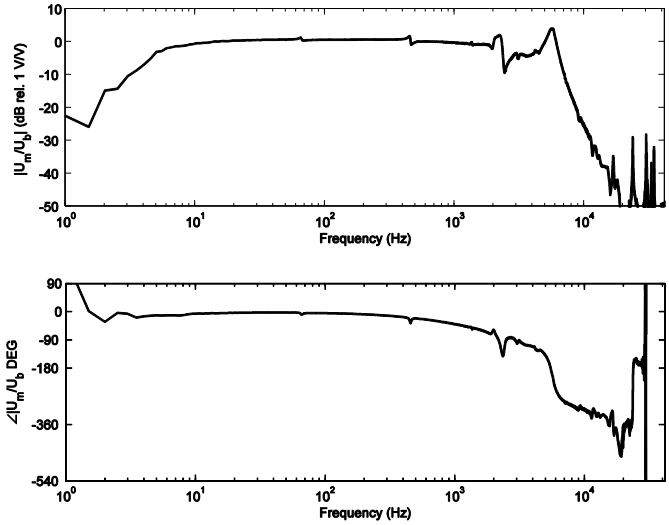

Figure 4.12: Measured FRF of the MEMS accelerometer.

The third block in Figure 4.11 represents the FRF of a MEMS accelerometer shown in Figure 4.12. The graph shows a phase response almost flat up to 2.5 kHz where it starts to drop.

A phase delay of 180º with a peak in the magnitude is visible at around 5.5 kHz due to the resonance frequency of the seismic mass of accelerometer. An additional phase lag is due to the low pass filter mounted on the MEMS accelerometer with cut off frequency of 2.5 kHz. The smaller peaks at lower frequency are due to the resonance frequencies of the L support where the MEMS is attached.

Finally, an integrator and an amplifier manufactured in ISVR have been included in the block diagram to complete the implementation of the velocity feedback loop. The front panel of the control box is shown in Figure 4.13. Each control channel has three checkpoints for monitoring the three stages in each channel: pre-integration, post-integration, and final, post-amplification check point.

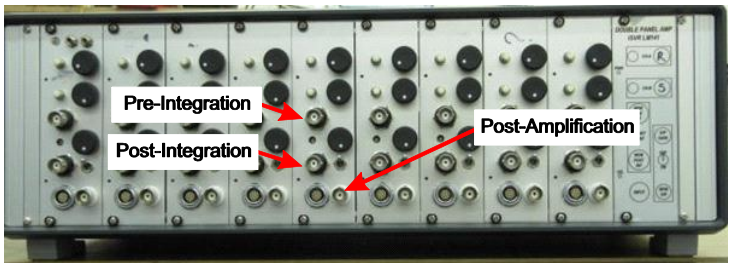

Figure 4.13: The front panel of the ISVR control box.

Figure 4.14 and Figure 4.15 show the measured FRFs of integrator and the amplifier of the ISVR control box shown in Figure 4.13. The -3dB corner frequency of the integrator is about 4 Hz. The amplifier is provided with a high pass filter with cut off frequency of 50 Hz which corresponds to a phase lag of 90º.

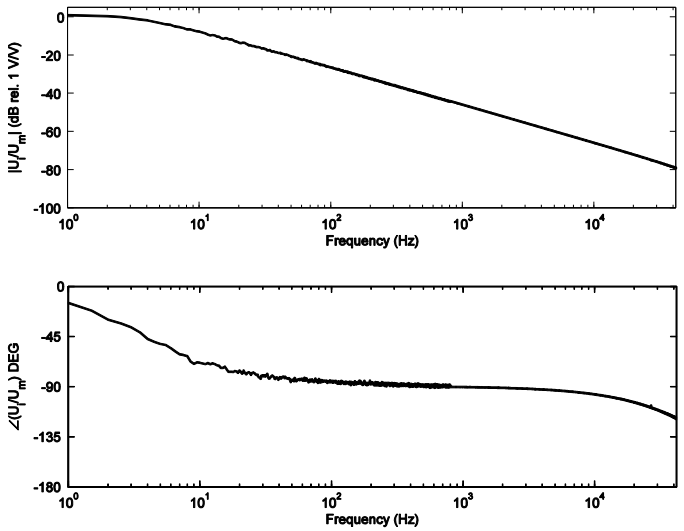

Figure 4.14: Measured FRF of the integrator of the ISVR controller.

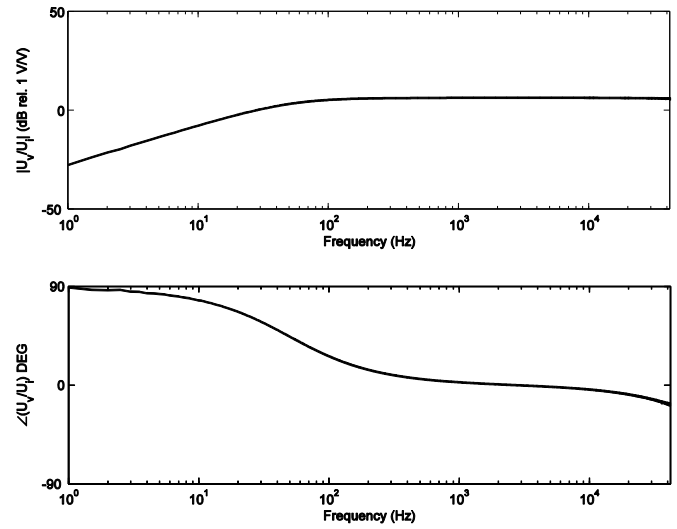

Figure 4.15: Measured FRF of the amplifier of the ISVR controller.

Figure 4.16 shows the Bode diagram of the open loop FRF between the voltage of signal feeding the actuator and the integrated and amplified output of the MEMS accelerometer (dotted line), and the same FRF (solid line) predicted using the individual responses of each element in Figure 4.11.

The plot shows that the prediction from the measured FRF of each component is in reasonable experimental agreement with the measurement. The phase of the open loop FRF is confined between ±90º up 500 Hz. From about 500 Hz the phase excited -90º and starts to drop because of the phase lag introduced by all the component of controller described so far. At 5.5 kHz a phase lag of -180º occurs due to the natural frequency of the MEMS.

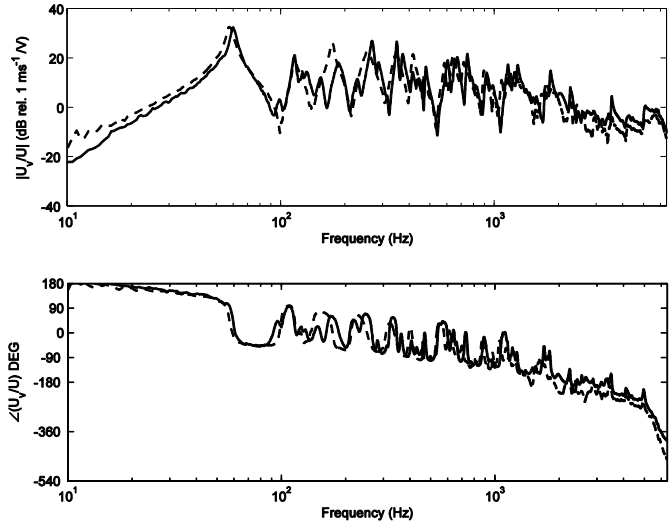

Figure 4.16: Measured open loop FRF of channel 5 (solid line) and predicted using the individual measured responses of each element of the feedback loop (dashed line).

4.3. Stability and performance analysis of single feedback loops

In this chapter the stability of the two control systems described in section 4.2 is studied. The final aim of the experiment is to tune the control gain of each independent control unit in order to maximise their power absorbed without leading the system to instability. The stability of each control unit is therefore assessed using the Nyquist criterion and the closed loop response is simulated in MATALB.

4.3.1. Stability and performance of single channel using B&K accelerometers

Figure 4.17 (a) shows the Nyquist plot of the open loop FRF when the control gain is adjusted to have 6 dB gain margin. Figure 4.17(b) shows a zoom at the origin axis of the Nyquist plot of the sensor-actuator open loop FRF. The plot shows that the locus cross the left hand side of the diagram indicating that the system is only conditionally stable. The gain margin is the maximum increase in gain that can be tolerated before the system gets unstable and is given by $1/\delta$ where δ is the distance indicated in Figure 3.17(b).

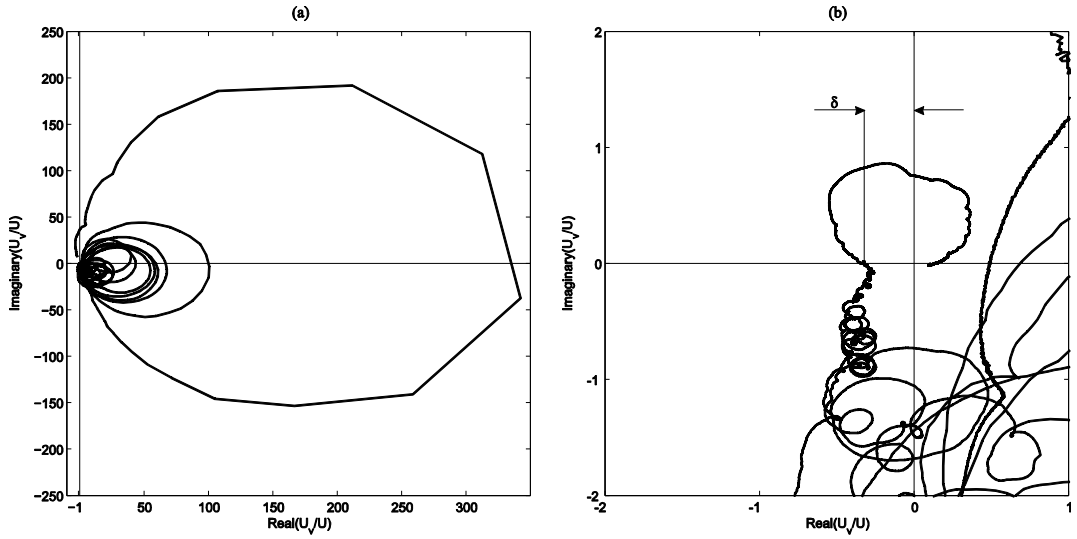

Figure 4.17: (a) Nyquist plot of the measured open loop FRF of channel 5 and (b) zoom at the origin using a B&K accelerometer

In order to study the performance of the control system and to investigate how the control system influences the dynamic of the panel, a MATLAB simulation has been carried out based on the measured responses. Firstly, the response of the panel at the control positions subjected to the primary excitation has been measured. The panel has been excited by a shaker fed with white noise. The nine FRFs between the force applied by the shaker, measured by a force sensor and the velocities measured by the nine B&K accelerometers have been measured. Secondly, the nine FRFs between the voltage driving the reactive actuator and the nine velocities have been measured. This analysis has been carried out for the all loops but only the results relative to loop number 5 are discussed in this chapter. The complete set of results relative to all the channels can be found in Appendix C.

The panel's PSD of the kinetic energy has been estimated as:

$$S_k(\omega) = \frac{M}{2R}\sum_{r=1}^{R}|\tilde{v}_r|^2. \tag{4.1}$$

where $|v_r|^2$ is the mean squared value of the velocity measured by the *r*-th accelerometer, *M* is the mass of the panel and *R* is the number of the accelerometers. Equation (4.1) gives a good approximation of the kinetic energy of the panel in the frequency range where the distance between adjacent accelerometers positions is smaller than half wavelength. The aim of the controller is to reduce the structural response at low frequency, where the wavelength is large.

Simulations of clamped-clamped aluminium panel of the same dimensions of the experimental panel and controlled by an ideal velocity feedback loop have been carried out. Figure 4.18 shows PSD of the sum of the mean squared values of the velocities calculated in (a) 49 evenly separated locations and (b) calculated in five locations on the panel. The estimate of the kinetic

energy is plotted when the control gain is zero (solid line), when the total kinetic energy is minimised (dashed line) and for very high values of control gain (dotted line). Comparing the two plots similar responses can be observed although the contributions of some modes at higher frequencies are not visible when 5 monitoring positions are considered. This estimate of the kinetic energy of the panel is used here to evaluate the performance of the controller, even though it is not used in the tuning process. Since the structural response is dominated by the low frequencies modes, it can be concluded that nine monitoring positions is a reasonable number to obtain good estimation of the total response of the panel when one or two control units are used.

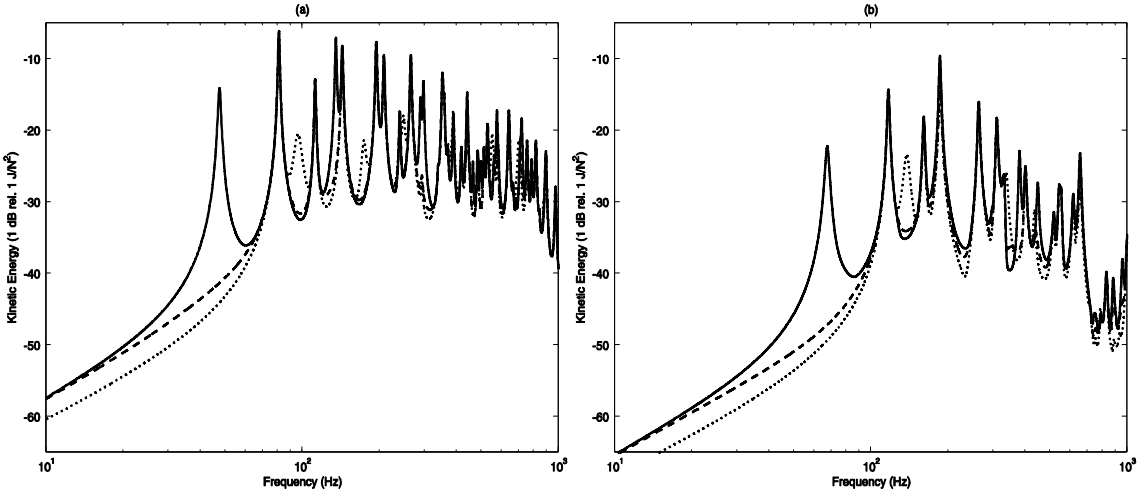

Figure 4.18: Simulated PSD of the estimated kinetic energy of a panel with no control (solid line), minimising the estimated frequency averaged kinetic energy of the panel (dashed line) and high control gain (dotted line) simulated using (a) 47 monitoring locations (b) 5 monitoring position.

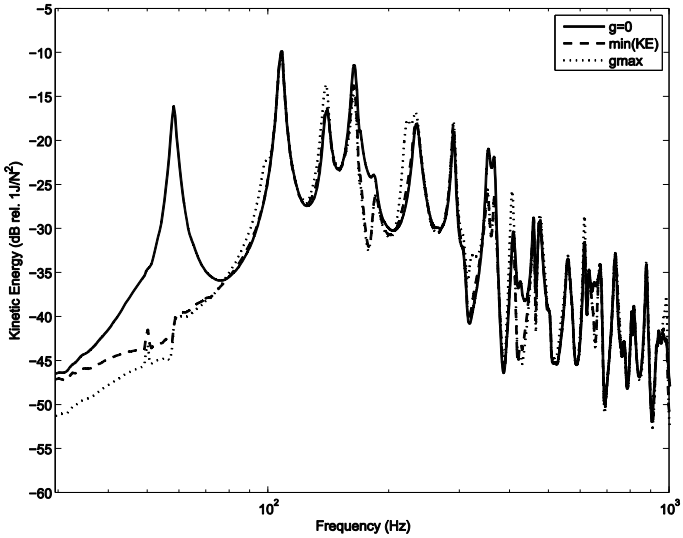

Figure 4.19: Simulated PSD of the kinetic energy of the panel obtained from measured responses without control (solid line), minimising the total kinetic energy of the panel (dashed-line) and with 6 dB gain margin (dotted-line).

Figure 4.19 shows the simulated PSD of kinetic energy of the panel without control, minimising the kinetic energy of the panel and when the control gain giving 6 dB gain margin is

implemented. The plot shows that the control unit is able to reduce the response of the panel at the first resonance frequency when the control gain is set to the value that minimises the frequency averaged kinetic energy of the panel. Implementing the control gain which guarantees 6 dB gain margin, the response of the panel is slightly increased at higher frequency indicating that the control unit starts to pin the panel at the control position. Because control unit number 5 is positioned in the centre of the panel only odd-odd modes can be controlled.

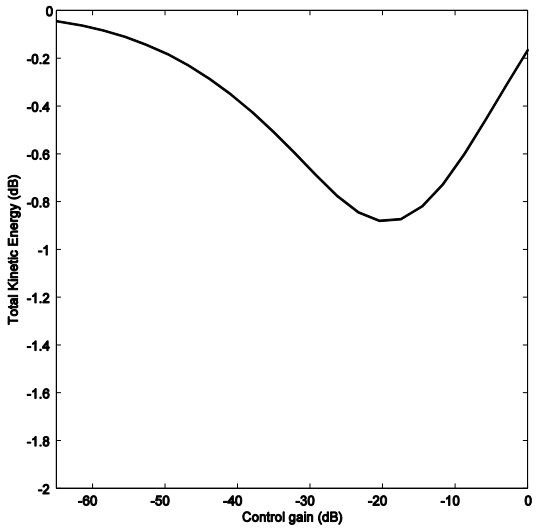

Figure 4.20: Simulated frequency averaged PSD of the kinetic energy of panel obtained from measured responses as function of the control gain number 5.

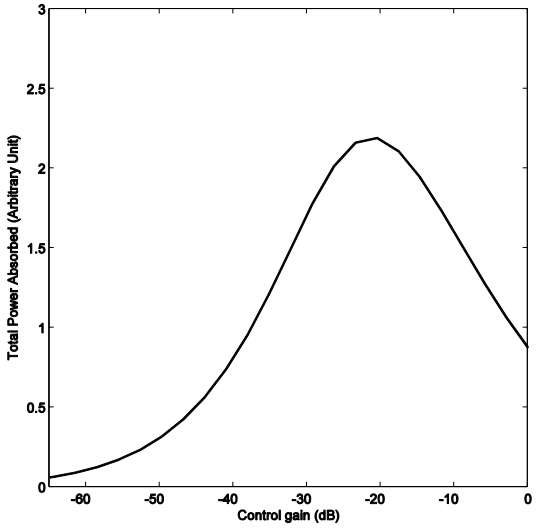

Figure 4.21: Simulated frequency averaged PSD of the power absorbed by control unit number 5 obtained from measured responses as function of the control gain number 5.

This is confirmed by the plot of Figure 4.20 which shows the frequency averaged kinetic energy as function of the control gain. Figure 4.21 shows the simulated total power absorbed by the control unit as function of the control normalised to the value giving 6 dB gain margin. The plot shows that the power absorbed is maximised for a single value of control gain. Using B&K

accelerometers allow the system to reach the maximum of power absorbed before the system gets unstable. Moreover the value of gain that maximises the power absorbed is about the same as the one that minimises the total kinetic energy of the panel.

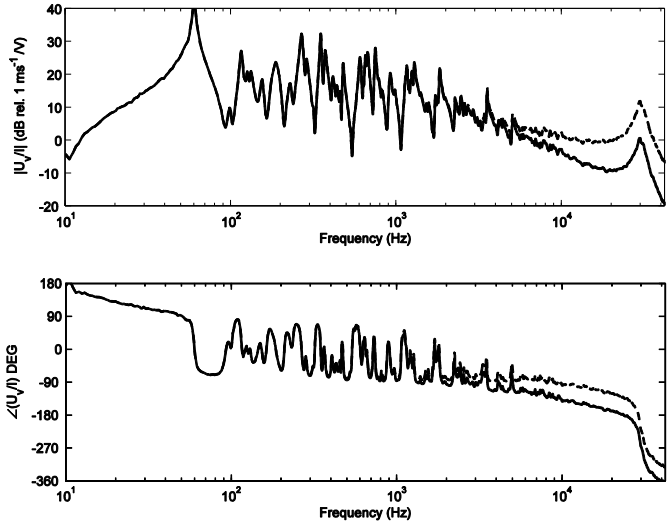

Figure 4.22: Measured open loop FRF of channel 5 driving the actuator with a current (dashed line), driving the actuator with a voltage (solid line)

Driving the actuator with a current eliminates the phase lag introduced by the electrodynamics behaviour of the actuator discussed in section 4.2.1. Figure 4.22 shows the open loop FRF driving the actuator with a current (dotted line) and open loop FRF driving the actuator with a voltage (solid line). The FRF is included between ±90° up to 5 kHz when the actuator is driven with a current while the phase starts to drop from 2.5 kHz in case of voltage driving. An abrupt phase lag with a peak in the magnitude is measured at about 35 kHz due to the resonance frequency of the accelerometer in both cases. The magnitude of the peak is much smaller in case of voltage driving because of the roll-off introduced by the coil of the actuator. Figure 4.23 shows the Nyquist plot of the open loop FRF between the current driving the actuator and the velocity measured by the sensor for 6 dB gain margin. If this plot is compared with the Nyquist plot of FRF of the voltage-driven actuator in Figure 4.17, it is clear that that the system becomes unstable for much smaller value of control gain when driven by a current. In fact the reduction achievable at the first resonance frequency in the response at the control position in case of current-driven actuator is about 20 times smaller than the one achievable with a voltage-driven actuator. Even though a phase lag is introduced by the electrodynamics behaviour of the actuator when driving with a voltage, this also brings a roll-off which lowers the magnitude of the peak due to the resonant frequency of the accelerometer in the open loop FRF, so that the control system can tolerate higher gain before instability occurs.

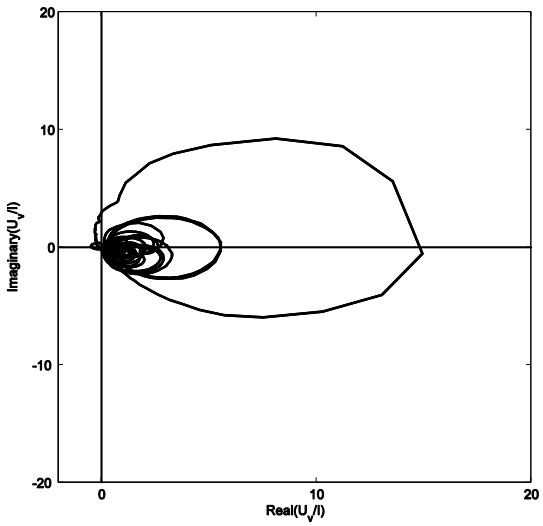

Figure 4.23: zoom at origin of Nyquist plot of the open loop FRF of channel 5 when the actuator is driven with a current.

4.3.2. Stability and performance of each channel

The same simulation described in section 4.3.1 has been carried out for all the channels.

Table 4.2: : value of control gains, normalised to that for a 6 dB gain margin, required to minimise the kinetic energy or maximise the power absorbed for each of the 9 control loops alone, and the consequential changes in kinetic energy.

Ch.	Feedback gain minimising kinetic energy (dB)	Reduction in kinetic energy (dB) minimising the kinetic energy	Feedback gain maximising the power absorbed (dB)	Reduction in kinetic energy (dB) when maximising the power absorbed	Ratio of gains maximising the power absorbed and minimising the kinetic energy	Increase in kinetic energy (dB) due to maximisation of power compared with minimising kinetic energy
1	-25.6	-1.6	-19.5	-1.3	0.8	0.3
2	-25.5	-1.9	-17.9	-1.5	0.7	0.4
3	-27.5	-1.5	-21.7	-1.2	0.8	0.3
4	-35.2	-0.5	-19.1	1.2	0.5	1.7
5	-19.5	-0.9	-21.2	-0.7	1.1	0.2
6	-19.7	-1.3	-23.8	-1.3	1.2	0.04
7	-12.8	-5.4	-21.0	-4.5	1.7	0.9
8	-22.5	-2.3	-15.4	-1.9	0.7	0.3
9	-26.0	-1.6	-20.1	-1.4	0.8	0.2

As shown in the Nyquist plots in Appendix C, all the single channels system are conditionally stable since the curves of the Nyquist plots enter in left hand side of the diagram but do not encircle the point (-1,0*j*). The control gains have been limited to be smaller than a certain values that lead the system to instability. The instability is mainly due to high frequency dynamic of the sensors.

Table 4.2 lists the values of control gain normalised to the value of gain that guarantee 6 dB gain margin that minimises the kinetic energy of the panel and maximises the power absorbed with the respective reductions in kinetic energy. In general, the two strategies of tuning each control unit give similar values of control gain and small differences in the reduction of kinetic energy.

Control unit number 4 seems to be rather different than the others and the maximisation of power absorbed seems to increase the overall kinetic energy of the panel by about 1 dB. It is not clear why this channel behaves so differently from the others. Another particular case is represented by channel 7 which seems to be the most efficient, providing 5 dB of reduction in the total kinetic energy. This behaviour is due to the fact that channel 7 is the closest to the primary source, so that the primary excitation is not able to efficiently excite the panel when high values of control gain number 7 are implemented. The same behaviour has been predicted in simulation results described in Chapter 3.

The sixth column of Table 4.2 shows the ratio between the control gain which minimises the total kinetic energy of the structure and the control gain which maximises the total power absorbed by the control unit. These values show that the ratio is higher or smaller than 1 depending on the position of the control unit with respect of the edges of the plate and the primary excitation.

4.3.3. Stability and performance of single channel using MEMS accelerometers

The control unit considered here is again number 5 located in the centre of the panel. Figure 4.24 shows the Nyquist plot of the open loop FRF when the control gain is adjusted to have 6 dB gain margin. The graph shows that the system is conditionally stable.

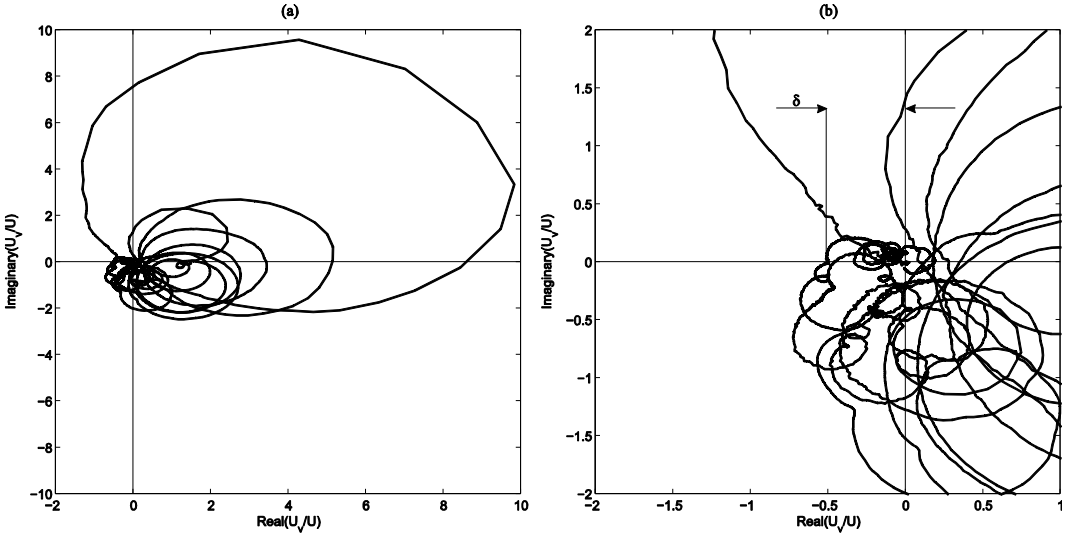

Figure 4.24: (a) Nyquist plot of the measured open loop FRF of channel 5 and (b) zoom at the origin using a MEMS accelerometer

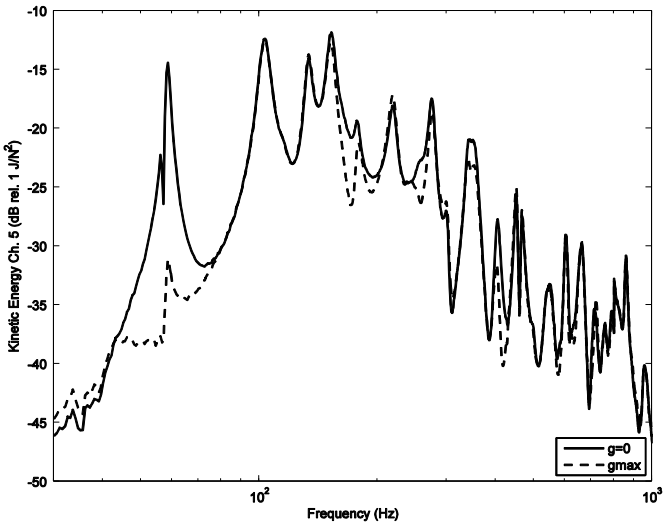

Figure 4.25: Simulated PSD of the kinetic energy of the panel obtained from measured responses without control (solid-line) and with 6 dB gain margin (dashed-line)

Figure 4.25 shows the PSD of kinetic energy of the panel without control and when the control gain giving 6 dB gain margin is implemented.

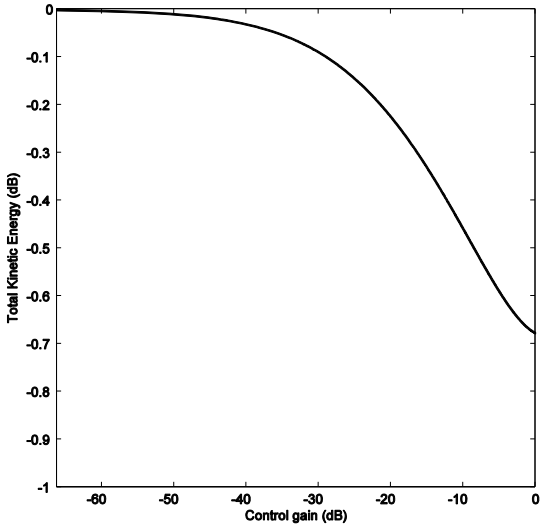

Figure 4.26: Simulated frequency averaged PSD of the kinetic energy of panel obtained from measured responses as function of the control gain number 5.

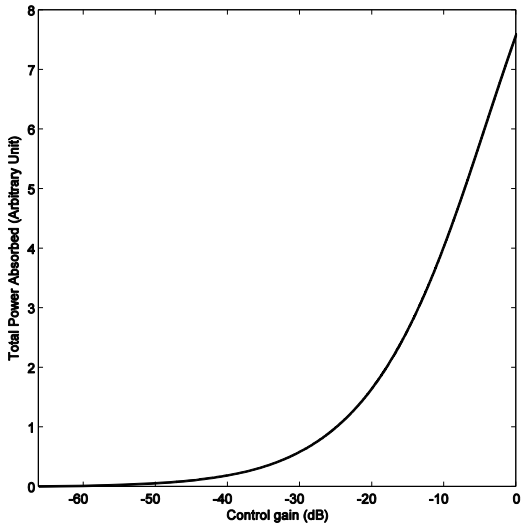

Figure 4.27: Simulated frequency averaged PSD of the power absorbed by control unit number 5 obtained from measured responses as function of the control gain number 5.

The effect of the controller when the maximum stable gain is implemented is to reduce the response of the panel at the first resonance. It is evident that the control unit is not able to pin the panel at the control position since new resonances are not visible in the structural response.

This is confirmed by Figure 4.26 and Figure 4.27 which show the frequency averaged kinetic energy and the frequency averaged power absorbed as function of the control gain normalised to the value of gain giving 6 dB gain margin. From the plots it is clear that with this configuration it is not possible to reach the control gain which minimise the total kinetic energy of the panel or maximises the power absorbed by the control unit before the system gets unstable. From the analysis of this configuration carried out in section 4.2, it can be concluded that the control gain is manly limited by the phase lag introduced by the MEMS sensor. It may be possible to re-

define the filters in the control loops to allow greater stable gains in the feedback controller, but this has not been attempted due to limitations of time.

4.4. Stability and performance analysis of a nine channel control system

In the third experiment performed within the scope of the stability investigation, the full 9×9 matrix of the sensor actuator frequency response functions, **H**(jω), is analysed using the generalised Nyquist criterion [14]. In order to perform such an analysis, the 9×9 matrix of the FRFs have been measured. The matrix, **H**(jω), is a fully populated matrix of the frequency response functions between the nine velocity sensors and the nine reactive actuators:

$$\mathbf{H}(j\omega) = \begin{bmatrix} \left(\frac{v}{u}(\mathrm{j}\omega)\right)_{1,1} & \left(\frac{v}{u}(\mathrm{j}\omega)\right)_{1,2} & \dots & \left(\frac{v}{u}(\mathrm{j}\omega)\right)_{1,9} \\ \left(\frac{v}{u}(\mathrm{j}\omega)\right)_{2,1} & \left(\frac{v}{u}(\mathrm{j}\omega)\right)_{2,2} & \dots & \left(\frac{v}{u}(\mathrm{j}\omega)\right)_{2,9} \\ \vdots & \vdots & \ddots & \vdots \\ \left(\frac{v}{u}(\mathrm{j}\omega)\right)_{9,1} & \left(\frac{v}{u}(\mathrm{j}\omega)\right)_{9,2} & \cdots & \left(\frac{v}{u}(\mathrm{j}\omega)\right)_{9,9} \end{bmatrix} \tag{4.2}$$

where $\left(\frac{v}{u}(\mathrm{j}\omega)\right)_{i,j}$ is the frequency response between the *i*-th velocity sensor and the *j*-th voltage driving the actuator. Assuming that the plant and the controller are individually stable, the generalised Nyquist criterion states [14] that the closed loop system is stable if and only if, for a stable open loop system, the locus of the determinant of the measured difference matrix, $D(\mathrm{j}\omega) = \det[\mathbf{I} + \mathbf{GH}(\mathrm{j}\omega)]$, where in this case **G** is the diagonal matrix of equal control gains, does not encircle or passes through the origin, as the angular frequency, ω , varies between $-\infty$ and $+\infty$. The determinant $D(j\omega)$ can be also written as the product of its eigenvalues to express the single polar plot defined by the locus of $D(j\omega)$ as series of more simple polar plots. The determined *D* can be written as [14]:

$$D(j\omega) = \det[\mathbf{I} + \mathbf{GH}(\mathrm{j}\omega)] = [[1 + \lambda_1(\mathrm{j}\omega)] \dots [1 + \lambda_9(\mathrm{j}\omega)]] \tag{4.3}$$

where $\lambda_i(\mathrm{j}\omega)$ are the eigenvalues of the matrix $\mathbf{GH}(\mathrm{j}\omega)$. The locus of equation (4.3) does not enclose the origin, provided that the locus of none of the eigenvalues, called characteristic loci, encircle the (-1,0j) point. In the general case of a multichannel system, the Nyquist criterion is not as simple to interpret as in the single channel case, since varying the control gains of different channel independently, the loci not only get bigger but they change their shape. Thus it is difficult to obtain a clear geometric guide to the relative stability system. Figure 4.28 shows the characteristic loci for the 9 channels control system. In the case considered here, however, with decentralised control using equal feedback gains, the magnitude of each eigenvalue is proportional to the feedback gain so each characteristic locus can be interpreted as a single-channel Nyquist plot with the whole system being unstable if any one of these is unstable.

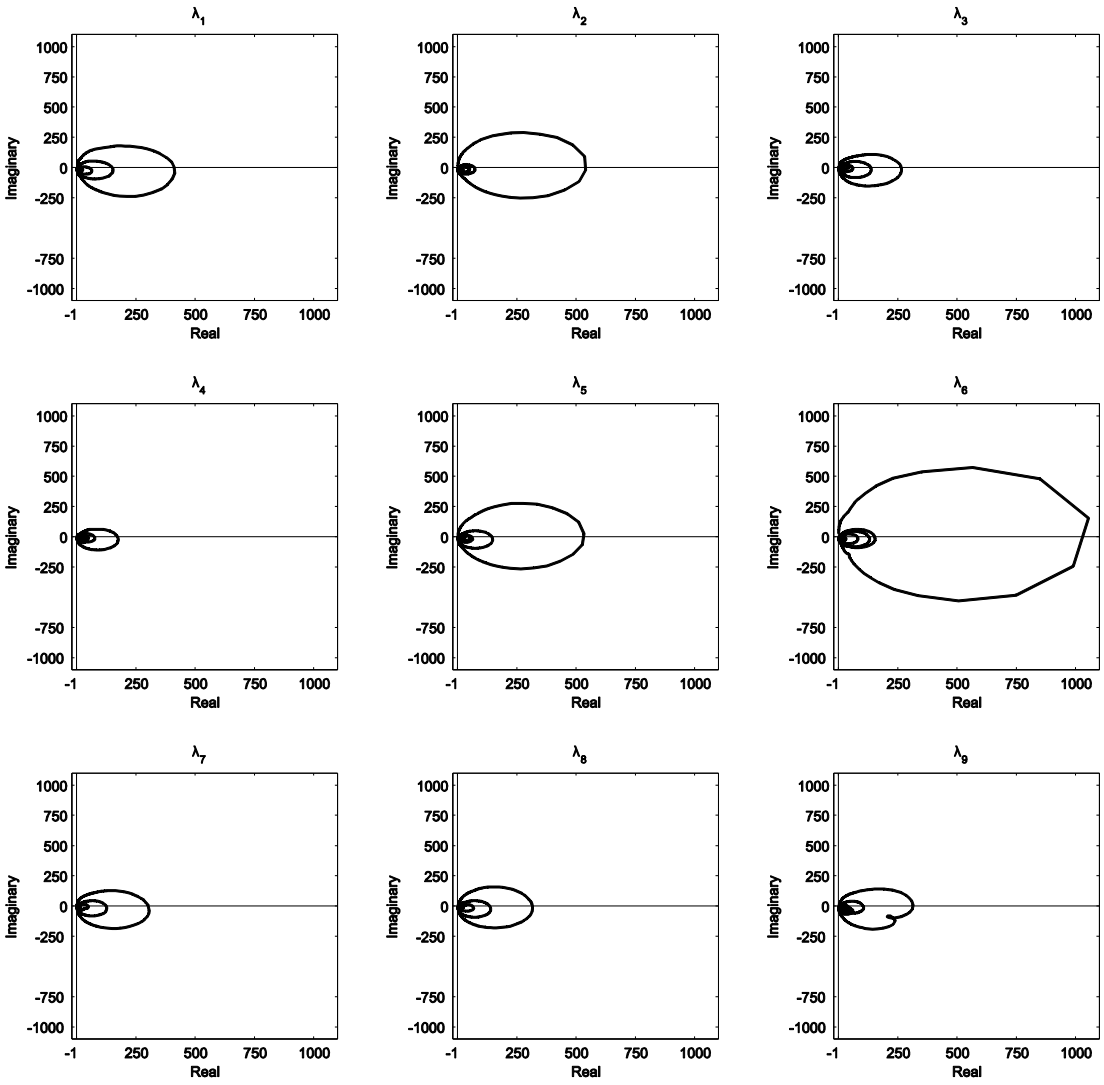

Figure 4.28: Measured characteristic loci of the nine channels control system

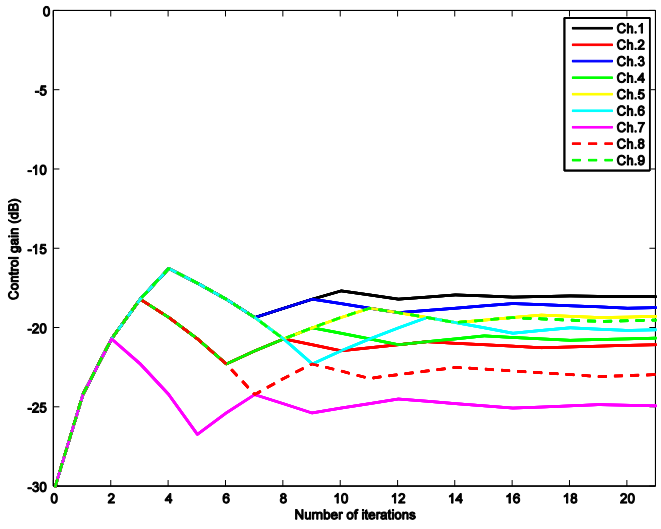

Figure 4.29: Simulations of the Convergence of algorithm to maximise the individual power absorbed by nine control units.

In order to evaluate the performance of the nine channels control system a MATLAB simulation has been carried out. Using the algorithm described in Chapter 3, the all nine control gains of the nine independent control units have been sequentially adjusted to maximise their power absorbed in a numerical simulation. Figure 4.29 shows the convergence of the control gains as function of the number of iterations.

In Table 4.3 are shown the values of control gains which maximise the power absorbed by each control unit normalised to the value of the control gain that guarantees 6 dB gain margin.

Table 4.3: Values of the control gains which maximise the power absorbed by each control unit

Ch.	1	2	3	4	5	6	7	8	9
g_{opt} (dB)	-18.0	-21.0	-18.7	-20.6	-19.2	-20.1	-24.9	-22.9	-19.5

Figure 4.30 shows the kinetic energy of the panel without control (solid line), when the power absorbed by each of the nine control unit is maximised (dashed line) and when the control gain that guarantees 6 dB gain margin is implemented (dotted line). The estimation of the kinetic energy of the panel is not accurate in this case because it has been estimated using the control velocities only. For this reason the pinning effect, when the maximum stable gain is implemented, cannot be seen. In order to get a better estimation, measurements in other positions on the panel are required. However, the plot shows that a reduction of the response of the panel up to 1 kHz can be achieved maximising the power absorbed by each control unit. The overall estimated reduction in terms of total kinetic energy of the panel is about 12 dB.

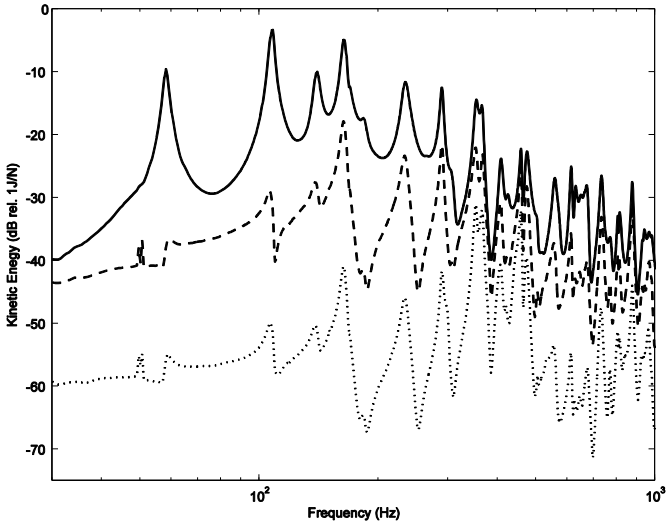

Figure 4.30: Simulated PSD of the kinetic energy of the panel obtained from measured responses without control (solid-line) maximising the individual power absorbed by nine feedback loops (dotted line) and with 6 dB gain margin (dashed-line).

4.5. Summary and conclusions

This chapter has described the panel for the experiments on decentralised velocity feedback using electromagnetic reactive actuators. The experimental panel is equipped with nine reactive actuators closely collocated with nine sensors. Two different types control configurations using two different sensors were tested: high performance B&K accelerometers and low cost MEMS accelerometers. All the components of the controller for the two configurations have also been described. The stability of the two configurations was assessed using the Nyquist criterion and simulations on the closed loop response were carried out. It was found that for the first configuration the control system is able to start to pin the panel and therefore the absorbed power is maximised before the system becomes unstable. For the configuration using MEMS accelerometers the system becomes unstable before the maximum of the power absorbed by the controller is reached. In the implementation of the self-tuning algorithm based on the maximisation of the absorbed power, described in Chapter 3, it is assumed that the absorbed power is maximised for a value of control gain smaller than the maximum stable one. Therefore the control configuration using B&K accelerometers has been chosen to carry out the experiments for the real time control presented in the next chapter.

5. Experimental implementation of self-tuning control

In this chapter experimental results on the performance of the control system are presented. Firstly, real time control with a single control unit is investigated by measuring the estimated kinetic energy of the panel and the power absorbed by the controller for wide range of the feedback gain. Secondly, results on a two channel control system, are discussed in order to verify possible interaction between control units. In the last section the algorithm to maximise the power absorbed by each of the two control units, as described in Chapter 3, is experimentally implemented.

5.1. Experimental setup of a self-tuning control unit

Figure 5.1 shows a scheme of the experimental setup of the self-tuning control unit. The velocity signal was amplified using a power amplifier and fed back to the voice-coil actuator. The gain of the amplifier was set to the maximum value. A digital taper-potentiometer was used to attenuate the velocity signal fed back to the actuator. The potentiometer is composed of 256 resistive sections, so that between each resistive section and both ends of the potentiometer are outputs tap points.

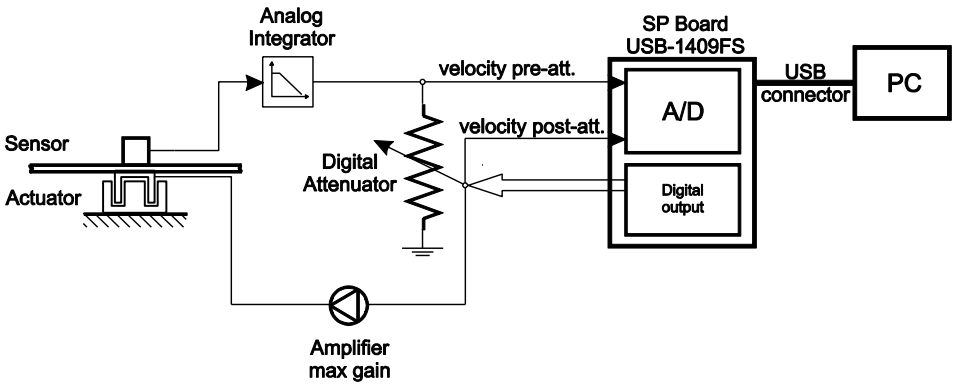

Figure 5.1: Scheme of an experimental self-tuning control unit

The tap point of the resistive array is set by an 8-bit digital control signal. The control of the device was accomplished via a 3-wire serial port interface using the digital output of a data acquisition device. The attenuation provided by the potentiometer was in the range 0 dB to -50 dB with 256 possible linear steps. However, only 23 steps where selected in order to have 2dB attenuation between successive steps.

The resolution in the attenuation was limited by the level of noise in the velocity signal. The solid line in Figure 5.2 shows the theoretical values of dB attenuation while the dots shows the 23 measured values of dB attenuation considered during the experiments as function of the wiper's position.

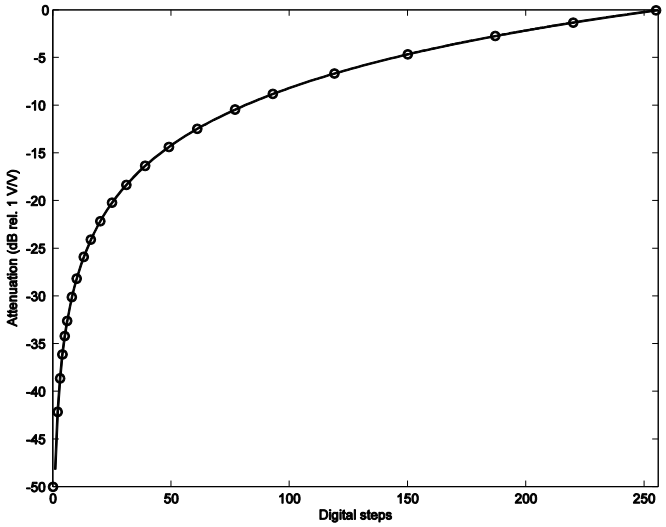

Figure 5.2: Attenuation introduced by the potentiometer in decibel against the position of the wiper.

For direct local velocity feedback, the secondary force at each position, f_r, is proportional to the measured velocity, v_r, in each channel via a feedback gain g_r. The power absorbed by this controller is then given by:

$$S_{Pr}(\omega) = \frac{1}{2}\mathrm{Re}\{\tilde{f}_r^* \tilde{v}_r\} = \frac{1}{2} g_r |\tilde{v}_r|^2 \tag{5.1}$$

The system is made self-tuning by using the algorithm described in Chapter 3. The algorithm sequentially varies the control gain of each loop, estimates the absorbed power and adapts the control gain to maximise this power. The velocity waveform is directly fed back to the actuator but the power is estimated off line, using the mean square velocity, and the control gain is changed in response to this estimate. Thus the tuning does not introduce any phase lag in the feedback.

Table 5.1: specifications of the acquisition device and the potentiometer

	Parameter	**Specification**
Data acquisition device	Manufacturer	Measurement Computing
	Model	USB-1408FS
	Number of analogue inputs	4
	Input ranges	±2 V
	Maximum sample frequency	48 kHz
	Resolution	14-bits
	Number of digital output	16
Potentiometer	Manufacturer	Maxim
	Model	DS1267
	Digital steps	256
	Attenuation range	-50 - 0 dB

The panel was excited with a shaker, fed with white noise signal in the frequency band of 10-1000 Hz. The velocity measured by the sensor was acquired for 10 seconds and sampling frequency of 3 kHz using the analogue input of the data acquisition device. The main specification of the data acquisition device and the potentiometer are summarised in Table 5.1. The acquired velocity signal was digitally filtered with a high-pass filter with a cut off frequencies of 52 Hz. The filter reduces the noise level at low frequency and the mains at 50 Hz, especially for high values of control gain when the measured velocity is very low. The power was calculated as the mean product of the measured velocity signal and the signal driving the actuator. This was implemented by taking the product of the pre-attenuation velocity signal and the post-attenuation velocity signal (see Figure 5.1). The control algorithm iteratively changes the attenuation, estimates the power and adapts towards the attenuation that maximises the power absorbed by the control unit, as described in Chapter 3.

5.2. Performance with real time control using a single control unit

In this section results for real time control using control unit number 5 are discussed although results for real time control using control unit number 1 can be found in Appendix D. Figure 5.3(a), shows the power spectral density (PSD) of the kinetic energy of the structure from the measured velocities of the panel, estimated from the integrated outputs of the 9 accelerometers, for different values of control gain corresponding to 0, -15 and -50 decibels of attenuation in the signal fed back to the actuator. Figure 5.3(b) shows the same results obtained

from numerical simulations of clamped-clamped aluminium panel of the same dimensions when the kinetic energy is calculated as the sum of the mean squared velocities at the position of the nine accelerometers using the mathematical model described in Chapter 3.

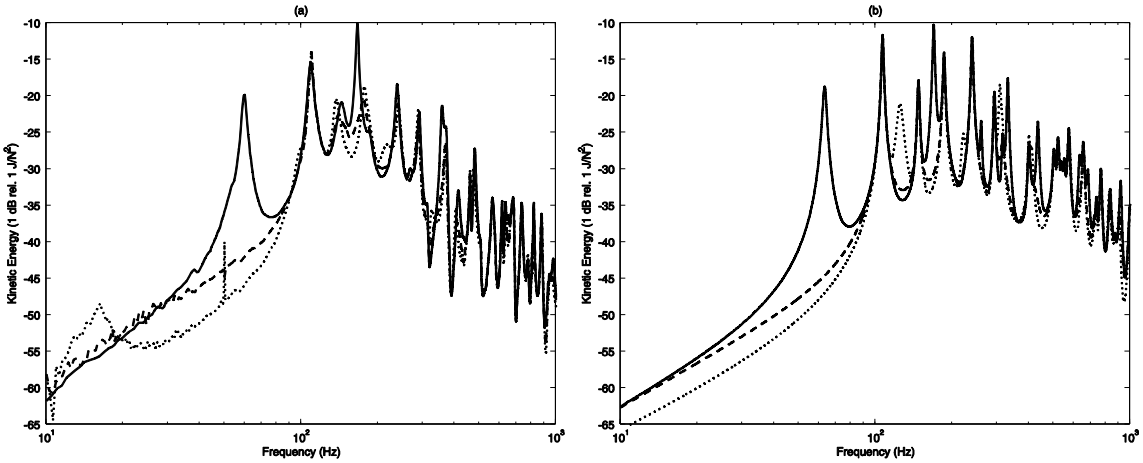

Figure 5.3: PSD of the estimated kinetic energy of panel with no control (solid line), minimising the estimated frequency averaged kinetic energy of the panel (dashed line) and high control gain (dotted line) a) measured and b) simulated

The masses of the sensors and the coil have also been included in the model. The modal damping used in the simulations has been estimated from experimental results as 2% for the first mode and 1% for all the others. The results show that the response of the panel is characterised by distinct lightly damped resonances at low frequencies. The dashed line in Figure 5.3(a) and (b) represents the response of the panel for the control gain that minimises the frequency averaged response of the panel. If the control gain exceeds this value, the response of the panel increases again (dotted-line), at other frequencies, eventually creating a new set of resonance frequencies. As already seen in Chapter 3, this is due to the fact that the control loop is pinning the panel at a control position and thus the resonance frequencies of the point-constrained clamped panel are shifted up. Since the control unit is placed in the centre of the panel only the first mode is most influenced by the controller and the first resonance due to the pinning appears at around 136 Hz. The peak at about 17 Hz, when the control gain is set at the maximum (dotted-line), is probably due to loss of accuracy of the sensor at low frequency.

The measured and simulated results are different in a number of aspects, however. The measured resonance frequencies of the uncontrolled structure are lower than the resonances calculated in the simulation. This is because the experimental boundary conditions do not produce perfect clamping. The experimental panel is clamped between two aluminium frames fixed with screws and has the first resonance frequency at about 58 Hz, compared with a calculated value of 62 Hz with fully clamped edges, although the results are close enough to make the comparison useful.

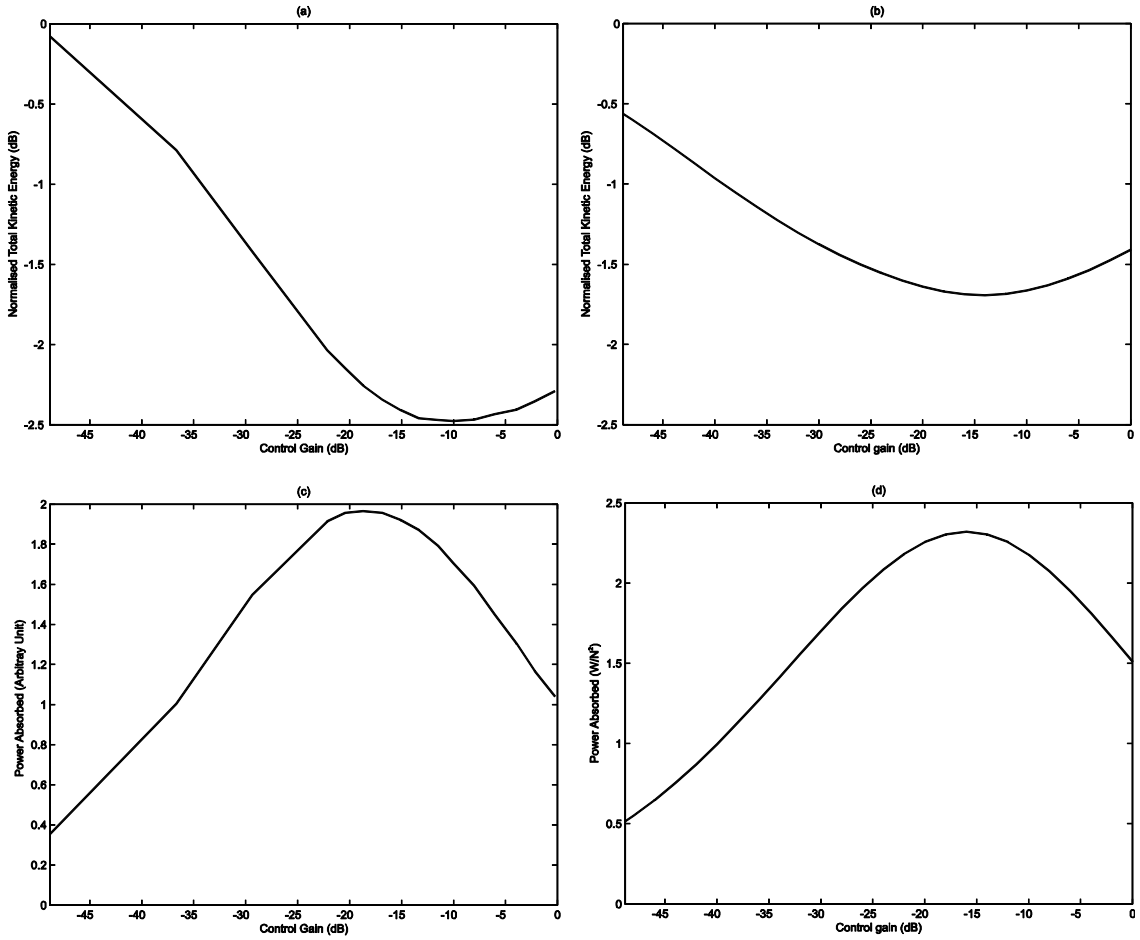

Figure 5.4: a) experimental and b) simulated results of the normalised total kinetic energy of the panel and c) experimental and d) simulated results of the total power absorbed as function of the control gain 5.

To obtain broadband control, the estimated kinetic energy and power absorbed by the controller have been averaged over the frequency band from 10 to 1000 Hz. Figure 5.4(a) shows the measured total kinetic energy of the panel, normalised to the total kinetic energy without control, plotted against the feedback gain, which is normalised by the maximum gain used in the experiment, while Figure 5.4(c) shows the measured total power absorbed by the control unit. The measurement units of the absorbed power have been omitted because the control gain used to estimate the absorbed power is the measured attenuation introduced by the potentiometer, not the real overall value of gain as shown in Figure 5.1. The experimental results show that the optimum value of the control gain which minimises the total kinetic energy is about -13 dB and produces a reduction in total kinetic energy of about -2.4 dB. The control gain which maximises the total power absorbed is about -17 dB and produces a reduction in the total kinetic energy of the panel of about -2.2 dB. Therefore, maximising the absorbed power produces a global structural response which is only about 0.2 dB higher than when the global response itself is minimised. This suggests that a good level of performance can be achieved with broadband excitation by maximising the power absorbed by the controller. Moreover the gradient of the total kinetic energy is very small around its minimum which means that a small error in the

tuning of the control gain it does not significantly affect the total response of the structure. Figure 5.4(b) and (d) shows the same results obtained from numerical simulations. The control gain in the simulation is normalised to the maximum control gain used in the experiments. Simulation and experimental results are in reasonable agreement. The major difference is that the maximum reduction in the response of the panel in simulation is about -1.6 dB, which is 1.8 dB less than the reduction achieved in the experiments. This could be due to the fact that the control unit in the experimental setup is not placed exactly symmetrically compared with the actual modal shapes, so that the control unit in the experimental setup is able to marginally control modes that are uncontrollable in the simulations.

5.3. Performance with real time control using two control units

In this section the real time control of a two channels control system is discussed. In this case the estimated total kinetic energy of the structure and the total power absorbed by the two control units have been measured for a wide range of combination of the two control gains. Figure 5.5(a) shows the total kinetic energy of the panel, estimated as the sum of mean squared velocities measured by the nine monitoring sensors normalised to the estimate total kinetic energy without control, while Figure 5.5(c) shows the total power absorbed by the two control units as a function of the two control gains. In this section, the power absorbed is normalised to the power absorbed when the two control gains are both set to -12 dB in order to make the comparison between experiential and theoretical results easier. The experimental results show that the combination of feedback gains that achieves a maximisation of total power absorbed by the two control units corresponds reasonably well to those that result in the minimisation of the total kinetic energy of the structure. A detailed analysis of Figure 5.5(a) and (c) shows that the minimum of the kinetic energy is about -3.7 dB when the two control gains are set to -17 and -15 dB. The power absorbed by the two control units produces a reduction of -3.5 dB in the total kinetic energy of the panel when the two control gains are set to -15dB and -15dB. These results suggest that, for broadband disturbances, controlling the response of the panel by locally tuning each control loop to maximise its own absorbed power results in global reduction of the panel's response, as seen earlier in Chapter 3. Moreover, the total kinetic energy of the panel as a function of the two control gains has a gradient that is low around its minimum; therefore a small error in the tuning of the two control gains has negligible effect on the total structural response. Experimental results are in reasonable agreement with the simulation results shown in Figure 5.5(b) and (d). A summary of the comparison between experimental and simulation results is shown in Table 5.2.

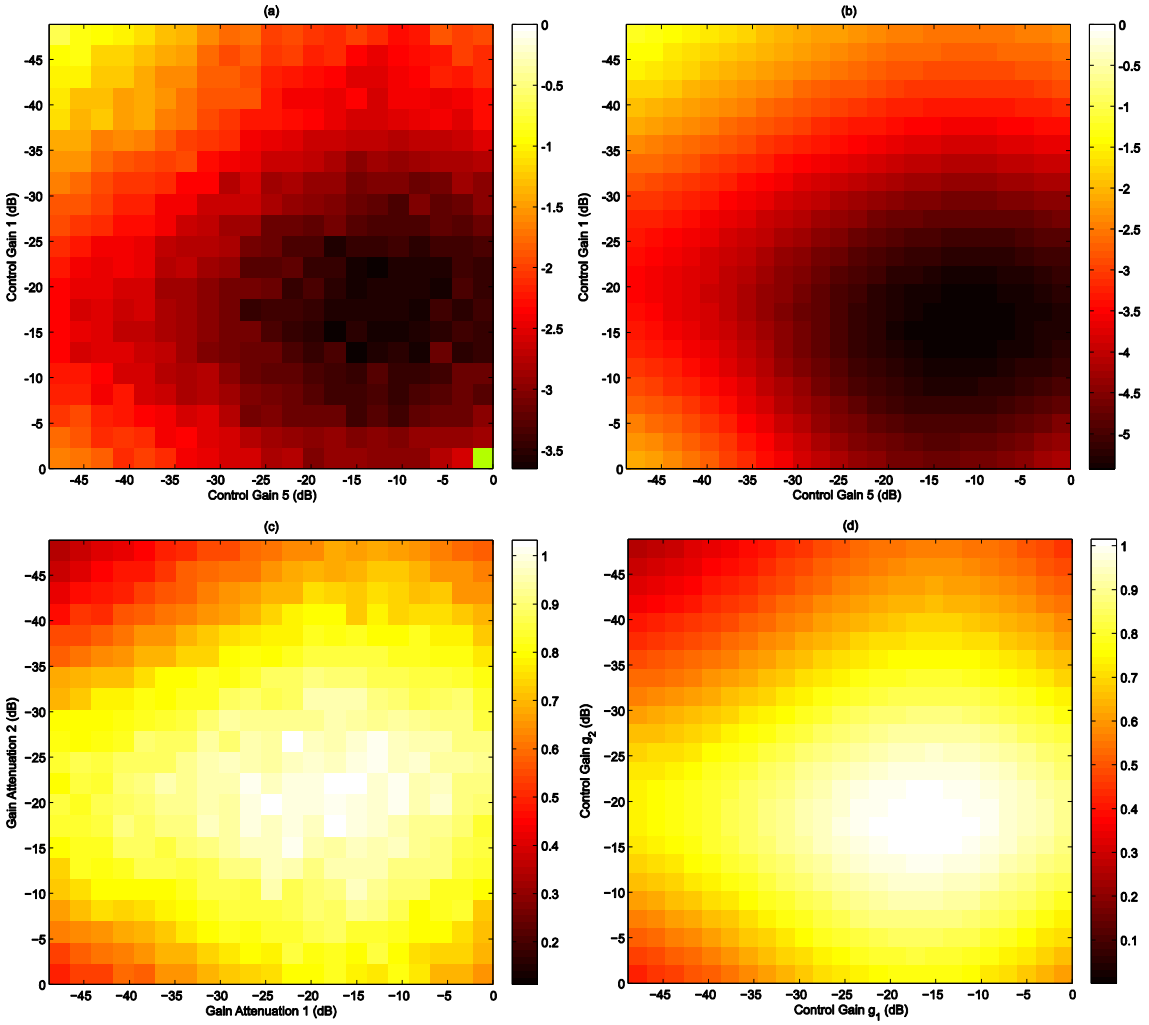

Figure 5.5: a) experimental and b) simulated results of the normalised total kinetic energy of the panel and c) experimental and d) simulated results of the total power absorbed as function of the two control gains.

Table 5.2: Comparison between experimental and simulation results for the two channels control system

	Experimental results		Simulation results	
Minimising Kinetic Energy	g_1=-15 dB	g_5=-17 dB	g_1=-14 dB	g_5=-18 dB
	Reduction in *KE* =-3.7		Reduction in *KE* =- 5.4 dB	
Maximising Power	g_1=-15 dB	g_5=-15 dB	g_1=-18 dB	g_5=-16 dB
	Reduction in *KE* =-3.5 dB		Reduction in *KE* =-5.3 dB	

Figure 5.6 shows the measured (on the left) and simulated (on the right) values of the individual power absorbed by the two control units as function of the two control gains. The results show that the power absorbed by each control unit is reduced when both control units are tuned to

their combined optimal values, compared with the power absorbed when they are individually tuned in the absence of the other.

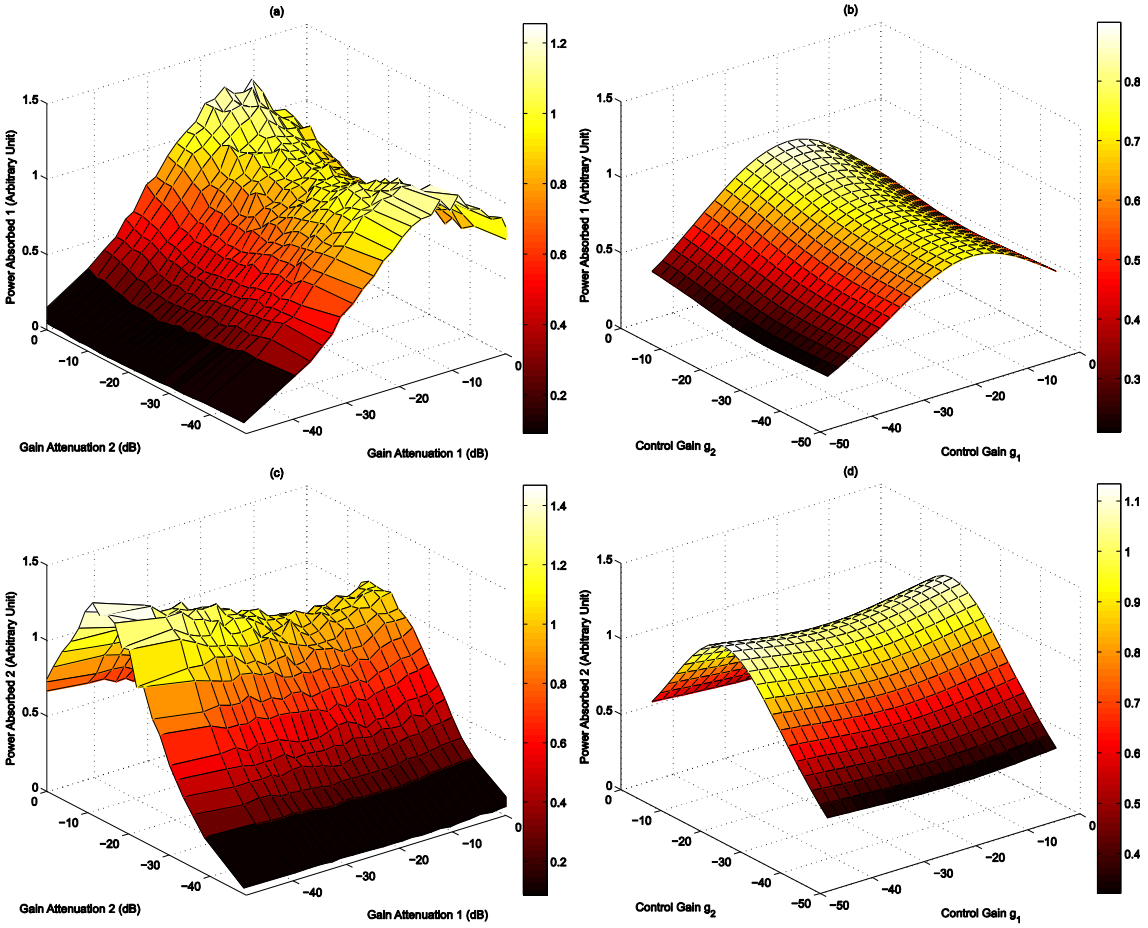

Figure 5.6: a) and c) experimental and b) and d) numerical results of the individual total power absorbed by control unit 1 and 5 as function of the two control gains.

The simultaneous maximisation of the local power in both control units, however, converges to the maximisation of the total absorbed power, as shown in Figure 5.5(d). An important aspect of the experimental curves in Figure 5.6, as far as a practical algorithm is concerned, is that if all the other control gains are fixed, the local power absorbed by one loop is still maximised by a single value of its control gain. Thus the adaptation can be performed as long as the estimation of the power absorbed by one channel is made when the control gain of the other is not varied. The self-tuning algorithm described in Chapter 3 can be used to sequentially adjust the individual control gains.

5.4. Experimental implementation of the self-tuning control algorithm

The experimental results presented in sections 5.2 and 5.3 have shown that for broadband stationary excitation a similar control performance is achieved minimising the total kinetic energy of the plate or maximising the power absorbed by each of the feedback loops. This

suggests that reductions in the overall vibration can be obtained by adapting the local feedback gains of the control units to maximise the total power absorbed by each control unit. In this section the performance of the algorithm to maximise the power absorbed by each of the two control units is described.

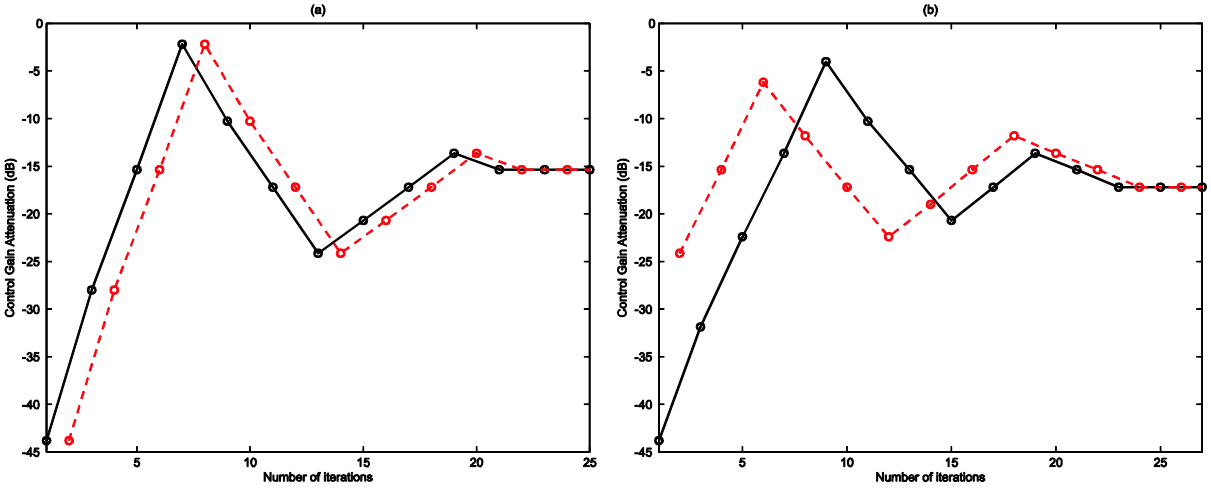

Figure 5.7: convergence of the self-tuning algorithm a) starting from g_1=-50 dB and g_5=-50 dB and b) starting from g_1=-50 dB and g_5=-25 dB

Figure 5.7 shows the convergence of the algorithm in terms of the two control gains when their initial values are a) both set to -50 dB and b) when the control gain 1 is set to -50 dB and control gain 5 is set to -25 dB. In this example, the initial value of α, which is the step by which the attenuation is decreased at the first iteration, is 13 dB and each iteration takes about 20 seconds. The algorithm is programmed to stop adjusting when α becomes smaller than 2 dB, which is the limit of resolution in this case. As shown in section 5.3 the optimum control gains which maximises the total absorbed power are g_1=-15dB and g_5=-15dB. Figure 5.7shows that the final setting of the two control gains in both cases is within ±4 dB of their optimum, a range of feedback gains that would result in a maximum error in the minimisation of the total kinetic energy of the structure of about 0.5 dB. Higher precision in the adaptation is difficult to achieve with the current arragement due to noise in the measurement of the control velocity. Figure 5.7(a) shows that the algorithm converges after 22 iterations to -15dB of attenuation for both channels. Figure 5.7(b) shows that the algorithm converges after 21 iterations to -15dB for channel 1 and -13dB for channel 5. When multiple feedback units are tuned simultaneously, the power absorbed by one control unit is influenced by the other, as seen in section 5.3. Therefore, the individual power absorbed by one control unit must be re-estimated, keeping the other gain constant, before this control gain is varied. One limitation of the current algorithm is thus that some global synchronisation is required for multichannel control systems to ensure the loops adapt sequentially. It may be possible to communicate the measured absorbed power between units, which would allow more global tuning strategies. Another limitation is that the level of

disturbance is assumed to be constant from one step to the next so that the measured change in power is due to the change in gain rather than a change in disturbance. The performance of this self-tuning system could also be improved by reducing the noise in the measurements, so that a shorter acquisition time would be required to obtain the same accuracy.

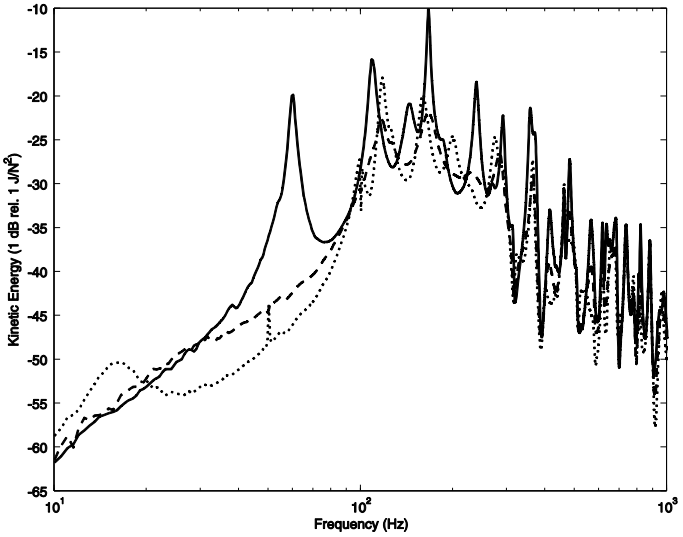

Figure 5.8: measured PSD of the kinetic energy of the panel without control (solid line), after the algorithm has converged (dashed-line) and implementing the maximum control gains on both channels (dotted-line).

Figure 5.8 shows the PSD of the measured kinetic energy of the panel for the uncontrolled structure (solid line), when the power absorbed by the two control units is maximised (dashed line) and when the maximum control gains are implemented. The plot shows that the response of the structure is damped at the first few resonances when the power absorbed by each control unit is maximised and the first mode is fully controlled. For very high control gain the two control units are able to begin to pin the panel, so that new resonances appears in the spectrum of the structural response (dotted-line). If all nine control units installed on the panel were used, it would be necessary to include additional monitoring sensors in the estimation of the panel's kinetic energy to correctly account for the modes generated when the controller pins the structure at the control positions.

The use of more than two control units has been discussed in Chapter 3 for a panel subjected to a broadband 'rain on the roof' excitation. The following simulations using nine self-tuning control units have been carried out when the panel is excited by a point force. Figure 5.9(a) shows the positions of the nine control units and monitoring positions while Figure 5.9(b) shows the values of the control gains of each unit after the self-tuning algorithm based on the maximisation of the absorbed power has converged.

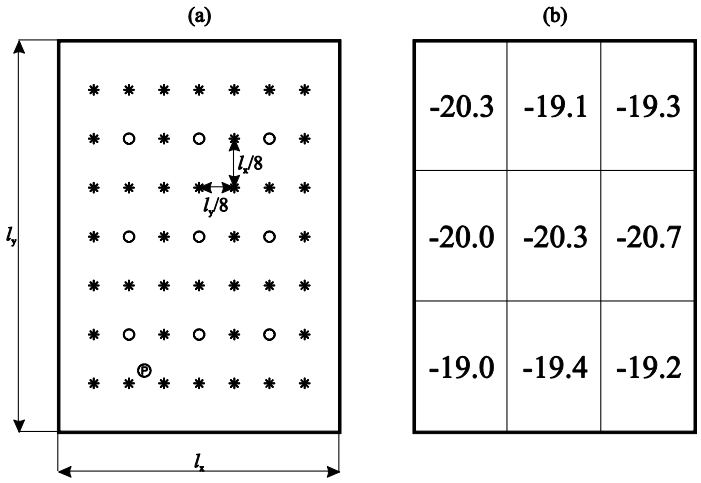

Figure 5.9: (a) Scheme of the panel with the control positions (o) and monitoring positions (*); (b) values of the control gains in dB that maximise the power absorbed of each control unit. P indicates the position of the primary excitation.

Figure 5.10 shows the PSD of the panel's kinetic energy without control (solid line), when the power absorbed by each control unit is individually maximised (dashed line), and when the kinetic energy is minimised using the same value of gain for each feedback loop (dotted-line). A total of 49 evenly separated velocity measurement locations have been monitored so that the kinetic energy of the panel is correctly estimated when the feedback loops implement very large feedback gains so that the panel is pinned at the control positions.

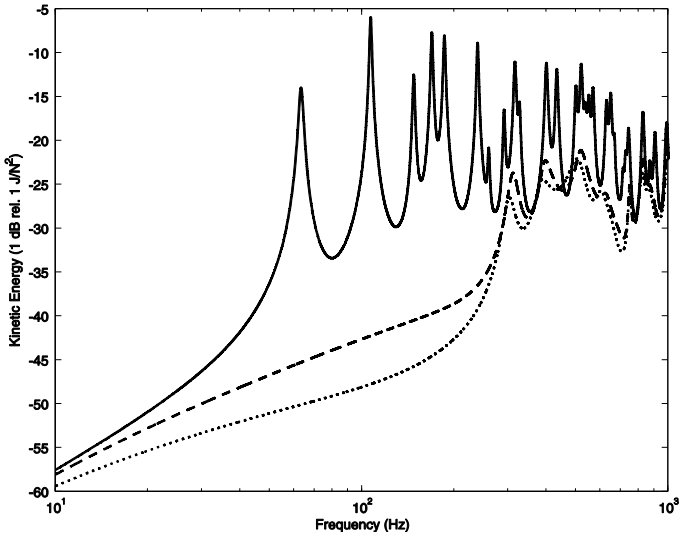

Figure 5.10: PSD of the total kinetic energy when g= 0 (solid line), the self-tuning algorithm is implemented (dashed line) and $g_{1\text{-}9}$=-13.0 dB (dotted line).

In the uncontrolled response of the panel (solid line) the contributions of some higher frequencies modes are greater when 49 instead of 9 velocities are considered. Although the PSD of the kinetic energy is shown up to 1 kHz the simulations have been performed with an excitation band up to 10 kHz to include the new resonances that would be created when high values of control gains are implemented. The plot shows that a very similar response is obtained

maximising the power absorbed by each control unit compared with the minimisation of the kinetic energy of the panel using equal gains. The overall reduction obtained from 1 Hz to 1 kHz normalised by the total kinetic energy of the panel without control after the self-tuning algorithm has converged is about 7.4 dB while the one obtained minimising the overall kinetic energy of the panel is about 8.1 dB. The use of nine feedback loops improves the performance of the control system providing 4 dB reduction in the total structural response more than the two channels controller described in section 5.3. Figure 5.11 show the convergence of the algorithm for the nine control gains tuning all control unit sequentially. In the simulations the initial value of the step by which the control gain is increased is 10 and the error in the estimation of the optimal control gain is ±0.2. Figure 5.11 shows that the algorithm converges to the optimum between these limits.

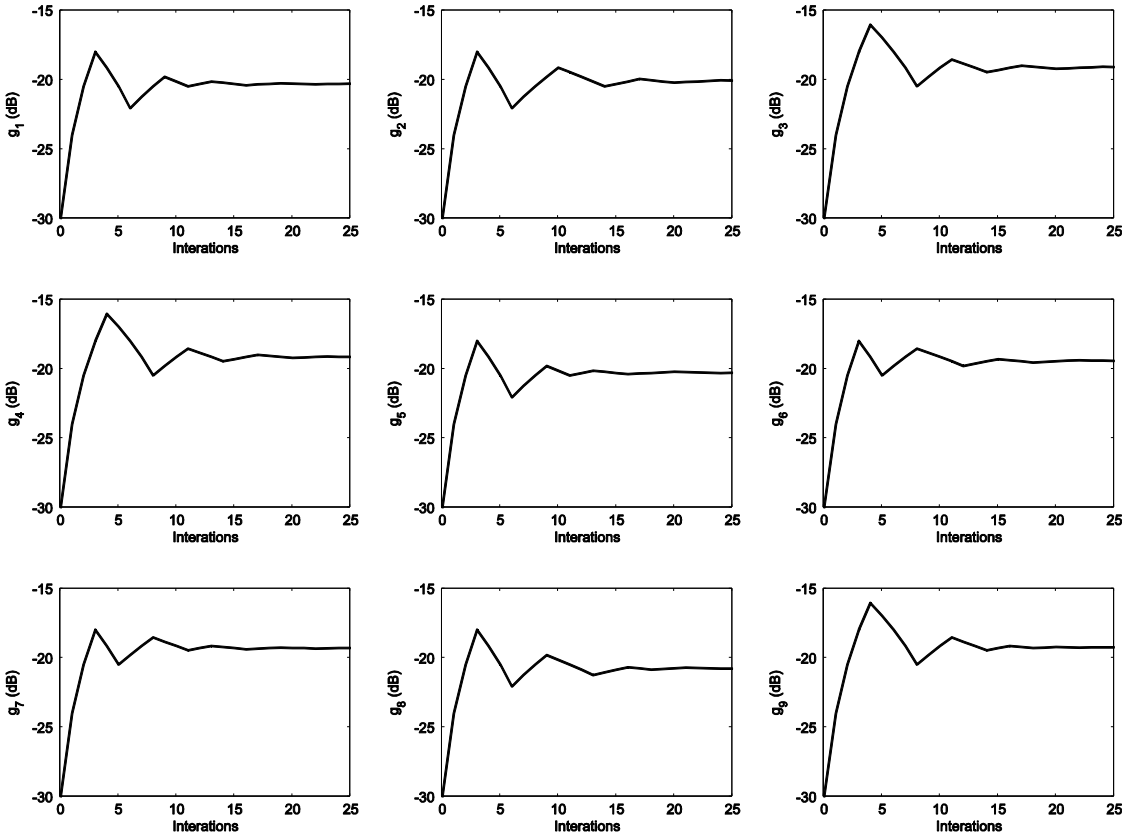

Figure 5.11: convergence of the control gains of the nine control units

5.5. Summary and conclusions

This chapter has presented an experimental implementation of multiple channel velocity feedback loops on a panel. Experimental results have shown that, for broadband excitation, the maximisation of the power absorbed gives good level of performance in practice if compared with the minimisation of the kinetic energy of the structure. The transition in the control action between optimum damping and pinning of the structure has been experimentally demonstrated. The implementation of a simple algorithm to adjust the control gains in a multichannel

configuration for a stationary disturbance has shown that each control unit can be made self-tuneable. A limitation of this algorithm is that a synchronisation in the tuning of multiple control units is required since the power absorbed by one feedback loop is influenced by all the others. Moreover, the current algorithm stops to monitor the absorbed power after the algorithm has converged being unable to track changes in the operating conditions.

A drawback of the electromagnetic reactive actuators used in these experiments is that they need a structure to react the force off. In the next part of the thesis the more convent inertial actuators are considered.

6. Maximisation of power absorbed using an inertial actuator in a velocity feedback loop

Although the principle of self-tuning to maximise power absorption has been demonstrated using reactive force actuators, it is often not possible to use these in practice, since there may be no solid structure to react the force off.

This chapter presents a preliminary study for the use of the more practical inertial actuators to control a lightly damped panel using a single velocity feedback. Inertial actuators react the generated force off a proof mass and have been widely used for active vibration control [7]. Above their natural frequency they can behave very much like ideal force actuators over a frequency band of several decades, before higher order resonances interfere with their dynamics [40]. When inertial actuator are employed, however, the feedback control loop is no longer unconditionally stable, even under ideal conditions, since the 180º phase shift in the response of the actuator below its natural frequency will give rise to low frequency instabilities if the feedback gain is too high.

6.1. Two port network of an electromechanical inertial actuator

The transducer assumed here to control the vibration of a structure is an electromagnetic inertial actuator. In such transducers the mechanical system is fully coupled with the electrical system, and these two coupled reactions can make the model complicated. In this section the mathematical model of an inertial actuator is derived. A two-port model of the actuator has been used to describe the electromechanical behaviour of the transducer when the actuator is attached to a generic structure [39]. Figure 6.1 shows the two-port model of the transducer. The mechanical system, to which the transducers is attached, is represented by its blocked force $\tilde{f}_b$ and its mechanical impedance $\tilde{Z}_{\mathrm{mb}}$. $\tilde{Z}_{\mathrm{mo}}$ represents the open circuit mechanical impedance of the actuator and $\tilde{Z}_{\mathrm{eb}}$ is the blocked electrical impedance of the transducer. $\tilde{T}_1$ and $\tilde{T}_2$ are the transduction coefficients that quantify the electromechanical coupling. $\tilde{T}_1$ describes the current produced per unit velocity when $\tilde{\imath}$ equal zero and $\tilde{T}_2$ describes the force produced per unit electric current when $\tilde{v}$ is equal zero.

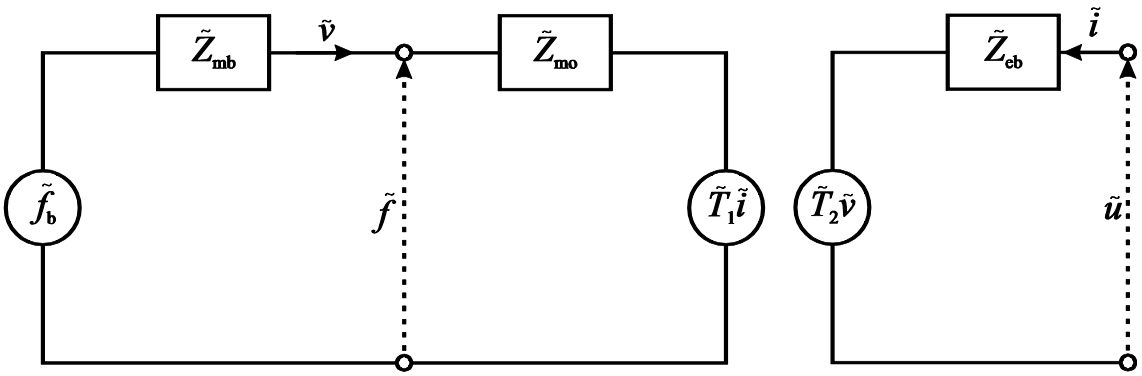

Figure 6.1: A two-port network model of a transducer.

From Figure 6.1, the following relations between the mechanical quantities (velocity $\tilde{v}$ and force $\tilde{f}$) and electrical quantities (voltage $\tilde{u}$ and current $\tilde{\imath}$) can be written:

$$\tilde{u} = \tilde{Z}_{\mathrm{eb}}\tilde{\imath} + \tilde{T}_1\tilde{v} \tag{6.1}$$

$$\tilde{f} = \tilde{T}_2\tilde{\imath} + \tilde{Z}_{\mathrm{mo}}\tilde{v} \tag{6.2}$$

Analytical expressions for the impedances and transduction coefficients are derived in Appendix E for a single degree of freedom inertial actuator. The force, $\tilde{f}$ generated by the actuator on the structure can be expressed as:

$$\tilde{f} = \tilde{f}_{\mathrm{b}} - \tilde{Z}_{\mathrm{mb}}\tilde{v}, \tag{6.3}$$

where $\tilde{Z}_{\mathrm{mb}}$ is the structural impedance and $\tilde{f}_{\mathrm{b}}$ is the blocked force necessary to pin the structure at control position. The velocity at control position can be written as:

$$\tilde{v} = \tilde{Y}_{\mathrm{c}}\tilde{f} + \tilde{Y}_{\mathrm{cp}}\tilde{f}_{\mathrm{p}}, \tag{6.4}$$

where $\tilde{Y}_{\mathrm{c}}$ is the mobility at control position, $\tilde{Y}_{\mathrm{cp}}$ is the cross mobility between the location of the primary excitation $\tilde{f}_{\mathrm{p}}$ and the control location. Setting equation (6.4) to zero the resulting force $\tilde{f}_{\mathrm{b}}$ is given by:

$$\tilde{f}_{\mathrm{b}} = -\frac{\tilde{Y}_{\mathrm{cp}}}{\tilde{Y}_{\mathrm{c}}}\tilde{f}_{\mathrm{p}}. \tag{6.5}$$

6.2. Velocity feedback using a current-driven inertial actuator

For a velocity feedback control using a current-driven inertial actuator, the current $\tilde{\imath}$ is proportional to the velocity $\tilde{v}$ via a control gain $-g$, and thus:

$$\tilde{\imath} = -\mathrm{g}\tilde{v} \tag{6.6}$$

Substituting equation (6.6) in (6.1) and (6.2) the voltage $\tilde{v}$ and the force $\tilde{f}$ become:

$$\tilde{u} = (\tilde{T}_1 - g\tilde{Z}_{\mathrm{eb}})\tilde{v}, \tag{6.7}$$

$$\tilde{f} = \left(-g\tilde{T}_2 + \tilde{Z}_{mo}\right)\tilde{v} = \tilde{Z}_{\mathrm{m}}\tilde{v}, \tag{6.8}$$

where $\tilde{Z}_{\mathrm{m}}$ is the total mechanical impedance presented by the transducer. In order to simulate the response of a lightly damped structure controlled by a velocity feedback using a current-driven inertial actuator the model derived in Chapter 3 for an ideal point force actuator can be used by substituting the real frequency independent control gain with the complex impedance $\tilde{Z}_{\mathrm{m}}$. Substituting equations (6.3) in (6.8), $\tilde{v}$ can be written as:

$$\tilde{v} = \frac{1}{-g\tilde{T}_2 + \tilde{Z}_{\mathrm{mb}} + \tilde{Z}_{\mathrm{mo}}}\tilde{f}_{\mathrm{b}}. \tag{6.9}$$

Substituting equation (6.9) in (6.6), $\tilde{\imath}$ is given by:

$$\tilde{\imath} = \frac{-g}{-g\tilde{T}_2 + \tilde{Z}_{\mathrm{mb}} + \tilde{Z}_{\mathrm{mo}}}\tilde{f}_{\mathrm{b}}. \tag{6.10}$$

The force $\tilde{f}$ can be obtained by substituting equation (6.9) in (6.8) giving:

$$\tilde{f} = \frac{-g\tilde{T}_2 + \tilde{Z}_{\mathrm{mo}}}{-g\tilde{T}_2 + \tilde{Z}_{\mathrm{mb}} + \tilde{Z}_{\mathrm{mo}}}\tilde{f}_{\mathrm{b}}. \tag{6.11}$$

The mechanical power absorbed by the controller is given by:

$$S_{\mathrm{P}}(\omega) = \frac{1}{2}Re\{\tilde{f}\tilde{v}^*\}, \tag{6.12}$$

substituting equations (6.11) and (6.9) in (6.12) yields:

$$S_{\mathrm{P}}(\omega) = \frac{Re\{(-g\tilde{T}_2 + \tilde{Z}_{\mathrm{mo}})\}}{2\left|-g\tilde{T}_2 + \tilde{Z}_{\mathrm{mb}} + \tilde{Z}_{\mathrm{mo}}\right|^2}\left|\tilde{f}_{\mathrm{b}}\right|^2. \tag{6.13}$$

6.3. Stability of a feedback loop using a current-driven inertial actuator

The stability of the control system is assessed using the Nyquist criterion. The open loop frequency response function for a single control channel can be derived from the velocity response at the control position in absence of primary excitation:

$$\tilde{v} = -\tilde{Y}_{\mathrm{c}}\tilde{f}\ . \tag{6.14}$$

Assuming that a current proportional to the velocity signal is fed back to the actuator, equation (6.8) can be substituted in equation (6.14) giving:

$$\tilde{v} = \tilde{Y}_{\mathrm{c}}g\tilde{T}_2\tilde{v} - \tilde{Y}_{\mathrm{c}}\tilde{Z}_{\mathrm{mo}}\tilde{v} + \tilde{Z}_{\mathrm{w}}\tilde{v}, \tag{6.15}$$

where the term $\tilde{Z}_w\tilde{v}$ has been included to take into account the effect of the base mass of the actuator whose impedance is $\tilde{Z}_w = j\omega M_{\mathrm{w}}$. Thus substituting equation (6.6) in equation (6.15) the open loop frequency response function can be written as:

$$\tilde{H}_i = \frac{\tilde{v}}{\tilde{\imath}} = -\frac{\tilde{Y}_{\mathrm{c}}\tilde{T}_2}{1 + \tilde{Y}_{\mathrm{c}}\tilde{Z}_{\mathrm{mo}} + \tilde{Y}_{\mathrm{c}}\tilde{Z}_{\mathrm{w}}} \tag{6.16}$$

Figure 6.2 shows the bode diagram of the open loop FRF of the current-drive inertial actuator, with the parameter listed in Table 6.1 used to control the simply supported panel of Chapter 3. The parameter of the inertial actuators were based on [41] but with stiffness modified to give lower natural frequency.

Table 6.1: characteristic of the inertial actuator

Parameter	**Value**
Electrical resistance of the coil	R=2.7 Ω
Base disc mass	M_{w}=9.5 g
Proof mass	M_{a}=24 g
Spring Stiffness	K_{a}=100 N/m
Natural frequency	ω_{a} =10 Hz
Viscous damping coefficient	C_{a}=1.96 N/ms^{-1}
Viscous damping coefficient	ζ_{a} =0.63
Transduction coefficient	Bl=2.6 NA^{-1}

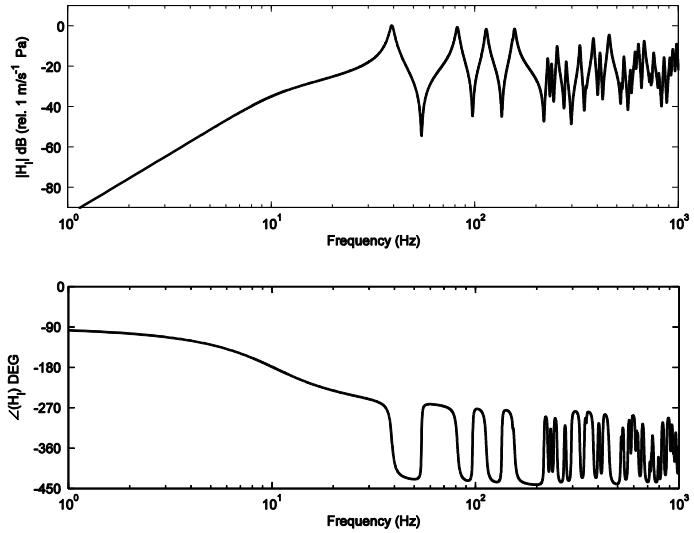

Figure 6.2: Open loop frequency response function of a current driven inertial actuator

Figure 6.2 shows a phase lag of 180º at round 10 Hz due to the resonance of the inertial actuator. For higher frequencies the actuator behaves like and ideal velocity feedback using a point actuation force with the phase response between -270º and -450º.

Figure 6.3 shows the Nyquist plot of the open loop FRF. The locus crosses the left hand side of the diagram indicating that the loop is only conditionally stable. In this case the gain margin, which represents the maximum gain that can be implemented before the system gets unstable, is about 34 dB.

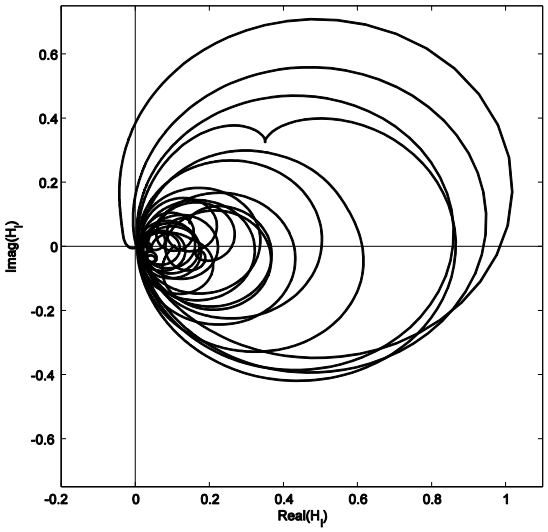

Figure 6.3: Nyquist plot of the open loop frequency response function of a current driven inertial actuator

Improvements in the stability can be achieved by using actuators with low natural frequency compared with the first structural resonance and with a relatively high internal damping. The level of damping of the inertial actuator chosen in the example might be difficult to achieve in practice. A natural frequency of 10 Hz also requires the use of a very soft suspensions, which

could cause high static displacement of the proof mass and likely stroke saturation for sudden changes of the primary disturbance leading the system to instability [42]. These slightly unrealistic parameters have been chosen for these simulations to have a more stable controller in order to gain a better understanding on the possibility to use the maximisation of power absorbed by the controller as a self-tuning strategy when an inertial actuator is employed. A practical possibility to increase the stability of the controller is to use an analogue compensator that shifts the apparent natural frequency of the inertial actuator at lower frequency as described in reference [43].

6.4. Minimisation of the kinetic energy and the maximisation of absorbed power using an inertial actuator

In this section simulation results of a simply supported panel subjected to 'rain-on-the-roof' excitation and controlled by a single velocity feedback control unit consisting of an inertial actuator collocated with an ideal velocity sensor are presented. The inertial actuator is driven with a current proportional to the measured velocity. The characteristics of the actuator are listed in Table 6.1. Figure 6.3 shows the kinetic energy of the panel used in Chapter 3 for increasing values of control gain g. The response of the panel is damped, even when the feedback gain is zero, due to the passive loading of the actuator, which acts primarily as a passive damper above its natural frequency. As the feedback gain is increased, significant attenuation is initially obtained at the first few panel resonances.

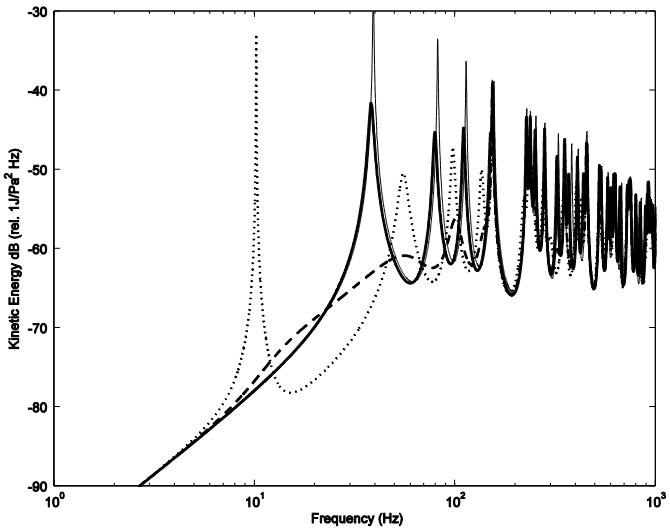

Figure 6.4: PSD of the panel's kinetic energy with a local velocity feedback controller driving the inertial actuator with a current proportional to the velocity before placing the actuator (faint line) when feedback gain is g=0 (solid-line), g=11 Asm^{-1} (dashed line), and g=51.4 Asm^{-1} (dotted line).

At higher gains, however, as well as the additional resonances due to pinning starting to appear, there is also significant enhancement of the vibration at the natural frequency of the actuator, due to the positive feedback in this frequency region caused by the phase response of the

actuator (dotted-line). The feedback gain in this case, in which the actuator is driven by a current, has units of Asm^{-1}, but since the assumed transduction coefficient, *Bl*, is 2.6 NA^{-1}, it has a similar numerical value to that used in Chapter 3.

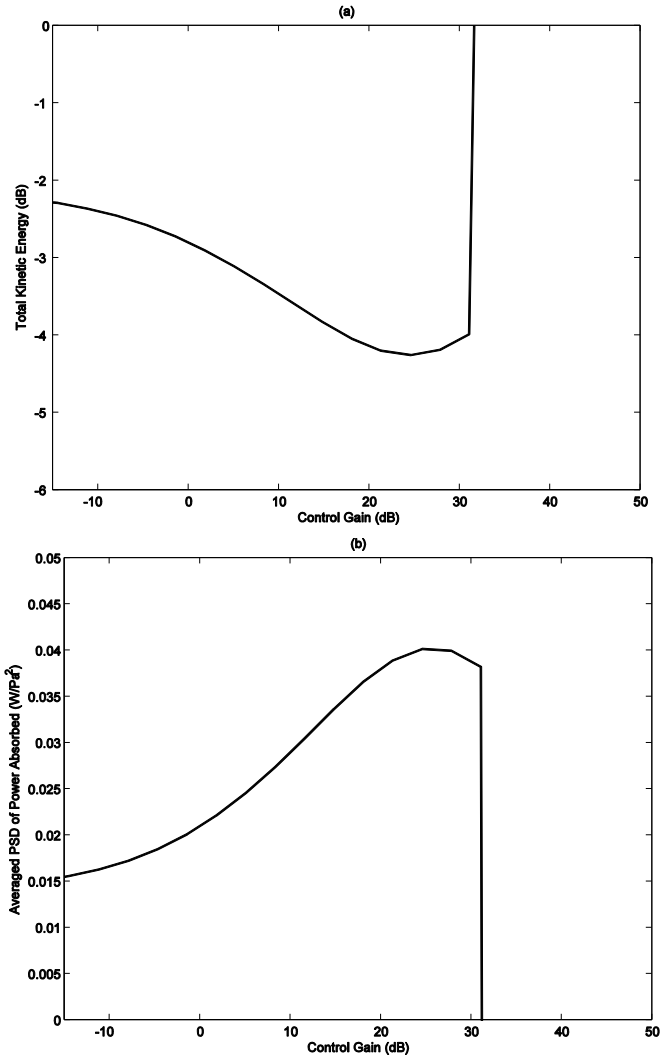

Figure 6.5: Total kinetic energy of the panel (a) and power absorbed by the controller (b) as function of feedback gain for a local velocity feedback controller driving an inertial actuator with a natural frequency of 10 Hz (solid line).

The total kinetic energy of the panel and local absorbed power is plotted as a function of feedback gain in Figure 6.5(a) and (b) for this case. These graphs are similar to those obtained for a point force actuator in Chapter 3, up until the critical gain is approached, for which the system becomes unstable. At low control gains, however the kinetic energy, normalised by that before the actuator is attached is reduced by about 2 dB and the power absorbed by the controller no longer tends to zero. This is because the passive response of the inertial actuator still dissipates mechanical power even when the actuator is undriven. As the feedback gain is increased towards the value for which the system becomes unstable, however, the kinetic energy becomes very large and the power absorbed becomes negative.

The frequency domain results are not valid for higher feedback gains. It is striking how quickly these curves deviate from those using an ideal force actuator as the instability is approached.

As equation (6.2) shows, the control force is no longer directly proportional to the input signal when using an inertial actuator, since the actuator has its own dynamics. In order to calculate the local power absorbed by the actuator, as the product of the force it produces multiplied by the local velocity, it is thus necessary to calculate an estimate of the force, $\hat{f}$, using estimates of the blocked response and undriven impedance $\hat{T}_2$ and $\hat{Z}_{\mathrm{mo}}$, so that:

$$\hat{f} = \hat{T}_2 \tilde{\imath} + \hat{Z}_{\mathrm{mo}} \tilde{v}. \tag{6.17}$$

as illustrated in Figure 6.6. This figure shows how this estimate of the absorbed power can be used to tune the feedback gain g. A compensator, C, is also included before the actuator, which is assumed to be unity here, but in general could be used to lower the apparent natural frequency of the actuator [43], in which case $\hat{T}_2$ would need to be estimated with this compensator in place, but $\hat{Z}_{\mathrm{mo}}$ is unaffected.

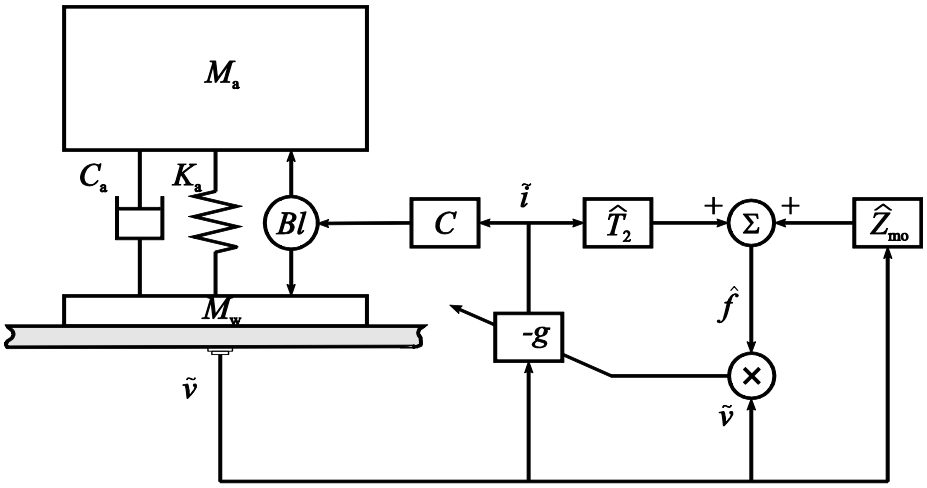

Figure 6.6: Self-tuning arrangement for direct velocity feedback with an inertial actuator in which C is a compensator for the actuator, and $\hat{T}_2$ and $\hat{Z}_{mo}$ are filters representing the blocked response and the mechanical impedance of the actuator and compensator, used to estimate the applied force, $\hat{f}$.

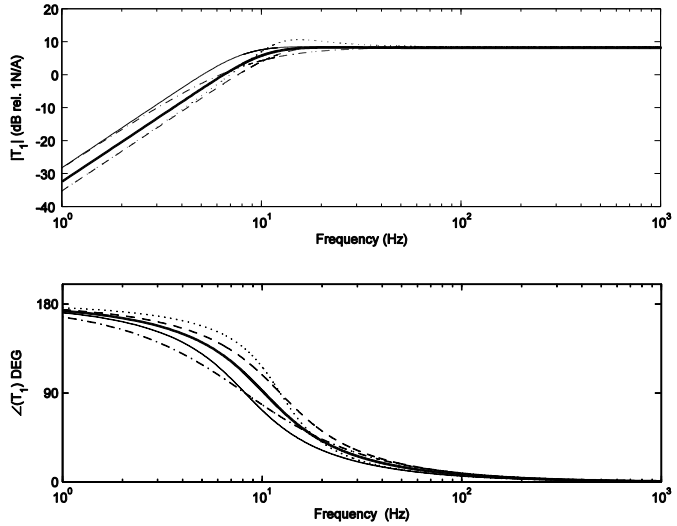

Figure 6.7: Blocked Frequency response of an inertial actuator, modelled as a single degree of freedom system with the parameters shown in table 1 (solid line) and with ± 20% variations in its natural frequency and damping. +20% ω_a +20% ζ_a (dashed line), +20% ω_a -20% ζ_a (dotted line), -20% ω_a +20%ζ_a (dash-dotted line), -20% ω_a -20% ζ_a (faint line).

One of the potential dangers in this approach is that the actuator dynamics are never known perfectly, and may change with time or operating temperature. A series of further simulations have thus been conducted with ±20% deviations in either the modelled natural frequency or modelled damping ratio of the actuator. Figure 6.7 shows the blocked actuator response $\hat{T}_2$ for various modifications of ω_a and ζ_a.

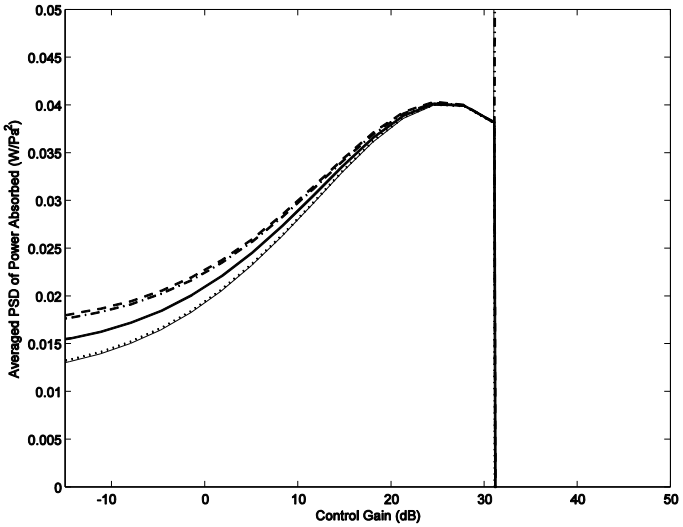

Figure 6.8: power absorbed by the controller as function of feedback gain for a local velocity feedback controller driving an inertial actuator with a natural frequency of 10 Hz (solid line). Also plotted is the estimated power absorbed when the actuator model is incorrectly identified+20% ω_a +20% ζ_a (dashed line), +20% ω_a -20% ζ_a (dotted line), -20% ω_a +20 ζ_a (dash-dotted line), -20% ω_a -20% ζ_a (faint line).

The effect of these deviations in the modelled response on the estimated absorbed power are also plotted in Figure 6.8, which shows that although the estimated power is somewhat in error

for low feedback gains, it retains the same shape near its peak as that with an accurate estimate of applied force and can thus still be reliably used to tune the feedback gain.

When the feedback gain is very close to instability, however, and the estimated natural frequency of the actuator is below the true value, there is a sharp spike in the estimated absorbed power. The true force is then very close to being out of phase with the input signal, *i*, but the estimated force will have less phase shift, since the phase of the estimated actuator response is lower than the true value, as can be seen in Figure 6.7. The estimated absorbed power thus becomes greater than the true power, since the large force and input signal appear to be closer to being in phase. This effect should not prevent the convergence of a practical controller, however, since it occurs so close to the point of instability, which the controller must in any case steer clear of at all cost.

The adaptation algorithm used to adjust the feedback gain based on the estimated power absorbed would thus have to be carefully designed not to stray too close to the unstable region. This is particularly important if the inertial actuator did not have such a low natural frequency, compared with the first structural resonance, as that assumed above. In that case, the maximum in the power absorption curve with an ideal force actuator could occur at a significantly higher feedback gain than the stability limit, so that the optimal feedback gain with the inertial actuator is very close to the limit of stability. This is illustrated in Figure 6.9, in which the actuator stiffness is increased so that its natural frequency is changed from 10 Hz to 20 Hz, which also changes the damping ratio from 0.63 to 0.35.

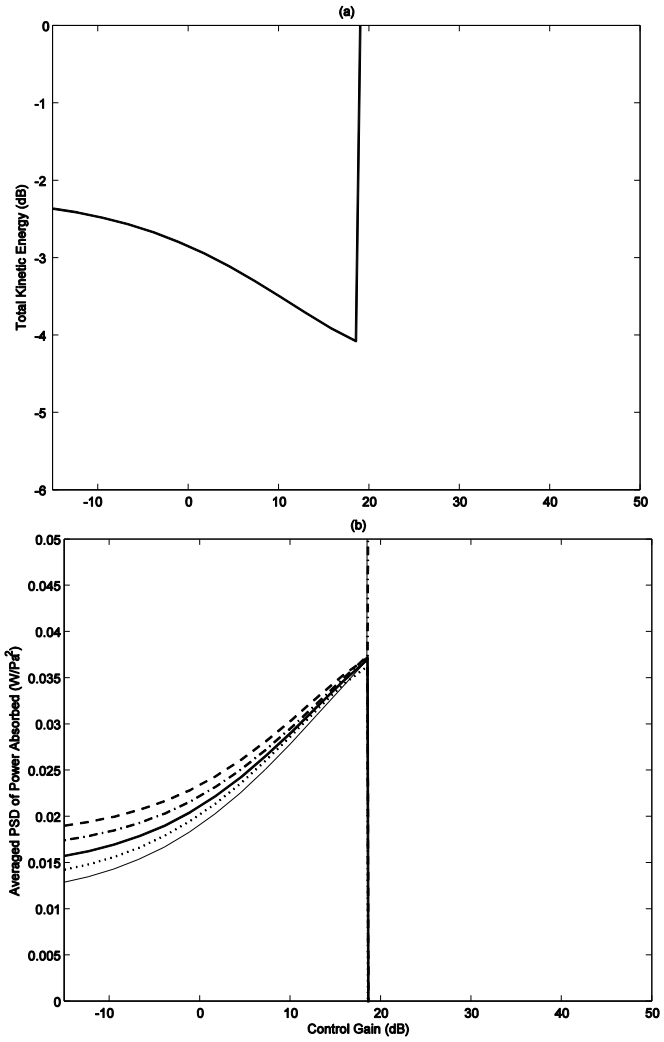

Figure 6.9: Total kinetic energy of the panel (a), and power absorbed by the controller (b) as a function of feedback gain for a local velocity feedback controller driving an inertial actuator with a natural frequency of 20 Hz. Also plotted is the estimated power absorbed when the actuator model is incorrectly identified; +20% ω_a +20% ζ_a (dashed line), +20% ω_a -20% ζ_a (dotted line), -20% ω_a +20% ζ_a (dash-dotted line), -20% ω_a -20% ζ_a (faint line).

The ratio of the maximum, stable feedback gain, $g_{\max}$, to the optimum feedback gain, g_{opt}, can be estimated by using the expression for these quantities derived in [17], which are:

$$g_{\max} \approx \frac{2\zeta_a M_1 \omega_1^2}{\omega_a} \tag{6.18}$$

$$g_{\text{opt}} \approx \frac{2M\omega_1}{\pi} \tag{6.19}$$

where M is the mass of the panel, ω_1 its first natural frequency, M_1 the apparent mass associated with the first mode at this frequency, assumed to be approximately M/π, and ω_a and ζ_a are the natural frequency and damping ratio of the actuator, so that:

$$\frac{g_{\max}}{g_{\text{opt}}} \approx \zeta_{\text{a}} \frac{\omega_1}{\omega_{\text{a}}} \tag{6.20}$$

This ratio is greater than unity in the simulations presented here when the actuator natural frequency is 10 Hz, as in Figure 6.5, but less than unity when the actuator natural frequency is 20 Hz, as in Figure 6.9. The right hand side of this equation thus provides a convenient rule of thumb for estimating how well suited a given inertial actuator is for controlling a panel with given natural frequency.

6.5. Summary and conclusions

Simulation with a velocity feedback loop including an inertial electromagnetic transducer have been used to illustrate that the maximisation of absorbed mechanical power again provides a reasonable approximation to the minimisation of the kinetic energy of the host structure. Care must be taken to ensure the feedback gain is below that which causes instability in this case. The minimum feedback gain can be increased either by lowering the natural frequency of the actuator or using an electrical compensator in the feedback loop. The characterisation of the actuator can also be used to calculate the applied force from the measured current and velocity, so that the absorbed power can again be estimated in practice. Pressures of time prevented an experimental investigation of such a control system.

The feedback control system described in this chapter requires the use of external power to drive the inertial actuator. In the next chapter the use of an idealised semi-active inertial actuator, often called dynamic vibration absorber, will be considered in controlling broadband vibration of a single degree of freedom system, which does not require an external power supply.

7. Broadband vibration control using a dynamic vibration absorber

This chapter presents the broadband vibration control of a single degree of freedom system using a dynamic vibration absorber. Dynamic vibration absorbers are single degree of freedom systems whose natural frequency is tuned to suppress the vibration at its point of attachment of a host structure. Tuning of a dynamic vibration absorber has previously been considered to minimise the kinetic energy of the host structure and here, after a brief review, the maximisation of the power dissipation within the absorber is also considered.

7.1. The dynamic vibration absorber

A widely used passive and semi-active device is the dynamic vibration absorber (DVA). Since its invention, in 1911 by Fhram [44], this devices have been widely studied. The DVA can be tuned in two different ways depending on the application. The first way of operating such a device aims to suppress the vibration only at a particular forcing frequency, in which case the device' s natural frequency is tuned to this excitation frequency. The damping of the device should then be as low as possible, so that it presents the greatest impedance to the host structure at the operating frequency. The device is then often known as a "vibration neutraliser", and considerable ingenuity has been put into tuning the device to track variations in the excitation frequency [6, 45, 46].

Alternatively the device can be used to attenuate the vibration due to a particular mode of the structure over a range of frequencies, when it is sometimes referred to as a "tuned mass damper" [3]. The optimum tuning of the natural frequency and damping ratio of the device then become less obvious and depend on exactly how the optimisation criterion is defined. The selected mode of the host structure is generally modelled as a single degree of freedom system for this optimisation, often without any inherent damping. Different optimisations of DVA's parameters for broadband frequency excitation have been proposed [47-54] and will be reviewed in greater detailed in the next section.

There is a vast literature on DVAs and although we do not aim to present a complete literature review, which is attempted in reference [45, 46], it is instructive to consider few examples of DVAs installed on different civil, maritime and mechanical systems.

One application of DVAs is to control the wind induced vibration of pipelines above the Arctic Circle as described in references [45, 55]. Figure 7.1 shows a scheme of the pipeline with a DVA per span attached.

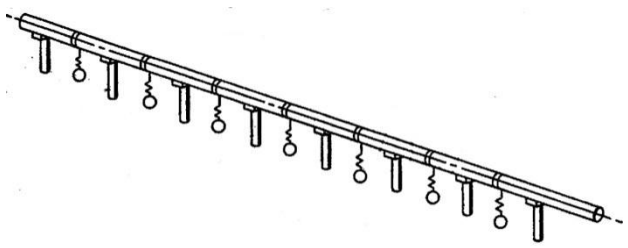

Figure 7.1: Pipeline with one DVA per span (figure taken from [55])

The vibration of the pipeline are characterised by cyclic lift force due to the vortex shedding phenomenon. For a span between 12 and 18 m as many as ten modes of the structure can be excited depending on the wind. This vibration can cause damage at the connections of the pipes due to mechanical fatigue.

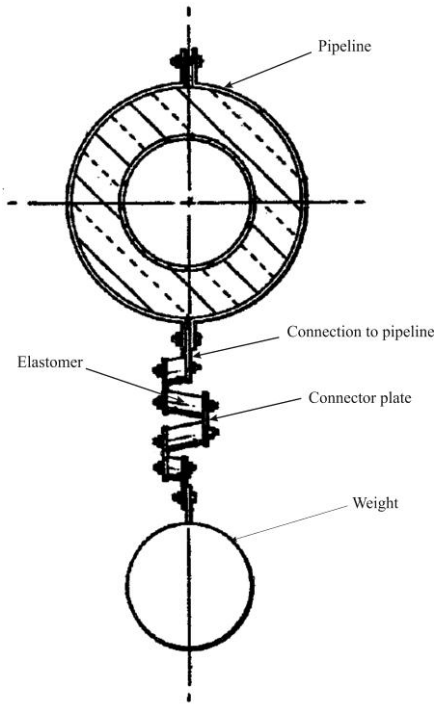

Figure 7.2: The DVA configuration to damp the pipeline vibration (figure taken from [55])

A dynamic vibration absorber has been designed with a resonance in this frequency region. Due to the severe environmental conditions at the Arctic Circle the design of a DVA to prevent changes of the stiffness and damping of the device can be difficult task. However if a change in the operation conditions could mistune the absorber by slightly changing its stiffness, the very high modal density of the pipeline ensures that the natural frequency of the DVA will always be near or at the resonance of the pipeline. Figure 7.2 shows a configuration of the dynamic vibration absorber, which has a mass of between 23 to 34 Kg, suspended using a series of elastomeric components in shear deformation. The modular design of the suspension allows changes in the damping and stiffness of individual devices. With use of DVAs in this

application, the root mean squared value of the displacement of the pipeline has been reported to be reduced by a factor of seven [45]. In this application the properties of the device are not controlled over time and so it is entirely passive.

As second example of a purely passive control using vibration absorbers is the Millennium footbridge in London. During the opening day the bridge presented high level of vibrations and after two days of limited access was closed. Modifications of the structure were implemented for a total cost of 5 million pounds and the bridge reopened after two years. The excitation to which the bridge is exposed are mainly due to the people walking on it. This produces a repeating pattern of vertical force but also a sideway force due the swing of the human body. The typical footfall rate for a normal walking is around 2 steps per second but in large crowds this rate can drop to 1.4 steps per second or lower. Thus the forcing frequency is generally in the region of 1.2–2.2 Hz. Since alternate footsteps apply forces in opposite lateral directions, the lateral forcing frequencies are half of footfall rate, in the range of 0.6–1.1 Hz. On the Millennium Bridge, even the lowest lateral mode at 0.475 Hz was excited. These low frequencies were excited by pedestrians adapting their gait to the vibration of the bridge by adopting a zigzag walk to help them balance [56, 57].

In the case of Millennium Bridge, a passive modification was studied and implemented to solve the problem. Two possible solutions were considered [58]. The first was to move the low resonances of the bridge in a frequency region away from the excitation frequency, by increasing the stiffness of the bridge. It was calculated that an increasing of the stiffness by seven times was necessary to fix the problem. It was then clear that a more suitable approach was to damp the structure. The vibration problem was finally fixed using 37 viscous dampers to attenuate lateral vibration modes of the bridge and 50 tuned mass damper 26 of which were used to damp the vertical modes of the bridge and 24 to control lateral modes. Even though vertical vibrations were not observed during initial opening of the bridge, the tuned mass dampers were installed as a precaution.

Figure 7.3: Millennium Bridge London (right picture) with DVA mounted beneath the deck to reduce its vibration level (left picture) from [59].

The vibration absorbers comprise masses between 1 and 3t supported on compression springs [58]. Viscous damping is provided by the presence of a paddle connected to the mass and suspended in a pot of viscous fluid. Figure 7.3 shows a picture of the millennium bridge in London and a DVA mounted beneath the deck.

An application of DVAs is to control the vibration of marine diesel engines [60]. In most cases, a practical means to reduce vibration is simply to detune the lowest natural frequencies away from the main dynamic excitation frequencies. This can be achieved by intervening on the mounts of heavy structures built on the engine which severely influence the whole dynamic of the system. The turbocharger of a Diesel engine can have a dominant effect on the global vibration of the engine due to its large mass. For new designs a firing order can be introduced to change the excitation forces at certain harmonic frequency. These solutions are hard to be implemented on existing engines already in operation. The company Wärtsiliä has reduced the vibrations mounting on their diesel engines using passive tuned vibration absorber [60]. The vibration control of an engine has to be effective on a wide frequency band and has to be capable to operate for thousands of running hours without maintenance. A prototype of the DVA is shown in Figure 7.4. The absorbed developed by Wärtsiliä consists of a vibrating mass disc supported by steel springs. Both are located in a cylindrical steel frame filled with damping oil. All the absorber's parameters, damping, stiffness and mass, can be separately adjusted for individual devices. The damping can by regulated by changing the oil flow inside the absorber. The analysis to design the vibration absorber starts with the measurements of the engine response and its structural modes. These measurements allow finding the theoretical best position and the direction of the absorber to obtain the best reduction of the overall vibration of the engine. For example on a 9 cylinder four stroke Wärtsiliä 46 engine, the most efficient mode to be controlled was identified as the first torsional mode at 29 Hz.

Figure 7.4: DVA to control the vibration of a Diesel engine from [60]

The absorbed was tuned at this excitation frequency and damping was chosen to obtain a broadband control. In this way the absorber could reduce the vibration level at more than one

harmonic order. Vibrations at all the three major excitation harmonics were reduced in both transversal and longitudinal directions.

An application of DVAs in which they are used as a semi-active device is the structural vibration control in aeronautic engineering. Aircraft engines can induce significant vibration into the fuselage. For example, jet engines produce vibrations that propagate through the structure which can cause considerable noise inside the cabin.

Adaptive tuneable vibration absorbers have been used to control the noise in the aft cabin of Douglas Aircraft DC9-V [13, 61, 62]. This aircraft is powered by two jet engines mounted to the aft fuselage structure. This causes the engine vibration to be transmitted to the fuselage radiating a high level of noise inside the cabin.

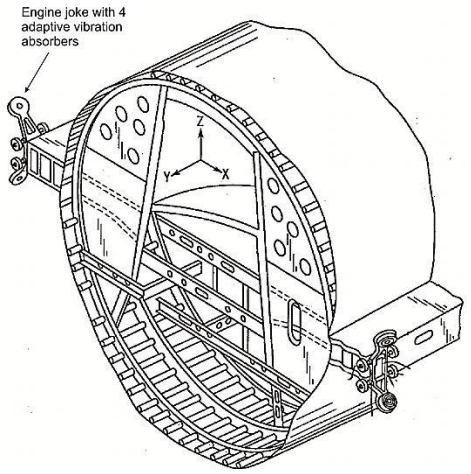

Figure 7.5: Adaptive vibration absorber mounted on the engine yokes of a Douglas DC9 aircraft from [61].

These two engines can generate a tonal excitation at their rotational speed and higher harmonics. Initially, Douglas placed four vibration absorbers on each engine as shown in Figure 7.5. They were tuned to neutralise the vibration transmission at the rotation frequency of the engines at the cruise speed. However, the frequency of the engine induced vibrations changes with the engine speed and the stiffness of the suspension of the absorber changed with the age of the device and operating temperature so that the vibration absorbers could be mistuned. For these reasons a semi-active device that can adapt to changes of the operating conditions was designed by Barry Controls and Hood Technology. The suspension of the DVA comprises two circular parallel rings connected with a plurality of flexible rods. An electrical motor is used to change the compression or tension on the rods in order to change the stiffness of the suspension and thus the natural frequency of the DVA. The DVAs are tuned independently during the flight by a controller. It is reported in reference [13] that 25 dB reduction at the noisiest seat are achieved at the engine tones and the system is able to adapt over the rpm range of 65-100 %.

7.2. Background in tuning the Dynamic vibration absorber

A survey of tuning criterion for dynamic vibration absorbers when used as tuned mass dampers has been presented by Asami [47], and some of the results from this paper are presented in Table 7.1. The original optimisation criterion used by Omondroyd and Den Hartog 1928 [63] was that the magnitude of the displacement was equal at the two peaks in the coupled displacement response after the device has been attached. This is also known as mini-max or H_∞ optimisation. Another optimisation criterion would be to minimise the mean square displacement of the host structure when excited by a random force of uniform power spectral density, as first proposed by Crandall and Mark in 1963 [49] and also now known as H_2 optimisation. A third possibility is to adjust the natural frequency and damping of the device such that the poles of the overall system have the greatest negative value, so that the transient response decays as quickly as possible. Asami *et al.* [47] attribute this result in Table 7.1 to Yamaguchi in 1988 [52], although the same criterion was also considered by Miller and Crawley in 1985 [51]. Krenk in 2005 [53] proposed a further method to tune the parameters of a DVA. He tuned the frequency ratio of the two decoupled oscillators using the same criterion proposed by Omondroyd and den Hartog [63] and proposed a new criterion for the optimal damping ratio. The damping ratio was chosen by simultaneously minimising the displacement of the main mass and the relative displacement of the two masses calculated at the natural frequency of the system when the damper was blocked.

Table 7.1: optimisation criteria of the dynamic vibration absorber on a lightly damped SDOF system. ζ_{opt} is the optimal damping ratio of the DVA and ν_{opt} is the optimal frequency ratio of the natural frequencies of the two uncoupled systems.

	Optimisation criterion	**Performance index**	**Objective**	**Proposed by:**	**Optimal parameters**
1	H_∞ Optimisation	$A_{1max} = \left\lvert \frac{x_1}{x_{st}} \right\rvert_{max}$	Minimise the maximum displacement of the primary mass	Ormondroyd & Den Hrtong 1928 [63]	$\zeta_{\text{opt}} = \sqrt{\frac{3\mu}{8(1+\mu)}}$ $\nu_{\text{opt}} = \frac{1}{1+\mu}$
2	H_2 Optimisation of the mean squared displacement	$I_1 = \frac{E[x_1^2]}{S_f \omega_1 / k_1^2}$	Minimise the total displacement of the primary mass over all frequency	Iwata 1982 [64], Warburton 1982 [54]	$\zeta_{\text{opt}} = \sqrt{\frac{\mu(4+3\mu)}{8(1+\mu)(2+\mu)}}$ $\nu_{\text{opt}} = \frac{1}{1+\mu}\sqrt{\frac{2+\mu}{2}}$
3	Stability Maximisation	$\Lambda = -\max_i(\text{Re}[s_i])$	Minimise the transient vibration of the system	Miller *et al.*1985 [51] Yamaguchi 1988 [52],	$\zeta_{\text{opt}} = \sqrt{\frac{\mu}{1+\mu}}$ $\nu_{\text{opt}} = \frac{1}{1+\mu}$
4	H_∞ Minimisation of relative displacement	$A_{1max} = \left\lvert \frac{x_1}{x_{st}} \right\rvert_{max}$ $A_{2max} = \left\lvert \frac{x_1 - x_2}{x_{st}} \right\rvert_{max}$	Minimisation of displacement of the main mass and relative displacement	Krenk 2005 [53]	$\zeta_{\text{opt}} = \sqrt{\frac{\mu}{2(1+\mu)}}$ $\nu_{\text{opt}} = \frac{1}{1+\mu}$
5	H_2 Minimisation of kinetic energy	$I_k = \frac{E[\dot{x}_1^2]}{2\pi S_f \omega_1 / k_1}$	Minimise the total kinetic energy of the primary mass over all frequencies	Warburton 1982 [54]	$\zeta_{\text{opt}} = \frac{\sqrt{\mu}}{2}$ $\nu_{\text{opt}} = \frac{1}{\sqrt{1+\mu}}$
6	H_2 Maximisation of the absorbed power	$I_{p2} = \frac{c_2 E[\lvert \dot{x}_1 - \dot{x}_2 \rvert^2]}{2\pi S_f \omega_1 / k_1}$	Minimise the total kinetic energy of the primary mass over all frequencies	This study	$\zeta_{\text{opt}} = \frac{\sqrt{\mu}}{2}$ $\nu_{\text{opt}} = \frac{1}{\sqrt{1+\mu}}$

He also demonstrate that for the frequency tuning proposed by Omondroyd and den Hartog [63], the complex locus of the natural frequencies has a bifurcation point corresponding to the maximum damping of the two modes. For lower damping ratio the two modes have the same modal damping. Warburton in 1982 [54] proposed the minimisation of the frequency averaged kinetic energy of the host structure as a tuning criterion.

In this section we consider a further criterion on which to optimise a dynamic vibration absorber based on the maximisation of the power dissipated by the absorber. It is found for a damped host structure, sometimes also called primary structure that the maximisation of the power

absorbed by the damper corresponds to the minimisation of the kinetic energy of the host structure.

7.3. Analysis

Figure 7.6 shows a scheme of a single degree of freedom system with a DVA. The primary system is subjected to a random excitation f_p, which is assumed to have a flat power spectral density and v_1 and v_2 are the velocities of mass m_1 and m_2.

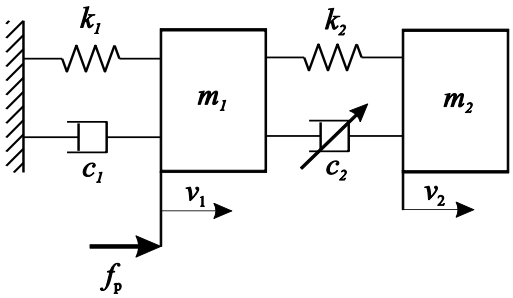

Figure 7.6: Scheme of the SDOF system with the DVA

Setting c_3 and k_3 to zero in equations (2.20) and (2.21), the velocities per unit input force of the two masses are given by:

$$\tilde{Y}_{11} = \frac{\tilde{v}_1}{\tilde{f}_p} = \\ = \frac{jk_2\omega - c_2\omega^2 - im_2\omega^3}{k_1k_2 + jc_2k_1\omega + ic_1k_2\omega - c_1c_2\omega^2 - k_2m_1\omega^2 - k_1m_2\omega^2 - k_2m_2\omega^2 - jc_2m_1\omega^3 - jc_1m_2\omega^3 - ic_2m_2\omega^3 + m_1m_2\omega^4} \quad (7.1)$$

$$\tilde{Y}_{12} = \frac{\tilde{v}_2}{\tilde{f}_p} = \\ = \frac{jk_2\omega - c_2\omega^2}{k_1k_2 + jc_2k_1\omega + ic_1k_2\omega - c_1c_2\omega^2 - k_2m_1\omega^2 - k_1m_2\omega^2 - k_2m_2\omega^2 - jc_2m_1\omega^3 - jc_1m_2\omega^3 - ic_2m_2\omega^3 + m_1m_2\omega^4} \quad (7.2)$$

The steady state response of the system can be expressed in terms of the five dimensionless parameters defined by:

$\mu = m_2/m_1$: mass ratio

$\nu = \omega_2/\omega_1$: natural frequency ratio

$\lambda = \omega/\omega_1$: forced frequency ratio

$\zeta_1 = c_1/(2m_1\omega_1)$: primary damping

$\zeta_2 = c_2/(2m_2\omega_2)$: secondary damping

(7.3)

where

$\omega_1 = \sqrt{k_1/m_1}$: natural frequency of the host / primary system

$\omega_2 = \sqrt{k_2/m_2}$: natural frequency of the DVA (7.4)

The five dimensionless coefficients defined in equations (7.3) and (7.4) can be written as:

$$\begin{aligned} \mu &= m_1^{-1} m_2 \\ \nu &= m_1^{1/2} k_1^{-1/2} m_2^{-1/2} k_2^{1/2} \\ \lambda &= \omega m_1^{1/2} k_1^{-1/2} \\ \zeta_1 &= 2^{-1} c_1 m_1^{-1/2} k_1^{-1/2} \\ \zeta_2 &= 2^{-1} c_2 m_2^{-1/2} k_2^{-1/2} \end{aligned} \tag{7.5}$$

and thus a generic dimensionless term can be written as:

$$a\nu^b \lambda^c \mu^d \zeta_2^e \zeta_1^f = 2^{-e-f} m_1^{b/2+c/2-d-f/2} k_1^{-b/2-c/2-f/2} m_2^{-b/2+d-c/2} k_2^{b/2-e/2} c_2^e c_1^f \omega^c \tag{7.6}$$

Each of the coefficient in equations (7.1) and (7.2) can be expressed in non-dimensional form by setting each of them equal to equation (7.6) and solving for the parameters *a*, *b*, *c*, *d*, *e*, *f*, so that equations (7.1) and (7.2) can be written as:

$$\tilde{\Gamma} = \sqrt{k_1 m_1}\,\tilde{Y}_{11}(j\lambda) = \frac{B_0 + (j\lambda)B_1 + (j\lambda)^2 B_2 + (j\lambda)^3 B_3}{A_0 + (j\lambda)A_1 + (j\lambda)^2 A_2 + (j\lambda)^3 A_3 + (j\lambda)^4 A_4} \tag{7.7}$$

$$\tilde{\Theta} = \sqrt{k_1 m_1}\,\tilde{Y}_{12}(j\lambda) = \frac{C_0 + (j\lambda)C_1 + (j\lambda)^2 C_2 + (j\lambda)^3 C_3}{A_0 + (j\lambda)A_1 + (j\lambda)^2 A_2 + (j\lambda)^3 A_3 + (j\lambda)^4 A_4} \tag{7.8}$$

where

$A_0 = \mu\nu^2$	$B_0 = 0$	$C_0 = 0$
$A_1 = 2\zeta_2\mu\nu + 2\zeta_1\mu\nu^2$	$B_1 = \mu\nu^2$	$C_1 = \mu\nu^2$
$A_2 = \mu\nu^2 + \mu + \mu^2\nu^2 + 4\zeta_2\zeta_2\mu\nu$	$B_2 = 2\zeta_2\mu\nu$	$C_2 = 2\zeta_2\mu\nu$
$A_3 = 2\zeta_2\mu\nu + 2\zeta_2\mu^2\nu + 2\zeta_1\mu$	$B_3 = \mu$	$C_3 = 0$
$A_4 = \mu$		

7.4. Minimisation of the total kinetic energy and maximisation of the power absorbed

If the aim of the DVA is to minimise the integral of the kinetic energy of the primary mass calculated over the frequency-band $\pm\infty$, the performance index to be minimised can be defined by:

$$I_{\mathrm{k}} = \frac{m_1 E[|\tilde{v}_1|^2]}{2\pi S_{\mathrm{f}} \omega_1 / k_1} \tag{7.9}$$

where $E[\ ]$ denotes the expectation value. The performance index I_{k} represents the ratio of the kinetic energy of the primary system to the excitation force with a uniform spectrum density $S_{\mathrm{f}}(\omega)$. The unit of $S_{\mathrm{f}}(\omega)$is $\mathrm{N^2s/rad}$. The constant $2\pi\omega_1/k_1$ is introduced to ensure that the performance index is dimensionless. The mean squared value of the velocity of the primary mass can be written as:

$$E[|\tilde{v}_1|^2] = \frac{S_{\mathrm{f}}\omega_1}{m_1 k_1} \int_{-\infty}^{+\infty} \left|\tilde{\Gamma}\right|^2 \mathrm{d}\lambda \tag{7.10}$$

Substituting equation (7.10) in equation (7.9) yields:

$$I_{\mathrm{k}} = \frac{1}{2\pi} \int_{-\infty}^{+\infty} |\tilde{\Gamma}|^2 \,\mathrm{d}\lambda \tag{7.11}$$

Thus, substituting equation (7.7) in (7.11) yields:

$$I_{\mathrm{k}} = \frac{1}{2\pi} \int_{-\infty}^{+\infty} \left| \frac{B_0 + (j\lambda)B_1 + (j\lambda)^2 B_2 + (j\lambda)^3 B_3}{A_0 + (j\lambda)A_1 + (j\lambda)^2 A_2 + (j\lambda)^3 A_3 + (j\lambda)^4 A_4} \right|^2 \mathrm{d}\lambda \tag{7.12}$$

Equation (7.12) can be integrated using the formula in reference [22] leading to:

$$I_{\mathrm{k}} = \frac{\zeta_1(4\zeta_2^2(\nu^3+\nu)+\mu\nu^3) + \zeta_2(4\zeta_2^2\nu^2 + (\mu+1)\nu^4 - 2\nu^2 + 1) + 4\zeta_2\zeta_1^2\nu^2}{4(\zeta_1^2(4\zeta_2^2((\mu+1)\nu^3+\nu)+\mu\nu^3) + \zeta_2\zeta_1(4\zeta_2^2(\mu+1)\nu^2 + (\mu+1)^2\nu^4 - 2\nu^2 + 1) + \zeta_2^2\mu\nu + 4\zeta_2\zeta_1^3\nu^2)} \tag{7.13}$$

On the other end the power absorbed by the DVA is the power dissipated by the damper c_2 and so the absorbed power can be written as:

$$S_{\mathrm{P}}(\omega) = \frac{1}{2}\mathrm{Re}\left\{\tilde{f}_{\mathrm{d}}^{*}[\tilde{v}_1 - \tilde{v}_2]\right\} \tag{7.14}$$

Where * denotes complex conjugate and the force $\tilde{f}_{\mathrm{d}}$ is the force produced by the damper given by:

$$\tilde{f}_{\mathrm{d}} = c_2(\tilde{v}_1 - \tilde{v}_2) \tag{7.15}$$

Substituting equation (7.15) in (7.14) the absorbed power becomes:

$$S_{\mathrm{P}}(\omega) = \frac{1}{2} c_2 |\tilde{v}_1 - \tilde{v}_2|^2 \tag{7.16}$$

In this case the non-dimensional performance index is defined by:

$$I_{\mathrm{p2}} = \frac{c_2 E[|\tilde{v}_1 - \tilde{v}_2|^2]}{2 S_{\mathrm{f}} \omega_1 / k_1} \tag{7.17}$$

which represents the ratio of power absorbed by the DVA to that generated by excitation force with a spectrum density S_{f} acting on a damper of value k_1/ω_1. The mean squared value of the relative velocity times the mechanical damping c_2 can be expressed as follow:

$$c_2 E[|\tilde{v}_1 - \tilde{v}_2|^2] = \frac{S_{\mathrm{f}} \omega_1}{k_1} 2\zeta_2 \mu\nu \int_{-\infty}^{+\infty} |\tilde{\Gamma} - \tilde{\Theta}|^2 d\lambda \tag{7.18}$$

Thus the performance index becomes:

$$I_{\mathrm{p2}} = \zeta_2 \mu\nu \int_{-\infty}^{+\infty} \left| \frac{D_0 + (j\lambda) D_1 + (j\lambda)^2 D_2 + (j\lambda)^3 D_3}{A_0 + (j\lambda) A_1 + (j\lambda)^2 A_2 + (j\lambda)^3 A_3 + (j\lambda)^4 A_4} \right|^2 d\lambda \tag{7.19}$$

where

$$D_0 = A_0 - B_0 = 0$$

$$D_1 = A_1 - B_1 = 0$$

$$D_2 = A_2 - B_2 = 0$$

$$D_3 = A_3 - B_3 = \mu$$

The integral over the frequency band between $\pm\infty$ of equation (7.19) can be calculated using the expression given in reference [22], leading to:

$$I_{\mathrm{p2}} = \frac{\pi(\zeta_2 \mu\nu(\zeta_2 + 4\zeta_1\zeta_2^2\nu + 4\zeta_1^2\zeta_2^2\nu^2 + \zeta_1(1+\mu)\nu^3))}{\begin{array}{c} 2(\zeta_1^2(4\zeta_2^2((\mu+1)\nu^3 + \nu) + \mu\nu^3) + \zeta_2\zeta_1(4\zeta_2^2(\mu+1)\nu^2 + (\mu+1)^2\nu^4 - 2\nu^2 + 1) \\ +\zeta_2^2\mu\nu + 4\zeta_2\zeta_1^3\nu^2) \end{array}} \tag{7.20}$$

Although the denominators in equations (7.13) and (7.20) are the same, the dependence of their numerators on ζ_2 and ν is clearly different.

In order to minimise the total kinetic energy of the primary mass m_1, the following conditions have to be satisfied:

$$\begin{cases} \dfrac{\partial I_{\mathrm{k}}}{\partial \zeta_2} = 0 \\ \dfrac{\partial I_{\mathrm{k}}}{\partial \nu} = 0 \end{cases} \tag{7.21}$$

while to maximise the total power absorbed by the DVA the following conditions have to be satisfy:

$$\begin{cases} \dfrac{\partial I_{\mathrm{p2}}}{\partial \zeta_2} = 0 \\ \dfrac{\partial I_{\mathrm{p2}}}{\partial \nu} = 0 \end{cases} \tag{7.22}$$

Differentiating the performance index I_{k} expressed in equation (7.13) with respect to ζ_2 and ν, and setting these equal to zero, yields a pair of simultaneous equations:

$$\begin{aligned} -\mu\nu[&(\zeta_1^2\mu(\mu+1)\nu^6 + \zeta_2^2(4\zeta_1^2\nu^2(4\zeta_1^2\nu^2 + (2\mu-3)\nu^2 + 2) + (\mu+1)\nu^4 - 2\nu^2 + 1) \\ &+ 2\zeta_1\zeta_2\mu\nu^3(4\zeta_1^2\nu^2 + 1) + 4(4\zeta_1^2 - 1)\zeta_2^4\nu^2 + 8\zeta_1\zeta_2^3\nu(4\zeta_1^2\nu^2 - 2\nu^2 \\ &+ 1))] = 0 \end{aligned} \tag{7.23a}$$

$$\begin{aligned} -\zeta_2\mu\big[&(\zeta_1^2\mu(\mu+1)\nu^6 + \zeta_2^2(4\zeta_1^2\nu^2(4\zeta_1^2\nu^2 + (2\mu+1)\nu^2 + 2) - 3(\mu+1)\nu^4 + 2\nu^2 + 1) \\ &+ 2\zeta_1\zeta_2\nu^3(4\zeta_1^2(\mu+1)\nu^2 - 2(\mu+1)\nu^2 + \mu + 2) + 4(4\zeta_1^2 - 1)\zeta_2^4\nu^2 \\ &+ 8\zeta_1\zeta_2^3\nu(4\zeta_1^2\nu^2 - \nu^2 + 1))\big] = 0 \end{aligned} \tag{7.23b}$$

Following the same procedure, the partial derivatives of the performance index I_{p2} expressed in equation (7.20) are given by:

$$\begin{aligned} \pi\zeta_1\mu\nu[&\zeta_1^2\mu(\mu+1)\nu^6 + \zeta_2^2(4\zeta_1^2\nu^2(4\zeta_1^2\nu^2 + (2\mu-3)\nu^2 + 2) + (\mu+1)\nu^4 - 2\nu^2 + 1) \\ &+ 2\zeta_1\zeta_2\mu\nu^3(4\zeta_1^2\nu^2 + 1) + 4(4\zeta_1^2 - 1)\zeta_2^4\nu^2 + 8\zeta_1\zeta_2^3\nu(4\zeta_1^2\nu^2 - 2\nu^2 + 1)] \\ &= 0 \end{aligned} \tag{7.24a}$$

$$\begin{aligned} \zeta_1\mu\nu\big[&(\zeta_1^2\mu(\mu+1)\nu^6 + \zeta_2^2(4\zeta_1^2\nu^2(4\zeta_1^2\nu^2 + (2\mu+1)\nu^2 + 2) - 3(\mu+1)\nu^4 + 2\nu^2 + 1) \\ &+ 2\zeta_1\zeta_2\nu^3(4\zeta_1^2(\mu+1)\nu^2 - 2(\mu+1)\nu^2 + \mu + 2) + 4(4\zeta_1^2 - 1)\zeta_2^4\nu^2 \\ &+ 8\zeta_1\zeta_2^3\nu(4\zeta_1^2\nu^2 - \nu^2 + 1))\big] = 0 \end{aligned} \tag{7.24b}$$

Simultaneous equation (7.23) and (7.24) are both satisfied for $\zeta_2 = 0$ and $\nu = 0$ corresponding to maximising I_{k} and I_{p2}. The other solutions can be found setting to zero the terms in squared brackets. If $\zeta_1 \neq 0$ the term in square brackets in equation (7.23a) is equal to the term in square brackets in equation (7.24a) and the term in square brackets in equation (7.23b) is equal to the

term in square brackets in equation (7.24b), which means that minimising the total kinetic energy and maximising the total power absorbed give the same solution.

If ζ_1 is equal zero the primary system is undamped. Equations (7.23a) and (7.23b) for $\partial I_{\mathrm{k}}/\partial\zeta_2$ and $\partial I_{\mathrm{k}}/\partial\nu$ then reduce to:

$$\begin{aligned} -1+(2+4\zeta_2^2)\nu^2-(1+\mu)\nu^4=0 \\ -1+(-2+4\zeta_2^2)\nu^2+3(1+\mu)\nu^4=0 \end{aligned} \tag{7.25}$$

Solving the two equations simultaneously the two positive real optimal values of $\zeta_{2\mathrm{opt}}$ and ν_{opt} are obtained as:

$$\begin{cases} \zeta_{2\mathrm{opt}}=\dfrac{\sqrt{\mu}}{2} \\ \nu_{\mathrm{opt}}=\dfrac{1}{\sqrt{1+\mu}} \end{cases} \tag{7.26}$$

The optimal condition in equations (7.26) is the same as in reference [54] although it has been independently derived because the result was unknown to the author at the time this research was carried out. In this case the performance index I_{p2}, however, becomes equal to $\pi/2$ if ζ_1 is exactly zero. The absorbed power is then independent of ζ_2 and ν, as can be seen from equation (7.23a) and equation (7.23b), since they both are proportional to ζ_1. Provided that ζ_1 has a very small value thus singular condition will not occur, these optimum values of ζ_2 and ν will be the same for maximising power absorption as ζ_1 tends to zero.

7.5. Comparison of tuning strategies

Figure 7.7 shows the performance index I_{p2} as function of ζ_2 when ν is equal ν_{opt} (top plot) and I_{p2} as function of ν when ζ_2 is equal $\zeta_{2\mathrm{opt}}$ (bottom plot) for different values of the primary damping ration ζ_1. The plot shows that when ζ_1 is equal zero the absorbed power is constant. The absorbed power has a maximum provided ζ_1 has a finite value.

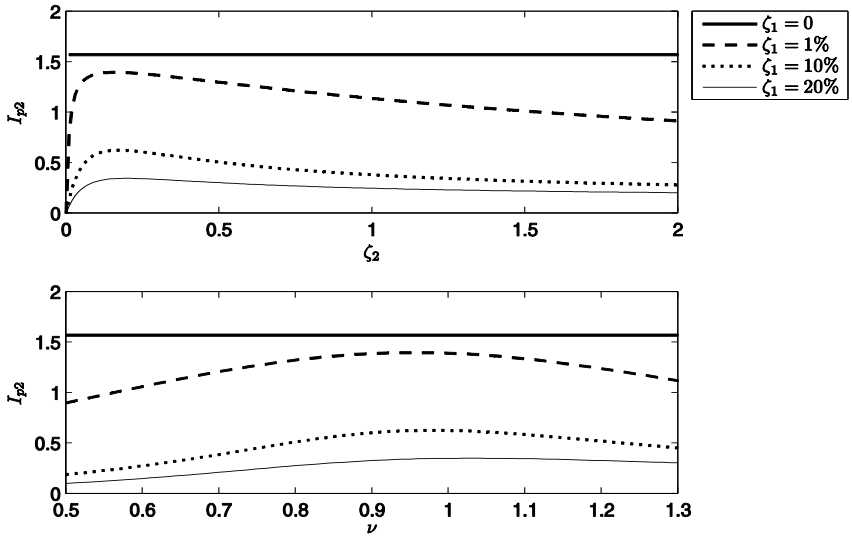

Figure 7.7: I_{p2} as function of ζ_2 when $\nu = \nu_{opt}$ (top plot) and I_{p2} as function of ν when $\zeta_2 = \zeta_{2opt}$ (bottom plot) for $\mu = 0.1$.

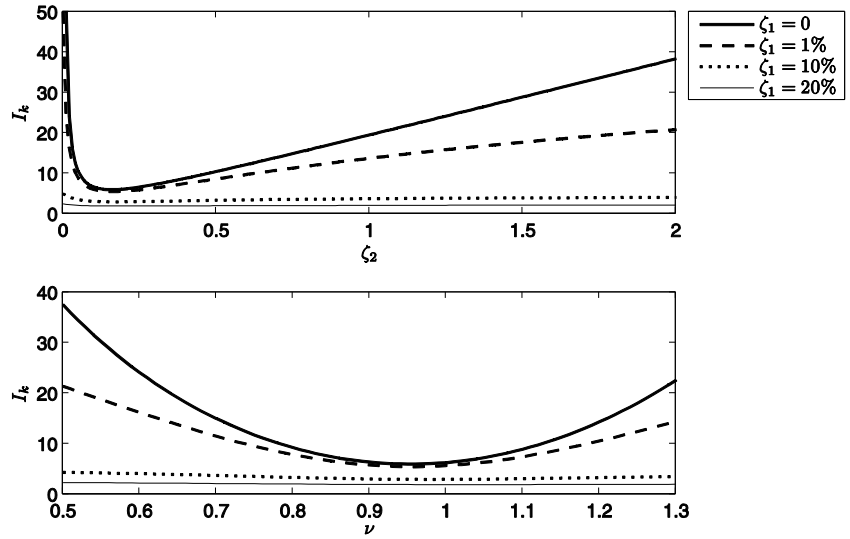

Figure 7.8: I_k as function of ζ_2 when $\nu = \nu_{opt}$ (top plot) and I_k as function of ν when $\zeta_2 = \zeta_{2opt}$ (bottom plot) for $\mu = 0.1$.

Figure 7.8 shows the performance index I_k as function of ζ_2 when ν is equal ν_{opt} (top plot) and I_k as function of ν when ζ_2 is equal ζ_{2opt} (bottom plot) for different values of the primary damping ration ζ_1. The plot shows that I_k is minimised for a single value of ζ_2 and ν. As ζ_1 is increased the gradient of I_k around the minimum decreases.

Figure 7.9(a) and (b) show the PSD of the velocity and displacement respectively of the primary mass in dimensionless form for five different strategies of tuning the DVA. In Figure 7.9(a) the area under the curve is minimised when the minimisation of kinetic energy is implemented. Figure 7.9(b) show that the H_∞ optimisation set the two peaks at the minimum magnitude and the area under the curve is minimised when the H_2 optimisation is implemented. The

minimisation stability optimisation is not designed to minimise the steady state response but only the transient response.

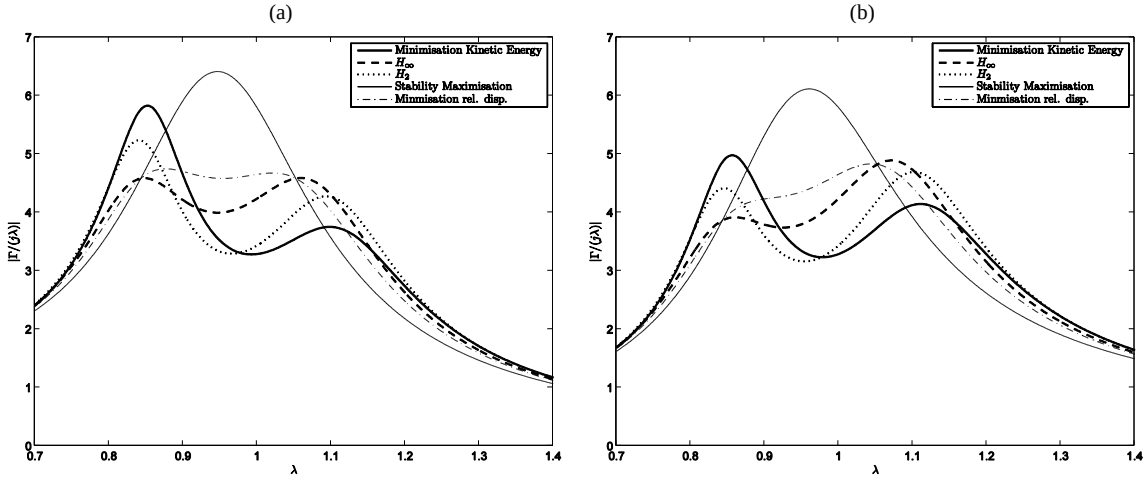

Figure 7.9: Optimal PSD a) of the dimensionless velocity and b) the displacement of the primary mass in dimensionless form when the four different criteria are implemented ($\zeta_1 = 0$, $\mu = 0.1$)

Figure 7.10 and Figure 7.11 show the optimal values of the frequency ratio and the damping ratio as function of the mass ratio for five different tuning strategies. The five tuning strategies give similar optimal values when μ is small. For grater values of μ the optimal conditions diverges. It is interesting to notice that for the minimisation of kinetic energy the optimal damping always increases for increasing values of μ. For all the other strategies the optimal damping ratio converges to a finite value.

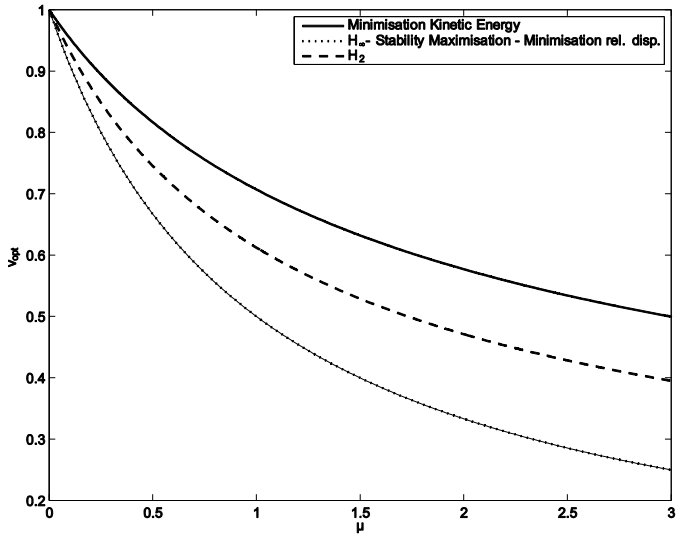

Figure 7.10: Optimal frequency ratio ν as function of the mass ratio μ for the 5 different tuning strategies

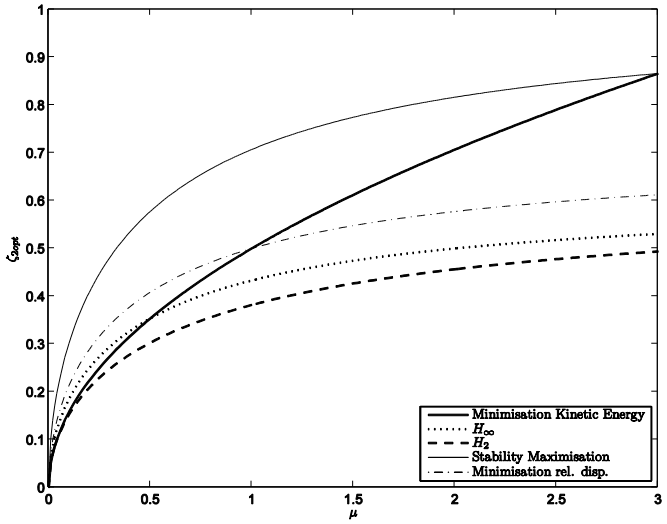

Figure 7.11: Optimal damping ratio ζ_2 as function of the mass ratio μ for the 5 different tuning strategies

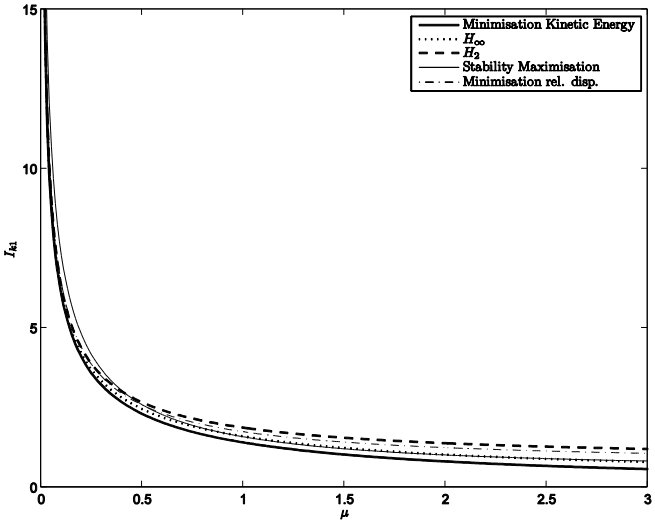

Figure 7.12: Performance index I_k as function of the mass ratio μ for the 5 different tuning strategies

Figure 7.12 shows the performance index I_k as function of the mass ratio μ when the optimal values for the different strategies are implemented. The curves in Figure 7.12 are obtained substituting the optimal value in Table 7.1 in equation (7.13). The plot shows that the lowest curve is the one obtained when the DVA is set to minimise the kinetic energy of the primary mass as one would expect.

7.6. Effect of damping in the host structures

It has not been possible to solve equations (7.23a) and (7.24a) when $\zeta_1 \neq 0$ in order to find analytical expression for $\zeta_{2\mathrm{opt}}$ and ν_{opt}.

In this case only an approximate solution of the location of the minimum of the total kinetic energy and thus the maximum of the total absorbed power can be found using the perturbation method. First of all it is assumed that the primary damping ζ_1 is so small that it is regarded as a

perturbation. To emphasize that ζ_1 is small a new symbol ε instead of the parameter ζ_1 is introduced:

$$\zeta_1 = \varepsilon \tag{7.27}$$

Next, the solutions of equation (7.23a) and (7.24a) (which it has been shown to be the same if $\zeta_1 \neq 0$) are assumed in the form of a power series of ε:

$$\begin{aligned} \nu &= \nu_0 + \varepsilon\nu_1 + \varepsilon\nu_2^2 + I \\ \zeta &= \zeta_{20} + \varepsilon\zeta_{21} + \varepsilon\zeta_{22}^2 + I \end{aligned} \tag{7.28}$$

Finally, equations (7.28) is substituted into equations (7.23), and collect terms of like powers of ε and equate them to zero (starting with the constant terms, the terms containing ε, the terms containing ε^2, and so on) so that the equation is satisfied for all values of ε. As a result, we have a series of equations from which we can determinate the unknown coefficients in equation (7.28) successively. The zero-order approximation leads to the result where υ_0 and ζ_{20} are the optimal values found in equations (7.26) when $\zeta_1 = 0$. Equating first order terms to zero, yields to:

$$\begin{aligned} a_1\zeta_{21} + a_2\nu_1 + a_3 &= 0 \\ b_1\zeta_{21} + b_2\nu_1 + b_3 &= 0 \end{aligned} \tag{7.29}$$

where

$a_1 = 2 + 2\mu$	$b_1 = 2\sqrt{\mu(1+\mu)}$
$a_2 = \sqrt{\mu(1+\mu)} + \mu^{3/2}\sqrt{1+\mu}$	$b_2 = 4 + 5\mu + \mu^2$
$a_3 = -2\mu\sqrt{1+\mu}$	$b_3 = -2\sqrt{\mu} - 2\mu^{3/2}$

In equations (7.29) the values of ν_0 and ζ_{20} have been already substituted. The solution of equitation (7.29) is given by:

$$\begin{aligned} \nu_1 &= \frac{\sqrt{\mu}}{2 + 2\mu} \\ \zeta_{21} &= \frac{3\mu}{4\sqrt{1+\mu}} \end{aligned} \tag{7.30}$$

The first order approximate solution of equations (7.23) and (7.24) is therefore given by:

$$\upsilon'_{\text{opt}} = \frac{1}{\sqrt{1+\mu}} + \zeta_1 \frac{\sqrt{\mu}}{2+2\mu}$$
$$\zeta'_{2\text{opt}} = \frac{\sqrt{\mu}}{2} + \zeta_1 \frac{3\mu}{4\sqrt{1+\mu}} \tag{7.31}$$

Figure 7.13(a) and (b) show the performance indexes I_k and I_{p2} as function of the damping ratio ζ_2 and the frequency ratio ν respectively when $\zeta_1 = 0.2$ and $\mu = 0.1$. Figure 7.13 shows that I_k has a global minimum which corresponds to the global maximum of I_{p2} represented by ○. The symbol × in Figure 7.13(a) and (b) mark the position of the optimum conditions when $\zeta_1 = 0$ while □ mark the first order approximate optimum given by equation (7.31).

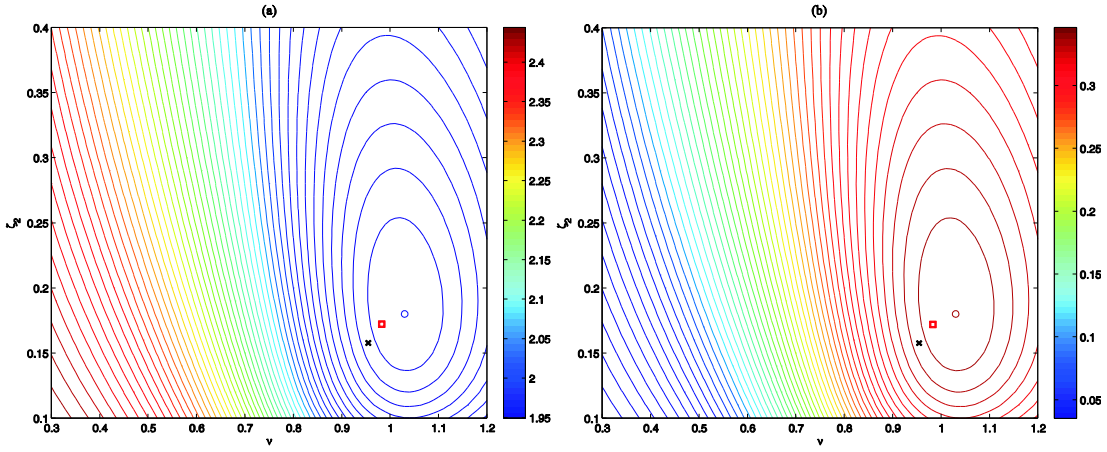

Figure 7.13: a) I_k and b) I_{p2} when $\zeta_1 = 0.2$ and $\mu = 0.1$. The solutions given by equations (7.26) are shown as ×, the approximate solutions given in equation (7.31) are shown as □, and the true minimum and maximum are shown as ○

7.7. Summary and conclusions

This chapter has discussed the use of a DVA for broadband control of a single degree of freedom system. It has been shown that even if the damping of the host structure is not very light, the ratio of natural frequencies and absorbed damping ratio that maximise the power dissipation in the damper are the same as those that minimise the kinetic energy of the host structure. If the power dissipation in the damper could be measured and the disturbance was stationary, the DVA could be made self-tuneable. This might be important if the damping mechanism of the absorber was level dependant, if it incorporated an element of coulomb damping for example, when subject to different disturbances. One way of implementing a dynamic vibration absorber with a variable damping is by using a shunted electromagnetic inertial actuator. In next chapter a preliminary study of broadband vibration control using such a device will be discussed.

8. Self-tuning and power harvesting with electromagnetic actuators

In Chapter 6 self-tuning of a direct velocity feedback control to reduce the response of a lightly damped structure, has been discussed. However, the implementation of the velocity feedback and the self-tuning requires energy. In this chapter the possibility is considered of using an electromagnetic transducer with an adaptable electrical load connected in series with the coil (this configuration is often called shunted electromagnetic transducer) that acts both as a passive damper and also as a source of electrical energy to drive the self-tuning circuit which makes the system energetically self-sufficient. In the first part of this chapter simulation results on reactive shunted actuators are presented then the case of an inertial shunted transducers is considered.

8.1. Regenerative system for vibration control

A regenerative vibration control system is defined as one that can extract and store vibrational energy from the system and use this energy to do useful work [65]. A necessary condition for a regenerative system to be passive is to absorb more energy than it is ever delivered to the system, so that the average over time absorbed power is positive. In the case of a shunted transducer the useful work can provide damping, and thus the system could also be termed semi-active. The use of shunted inertial actuators for vibration control was investigated in references [9] and [10] making the shunt adaptive, but in both of these papers the aim was to control a single mode with a largely reactive shunt impedance rather than to optimally add damping. It was shown in reference [66] that the power harvested by a shunted inertial actuator attached to a beam is maximised for a single value of the resistive shunt impedance when the beam is excited at its first natural frequency. In this chapter, shunted electromechanical actuators are considered for the control of vibration on different lightly damped structures when excited by a broadband disturbance. The power harvested by the control system could be used to drive a self-tuning circuit, which is designed to automatically adjust the shunt to minimise the vibration of the structure. The total kinetic energy of the structure averaged over the frequency is taken as the benchmark to evaluate two other self-tuning strategies: the maximisation of the total mechanical power absorbed by the control system and maximisation of the electrical power harvested by shunt. Two types of actuators are considered: shaker and inertial actuator. The first one produces a force reacting off a rigid structure while the second reacts off a moving mass. In the last part of this chapter the use of shunted inertial actuator as dynamic vibration absorbed to control the vibration of single degree of freedom system is considered.

8.2. Mathematical model for a shunted electromagnetic actuator

The behaviour of a shunted electromagnetic actuator can be described using the two port model derived in the Chapter 6. In the case of a shunted electromagnetic transducer the voltage u across the external load can be written as:

$$\tilde{u} = -\tilde{\mathrm{Z}}_{\mathrm{L}}\tilde{\imath}. \tag{8.1}$$

where $\tilde{\mathrm{Z}}_{\mathrm{L}}$ is the electrical impedance of the shunt. Substituting equation (8.1) in (6.1) and (6.2) the current $\tilde{\imath}$ and the force $\tilde{f}$ are given by:

$$\tilde{\imath} = \frac{-\tilde{T}_1}{\tilde{Z}_{\mathrm{eb}} + \tilde{Z}_{\mathrm{L}}}\tilde{v}, \tag{8.2}$$

$$\tilde{f} = \left(\tilde{Z}_{\mathrm{mo}} - \frac{-\tilde{T}_1\tilde{T}_2}{\tilde{Z}_{\mathrm{eb}} + \tilde{Z}_{\mathrm{L}}}\right)\tilde{v} \tag{8.3}$$

so that the total mechanical impedance of the transducer can be derived from equation (8.3) as:

$$\frac{\tilde{f}}{\tilde{v}} = \tilde{Z}_{\mathrm{m}} = \tilde{Z}_{\mathrm{mo}} - \frac{\tilde{T}_1\tilde{T}_2}{\tilde{Z}_{\mathrm{eb}} + \tilde{Z}_{\mathrm{L}}}. \tag{8.4}$$

Substituting equations (6.3) in (8.3) the velocity $\tilde{v}$ can be written as:

$$\tilde{v} = \frac{\tilde{\mathrm{Z}}_{\mathrm{eb}} + \tilde{\mathrm{Z}}_{\mathrm{L}}}{-\tilde{T}_1\tilde{T}_2 + \left(\tilde{Z}_{\mathrm{eb}} + \tilde{Z}_{\mathrm{L}}\right)\left(\tilde{\mathrm{Z}}_{\mathrm{mb}} + \tilde{\mathrm{Z}}_{\mathrm{mo}}\right)}\tilde{f}_{\mathrm{b}}. \tag{8.5}$$

Substituting equation (8.5) in (8.2), the current $\tilde{\imath}$ is given by:

$$\tilde{\imath} = \frac{\tilde{T}_1}{\tilde{T}_1\tilde{T}_2 - \left(\tilde{Z}_{\mathrm{eb}} + \tilde{Z}_{\mathrm{L}}\right)\left(\tilde{\mathrm{Z}}_{\mathrm{mb}} + \tilde{\mathrm{Z}}_{\mathrm{mo}}\right)}\tilde{f}_{\mathrm{b}}. \tag{8.6}$$

The force $\tilde{f}$ can be obtained by substituting equation (8.5) in (8.3) giving:

$$\tilde{f} = \frac{-\tilde{T}_1\tilde{T}_2 + \left(\tilde{Z}_{\mathrm{eb}} + \tilde{Z}_{\mathrm{L}}\right)\tilde{Z}_{\mathrm{mo}}}{-\tilde{T}_1\tilde{T}_2 + \left(\tilde{Z}_{\mathrm{eb}} + \tilde{Z}_{\mathrm{L}}\right)\left(\tilde{\mathrm{Z}}_{\mathrm{mb}} + \tilde{\mathrm{Z}}_{\mathrm{mo}}\right)}\tilde{f}_{\mathrm{b}}. \tag{8.7}$$

Substituting equations (8.5) and (8.7) in (6.12) the mechanical power absorbed can be written as:

$$S_{\mathrm{P}}(\omega) = \frac{Re\{\tilde{Z}_{\mathrm{m}}\}}{2\left|-\tilde{T}_1\tilde{T}_2 + \left(\tilde{Z}_{\mathrm{eb}} + \tilde{Z}_{\mathrm{L}}\right)\left(\tilde{\mathrm{Z}}_{\mathrm{mb}} + \tilde{\mathrm{Z}}_{\mathrm{mo}}\right)\right|^2}\left|\tilde{f}_{\mathrm{b}}\right|^2, \tag{8.8}$$

The electrical power dissipated in the electrical impedance $\tilde{Z}_{\mathrm{L}}$, which is also the power that can be potentially harvested, is given by:

$$S_{\mathrm{H}}(\omega) = \frac{1}{2}Re\{\tilde{u}\tilde{\imath}^*\} = \frac{|\tilde{\imath}|^2}{2}Re\{\tilde{Z}_L\}. \tag{8.9}$$

Substituting equation (8.6) in (8.9) yields:

$$S_{\mathrm{H}}(\omega) = \frac{\left|\tilde{T}_1\right|^2 Re\{\tilde{Z}_L\}}{2\left|-\tilde{T}_1\tilde{T}_2 + \left(\tilde{Z}_{\mathrm{eb}} + \tilde{Z}_{\mathrm{L}}\right)\left(\tilde{\mathrm{Z}}_{\mathrm{mb}} + \tilde{\mathrm{Z}}_{\mathrm{mo}}\right)\right|^2}\left|\tilde{f}_{\mathrm{b}}\right|^2. \tag{8.10}$$

8.3. Broadband vibration control using a shunted shaker

In this section the use of a shunted shaker for broadband control of lightly damped structures is investigated. The effect of the shaker on a vibrating structure can be described using the two port model derived in the previous section. Assuming that a shaker is modelled as a single degree of freedom system and is reacting off a rigid structure, the open loop mechanical impedance $\tilde{\mathrm{Z}}_{\mathrm{mo}}$, the blocked electrical impedance $\tilde{Z}_{\mathrm{eb}}$ and the transduction coefficient $\tilde{T}_1$ and $\tilde{T}_2$ can be calculated as:

$$\tilde{Z}_{\mathrm{mo}} = j\omega M_s + \frac{K_s}{j\omega} + C_s\,, \tag{8.11}$$

$$\tilde{Z}_{\mathrm{eb}} = R + j\omega L\,, \tag{8.12}$$

$$T_1 = -T_2 = Bl. \tag{8.13}$$

where M_{s}, K_{s} and C_{s} are the moving mass, the suspension's stiffness and the mechanical damping of the shaker, R and L are the resistance and the inductance of the coil, B is the manganic flux of the permanent magnet and l is the length of the coil. Substituting equations (8.11), (8.12) and (8.13) in equation (8.4), the mechanical impedance of the shunted shaker becomes:

$$\frac{\tilde{f}}{\tilde{v}} = \tilde{Z}_{\mathrm{m}} = j\omega M_s + \frac{K_s}{j\omega} + C_s + \frac{(Bl)^2}{R + Z_{\mathrm{L}}}. \tag{8.14}$$

Two commercial devices have been selected and simulations have been carried out to predict their mechanical impedance. The first is a V201 shaker made by LDS which has a conventional suspension; the second is a coil and magnate device in which the coil is free to move in the magnet. The main parameters of the two shakers are listed in Table 8.1.

Table 8.1: Main parameters of two different reactive actuators

	LDS V201	**H2W Technologies HCC10-15-023-1X**
Open circuit mechanical damping	1.85	~0
Close circuit mechanical damping	17.33	13.87
Open circuit damping ratio	8%	0%
Close circuit damping ratio	8.37	
Suspension's stiffness (N/m)	6650	0
Moving mass (Kg)	0.020	0.056 (coil)
Bl (N/A)	5.13	10.2
Electrical resistance (Ω)	1.7	7.5

Figure 8.1 shows the simulated mechanical impedance of the two shunted shakers. The arrows in the plots indicate increasing values of the resistive load in the shunt.

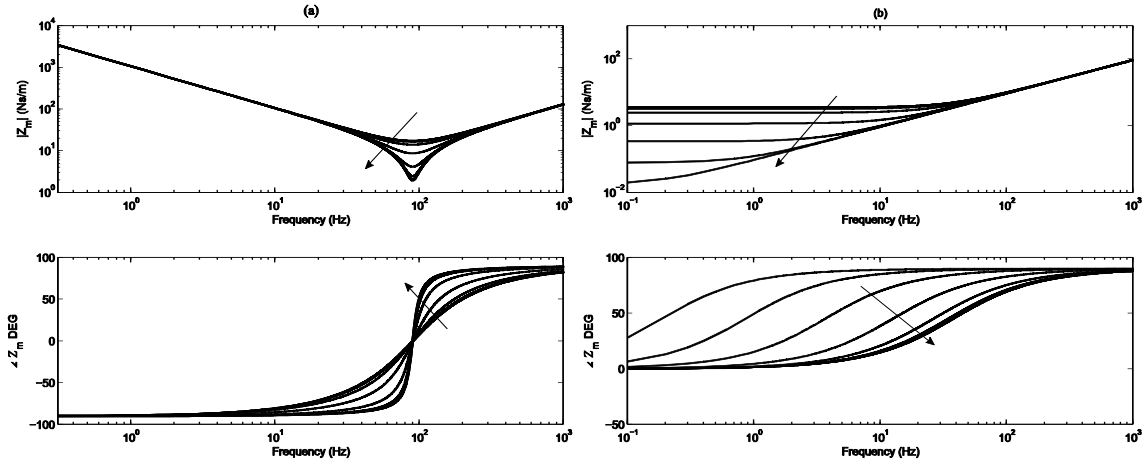

Figure 8.1: Mechanical impedances of (a) LDS V201, and (b) the H2W Technologies shaker

Figure 8.1(a) shows the mechanical impedance of the LDS shaker. In the plot different frequency regions can be observed. A low frequency region, where the impedance is stiffness controlled and total impedance $\tilde{Z}_{\mathrm{m}}$can be approximated as $K_{\mathrm{s}}/(j\omega)$; A frequency region around

the natural frequency of the shaker where the total impedance $\tilde{Z}_{\mathrm{m}}$ is damping controlled and can be approximated as:

$$C' = C_s + \frac{(Bl)^2}{R + R_{\mathrm{L}}} \tag{8.15}$$

where R_{L} is the resistive load. A high frequency region where the impedance is mass control and the total impedance $\tilde{Z}_{\mathrm{m}}$ can be approximated as $j\omega M_s$.

The maximum damping produced by the shunted shaker is reached when R_{L} is equal zero and therefore depends on the value of the transduction coefficient *Bl* and the internal electrical resistance of the coil. Approximating the impedance of the shaker by $K_s/(j\omega)$ at low frequency and by $j\omega M_{\mathrm{s}}$ at high frequency, the region where the shaker behaves approximately like a damper is given by the difference between the frequencies at which $|K_s/(j\omega)|$ is equal C' and at which $|j\omega M_s|$ is equal to C':

$$\frac{K_s}{C'} < \omega_{\mathrm{n}} < \frac{C'}{M_{\mathrm{s}}} \tag{8.16}$$

which, for the LDS shaker, is from about 60 Hz to 132 Hz when R_{L} is equal zero.

Figure 8.1(b) shows the mechanical impedance of the H2W shunted actuator for different values of the resistive load R_{L}. This shaker is not equipped with a suspension so its mechanical impedance is not stiffness control at low frequency. At high frequency the mechanical impedance of the H2W shunted shaker is mass controlled and is independent on the value of the resistive load. At low frequency the force generated by the shaker is proportional to the value of the shunt and increases as the resistive load decreases. Using equation (8.16) the frequency region where the shaker is capable to produce damping on the structure to which it is attached is from 0 Hz up to 39 Hz when R_{L} is equal zero.

8.3.1. Control of a beam using a shunted shaker

In this subsection simulation results are presented of an aluminium simply supported beam excited by broadband white noise point force and controlled by a H2W shunted shaker. A scheme of the beam with the shaker is shown in Figure 8.2 where f_{p} is the primary excitation. Table 8.2 summarises the physical and geometrical parameters of the simply supported beam. The dimensions of the beam have been chosen such that the first two structural resonances are well below 39 Hz where the shunted shaker behaves like a damper.

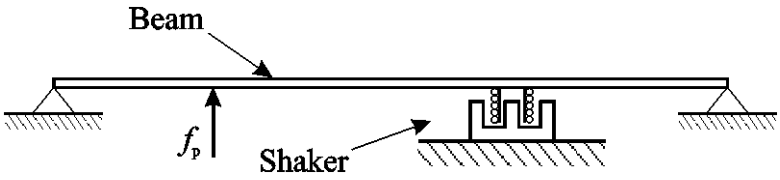

Figure 8.2: Simply supported beam excited by the primary force f_p and controlled by a shaker

Assuming the coil is attached to the structure and this has mass M_s, the mechanical impedance of the shunted shaker in this case is:

$$\tilde{Z}_{\mathrm{m}} = j\omega M_s + C_s + \frac{(Bl)^2}{R + R_{\mathrm{L}}}. \tag{8.17}$$

Table 8.2: Geometrical and physical parameters of the beam.

Value	**Parameter**
Dimensions	l =1 m
Thickness	h=0.001 m
Width	d=0.03 m
Mass density	ρ=2700 kg/m^3
Young's modulus	E=7×10^{10} N/m^2
Poisson ratio	ν_1=0.33
Loss Factor	η=0.01
Primary source position	0.4×l
Secondary source position	0.7×l

Figure 8.3 shows the PSD of the kinetic energy of the beam for different value of the resistive load impedance R_{L}. The faint line in the plot shows the PSD of the kinetic energy of the beam before the actuator is attached to the structure. For very high values of the resistive load R_{L} (solid line), only little damping is added but the resonances of the beam are shifted down in frequency compared with the beam without the actuator attached due to the added mass of the coil.

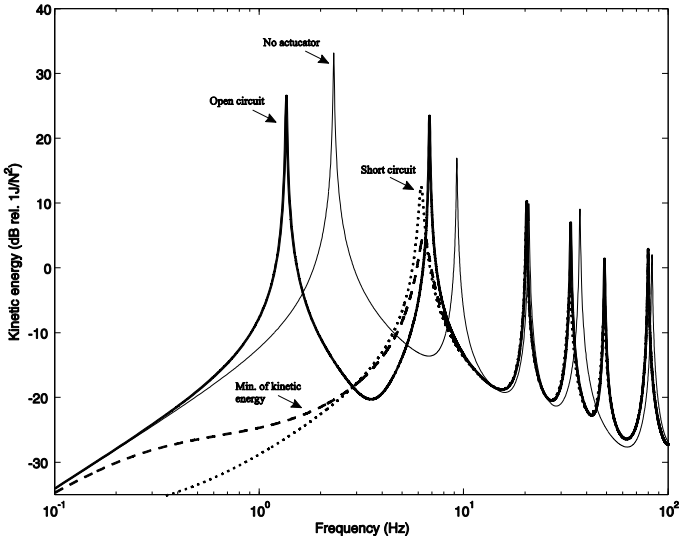

Figure 8.3: PSD of the kinetic energy of the beam without actuator (faint line), when the actuator is attached but open circuit (solid line), minimising the total kinetic energy (dashed line) and for the actuator short circuit (dotted line).

When R_L is decreased from a very high value, the effect of the shaker is to damp the first two resonances of the beam (dashed line). At higher frequency the value of the shunt does not influence the response of the beam. When R_L is equal zero, so the actuator is short circuit, the effect of the shaker begins to pin the beam at the position where it is attached so that the kinetic energy of the beam increases in the frequency region around the second resonance (dotted line).

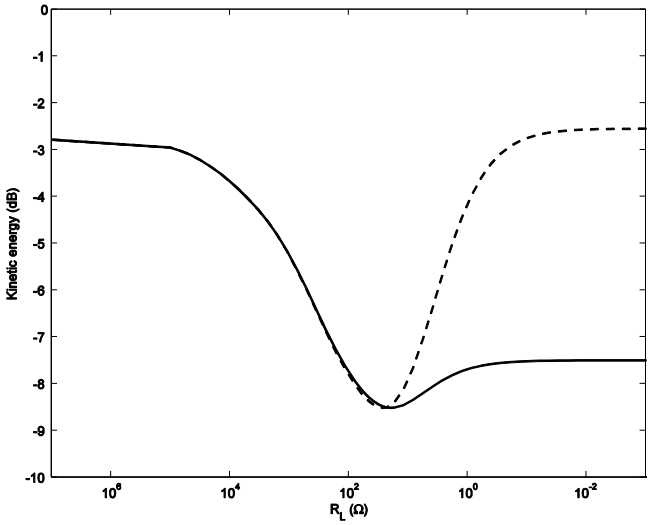

Figure 8.4: Total kinetic energy of the beam averaged over 0-800 Hz, normalised to that before the actuator is attached as function of decreasing value of R_L (solid line) and when the internal resistance of the actuator is set to zero (dashed line).

Figure 8.4 shows the total kinetic energy of the beam averaged over a frequency band between 0-800 Hz as function of decreasing value of the resistive load R_L. The total kinetic energy is normalised by the total kinetic energy of the beam before the shaker is attached, thus, about -3 dB of global reduction are due to the mass of the shaker. The graph shows that the effect of the shunted shaker is to reduce the total response of the beam as the load R_L is decreased until it reaches an optimum value for R_L of about 20 Ω. For lower values of R_L the effect of the shaker is to constrain the motion of the beam at control position and approximate a pinned boundary condition so that the total response increases again. The dashed line in Figure 8.4 shows the total kinetic energy of the beam in the ideal case of internal resistance of the actuator equal zero. From equation (8.17) it can be seen that in the case R and R_L are both equal zero, the mechanical impedance of the actuator tends to infinity. This means that the controller is able to pin the structure at control position behaving like an ideal skyhook damper.

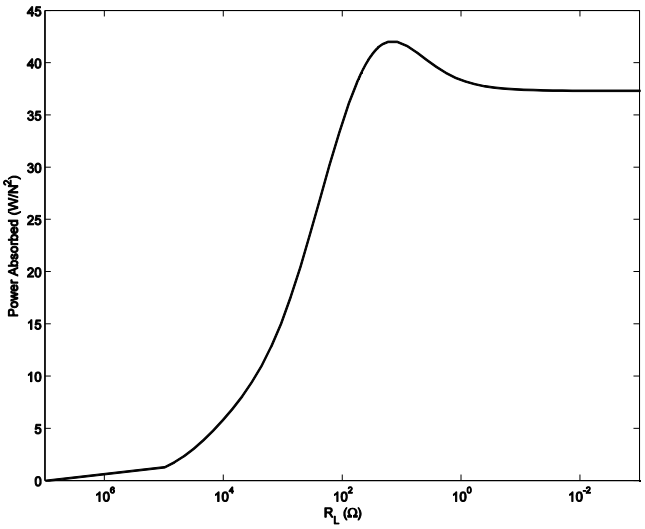

Figure 8.5: total absorbed power averaged over 1-800 Hz as function of the decreasing value of the resistive load R_L

Figure 8.5 shows the mechanical power absorbed by the shaker averaged between 0-800 Hz as function of R_L. The plot shows that for very high values of R_L the absorbed power goes to zero. When R_L is decreased the absorbed power increases until it reaches a maximum when R_L is about 12 Ω. The maximum of absorbed power roughly corresponds to the minimum of kinetic energy so that maximising the absorbed power almost minimises the overall vibration of the structure. When R_L is further decreases the power absorbed by the shunted shaker decreases. The absorbed power could be estimated by measuring the velocity and estimating the control force using equation (8.3). If the adaptation of the electrical load is made automatically the system could adapt itself to the optimum. The self-tuning could thus be accomplished with a single accelerometer. In principle, the velocity could also be deduced from the voltage and current in the coil, if a sufficiently accurate model of the transducer was available.

Figure 8.6 shows the power dissipated by the shunt transducer, which is also the power that could be potentially harvested as function of the electrical load R_L. As one would expect the harvested power by the shunt is zero when R_L is zero and is again zero for high value of R_L, which means the circuit is open. However, the plot shows that the harvested power is maximised by a single value of the electric load and the maximum roughly corresponds to the minimum of kinetic energy.

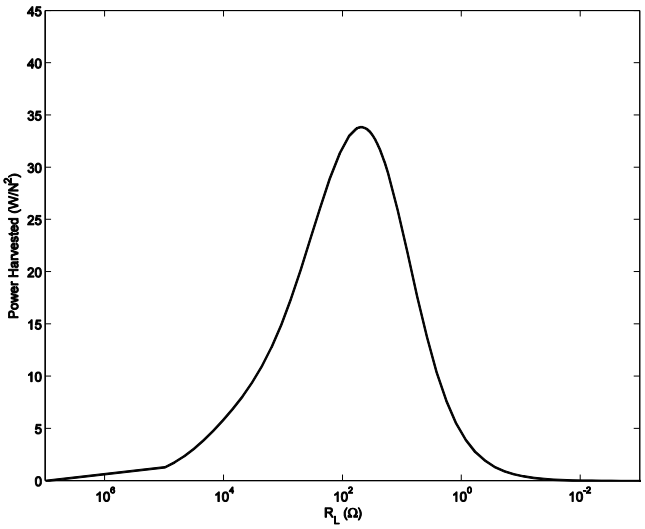

Figure 8.6: total harvested power averaged over 1-800 Hz as function of the decreasing value of the resistive load R_L

This suggests that instead of using the mechanical power absorbed by the transducer as the cost function to be maximised in the self-tuning adaptation, the harvested electrical power could be used instead. The harvested electrical power is proportional to the mean square voltage across the coil divided by the resistance of the electrical load R_L and is thus very simple to estimate. The power absorbed by the shunt could also potentially be used to power the circuit used for the self-tuning system, so that no external power would be required. Table 8.3 shows a comparison between the minimisation of the total kinetic energy of the panel and the other two self-tuning strategies. Although the optimal values of R_L are different for the three strategies, the global reduction in terms of kinetic energy of the beam is only 0.1 dB less for the maximisation of the mechanical power absorption and 0.3 dB for the maximisation of the harvested power.

Table 8.3: comparison between maximisation of kinetic energy, maximisation the total absorbed and harvested power

	R_L (Ω)	Attenuation in kinetic energy (dB)	Absorbed power (W/N^2)	Harvested power (W/N^2)
Minimisation of kinetic energy	20	-8.5	41.9	30.5
Maximisation of absorbed mechanical power	12	-8.4	42.0	25.9
Maximisation of harvested electrical power	49	-8.2	39.0	33.8

The simulation results shown so far assume that the structure under control has the first two natural frequencies well below the upper frequency of damping control in Figure 8.1, of 39 Hz (i.e. $\omega_1 = 1$ Hz and $\omega_2 = 7$ Hz after the shaker has been attached in this case) which implies a very long and thin beam. The response of such a structure may be difficult to measure because of the very low natural frequencies.

8.4. Vibration control using a shunted inertial actuator

The use of a shunted shaker for vibration control assumes the presence of a rigid structure where the actuator can react off. In this section, the more practical case of a shunted inertial actuator for vibration control is considered. The actuator produces a force on the structure by reacting off a moving mass. The dynamic behaviour of the actuator thus limits the frequency band where it behaves like a damper when is shunted with a pure resistive load. The first part of this section discusses the possibility of using a shunted actuator to optimally control the broadband vibration of lightly damped structures. In this case it is necessary that the first resonance of the structure is in the frequency region where the actuator behaves like a damper. In the second part the possibility of using a shunted inertial actuator as vibration absorber is investigated.

8.4.1. Broadband vibration control using a shunted inertial actuator

The two port network model derived in Chapter 6 is used here to describe the behaviour of the shunted inertial actuator. All the impedances relative to an inertial actuator are derived in Appendix E. The characteristics of the actuator used to carry out the simulations are listed in Table 8.4. The natural frequency of the actuator is 10 Hz, but the transduction coefficient *Bl* is assumed to be somewhat greater than that of the commercial actuators considered below in order to emphasis the effect of the shunt. The base mass of the actuator is considered to be negligible. This ideal case is considered in order to get a better understanding of the behaviour of a shunted electromagnetic inertial actuator for broadband control of lightly damped structures.

Table 8.4: Assumed parameters of an idealised inertial actuator

Electrical resistance (Ω) R	3
Mechanical stiffness (N/m) K_a	2000
Open circuit mechanical damping (N/ms^{-1}) C_a	1.26
Closed circuit mechanical damping (N/ms^{-1}) C'	534
Open Circuit damping ratio ζ_o	0.02
Close circuit damping ratio ζ_a	8.5
Vibrating mass (Kg) M_a	0.5
Base mass (Kg) M_w	0
Electromagnetic transducer constant (N/A) Bl	40
Natural frequency (Hz) ω_a	10

Figure 8.7 shows the simulated open circuit mechanical impedance, $\tilde{Z}_{\mathrm{mo}}$. The plot shows that $\tilde{Z}_{\mathrm{mo}}$ presents a resonance due to the natural frequency of the actuator at 10 Hz and is equal to the mechanical damping of the actuator c at high frequency.

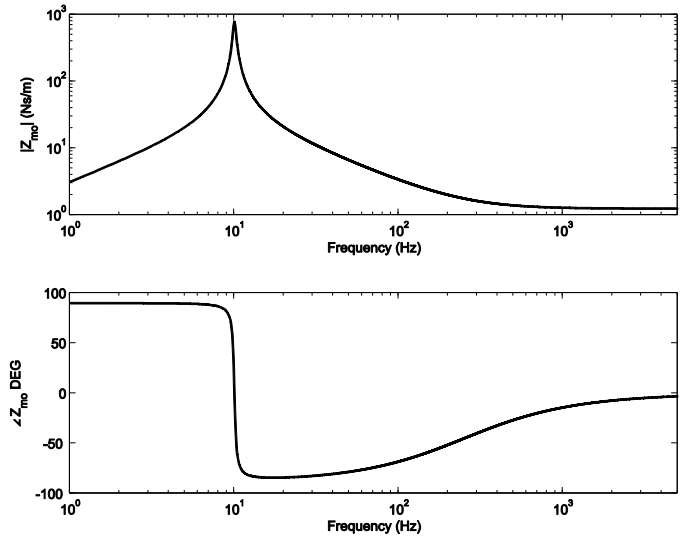

Figure 8.7: open circuit mechanical impedance $\tilde{Z}_{mo}$ of the idealised inertial actuator

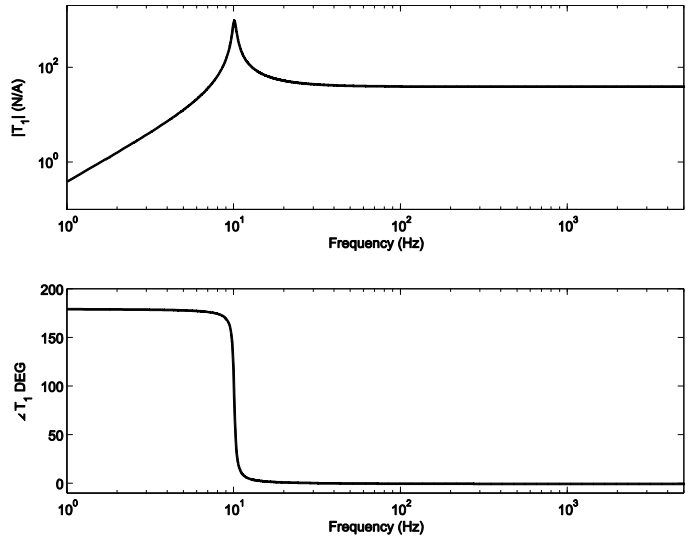

Figure 8.8: transduction frequency response function $\tilde{T}_1$.

Figure 8.8 shows the transduction coefficient $\tilde{T}_1$ which now has a non-trivial frequency response as derived in Appendix E. The graph again shows a resonance at 10 Hz with a phase shift of 180°. At higher frequency the phase goes to zero and $\tilde{T}_1$ is real and equal to *Bl*. Figure 8.9 shows the blocked electrical impedance, $\tilde{Z}_{\mathrm{eb}}$ of the actuator. The graph shows a peak at 10 Hz and from about 400 Hz $\tilde{Z}_{\mathrm{eb}}$ is equal to the electrical resistance of the coil.

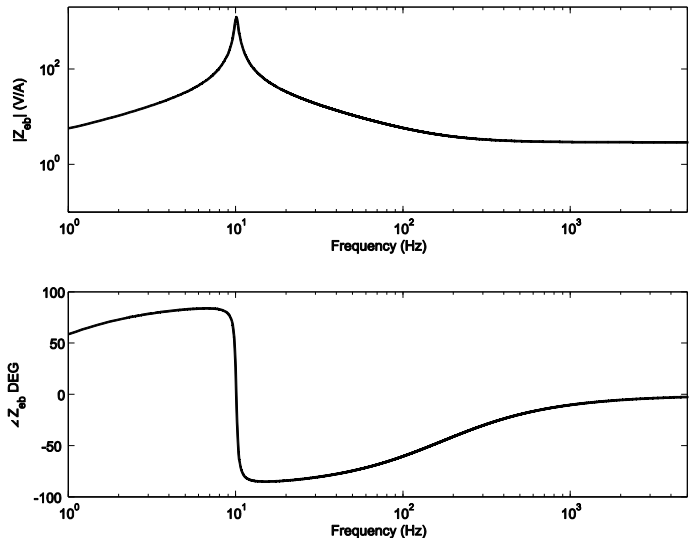

Figure 8.9: blocked electrical impedance $\tilde{Z}_{eb}$ of the idealised inertial actuator

Substituting the expressions of the $\tilde{Z}_{\mathrm{mo}}$, $\tilde{T}_1$, $\tilde{T}_2$ and $\tilde{Z}_{\mathrm{eb}}$ for an inertial actuator given in Appendix E in equation (8.4) and after some algebraic manipulations, the total mechanical impedance $\tilde{Z}_{\mathrm{m}}$, presented by the shunted transducer can be expressed as:

$$\tilde{Z}_{\mathrm{m}} = \frac{j\omega M_{\mathrm{a}}(K_{\mathrm{a}} + j\omega C')}{K_{\mathrm{a}} + j\omega C' - \omega^2 M_{\mathrm{a}}}, \tag{8.18}$$

where $C' = C_\mathrm{a} + (Bl)^2/(R + R_L)$ is the close circuit mechanical damping assuming the shunt Z_L is resistive, R_L. Equation (8.18) is of the same form of the open loop mechanical impedance of the actuator (equation (E.4)) but with a modified damping constant that depends on the transduction coefficient *Bl* and the total electrical resistance (internal electrical resistance of the coil plus the electrical resistive load). The damping ratio of the shunted actuator is given by:

$$\zeta_\mathrm{a} = \frac{C'}{2\sqrt{K_\mathrm{a} M_\mathrm{a}}}, \tag{8.19}$$

Figure 8.10(a) shows the total mechanical impedance of the actuator $\tilde{Z}_\mathrm{m}$, when $R_\mathrm{L} = 0.5$ kΩ, so that the closed loop damping ratio of the actuator ζ_a is about 0.07.

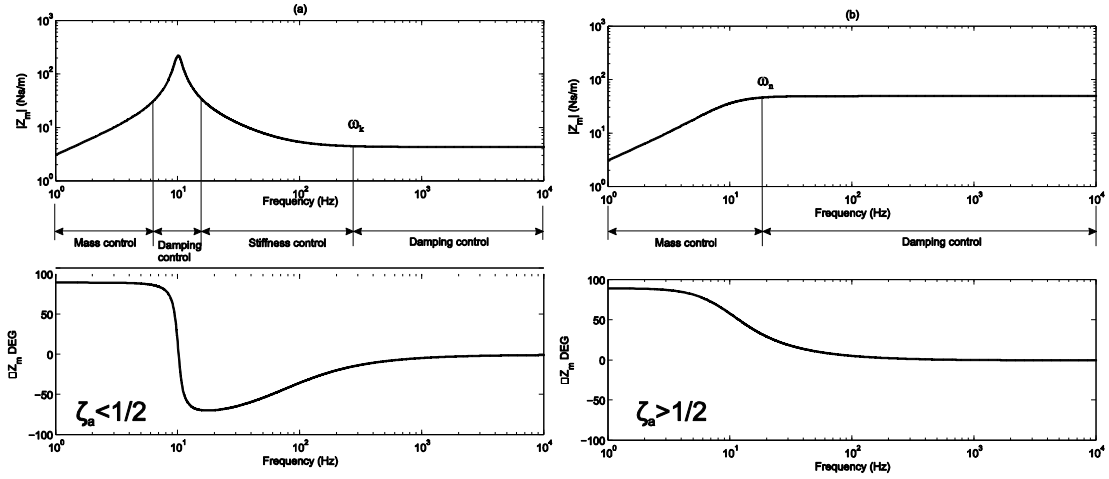

Figure 8.10: a) total mechanical impedance $\tilde{Z}_m$ of the idealised inertial actuator for $\zeta_\mathrm{a} < 1/2$ and for b) $\zeta_\mathrm{a} > 1/2$.

In Figure 8.10(a) four different frequency regions can be observed. A low frequency region, where the impedance is mass controlled and total impedance $\tilde{Z}_\mathrm{m}$ can be approximated as $j\omega M_\mathrm{a}$; A frequency region around the natural frequency of the actuator ω_a, where the total impedance $\tilde{Z}_\mathrm{m}$ is damping controlled so that $\tilde{Z}_\mathrm{m}$ can be approximated as $M_\mathrm{a} k/c'$; a frequency region between ω_a and ω_k, where the impedance is stiffness control and the total impedance $\tilde{Z}_\mathrm{m}$ can be approximated as $K_\mathrm{a}/(j\omega)$ and finally a high frequency region where the total impedance $\tilde{Z}_\mathrm{m}$ can be approximated as C'. This occurs when ω is greater than ω_k, which is the cut-off frequency above which the actuator behaves like a damper and is equal to:

$$\omega_k = \frac{k}{c'} = \frac{\omega_\mathrm{a}}{2\zeta_\mathrm{a}}. \tag{8.20}$$

If $\zeta_a = 1/2$, this cut-off frequency corresponds to the natural frequency of the actuator and becomes smaller than ω_a if $\zeta_a > 1/2$. Figure 8.10(b) shows the total mechanical impedance $\tilde{Z}_m$ when $R_L = 30\ \text{k}\Omega$ so that $\zeta_a = 0.8$ and in this case only two different frequency regions are important. The plot shows that at low frequencies the impedance is mass controlled and can be approximate as $j\omega M_a$. At higher frequencies the actuator behaves like a damper with mechanical damping equal to C'. The transition between these two regions now happens at the new cut-off frequency ω_n given by:

$$\omega_n = \frac{c'}{M_a} \tag{8.21}$$

For completeness Figure 8.11 shows the total impedance of the actuator $\tilde{Z}_m$ for many different values of R_L. The electrical load R_L is varied from zero to 10^5 Ohm. The arrow in Figure 8.11 indicates increasing values of R_L. The graph shows that when R_L=0 the cut off-frequency beyond which the impedance is dominated by the damping, ω_n, is about 180 kHz. As the resistive load increases the cut off frequency ω_n decreases and becomes equal to the natural frequency of the actuator when $R_L = 50\ \Omega$, so that ζ_a=1/2. If R_L is further increased ω_n becomes smaller than natural frequency of the actuator and the cut-off frequency now becomes ω_k, beyond which the actuator again behaves like a damper. It should be noted that it has been assumed that the coil has no inductance, which would limit the value of $|\tilde{Z}_m|$ at high frequencies if R_L was small.

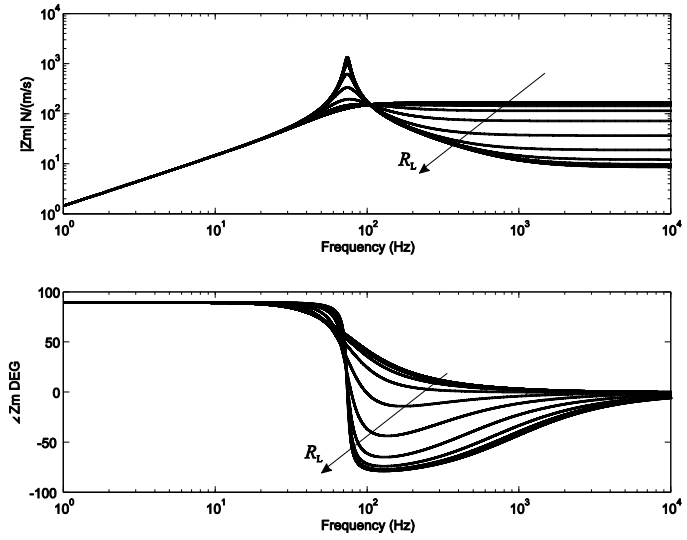

Figure 8.11: Total impedance $\tilde{Z}_m$ of the actuator varying R_L from 0 to $10^5\ \Omega$.

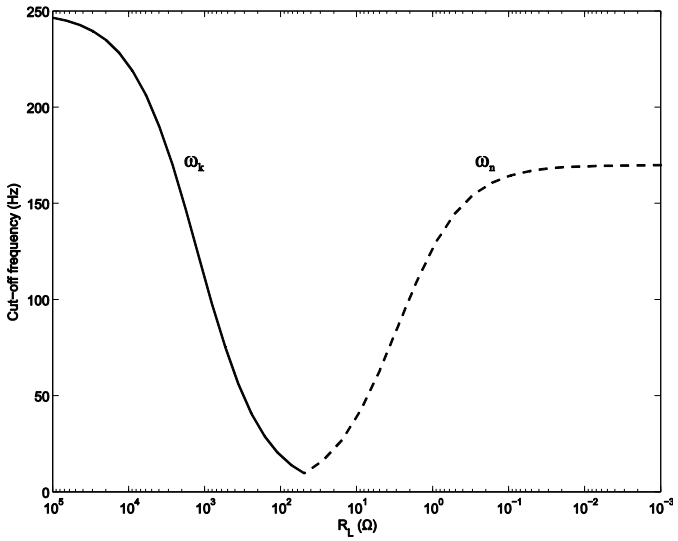

Figure 8.12: cut-off frequency of the idealised actuator as function of decreasing values of R_{L}

Figure 8.12 shows the cut-off frequency of the idealised actuator as function of decreasing values of R_{L}. The plot shows that for high values of the resistive load the cut-off frequency, ω_{k}, beyond which the actuator behaves like a damper, is around 250 Hz. As R_{L} is decreased the cut-off frequency decreases, and for R_{L} about 50 Ω the cut off frequency ω_{k} becomes equal to the natural frequency of the actuator. For lower values of the resistive load, ζ_{a} is greater than 1/2 and the cut-off frequency ω_{n} increases again.

In the frequency region where the total mechanical impedance of the actuator is real the control system behaves like a skyhook damper of damping constant given by:

$$\frac{\tilde{f}}{\tilde{u}} = C_{\mathrm{a}}\left(1 + \frac{(Bl)^2}{C_{\mathrm{a}}(R + R_{\mathrm{L}})}\right). \tag{8.22}$$

Equation (8.22) shows that the damping provided to the structure can vary from a minimum of C_{a}, the internal damping of the actuator if R_{L} is very high to $C_{\mathrm{a}} + (Bl)^2/(R\ )$ when R_{L} is zero. This means that the maximum damping achievable depends on the dimensionless parameter $(Bl)^2/(C_{\mathrm{a}}R)$ which suggests that the performance of the transducer increases for well coupled actuator with a strong magnet and low internal resistance, as also derived in the power harvesting analysis in reference [66]. The effect of various actuator design choices and this important non-dimensional parameter will now be briefly explained. The value of the magnetic flux *B* depends on the type of material used to build the permanent magnet. Materials with high magnetic saturation values, such as Ne-Fe-B, have to be chosen [67]. The resistance of the coil depends on its length and is therefore given by:

$$R = \rho_1 \frac{l}{Q}, \tag{8.23}$$

where ρ_1 is the resistivity of the coil's material and Q is the cross section of the wire. Substituting equation (8.23) into equation (8.22) in the case when $R_L = 0$ gives an expression of the maximum damping that can be produced by the actuator as:

$$C'_{\max} = C_a + \frac{B^2 l Q}{\rho_1}. \tag{8.24}$$

A scheme of the cross section of a permanent magnet with the coil is shown in Figure 8.13.

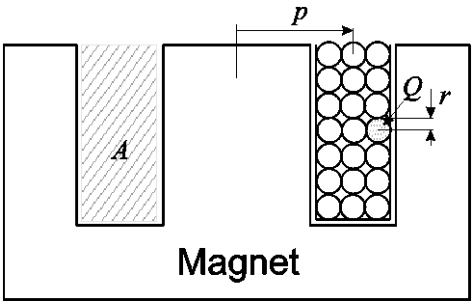

Figure 8.13: Scheme of the cross-section of permanent magnet and the coil

The length of the wire is given by:

$$l = 2\pi K \left(\sum_{i=0}^{\frac{(N-1)}{2}} p - id + \sum_{i=0}^{\frac{(N-1)}{2}} p + id \right), \text{ if N is odd} \tag{8.25}$$

$$l = 2\pi K \left(\sum_{i=0}^{\frac{N}{2}-1} p - \frac{d}{2} - id + \sum_{i=0}^{\frac{N}{2}-1} p + \frac{d}{2} + id \right), \text{ if N is even} \tag{8.26}$$

where N is the number of turns in the horizontal direction, K is the number of turns in the vertical direction, p is the average diameter of the coil and d is the diameter of the wire. Both equation (8.25) and (8.26) can be simplified leading to:

$$l = 2\pi p K N \tag{8.27}$$

The total number of turns can be written as:

$$NK = \frac{A}{Q}, \tag{8.28}$$

where it is assumed that the coil fills the entire area *A* inside the magnet. Substituting equation (8.28) in (8.27) and then in (8.24) the maximum mechanical damping generated by the shunted inertial actuator can be written as:

$$C'_{\max} = C_{\mathrm{a}} + \frac{B^2 2\pi A p}{\rho_1}, \tag{8.29}$$

Equation (8.29) shows that $C'_{\max}$ does not depend on the number of turns of the coil but only on the magnetic flux, the geometry of the permanent magnet and the resistivity of the wire. It is also interesting to estimate how the additional damping due to a shunted electromagnetic device scales with the size of the device. We can write equation (8.29) as:

$$\frac{C'_{\max}}{C_{\mathrm{a}}} = 1 + \frac{B^2 2\pi A p}{\rho_1 C_{\mathrm{a}}}, \tag{8.30}$$

where the second term is equal to the non-dimensional parameter $(Bl)^2/(C_{\mathrm{a}}R)$ defined above, which is equal to the additional electromagnetic damping divided by the mechanical damping of the device. The saturated flux density in the ferrous parts of the actuator limits the value of *B*, which is thus reasonably independent of scaling, as is the material resistivity, ρ_1. The way in which the mechanical damping scales depends to some extent on the detailed mechanism of damping, but can generally be assumed to scale as [L^2] [68] where scaling notation described by Madou (1997) [69] has been used. In equation (8.30) *A* and *p* clearly scale as [L^2] and [L^1], so that the normalised electromagnetic damping, $(Bl)^2/(C_{\mathrm{a}}R)$, must scale as [L^2]. The effectiveness of such an electromagnetic damper thus improves greatly as the size of the device gets larger.

A number of commercial inertial actuators have been considered for an experimental study. Table 8.5 summarised the main parameters of different actuators manufactured by different companies.

Table 8.5: Physical parameters of inertial actuators

	ULTRA	**IV40 Data Physics**	**Motran IFX30-100**	**Mcromega IA-01**
Electrical resistance (Ω)	3.15	1.5	1.63	3
Mechanical stiffness (N/m)	110,190	58,517	20,600	95.62
Open circuit mechanical damping (N/ms^{-1})	9.4	16	44	1.40
Closed circuit mechanical damping (N/ms^{-1})	25.4	36.9	105.34	2.25
Open Circuit damping ratio	3%	3%	20%	40%
Close circuit damping ratio	7.2%	6.9%	48%	64%
Vibrating mass (Kg)	0.28	1.21	0.58	0.032
Base mass (Kg)	0.14	?	0.36	0.053
Mass ratio	2		1.6	0.6
Electromagnetic transducer constant Bl (N/A)	7.1	5.6	10.1	1.6
Natural frequency (Hz)	99.8	35	30	8.7
Cut-off frequency (Hz)	2,000	1,000	100	300
$(Bl)^2/(cR)$	1.7	1.3	1.42	0.6

Figure 8.14 shows the open circuit mechanical impedance (solid line) and the closed circuit mechanical impedance (dashed line) of the four inertial actuators of Table 8.5. It is interesting to notice that the dimensionless parameter $(Bl)^2/(cR)$ is only of order 1 for the four actuators in Table 8.5. For the inertial actuator used in the simulations in Chapter 6 this parameter was about 1.9 and for the ideal actuator of Table 8.4 is about 423.

According to equation (8.20), the mechanical impedance of the ULTRA actuator (top left plot) shows a cut-off frequency from which the actuator starts to behave like a damper of about 1.6 kHz, when R_L is equal 10^6 Ω, and about 714 Hz, when R_L is zero. The Data physics actuator (top right plot) shows a cut-off frequency where the actuator starts to behave like a damper of about 583 Hz when R_L is equal 10^6 Ω and about 250 Hz when R_L is zero. In the of case the Motran actuator the cut-off frequency from which the actuator behaves like a damper is about 75 Hz when R_L is equal 10^6 Ω (dashed line) and is about 31.2 Hz when R_L is equal zero (solid line).

As show in Table 8.5, the MICROMEGA inertial actuator can provide the highest close circuit damping ratio and it is the only model to have it greater than 1/2. Its cut-off frequency is about 10.9 Hz according to equation (8.20) when R_L is equal 10^6 and is about 11.2 Hz according to equation (8.21) when R_L is equal zero.

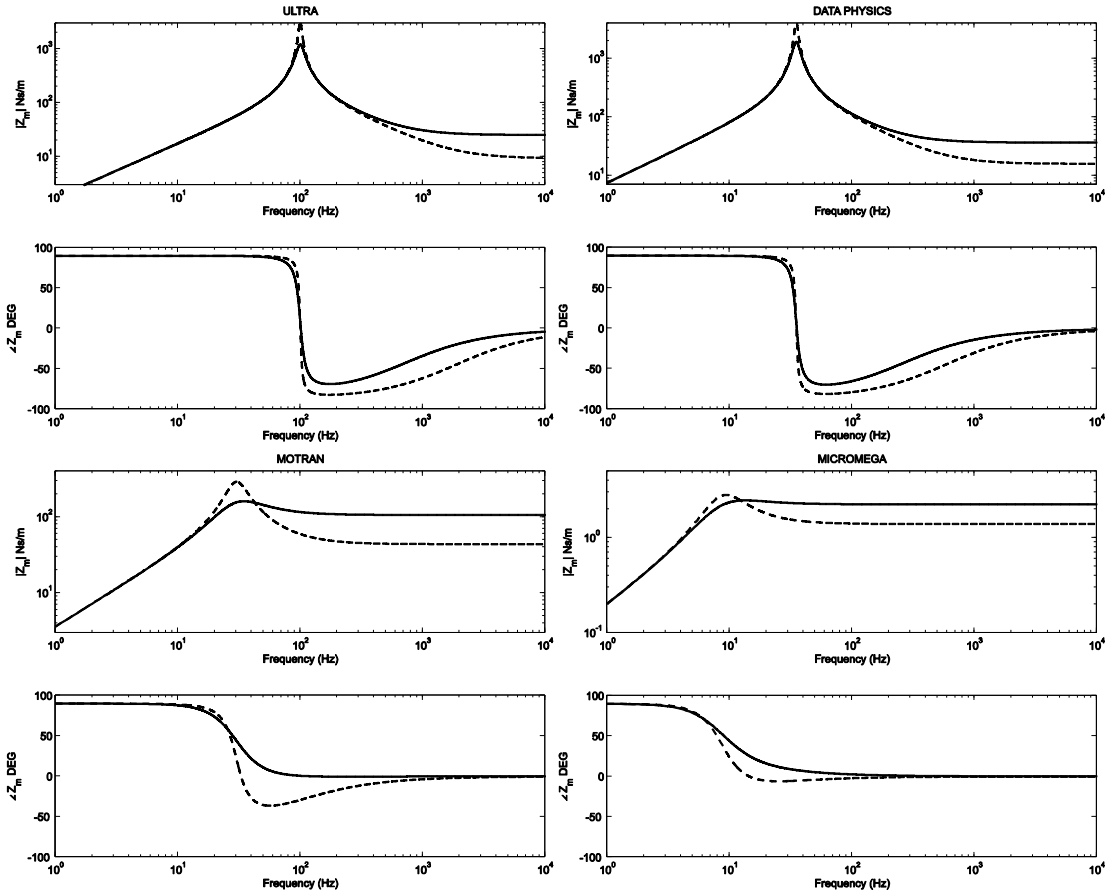

Figure 8.14: Calculated mechanical impedance of four commercial actuators when open circuit (dashed line) and short circuit (solid line). These are: Ultra actuator (top left plot), Data physics actuator (top right plot), Motran actuator (bottom left plot) and Micromega (bottom right plot)

8.4.2. Broadband control of a cantilever beam using a shunted inertial actuator

This section discusses the vibration control of a cantilever beam, excited by a broadband white noise point force using a shunted inertial actuator.

The damping ratio of the first mode of the beam when the actuator is shunted with a resistive load is given by:

$$\zeta = \frac{C'}{2\omega_1 M_1} \tag{8.31}$$

where C' is the close circuit mechanical damping provided by the actuator, ω_1 is the first resonance of the beam. M_1 is the apparent mass of the first mode which depends on the position

of the actuator on the structure. The modal point response of an undamped structure at control position can be written as [25]:

$$\widetilde{\mathrm{Y}}_{\mathrm{c}} = \sum_{r=1}^{\mathrm{R}} \frac{\mathrm{j}\omega\phi(x_{\mathrm{c}})_r^2}{M_{\mathrm{r}}[\omega_r^2 - \omega^2]} \tag{8.32}$$

where $\phi(x_{\mathrm{c}})_{\mathrm{r}}$ is the r-th modeshape calculated at control position, x_{c} is the coordinate of the control position along the beam, $\mathrm{M_r}$ is the modal mass, ω_r is the r-th natural frequency and R is the number of modes taken into account. The contribution of the first mode can be seen as the response of a single degree of freedom system having the same natural frequency of the first resonance of the structure and an apparent mass equal to the ratio between the modal mass and the mode shape squared calculated at control position. The apparent mass at the tip of a cantilever beam is given by $\mathrm{M_s}/4$ where $\mathrm{M_s}$ is the total mass of the beam. Since the first resonance of beam is very well separated from higher resonances, the contribution of higher modes does not significantly affect the response at low frequency. If the aim of the controller is to critically damp the first structural mode ($\zeta = 1$), setting equation (8.31) equal one, the mechanical damping C' must be given by:

$$C' = 2\omega_1 M_1 \tag{8.33}$$

Substituting equation (8.33) in (8.21) and assuming a damping ratio of the inertial actuator ζ_{a} to be greater than 0.5, the cut-off frequency above which the actuator behaves like a damper, ω_{n}, is given by:

$$\omega_{\mathrm{n}} = 2\omega_1 \frac{M_1}{M_{\mathrm{a}}}. \tag{8.34}$$

Thus the ratio between the first natural frequency of the beam and the natural frequency of the actuator is given by:

$$\frac{\omega_1}{\omega_{\mathrm{n}}} = \frac{1}{2}\frac{M_{\mathrm{a}}}{M_1}. \tag{8.35}$$

Substituting the expression of the apparent mass when the actuator is placed at the tip of a cantilever beam in equation (8.35) yields:

$$\frac{\omega_1}{\omega_{\mathrm{n}}} = 2\mu \tag{8.36}$$

where μ is the ratio between the moving mass of the actuator M_{a} and the total mass of the structure M_{s}. Assuming $\mu = 1$, the first natural frequency of the beam has to be twice the cut-off

frequency where the actuator starts to behave like a damper in order to critically damp the first mode of the beam.

The following simulation results are carried out on a cantilever beam using the ideal inertial actuator of Table 8.4, with a natural frequency of 10 Hz. The geometrical and physical parameters of the beam are summarised in Table 8.6.

Table 8.6: Geometrical and physical parameters of the cantilever beam.

Value	**Parameter**
Dimensions	l=0.38 m
Thickness	h=0.016 m
Width	d=0.03 m
Mass density	ρ=2700 kg/m^3
Young's modulus	E=7×10^{10} N/m^2
Poisson ratio	ν_1=0.33
Loss Factor	η=0.01
Mass of the beam	M=0.5 Kg
μ	1
Primary source position	l/2
Secondary source position	l
1st natural frequency	ω_1=90 Hz

The mass of the cantilever beam has been chosen to have $\mu = 1$. The ideal inertial actuator is placed at the tip of a cantilever beam. The maximum mechanical damping that can be generated by the shunted inertial actuator is about 535 N/m/s and from Figure 8.12 the maximum cut-off frequency ω_n above which the actuator behaves like a shy hook damper is about 180 Hz. The first natural frequency of the structure has to be twice the cut-off frequency of the actuator and therefore, for this ideal actuator, it is necessary that $\omega_1 < 360$ Hz to critically damp the first mode. In this example the first natural frequency of the beam is much higher than the natural frequency of the actuator and the open circuit mechanical damping is low, therefore the passive dynamic of the actuator marginally influence the response of the beam.

The faint line in Figure 8.15 shows the kinetic energy of the beam before the actuator is placed on the beam. When the actuator is shunted with a very high resistance the response of the beam is slightly more damped at the resonance frequencies due to the passive effect of the actuator. As the resistive load R_L is decreased the actuator provides damping to the structure so that the

first few resonances of the structure are very well damped (dashed line). When the shunting resistance is zero the electromagnetic coupling is so strong that the relative motion between the coil and the magnet teds to zero and the first natural frequency of the structure is shifted at lower frequency due to the additional mass of the magnet (solid line).

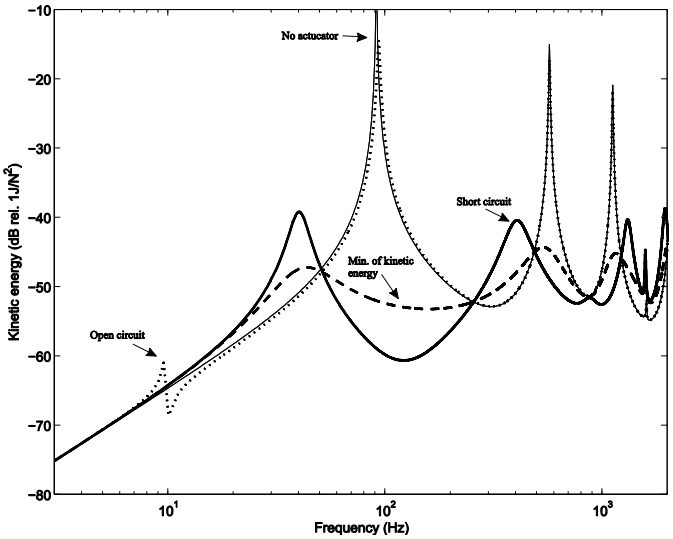

Figure 8.15: PSD of the kinetic energy of the beam without actuator (faint line), when the actuator is attached but open circuit (dotted line), minimising the total kinetic energy (dashed line) and for the actuator short circuit (solid line).

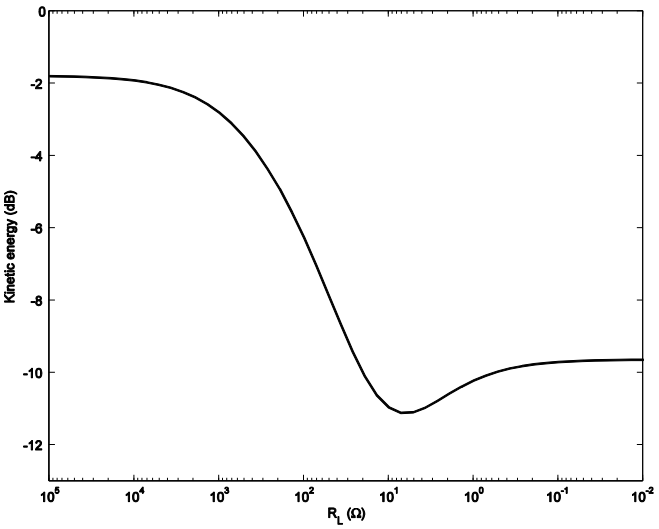

Figure 8.16: Total kinetic energy of the panel normalised by that one before the actuator is attached as function of decreasing values of R_L.

Figure 8.16 shows the total kinetic energy of beam for different values of the resistive load R_L. The total kinetic energy of the beam presents an optimum value when R_L of about 6.3 Ω giving an overall reduction of about -11 dB. For lower values of R_L the effect is to begin to pin the relative motion between the magnet and the coil of the actuator so that the total response of the structure increases again.

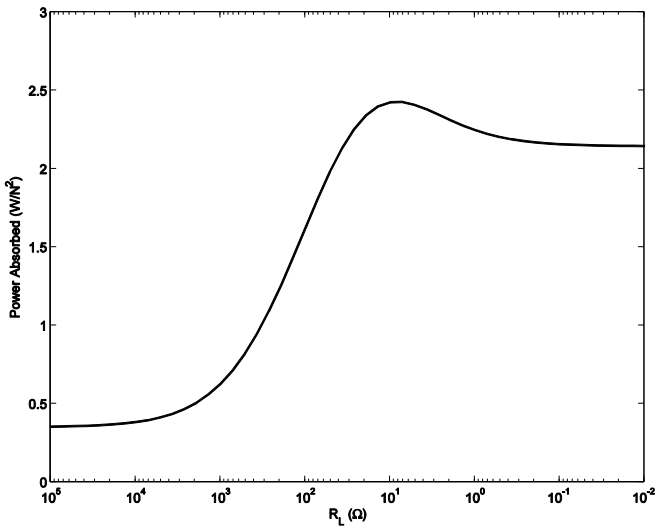

Figure 8.17: Total mechanical power absorbed by the shunted actuator as function of decreasing values of R_L.

Figure 8.17 shows the mechanical power dissipated by the inertial actuator as function of the resistive load R_L. When the actuator is shunted with a very high resistance the mechanical power dissipated does not go to zero because of the internal damping of the actuator. When R_L is decreased the power absorbed increases until it reaches a maximum. If R_L is further increased the absorbed power decreases again. The maximum of the mechanical absorbed power roughly corresponds with the minimum of the total kinetic energy of the beam. An algorithm that changes the electrical resistance R_L, estimates the mechanical absorbed power and converge to its maximum could be implemented to make the system self-tuneable with the aim of minimising the overall structural vibration.

Figure 8.18 shows the power dissipated by the resistive load, which is also the power that could be potentially harvested as function of decreasing values of R_L. As one would expect the power dissipated by the shunt is zero when R_L is equal zero and is again zero for very high values of R_L which means that the circuit is open. The harvested power is maximised when R_L is about 21.2 Ω which is a quite different value compared with the minimisation of the kinetic energy and maximisation of the absorbed power.

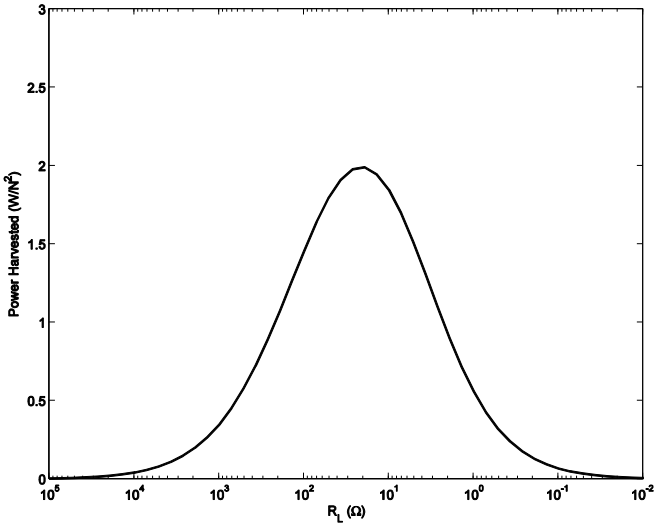

Figure 8.18: Total power harvested by the shunted transducer as function of decreasing values of R_L.

Table 8.7 shows a comparison between the minimisation of the total kinetic energy of the panel and the other two self-tuning strategies. Although the optimal values of R_L are different for the three strategies, the global reduction in terms of kinetic energy of the beam is only 0.1 dB less for the maximisation of the mechanical power absorption. When the harvested power is maximised the reduction in the total kinetic energy of the beam is about 1 dB less compared with the minimisation of the kinetic energy. In this case the maximisation of the harvested power gives good performance compared with the minimisation of the kinetic energy of the structure.

Table 8.7: comparison between maximisation of kinetic energy, maximisation the total absorbed and harvested power

	R_L (Ω)	Attenuation in kinetic energy (dB)	Absorbed power (W/N^2)	Harvested power (W/N^2)
Minimisation of kinetic energy	6.3	-11.2	2.42	1.63
Maximisation of absorbed power	8.4	-11.1	2.43	1.77
Maximisation of harvested power	21.2	-10	2.31	1.99

However, if a commercial actuator is considered, the transduction coefficient *Bl* is usually much lower than the one considered in the simulations. Moreover if the base mass of the inertial actuator is taken into account equation (8.35) becomes:

$$\frac{\omega_1'}{\omega_n} = \frac{1}{2}\frac{M_a}{M_1 + M_w} \tag{8.37}$$

where ω_1' is the first natural frequency of the beam with the base mass of the actuator M_{w} attached. In this case, setting equation (8.37) equal to two so that the frequency where the actuator starts to behave like a damper is half of the first natural frequency of the beam, the mass of the beam is equal to $M_{\mathrm{s}} = M_{\mathrm{a}} - 4M_{\mathrm{w}}$. For all the actuators in Table 8.5 $M_s = M_{\mathrm{a}} - 4M_{\mathrm{w}}$ is less than zero.

This result suggests that with the commercial actuators considered it is impossible to use a shunted device to critically damp the first mode of a cantilever beam.

8.4.3. Broadband control of a panel using a shunted inertial actuator

In this section the possibility of broadband control of a panel using a shunted inertial actuator is investigated. The optimal value of a skyhook damper to obtain a broadband control for a finite plate roughly corresponds to the impedance of an infinite plate of the same thickness [17] which is given by:

$$C_{\mathrm{opt}} = 8h^2\sqrt{\frac{E\rho}{12(1-\nu_1^2)}} \tag{8.38}$$

where h is the thickness of the panel, E is the Young's module, ρ is the density and ν_1 the Poisson's coefficient of the panel's material. Substituting equation (8.38) in (8.21) and assuming that the damping ratio of the shunted inertial actuator ζ_{a} to be greater than 0.5 the cut off frequency above which the actuator behaves like a damper is given by:

$$\omega_{\mathrm{n}} = \frac{8h^2}{M_{\mathrm{a}}}\sqrt{\frac{E\rho}{12(1-\nu_1^2)}} \tag{8.39}$$

The first natural frequency of a simply supported panel is given by:

$$\omega_{11} = 2h\left(\frac{\pi}{L}\right)^2\sqrt{\frac{E}{12(1-\nu_1^2)\rho}} \tag{8.40}$$

where, the panel has been considered square and of side L. From equation (8.39) and (8.40) the ratio between the first natural frequency of the panel and the natural frequency of the actuator is given by:

$$\frac{\omega_{11}}{\omega_{\mathrm{n}}} = \frac{\pi^2}{4}\frac{M_{\mathrm{a}}}{M_{\mathrm{s}}} \approx 2.4\mu \tag{8.41}$$

where M_{s} is the mass of the panel. Equation (8.41) shows that if $\mu = 1$ the first natural frequency of the panel has to be about 2.4 times the cut-off frequency from which the actuator behaves like a damper to optimally control the vibration of the structure.

If the base mass of the actuator is taken into account, equation (8.41) can be written as:

$$\frac{\omega'_{11}}{\omega_{\mathrm{n}}} \approx 2.4\frac{M_{\mathrm{a}}}{M_{\mathrm{s}} + M_{\mathrm{w}}} \tag{8.42}$$

where ω'_{11} is the first natural frequency of the panel with the base mass of the actuator M_{c} attached. If $M_{\mathrm{a}}/(M_{\mathrm{s}} + M_{\mathrm{w}})$ is set to one so that the ω'_{11} is about 2.4 times ω_{n}, M_{s} is equal to $M_{\mathrm{a}} - M_{\mathrm{w}}$. For the Micromega actuator, which is the only one to have the closed loop mechanical damping grater that 0.5, the moving mass minus the base mass is less than zero. This demonstrates that it is impossible to optimally control the broadband vibration of a plate using a shunted commercial actuator listed in Table 8.5.

8.4.4. Shunted inertial actuator used as dynamic vibration absorber (DVA)

A shunted inertial actuator can be used as a dynamic vibration absorber (DVA) if it is tuned at the natural frequency of system under control. The mechanical damping of a shunted inertial actuator can be changed by varying the value of the resistive load of the shunt. In Chapter 7 the optimal damping ratio of a DVA that minimises the total kinetic energy of an undamped SDOF system was found to be $\sqrt{\mu}/2$ where μ is the mass ratio between the mass under control and the moving mass of the DVA when the frequency ratio between DVA and the SDOF is set to $1/\sqrt{1+\mu}$. For a *lightly* damped SDOF system, the same expression of the optimal damping ratio and frequency ratio can be used with good approximation. If a shunted inertial actuator is to be used to control a SDOF system, the value of optimal mechanical damping ratio has to be greater than the open circuit mechanical damping ratio of the actuator, ζ_{open} and smaller than the close circuit mechanical damping ratio, ζ_{close} to be able to minimise the overall kinetic energy of the mass under control. Thus:

$$\zeta_{\mathrm{open}} < \frac{\sqrt{\mu}}{2} < \zeta_{\mathrm{close}} \tag{8.43}$$

Substituting the expression of the mass ratio in equation (8.43) the mass of the SDOF cannot excide the limit values given by:

$$\frac{M_{\mathrm{a}}}{(2\zeta_{\max})^2} < M_s < \frac{M_{\mathrm{a}}}{(2\zeta_{\mathrm{open}})^2} \tag{8.44}$$

where M_s is the mass of the SDOF system. Table 8.8 lists the limiting values of the controllable mass M_s for the four inertial actuators of Table 8.5. The table shows that for the first two actuators (ULTRA and Data Physics) the mass M_s is high compared to the moving mass of the actuator. As shown in Chapter 7 the performance of the DVA decreases for high values of μ and thus the performance of the first two actuators would be very low. For the Micromega actuator it is not possible to control a single degree of freedom system because the base mass is already bigger than M_s.

Table 8.8: limit values of the mass of the SDOF system to be controlled with different commercial inertial actuators

Actuator	**Mass of the SDOF system under control (Kg)**
ULTRA	$13.3 < M_s < 97.7$
IV40 Data Physics	$62.9 < M_s < 334.7$
Motran IFX30-100	$0.6 < M_s < 3.6$
Micromega IA-01	$0.02 < M_s < 0.05$

The Motran actuator can be used to minimise the kinetic energy of a SDOF system having a vibrating mass between 0.6 Kg and 3.6 Kg. Figure 8.19 shows the kinetic energy of a SDOF system having a mass of 2 Kg so that $\mu = 4$, a stiffness of 9.16×10^4 N/m and damping ratio of 2%. The stiffness has been chosen such that the frequency ratio between the actuator and SDOF system is given by $1/\sqrt{\mu+1}$. The faint line in Figure 8.19 shows the kinetic energy of SDOF with no actuator. The dotted line shows the kinetic energy of SDOF system when the actuator is attached but open circuit. If the electric load is decreased the two resonances of the system are more damped (dashed line) and when the R_L is zero the response of SDOF shows a single natural frequency because the electromagnetic coupling is so strong that the relative velocity between the mass of SDOF system and the mass of the DVA tends to zero.

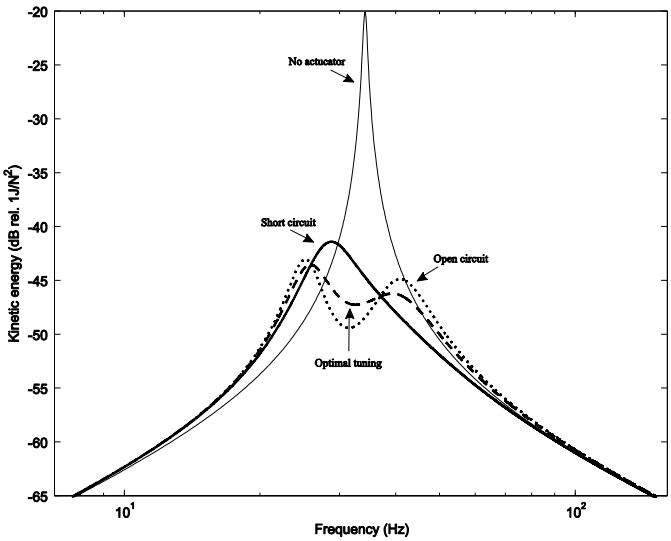

Figure 8.19: PSD of the kinetic energy of the SDOF actuator (faint line), when the actuator is attached but open circuit (dotted line), for the optimal tuning (dashed line) and for the actuator short circuit (solid line).

Figure 8.20 shows kinetic energy of the SDOF system integrated between 1 Hz and 1 kHz normalise to the total kinetic energy of system before the DVA is attached. When the coil circuit is open circuit, the total kinetic energy is attenuated by 31.3 dB because of the passive effect of the actuator. As the R_L is decreased the total kinetic energy starts to decrease until it reaches a minimum when R_L is about 4.93 Ω. If R_L is further decreased the total kinetic energy increases again. The extra attenuation due to the resistive shunt is, however only about 0.2 dB.

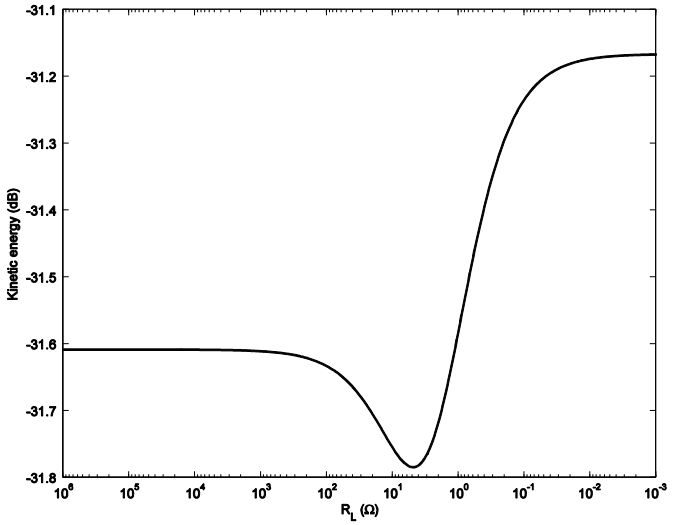

Figure 8.20: 1 Hz-10 kHz integrated kinetic energy of the SDOF system normalised to that without the actuator attached as function of decreasing value of R_L normalised to the kinetic energy of the SDOF system before the actuator is placed

Figure 8.20 shows the integrated mechanical power absorbed by the shunted inertial actuator given by:

$$P = \left(c + \frac{(Bl)^2}{R + R_{\mathrm{L}}}\right) \int_0^{\omega_{\max}} |\mathrm{u_R}|^2 d\omega \tag{8.45}$$

where $\mathrm{u_R}$ is the relative velocity of the two masses. As shown in equation (8.45), when the coil circuit is open ($R_{\mathrm{L}} \to \infty$) the absorbed power is quite high because the open circuit mechanical damping *c* of the Motran actuator is high.

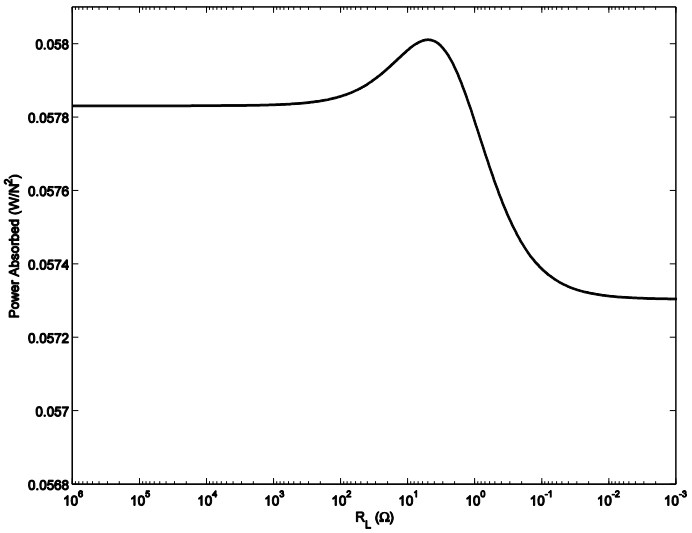

Figure 8.21: 1 Hz-10 kHz integrated mechanical power absorbed by the shunted inertial actuator as function of decreasing values of R_{L}

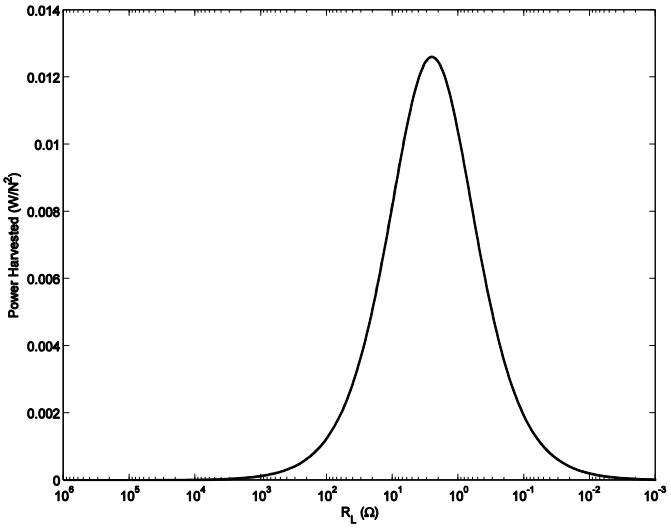

Figure 8.22: 1 Hz-10 kHz integrated power harvested by the shunted inertial actuator as function of decreasing values of R_{L}

The mechanical power absorbed is maximised when R_{L} is equal 5.05 Ω. In Chapter 7 it has been shown that the minimum of the total kinetic energy and the maximum of the power absorbed correspond if they are both integrated over and infinite frequency band. In this case the numerical integration is made over a finite frequency band therefore the value of R_{L} that

minimise the total kinetic energy and value of R_L that maximise the power absorbed are slightly different. The current circulating in the coil $\tilde{\imath}$ is proportional to the relative velocity v_r and is given by:

$$\tilde{\imath} = \frac{Bl}{R + R_L}\tilde{v}_R \tag{8.46}$$

The power dissipated by the shunt is given by the value of the shunt resistance times the mean squared value of the current $\tilde{\imath}$ integrated over the frequency which leads to:

$$P_H = \frac{R_L}{(R + R_L)^2}(Bl)^2 \int_0^{\omega_{max}} |\tilde{v}_R|^2 d\omega \tag{8.47}$$

Figure 8.22 shows the power dissipated the shunt which is also the power that can be potentially harvested. The plot shows that the harvested power is zero when the circuit is open and is again zero when R_L is equal zero as one would expect. When R_L is equal 2.53 Ω the harvested power is maximised.

Comparing equation (8.45) and (8.47) it is evident that the mechanical absorbed power and the harvested power are maximised for a different value of R_L. Although from the simulation results the values of R_L that maximise the mechanical absorbed power and maximise the harvested power are very close, the attenuation in the total kinetic energy is about the same for the two method of tuning the DVA as shown in Table 8.9.

Table 8.9: comparison between three different strategies of tuning the DVA

	R_L (Ω)	Attenuation in the kinetic energy of the SDOFs (dB)
Minimisation of the kinetic energy of the SDOFs	4.93	-31.78
Maximisation of the mechanical absorbed power	5.05	-31.78
Maximisation of the harvested power	2.53	-31.74

8.5. Summary and conclusions

This chapter provides a preliminary discussion of shunted electromagnetic transduces as tuneable damping elements. The potential advantage of such device are that the changes to the electrical shunt impedance are relatively easy to implement, and that the power that would otherwise be dissipated in the shunt could, potentially, be harvested to provide power for the

tuning circuit. It may be even possible to use a measurement of the electrical power harvested as cost function with which to adapt the shunt impedance. This would provide an attractive self-powering and self-tuning damping device.

A two port network formulation has been used to analyse the behaviour of both reactive and inertial electromagnetic shunted transducers. Simulations have than been performed of laboratory-scale devices, with masses of less than about 1 Kg, used to control idealised structures such as beams and panels. Although the analysis is interesting, the final predicted results have generally been disappointing, with the additional reductions in structural response due to shunting the device being small relative to the reductions due to the inherent passive behaviour of the devices themselves when they are open circuit. For this reason, and in the interests of time, this concept has not been explored experimentally.

It has been shown, however, that the additional damping due to shunting the transducer normalised by the passive damping of the device, scales as the square of the length-scale. Thus although the effects predicted using laboratory-scale devices are modest, they would be much more significant for the very large electromagnetic devices used to control the motion in civil engineering structures and that large arrays of miniaturised devices would be less effective than a single larger device.

9. Conclusions and suggestions for further work

9.1. Conclusions

Vibration control systems can be classified as passive or active, depending on whether or not external power is required. A passive system that can change its properties during time is often defined as semi-active. An advantage of semi-active and active control system is that they can adapt themselves to operate in different environmental and operating conditions.

Conventional control design is often based on a time-invariant assumption for the system and signals under consideration, which means that the control system and the mechanism of generating the control signal have constant coefficients. In self-tuning systems, control and signal processing algorithms have coefficient which can vary with time so that the controller can change its parameters in order to maintain a required performance when the operating conditions change. This is done by the addition of an adjusting mechanism which monitors the system, compares its status with the required one and adjusts the coefficients of the controller.

This is the broad subject of this thesis. In particular self-tuning broadband vibration control, based on the maximisation of the power absorbed by the controller in several either semi-active or active control configurations was investigated. The power absorbed was chosen as a cost function for the implementation of self-tuning control because its estimation can be done using signals available locally, within the controller, avoiding the use of extra sensors to monitor the global status of the system under control.

The first application considered was the optimisation of the damping coefficient of a single end grounded damper used to control the vibration of two coupled oscillators. One of the two vibrating masses was subjected by a broadband disturbance while the damper was acting on the other mass. If the two oscillators were connected by a spring, it has been demonstrated that the maximisation of the power absorbed by the damper corresponds to the minimisation of the kinetic energy of the excited mass. In the general case where the oscillator were coupled by a spring and a damper, numerical results showed that maximising the power absorbed by the damper approximately minimises the kinetic energy of the entire system.

The analysis was extended to a distributed multi degree of freedom system. Different homogenous structures such as panels and beams were considered subjected to a broadband disturbance and controlled by a velocity feedback using an ideal velocity sensor collocated with a point force actuator. Different tuning strategies for the control gain of independent feedback loops were compared, taking the minimisation of the kinetic energy of the entire structure as a benchmark. It would be inconvenient to use the kinetic energy as cost function in a practical

self-tuning system because it is a global property and its measurement would require a dense array of sensors over the whole structure. Tuning the feedback gains on this criterion thus defeats the idea of having entirely locally-acting control loops. Two different tuning strategies were considered: the maximisation of the power absorbed by the controller and the maximisation of the control stability of the first mode of the structure. It was shown, by numerical simulations, that the two strategies give similar results in terms of the broadband attenuation of the structural response.

An advantage of using the mechanical power absorbed by the controller as a cost function in the self-tuning process, is that it can be measured entirely locally. In this application the force was generated by the ideal actuator and was made proportional to the measured velocity. The absorbed power could thus be readily estimated from the mean square value of the measured velocity and the feedback gain, thus providing a simple measurement of an entirely local parameter that could be used to tune the gains. An algorithm was implemented to adjust the control gains of independent control units implemented on a panel subject to broadband random excitation. The adaptation was performed using the feedback signal only.

These theoretical studies constituted the base of the experimental implementation of multichannel control of a clamped aluminium panel excited by a shaker fed with white noise. Two control units were initially employed, each consisting in a voice coil actuator closely collocated with an accelerometer. The coil was attached to the panel and the magnet was mounted on a relatively rigid structure where the actuators could react the force off. Particular care was taken in the design of the controller in order to guarantee the stability of the control system for values of control gains higher than the one producing the transition in the control action between optimum damping and pinning of the structure. The algorithm for the maximisation of the power absorbed was experimentally implemented, achieving an overall reduction of the panel's response similar to the minimisation of the kinetic energy of the structure.

Although the principle of self-tuning to maximise power absorption has been demonstrated using reactive force actuators, it is often not possible to use reactive actuators in practice, since there may be no solid structure to react the force against. Therefore simulations were carried out with velocity feedback loop including an inertial electromagnetic actuator for broadband vibration control. It was illustrated that maximising the absorbed power again provides a reasonable approximation to minimising the kinetic energy of the host structure. One aspect of self-tuning that becomes particularly important with use of inertial actuators is the need to avoid feedback gains for which the system becomes unstable, since this will cause significant enhancement of the vibration and, potentially, damage. The optimal feedback gain can be kept well below the unstable limit provided the actuator resonance is well damped, although this is

not always possible in practice. It was also shown that the characterisation of the actuator could also be used to calculate the control force from the measured velocity and current, so that the power can be estimated.

This type of active self-tuning control requires external energy, therefore a semi-active control system was also considered. A model of a dynamic vibration absorber attached to a lightly damped single degree of freedom system was used to compare the maximisation of the power absorbed by the controller with the minimisation of the kinetic energy of the host structure. The parameters involved in the optimisation were the frequency ratio of the natural frequencies of the decoupled SDOF systems and their damping ratios. It was demonstrated analytically that the two optimisations are exactly the same even when considerable damping was introduced in the system under control.

A preliminary study of a self-tuning semi-active controller using electromechanical inertial actuator was finally carried out. This system consisted of an electromechanical inertial transducer with an adaptable electrical shunt that acted as a passive damper and also as a potential source of electrical energy to drive the self-tuning circuit. The advantages of such a device are that the changes in the shunt are relatively easy to implement, and that the power dissipated by the shunt could be harvested to drive the self-tuning system. Simulation results suggested that it may even be possible to use a measurement of the electrical power harvested as a cost function to adapt the shunt. It was shown that for laboratory scale devices, the additional damping provided by shunting the device was small compared with the inherent passive damping of the open circuit device. It was also shown, however, that the additional damping due to shunting the transducers normalised by the passive damping of the device, scales as the square of its length scale. Thus although the effect of shunting the transducer is limited for laboratory size transduces it may be more significant for large scale devices, for example in civil engineering applications.

9.2. Suggestions for further work

Further work could progress in the directions listed below.

- Theoretical analysis of the maximisation of the power absorbed by the controller as a tuning strategy in the presence of different types of broadband excitations (i.e. Turbulent Boundary Layer).
- The study of alternative tuning algorithms, capable of continuously monitoring the absorbed power, even after the algorithm has converged, to track changes in the operating conditions. The development of the new algorithm should ideally overcome a limitation of the current method, which is the need for synchronisation of the adaptation when more than one control unit is used.

- Stability issues due to the frequency response of MEMS accelerometers used as feedback sensors could potentially be solved by designing a compensator that increases the gain margin in this case.
- Experimental implementation of the self-tuning control for velocity feedback using inertial actuators. For this application the adaptation is more complicated due to the instability issues introduced by the dynamics of the actuators. This may involve a modification of the algorithm to guarantee that the control gain never exceeds the maximum stable value.
- Problems related with instability of the controller due to the saturation of the displacement of the proof mass of the actuator also have to be considered in the experimental implementation of feedback control using inertial actuators.
- Simulation studies and experiments could be carried out in semi-active control using shunted inertial actuator for large scale actuators typically used in civil engineering applications.

Appendix A: Case of a simplified two DOF system controlled by a grounded damper

This section presents the formulation to obtain analytical expressions of the optimal mechanical damping c_3 that minimises the kinetic energy of the mass m_1, maximise the power absorbed of damper 3 and minimise the total kinetic energy of the system in Figure A.1. Compared with the case of a general two DOF system, the parameters c_2 and k_3 are set to zero.

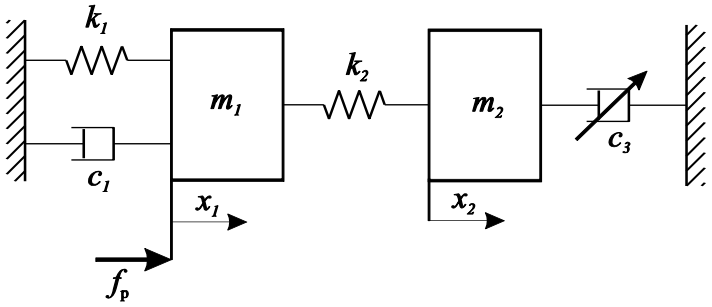

Figure A.1: Two DOF system controlled by a grounded damper with c_2 and k_3 equal zero

A.1 Analysis

Assuming c_2 and k_3 equal zero, the steady state response of the system can be expressed in terms of the five dimensionless parameters defined by:

$\mu = m_2/m_1$: mass ratio

$\nu = \omega_2/\omega_1$: natural frequency ratio

$\lambda = \omega/\omega_1$: forced frequency ratio

$\zeta_1 = c_1/(2m_1\omega_1)$: primary damping (A.1)

$\zeta_2 = c_3/(2m_2\omega_2)$: secondary damping

where

$\omega_1 = \sqrt{k_1/m_1}$: natural frequency of the host / primary system

$\omega_2 = \sqrt{k_2/m_2}$: natural frequency of the DVA (A.2)

The mobility function $\tilde{Y}_{11}$ and $\tilde{Y}_{12}$ can be written in non-dimentional form as:

$$\tilde{\Pi} = \sqrt{k_1 m_1}\tilde{Y}_{11}(j\lambda) = \frac{B_0 + (j\lambda)B_1 + (j\lambda)^2 B_2 + (j\lambda)^3 B_3}{A_0 + (j\lambda)A_1 + (j\lambda)^2 A_2 + (j\lambda)^3 A_3 + (j\lambda)^4 A_4} \quad \text{(A.3)}$$

$$\widetilde{\Lambda} = \sqrt{k_1 m_1}\widetilde{Y}_{12}(j\lambda) = \frac{C_0 + (j\lambda)C_1 + (j\lambda)^2 C_2 + (j\lambda)^3 C_3}{A_0 + (j\lambda)A_1 + (j\lambda)^2 A_2 + (j\lambda)^3 A_3 + (j\lambda)^4 A_4} \quad \text{(A.4)}$$

where:

$A_0 = \mu\nu^2$	$B_0 = 0$	$C_0 = 0$
$A_1 = 2\zeta_2\mu\nu + 2\zeta_1\mu\nu^2 + 2\mu^2\nu^3\zeta_2$	$B_1 = \mu\nu^2$	$C_1 = \mu\nu^2$
$A_2 = \mu\nu^2 + \mu + \mu^2\nu^2 + 4\zeta_2\zeta_2\mu\nu$	$B_2 = 2\zeta_2\mu\nu$	$C_2 = 0$
$A_3 = 2\zeta_2\mu\nu + 2\zeta_1\mu$	$B_3 = \mu$	$C_3 = 0$
$A_4 = \mu$		

This configuration has been proposed by Cheung *et al.* in 2011 [48] who found an analytical expression of the optimum damping ratio ζ_2 that minimise the total displacement of the mass m_1. In this section analytical expressions of the damping ratio ζ_2 which minimise the kinetic energy of the mass m_1 and minimise the total kinetic energy of the entire system when ζ_1 is equal zero are derived.

A.2 Minimisation of the total kinetic energy and maximisation of the power absorbed

The damper in this case can either be adapted to minimise the kinetic energy of m_1, or the total kinetic energy of m_1 and m_2, or to maximise the absorbed power. In this section we compare these strategies

If the aim of the tuneable damper c_3 is to minimise the integral of the kinetic energy of the mass m_1 calculated over the frequency-band $\pm\infty$, the performance index to be minimised can be defined by:

$$I_{k1} = \frac{m_1 E[|\tilde{v}_1|^2]}{2\pi S_f \omega_1 / k_1} \quad \text{(A.5)}$$

where $E[\ ]$ denotes the expectation value. The performance index I_{k1} represents the ratio of the kinetic energy of the mass m_1 to the excitation force with a uniform spectrum density S_f. The unit of S_f is N^2s/rad. The constant $2\pi\omega_1/k_1$ is introduced to ensure that the performance index is dimensionless. The mean squared value of the velocity of the primary mass can be written as:

$$E[\tilde{v}_1^2] = \frac{S_f \omega_1}{m_1 k_1}\int_{-\infty}^{+\infty} \left|\widetilde{\Pi}\right|^2 d\lambda \quad \text{(A.6)}$$

Substituting equation (A.6) in equation (A.5) yields:

$$I_{\mathrm{k1}} = \frac{1}{2\pi}\int_{-\infty}^{+\infty} |\widetilde{\Pi}|^2 \, d\lambda \tag{A.7}$$

Thus, substituting equation (A.3) in (A.7) yields:

$$I_{\mathrm{k1}} = \frac{1}{2\pi}\int_{-\infty}^{+\infty} \left| \frac{B_0 + (j\lambda)B_1 + (j\lambda)^2 B_2 + (j\lambda)^3 B_3}{A_0 + (j\lambda)A_1 + (j\lambda)^2 A_2 + (j\lambda)^3 A_3 + (j\lambda)^4 A_4} \right|^2 \mathrm{d}\lambda \tag{A.8}$$

Equation (A.8) can be integrated using the formula in reference [22] leading to:

$$I_{\mathrm{k1}} = \frac{\begin{array}{c} 4\nu^2\zeta_1^2\zeta_2 + \zeta_1\left(\mu\nu^3 + 4(\nu + (1+\mu)\nu^3)\zeta_2^2\right) + \\ \zeta_2(1 + 2(-1+\mu)\nu^2 + (1 - \mu + \mu^2)\nu^4 + 4(\nu^2 + \mu\nu^4)\zeta_2^2) \end{array}}{\begin{array}{c} 2(4\nu^2\zeta_1^3\zeta_2 + \mu\nu^5\zeta_2^2 + \zeta_1^2(\mu\nu^3 + 4(\nu + (1+\mu)\nu^3)\zeta_2^2) + \\ \zeta_1\zeta_2(1 + 2(-1+\mu)\nu^2 + (1+\mu^2)\nu^4 + 4(\nu^2 + \mu\nu^4)\zeta_2^2)) \end{array}} \tag{A.9}$$

If the aim of the tuneable damper c_3 is to minimise the integral of the kinetic energy of the entire system, and thus the kinetic energy of mass 1 plus the kinetic energy of mass 2 calculated over the frequency-band $\pm\infty$, the performance index to be minimised can be defined as:

$$I_{\mathrm{k}} = \frac{m_1 E[|\tilde{v}_1|^2]}{2\pi S_{\mathrm{f}}\omega_1/k_1} + \frac{m_1\mu E[|\tilde{v}_2|^2]}{2\pi S_{\mathrm{f}}\omega_1/k_1} \tag{A.10}$$

The mean squared value of the velocity of the mass m_2 can be written as:

$$E[\tilde{v}_2^2] = \frac{S_{\mathrm{f}}\omega_1}{m_1 k_1}\int_{-\infty}^{+\infty} \left|\widetilde{\Lambda}\right|^2 d\lambda \tag{A.11}$$

Substituting equation (A.11) in equation (A.10) yields:

$$I_{\mathrm{k}} = I_{k1} + I_{k2} = \frac{1}{2\pi}\int_{-\infty}^{+\infty} |\Pi|^2 \, d\lambda + \frac{\mu}{2\pi}\int_{-\infty}^{+\infty} |\tilde{\Lambda}|^2 \, d\lambda \tag{A.12}$$

Thus, using equation (A.4) the quantity I_{k2} can be written as:

$$I_{\mathrm{k2}} = \frac{\mu}{2\pi}\int_{-\infty}^{+\infty} \left| \frac{C_0 + (j\lambda)C_1 + (j\lambda)^2 C_2 + (j\lambda)^3 C_3}{A_0 + (j\lambda)A_1 + (j\lambda)^2 A_2 + (j\lambda)^3 A_3 + (j\lambda)^4 A_4} \right|^2 \mathrm{d}\lambda \tag{A.13}$$

Equation (A.13) can be integrated using the formula in reference [22] leading to:

$$I_{\mathrm{k2}} = \frac{\mu\nu^3(\zeta_1 + \nu\zeta_2)}{\begin{array}{c} 2(4\nu^2\zeta_1^3\zeta_2 + \mu\nu^5\zeta_2^2 + \zeta_1^2(\mu\nu^3 + 4(\nu + (1+\mu)\nu^3)\zeta_2^2) \\ +\zeta_1\zeta_2(1 + 2(-1+\mu)\nu^2 + (1+\mu^2)\nu^4 + 4(\nu^2 + \mu\nu^4)\zeta_2^2)) \end{array}} \tag{A.14}$$

And thus substituting equations (A.9) and (A.14) in (A.12) leads to:

$$I_{\mathrm{k}} = \frac{\begin{array}{c}\zeta_2 + \nu(2\mu\nu^2\zeta_1 + \nu(-2 + \nu^2 + \mu(2 + \mu\nu^2) + 4\zeta_1^2)\zeta_2 + \\ 4(1 + (1 + \mu)\nu^2)\zeta_1\zeta_2^2 + 4\nu(1 + \mu\nu^2)\zeta_2^3)\end{array}}{\begin{array}{c}2(4\nu^2\zeta_1^3\zeta_2 + \mu\nu^5\zeta_2^2 + \nu\zeta_1^2(\mu\nu^2 + 4(1 + (1 + \mu)\nu^2)\zeta_2^2) + \\ \zeta_1\zeta_2(1 + 2(-1 + \mu)\nu^2 + (1 + \mu^2)\nu^4 + 4(\nu^2 + \mu\nu^4)\zeta_2^2))\end{array}} \tag{A.15}$$

The power absorbed by the tuneable damper can be written as:

$$S_{P3}(\omega) = \frac{1}{2} Re\{\tilde{f}_{\mathrm{d}}^{*}\tilde{v}_2\} \tag{A.16}$$

where the force $\tilde{f}_{\mathrm{d}}$ is the force produced by the damper given by:

$$\tilde{f}_{\mathrm{d}} = c_3\tilde{v}_2 \tag{A.17}$$

Substituting equation (A.17) in (A.16) the absorbed power becomes:

$$S_{P3}(\omega) = \frac{1}{2} c_3|\tilde{v}_2|^2 \tag{A.18}$$

In this case the non-dimensional performance index is defined by:

$$I_{\mathrm{p3}} = \frac{c_3 E[|\tilde{v}_2|^2]}{2S_{\mathrm{f}}\omega_1/k_1} \tag{A.19}$$

which represents the ratio of power absorbed by the tuneable damper to that generated by the excitation force with a spectrum density S_{f} acting on a damper of value k_1/ω_1. The mean squared value of the relative velocity times the mechanical damping c_3 can be expressed as follow:

$$c_3 E[|\tilde{v}_2|^2] = \frac{S_{\mathrm{f}}\omega_1}{k_1} 2\zeta_2\mu\nu \int_{-\infty}^{+\infty} |\tilde{\Lambda}|^2 d\lambda \tag{A.20}$$

Thus the performance index becomes:

$$I_{\mathrm{p3}} = \zeta_2\mu\nu \int_{-\infty}^{+\infty} |\tilde{\Lambda}|^2 d\lambda \tag{A.21}$$

Substituting equation (A.4) in (A.21) I_{p3} becomes:

$$I_{\mathrm{p3}} = \frac{\begin{array}{c}\pi\mu\nu^4\zeta_2(\zeta_1 + \nu\zeta_2)\end{array}}{\begin{array}{c}2(4\nu^2\zeta_1^3\zeta_2 + \mu\nu^5\zeta_2^2 + \zeta_1^2(\mu\nu^3 + 4(\nu + (1 + \mu)\nu^3)\zeta_2^2) \\ +\zeta_1\zeta_2(1 + 2(-1 + \mu)\nu^2 + (1 + \mu^2)\nu^4 + 4(\nu^2 + \mu\nu^4)\zeta_2^2))\end{array}} \tag{A.22}$$

In order to minimise the kinetic energy of the mass m_1, the following conditions have to be satisfied:

$$\begin{cases} \dfrac{\partial I_{\mathrm{k1}}}{\partial \zeta_2} = 0 \\ \dfrac{\partial I_{\mathrm{k1}}}{\partial \nu} = 0 \end{cases} \tag{A.23}$$

while to minimise the total kinetic energy of the entire system the following conditions have to be satisfy:

$$\begin{cases} \dfrac{\partial I_{\mathrm{k}}}{\partial \zeta_2} = 0 \\ \dfrac{\partial I_{\mathrm{k}}}{\partial \nu} = 0 \end{cases} \tag{A.24}$$

Finally to maximise the total power absorbed by the tuneable damper the following conditions have to be satisfy:

$$\begin{cases} \dfrac{\partial I_{\mathrm{p3}}}{\partial \zeta_2} = 0 \\ \dfrac{\partial I_{\mathrm{p3}}}{\partial \nu} = 0 \end{cases} \tag{A.25}$$

Differentiating the performance index I_{k1} expressed in equation (A.9) with respect to ζ_2 and ν, and setting these equal to zero, yields to a pair of simultaneous equations:

$$\begin{aligned} -\mu\nu^5[\mu\nu^2\zeta_1^2 + 2\mu\nu^3\zeta_1\zeta_2 + \zeta_2^2 - 2\nu^2\zeta_2^2 + 2\mu\nu^2\zeta_2^2 + \nu^4\zeta_2^2 - \mu\nu^4\zeta_2^2 + \mu^2\nu^4\zeta_2^2 - 4\zeta_1^2\zeta_2^2 \\ - 4\mu\nu^2\zeta_1^2\zeta_2^2 - 8\nu\zeta_1\zeta_2^3 - 8\mu\nu^3\zeta_1\zeta_2^3 - 4\nu^2\zeta_2^4 - 4\mu\nu^4\zeta_2^4] = 0 \end{aligned} \tag{A.26a}$$

$$\begin{aligned} -\mu\nu^3\zeta_2[\mu\nu^3\zeta_1^2 + 4\zeta_1\zeta_2 - 4\nu^2\zeta_1\zeta_2 + 4\mu\nu^2\zeta_1\zeta_2 + 2\mu\nu^4\zeta_1\zeta_2 + 8\nu^2\zeta_1^3\zeta_2 + 5\nu\zeta_2^2 - 6\nu^3\zeta_2^2 \\ + 6\mu\nu^3\zeta_2^2 + \nu^5\zeta_2^2 - \mu\nu^5\zeta_2^2 + \mu^2\nu^5\zeta_2^2 + 12\nu\zeta_1^2\zeta_2^2 + 16\nu^3\zeta_1^2\zeta_2^2 \\ + 4\mu\nu^3\zeta_1^2\zeta_2^2 + 24\nu^2\zeta_1\zeta_2^3 + 8\nu^4\zeta_1\zeta_2^3 + 8\mu\nu^4\zeta_1\zeta_2^3 + 12\nu^3\zeta_2^4 + 4\mu\nu^5\zeta_2^4] \\ = 0 \end{aligned} \tag{A.28b}$$

Following the same procedure for I_{k} and I_{p3}, the partial derivates of the performance index I_{k} expressed in equation (A.15) are given by:

$$\begin{aligned} -\mu\nu^3[\zeta_1^2 - 2\nu^2\zeta_1^2 + 2\mu\nu^2\zeta_1^2 + \nu^4\zeta_1^2 + \mu^2\nu^4\zeta_1^2 + 4\nu^2\zeta_1^4 + 4\mu\nu^5\zeta_1\zeta_2 + 8\nu\zeta_1^3\zeta_2 + 8\nu^3\zeta_1^3\zeta_2 \\ + 8\mu\nu^3\zeta_1^3\zeta_2 + \nu^2\zeta_2^2 - 2\nu^4\zeta_2^2 + 2\mu\nu^4\zeta_2^2 + \nu^6\zeta_2^2 + \mu^2\nu^6\zeta_2^2 + 12\nu^2\zeta_1^2\zeta_2^2 \\ + 4\nu^4\zeta_1^2\zeta_2^2 + 12\mu\nu^4\zeta_1^2\zeta_2^2 - 4\nu^4\zeta_2^4 - 4\mu\nu^6\zeta_2^4] = 0 \end{aligned} \tag{A.27a}$$

$$-\mu\nu^2\zeta_2[-3\zeta_1^2+2\nu^2\zeta_1^2-2\mu\nu^2\zeta_1^2+\nu^4\zeta_1^2+\mu^2\nu^4\zeta_1^2-4\nu^2\zeta_1^4+4\mu\nu^5\zeta_1\zeta_2-8\nu\zeta_1^3\zeta_2 + 5\nu^2\zeta_2^2-6\nu^4\zeta_2^2+6\mu\nu^4\zeta_2^2+\nu^6\zeta_2^2+\mu^2\nu^6\zeta_2^2-4\nu^2\zeta_1^2\zeta_2^2+12\nu^4\zeta_1^2\zeta_2^2 + 4\mu\nu^4\zeta_1^2\zeta_2^2+16\nu^3\zeta_1\zeta_2^3+8\nu^5\zeta_1\zeta_2^3+8\mu\nu^5\zeta_1\zeta_2^3+12\nu^4\zeta_2^4+4\mu\nu^6\zeta_2^4] = 0 \quad \text{(A.29b)}$$

and the partial derivates of the performance index I_{p3} expressed in equation (A.22) are given by:

$$\mu\nu^5\zeta_1[\mu\nu^2\zeta_1^2+2\mu\nu^3\zeta_1\zeta_2+\zeta_2^2-2\nu^2\zeta_2^2+2\mu\nu^2\zeta_2^2+\nu^4\zeta_2^2-\mu\nu^4\zeta_2^2+\mu^2\nu^4\zeta_2^2-4\zeta_1^2\zeta_2^2 - 4\mu\nu^2\zeta_1^2\zeta_2^2-8\nu\zeta_1\zeta_2^3-8\mu\nu^3\zeta_1\zeta_2^3-4\nu^2\zeta_2^4-4\mu\nu^4\zeta_2^4] = 0 \quad \text{(A.28a)}$$

$$\mu\nu^3\zeta_1\zeta_2[\mu\nu^3\zeta_1^2+4\zeta_1\zeta_2-4\nu^2\zeta_1\zeta_2+4\mu\nu^2\zeta_1\zeta_2+2\mu\nu^4\zeta_1\zeta_2+8\nu^2\zeta_1^3\zeta_2+5\nu\zeta_2^2-6\nu^3\zeta_2^2 + 6\mu\nu^3\zeta_2^2+\nu^5\zeta_2^2-\mu\nu^5\zeta_2^2+\mu^2\nu^5\zeta_2^2+12\nu\zeta_1^2\zeta_2^2+16\nu^3\zeta_1^2\zeta_2^2 + 4\mu\nu^3\zeta_1^2\zeta_2^2+24\nu^2\zeta_1\zeta_2^3+8\nu^4\zeta_1\zeta_2^3+8\mu\nu^4\zeta_1\zeta_2^3+12\nu^3\zeta_2^4+4\mu\nu^5\zeta_2^4] = 0 \quad \text{(A.30b)}$$

Simultaneous equation (A.26) and (A.27) and (A.28) are all satisfied for $\zeta_2 = 0$ and $\nu = 0$ corresponding to minimising I_{k1} and I_{k} and maximise I_{p3}. The other solutions can be found setting to zero the terms in squared brackets. If $\zeta_1 \neq 0$ the term in square brackets in equation

(A.26a) is equal to the term in square brackets in equation (A.28a) and the term in square brackets in equation (A.26b) is equal to the term in square brackets in equation (A.28b) which means that conditions for the minimisation of the kinetic energy of the mass m_1 are the same of those for the maximisation of the total power absorbed.

The total kinetic energy of the system is minimised for a different value of ζ_2 and ν, however, if ζ_1 is equal zero the primary system is undamped. Equations (A.26a) and (A.26b) for $\partial I_{\mathrm{k1}}/\partial\zeta_2$ and $\partial I_{\mathrm{k1}}/\partial\nu$ then reduce to:

$$1+2(-1+\mu)\nu^2 — 1+\mu-\mu^2\nu^4-4(\nu^2+\mu\nu^4)\zeta_2^2 = 0$$
$$5+6(-1+\mu)\nu^2 — 1+\mu-\mu^2\nu^4+4\nu^2(3+\mu\nu^2)\zeta_2^2 = 0 \quad \text{(A.29)}$$

And equation (A.28a) and (A.28b) for $\partial I_{\mathrm{k}}/\partial\zeta_2$ and $\partial I_{\mathrm{k}}/\partial\nu$ then reduce to:

$$1+2(-1+\mu)\nu^2+(1+\mu^2)\nu^4-4(\nu^2+\mu\nu^4)\zeta_2^2 = 0$$
$$5+6(-1+\mu)\nu^2+(1+\mu^2)\nu^4+4\nu^2(3+\mu\nu^2)\zeta_2^2 = 0 \quad \text{(A.30)}$$

For the complexity of equations (A.29) and (A.30) it has not been possible to find explicitly expression for ζ_2 and ν. However, if the value of ν is fixed the optimum damping that minimise I_{k1} is given by:

$$\zeta_{2\text{optk1}} = \frac{\sqrt{1 - 2\nu^2 + 2\mu\nu^2 + \nu^4 - \mu\nu^4 + \mu^2\nu^4}}{\sqrt{4\nu^2 + 4\mu\nu^4}} \tag{A.31}$$

and the optimum damping that minimise I_k is given by:

$$\zeta_{2\text{optk}} = \frac{\sqrt{1 - 2\nu^2 + 2\mu\nu^2 + \nu^4 + \mu^2\nu^4}}{\sqrt{4\nu^2 + 4\mu\nu^4}} \tag{A.32}$$

The difference between $\zeta_{2\text{optk}}$ and $\zeta_{2\text{opt1}}$ is given by:

$$\zeta_{2\text{optk}} - \zeta_{2\text{optk1}} = \frac{1}{2}\sqrt{\frac{\mu\nu^2}{1 + \mu\nu^2}} \tag{A.33}$$

Equation (A.33) shows that the difference between the two optimum values is smaller than 0.5 for all the value of μ and ν. Figure A.2 shows the two optimum values of the damping ratio $\zeta_{2\text{opt1}}$ and $\zeta_{2\text{optk}}$ as function of the mass ratio μ when $\nu = 1.5$. The plot shows that the difference of two optimum values never exceeded 0.5.

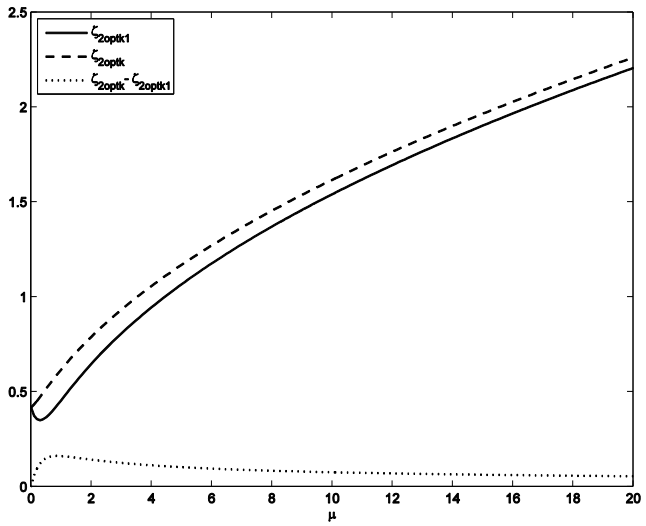

Figure A.2: $\zeta_{2\text{optk1}}$ (solid-line), $\zeta_{2\text{optk}}$ (dashed line) and $\zeta_{2\text{optk}}$-$\zeta_{2\text{optk1}}$ (dotted line) as function of the mass ratio μ when $\nu = 1.5$.

The performance index I_{p3}, however, becomes equal to π if ζ_1 is exactly zero. The absorbed power is then independent on ζ_2 and ν, as can be seen from equation (A.28a) and equation (A.28b), since they both are proportional to ζ_1.

Appendix B: Mathematical model of a distributed structure controlled by multiple velocity feedback loops

B.1 Natural frequencies and mode shapes for beams and panels

- **Beam**

The natural frequencies of a beam of length *l* with any type of boundary condition are given by:

$$\omega_n = \sqrt{\frac{EI}{\rho A}} k_{nb}^2 \qquad \text{where} \qquad n = 1, 2, 3, \ldots \tag{B.1}$$

where E is Young's modulus of the beam material, I is the second order moment of inertia of the beam cross-section area *A*, ρ is the material's density, and k_{nb} is a constant depending on the boundary conditions.

Table B.1:Natural frequencies of a beam

Boundary conditions	ω_n	
	n	$k_{nb}l$
Simply supported	1, 2, …	$n\pi$
Clamped at both ends	1	4.73004
	2	7.85320
	3	10.9956
	4	14.1372
	5	17.2788
	6, 7, …	$(2n+1)\pi/2$
Cantilever	1	1.87510
	2	4.69409
	3	7.85476
	4	10.9955
	5	14.1372
	6, 7, …	$(2n-1)\pi/2$

Table B.1 and 2 show the values of k_{nb} and the modeshapes respectively for a both ends simply supported beam, both ends clamped beam and a cantilever beam. The modeshape are normalised such that $\int_0^l \phi^2(x)dx = l$

Table B.2: Characteristic beam functions

Boundary conditions	$\phi_{1,3,5,\ldots}(x)$ with $i = (n+1)/2$	$\phi_{2,4,6,\ldots}(x)$ with $j = n/2$
Simply supported at both ends	$\phi_n(x) = \sqrt{2}\sin\left(\frac{n\pi x}{l_x}\right)$	
clamped at both ends	$\phi_n(x) = \sqrt{2}\left\{\cos\left[\gamma_i\left(\frac{x}{l_x}-\frac{1}{2}\right)\right] + k_n\cosh\left[\gamma_i\left(\frac{x}{l_x}-\frac{1}{2}\right)\right]\right\}$ $k_n = \frac{\sin\left(\frac{1}{2}\gamma_i\right)}{\sinh\left(\frac{1}{2}\gamma_i\right)}$ with $\tan\left(\frac{1}{2}\gamma_i\right) + \tanh\left(\frac{1}{2}\gamma_i\right) = 0$	$\phi_n(x) = \sqrt{2}\left\{\cos\left[\gamma_j\left(\frac{x}{l_x}-\frac{1}{2}\right)\right] + k_n\cosh\left[\gamma_j\left(\frac{x}{l_x}-\frac{1}{2}\right)\right]\right\}$ $k_n = \frac{\sin\left(\frac{1}{2}\gamma_j\right)}{\sinh\left(\frac{1}{2}\gamma_j\right)}$ with $\tan\left(\frac{1}{2}\gamma_i\right) - \tanh\left(\frac{1}{2}\gamma_i\right) = 0$
Cantilever beam	$\phi_n(x) = \sqrt{2}\left\{\cos\left[\frac{\gamma_n x}{l_x}\right] + \cosh\left[\frac{\gamma_n x}{l_x}\right] + k_n\sin\left[\frac{\gamma_n x}{l_x}\right] - \sinh\left[\frac{\gamma_n x}{l_x}\right]\right\}$ $k_n = \frac{\sin\gamma_n - \sinh\gamma_n}{\cos\gamma_n - \cosh\gamma_n}$ with $\cos\gamma_n\cosh\gamma_n = -1$	

Note that the first values for γ in Table B.2 can be determined using numerical root-finding methods, where it is important to yield results with a high precision. For values larger than 10 the numerical methods can fail to determine the roots correctly. For *i* greater than 10, γ_i is given by:

$$\frac{(4i+1)\pi}{2} \quad \text{for} \quad \tan\left(\frac{1}{2}\gamma_i\right) - \tanh\left(\frac{1}{2}\gamma_i\right) = 0$$

$$\frac{(4i-1)\pi}{2} \quad \text{for} \quad \tan\left(\frac{1}{2}\gamma_i\right) - \tanh\left(\frac{1}{2}\gamma_i\right) = 0$$

$$\frac{(2i-1)\pi}{2} \quad \text{for} \quad \cos\gamma_i\cosh\gamma_i = -1$$

- **Plate**

The natural frequencies of a panel of dimensions $l_x \times l_y$ with any type of boundary condition are given by:

$$\omega_{mn} = \sqrt{\frac{Eh^2}{12\rho(1-\upsilon^2)}}\left(\frac{\pi}{l_x}\right)^2 q_{mn} \tag{B.2}$$

where $q_{mn} = \sqrt{G_x^4(m) + G_y^4(n)(l_x/l_y)^4 + 2(l_x/l_y)^2[\upsilon H_x(m)H_y(n) + (1-\upsilon)J_x(m)J_y(n)]}$.

The constants G_x, H_x, J_x and G_y, H_y, J_y are given in Table B.2 for a all-sides simply supported panel and a all-sides clamped panel.

Table B.3: Values of the constants G_x, H_x and J_x. He values of the constants G_y, H_y and J_y are the same for equivalent boundary conditions

Boundary conditions	m	G_x	H_x	J_x
Simply supported	1, 2, 3, …	m	m^2	m^2
Clamped	1 2, 3, …	1.506 $m+\frac{1}{2}$	1.248 $\left(m+\frac{1}{2}\right)^2\left[1-\frac{4}{(2m+1)\pi}\right]$	1.248 $\left(m+\frac{1}{2}\right)^2\left[1-\frac{4}{(2m+1)\pi}\right]$

The mass-normalised modeshapes $\phi_{mn}(x,y)$ are given by:

$$\phi_{mn}(x,y) = \phi_m(x)\phi_n(y) \tag{B.3}$$

where mass-normalised characteristic beam mode functions are given in Table B.2.

B.2 Deterministic model of a distributed structure excited by a primary point force and controlled by multiple velocity feedback loops

In this section, the implementation of *R* direct velocity feedback control loops on a distributed lightly damped structure is considered. The velocities at the control positions and the control forces are grouped into the following column vectors:

$$\tilde{\mathbf{v}}_{\mathrm{c}} = \begin{bmatrix} \tilde{v}_{c1}(j\omega) \\ \vdots \\ \tilde{v}_{c\mathrm{R}}(j\omega) \end{bmatrix}, \tag{B.4}$$

$$\tilde{\mathbf{f}}_{\mathrm{c}}(j\omega) = \begin{bmatrix} \tilde{f}_{c1}(j\omega) \\ \vdots \\ \tilde{f}_{c\mathrm{R}}(j\omega) \end{bmatrix}, \tag{B.5}$$

where $v_{c\mathrm{r}}$ and $f_{c\mathrm{r}}$ are the velocity and the force at *r*-th control position. The velocities at the control positions, can be expressed in the following matrix form:

$$\tilde{\mathbf{v}}_{\mathrm{c}} = \boldsymbol{\phi}_c \tilde{\mathbf{a}}, \tag{B.6}$$

where, in this case, $\boldsymbol{\phi}_c$ is a $(R \times N)$ matrix whose rows are the modal vectors $\boldsymbol{\phi}_{cr} = [\phi_{cr,1}(x,y) \quad \phi_{cr,2}(x,y) \quad \cdots \quad \phi_{cr,N}(x,y)]$ at the *r*-th control position:

$$\boldsymbol{\phi}_c = \begin{bmatrix} \boldsymbol{\phi}_{c1} \\ \vdots \\ \boldsymbol{\phi}_{c\mathrm{R}} \end{bmatrix} = \begin{bmatrix} \phi_{c1,1}(x,y) & \phi_{c1,2}(x,y) & \cdots & \phi_{c1,N}(x,y) \\ & \vdots & & \\ \phi_{cR,1}(x,y) & \phi_{cR,2}(x,y) & \cdots & \phi_{cR,N}(x,y) \end{bmatrix}, \tag{B.7}$$

Also, $\tilde{\mathbf{a}}$ is the column vector with the first *N* modal excitation terms due to both primary and control excitations given by:

$$\tilde{\mathbf{a}} = \tilde{\mathbf{a}}_c + \tilde{\mathbf{a}}_p \tag{B.8}$$

However, assuming multiple primary and multiple control forces these two vectors are given by:

$$\tilde{\mathbf{a}}_p = \tilde{\boldsymbol{\Omega}} \boldsymbol{\phi}_p^T \tilde{\mathbf{f}}_p \tag{B.9}$$

$$\tilde{\mathbf{a}}_c = \tilde{\boldsymbol{\Omega}} \boldsymbol{\phi}_c^T \tilde{\mathbf{f}}_c \tag{B.10}$$

$\boldsymbol{\Omega}$ is the diagonal matrix of the resonant terms Ω_n given by:

$$\tilde{\Omega}_n = \frac{j\omega}{M_n[\omega_n^2 - \omega^2 + j2\zeta_n\omega_n\omega]} \tag{B.11}$$

where M_n is *n*-th the modal mass, ζ_n is the *n*-th viscous damping ratio and ω_n is the *n*-th natural frequency.

$\boldsymbol{\phi}_p$ is a $(R \times N)$ matrix whose rows are the modal vectors $\boldsymbol{\phi}_{ps} = [\phi_{ps,1}(x,y) \quad \phi_{ps,2}(x,y) \cdots \quad \phi_{ps,N}(x,y)]$ at the *s*-th primary position:

$$\boldsymbol{\phi}_s = \begin{bmatrix} \boldsymbol{\phi}_{p1} \\ \vdots \\ \boldsymbol{\phi}_{pS} \end{bmatrix} = \begin{bmatrix} \phi_{p1,1(x,y)} & \phi_{p1,2}(x,y) & \cdots & \phi_{p1,N} \\ & \vdots & & \\ \phi_{pS,1(x,y)} & \phi_{pS,2}(x,y) & \cdots & \phi_{pS,N}(x,y) \end{bmatrix}. \tag{B.12}$$

Finally $\mathbf{f}_p$ is the vector with the forces at the *S* primary positions:

$$\tilde{\mathbf{f}}_p = \begin{bmatrix} \tilde{f}_{p1}(j\omega) \\ \vdots \\ \tilde{f}_{pS}(j\omega) \end{bmatrix}, \tag{B.13}$$

If decentralised velocity feedback loops are implemented, then it is possible to write:

$$\tilde{\mathbf{f}}_c = -\mathbf{G}\tilde{\mathbf{v}}_c, \tag{B.14}$$

where $\mathbf{G}$ is a diagonal matrix of the control gains relative to each single control loop:

$$\mathbf{G} = \begin{bmatrix} g_1 & & 0 \\ & \ddots & \\ 0 & & g_R \end{bmatrix}, \tag{B.15}$$

Substituting equation (B.15), in equation (B.10) and then equations (B.9) and (B.10) in (B.8) yields:

$$\tilde{\mathbf{a}} = \tilde{\mathbf{\Omega}}\boldsymbol{\phi}_p^T\tilde{\mathbf{f}}_p - \tilde{\mathbf{\Omega}}\boldsymbol{\phi}_c^T\mathbf{G}\tilde{\mathbf{v}}_c, \tag{B.16}$$

which, after substitution into equation (B.6) and some further mathematical manipulations, yields:

$$\tilde{\mathbf{v}}_c = \tilde{\mathbf{Q}}\tilde{\mathbf{f}}_p, \tag{B.17}$$

where $\tilde{\mathbf{Q}}$ is given by:

$$\tilde{\mathbf{Q}} = [\left(\mathbf{I} + \boldsymbol{\phi}_c\tilde{\mathbf{\Omega}}\boldsymbol{\phi}_c^T\mathbf{G}\right)^{-1}\boldsymbol{\phi}_c\tilde{\mathbf{\Omega}}\boldsymbol{\phi}_p^T]. \tag{B.18}$$

Thus, substituting (B.17) in (B.16) $\tilde{\mathbf{a}}$ becomes:

$$\tilde{\mathbf{a}} = \tilde{\mathbf{J}}\tilde{\mathbf{f}}_p, \tag{B.19}$$

where $\tilde{\mathbf{J}}$ is given by:

$$\tilde{\mathbf{J}} = \tilde{\mathbf{\Omega}}\boldsymbol{\phi}_p^T - \tilde{\mathbf{\Omega}}\boldsymbol{\phi}_c^T\mathbf{G}\tilde{\mathbf{Q}}, \tag{B.20}$$

The transverse velocity at a generic point of the plate $v(x, y, \omega)$ depends on both forces $\tilde{\mathbf{f}}_\mathrm{p}$ and $\tilde{\mathbf{f}}_\mathrm{c}$, and it can be expressed with the following matrix equation:

$$\tilde{v}(x, y, \omega) = \boldsymbol{\phi}_{xy}\tilde{\mathbf{a}} = \boldsymbol{\phi}_{xy}\tilde{\mathbf{J}}\tilde{\mathbf{f}}_\mathrm{p} \tag{B.21}$$

Where $\boldsymbol{\phi}_{xy} = [\phi_{xy,1}(x, y) \quad \phi_{xy,2}(x, y) \quad \cdots \quad \phi_{xy,N}(x, y)]$ is a row vector with the first N natural modes of the plate at the generic (x, y) position on the plate. The instantaneous total kinetic energy of the structure is given by the product of the mass structure per unit area and the squared velocity integrated over the surface of the structure:

$$K(t) = \frac{1}{2}\int_S \rho h\, v^2(x, y, t)ds \tag{B.22}$$

where S is the surface of the structure. Assuming ρh to be constant over the surface of the structure $K(t)$ becomes:

$$K(t) = \frac{1}{2}\rho h \int_S v^2(x,y,t)ds \tag{B.23}$$

The time-averaged total panel energy is given by:

$$\overline{K}(t) = \frac{1}{2}\rho h \int_S \frac{1}{T}\int_0^T v^2(x,y,t)dt\, ds \tag{B.24}$$

Where T is a suitable period of time over which the mean squared velocity is estimated Assuming time-harmonic vibration the time averaged integral can be rewritten in terms of the magnitude of the complex velocity to give:

$$\frac{1}{T}\int_0^T v^2(x,y,t)dt = \frac{1}{2}|\tilde{v}(x,y,\omega)|^2 \tag{B.25}$$

which yields the time-averaged total kinetic energy of the panel as:

$$\overline{K} = K(\omega) = \frac{\rho h}{4}\int_S |\tilde{v}(x,y,\omega)|^2 ds \tag{B.26}$$

Substituting equation (B.21) in (B.26) and considering the orthogonality condition of the natural modes yields:

$$K(\omega) = \frac{\rho h}{4}\int_S \tilde{\mathbf{f}}_p^H \tilde{\mathbf{J}}^H \boldsymbol{\phi}_{xy}^H \boldsymbol{\phi}_{xy} \tilde{\mathbf{J}} \tilde{\mathbf{f}}_p ds = \frac{1}{4} M \tilde{\mathbf{J}}^H \tilde{\mathbf{J}}, \tag{B.27}$$

The instantaneous total power absorbed by multiple feedback loops is given by:

$$P(t) = \frac{1}{2}\mathbf{f}^T(t)\mathbf{v}(t) = \frac{1}{2}\mathrm{trace}(\mathbf{f}_c(t)\mathbf{v}_c^T(t)) \tag{B.28}$$

and considering proportional control equation (20) can be rewritten as:

$$P(t) = \frac{1}{2}\mathrm{trace}(\mathbf{G}\mathbf{v}_c(t)\mathbf{v}_c^T(t)) \tag{B.29}$$

The time-averaged total power absorbed is given by:

$$\bar{P}(t) = \frac{1}{2}\mathrm{trace}(\mathbf{G}\frac{1}{T}\int_0^T \mathbf{v}_c(t)\mathbf{v}_c^T(t)dt) \tag{B.30}$$

Assuming time-harmonic vibration the time averaged integral can be rewritten in terms of the magnitude of the complex velocity to give:

$$\bar{P} = P(\omega) = \frac{1}{4}\text{trace}(\mathbf{G}|\tilde{\mathbf{v}}_c(x,y,\omega)|^2) \tag{B.31}$$

which after substitution of equation (B.17) in (B.31) gives:

$$P_{abs}(\omega) = \tfrac{1}{4}\text{trace}(\mathbf{G}\tilde{\mathbf{Q}}\tilde{\mathbf{Q}}^{\text{H}}), \tag{B.32}$$

The individual power absorbed by the *r*-th control loop is given by the *r*-th diagonal term of the matrix $\mathbf{G}\tilde{\mathbf{Q}}\tilde{\mathbf{Q}}^{\text{H}}$.

B.3 Stochastic model of a distributed structure excited by a rain on the roof disturbance and controlled by multiple velocity feedback loops

In this section, the implementation of *R* direct velocity feedback control loops on a lightly damped flexible structure subject to a random excitation 'rain-on-the-roof' is considered.

When a distributed force is acted on the plate, the modal excitation term $\tilde{\mathbf{a}}_p$ in equation (B.8) becomes:

$$\tilde{\mathbf{a}}_p = \tilde{\mathbf{\Omega}}\tilde{\mathbf{q}}, \tag{B.33}$$

where $\tilde{\mathbf{q}} = [\tilde{F}_1(j\omega) \quad \tilde{F}_2(j\omega) \quad \cdots \quad \tilde{F}_N(j\omega)]^T$ is a column vector whose *n*-th term is the random excitation on the *n*-th natural mode of the structure given by:

$$\tilde{F}_n(j\omega) = \int_S \phi_n(x,y)\tilde{f}(x,y,\omega)dS, \tag{B.34}$$

where $\tilde{f}$ is the spatially random force acting on the structure. Thus, the same formulation as that presented for the deterministic model can be used to derive the response of the structure under control.

The velocities at control positions are given in equation (B.6) where the column vector $\tilde{\mathbf{a}}$ with the first N modal excitation terms due to both random and control excitations, $\tilde{\mathbf{a}}_{\text{p}}$ and $\tilde{\mathbf{a}}_c$ respectively is given by:

$$\tilde{\mathbf{a}} = \tilde{\mathbf{a}}_{\text{c}} + \tilde{\mathbf{\Omega}}\tilde{\mathbf{q}}. \tag{B.35}$$

Substituting equation (B.14) in (B.10) and then in (B.35) **a** can be written as:

$$\tilde{\mathbf{a}} = \tilde{\mathbf{\Omega}}\boldsymbol{\phi}_c^T\mathbf{G}\tilde{\mathbf{v}}_c + \tilde{\mathbf{\Omega}}\tilde{\mathbf{q}}. \tag{B.36}$$

Substituting equation (B.36) in (B.6) and some further mathematical manipulations, yields:

$$\tilde{\mathbf{v}}_c = \tilde{\mathbf{U}}\tilde{\boldsymbol{\Omega}}\tilde{\mathbf{q}}, \tag{B.37}$$

where $\tilde{\mathbf{U}}$ is given by:

$$\tilde{\mathbf{U}} = (\mathbf{I} + \boldsymbol{\phi}_c\tilde{\boldsymbol{\Omega}}\boldsymbol{\phi}_c^T\mathbf{G})^{-1}\boldsymbol{\phi}_c. \tag{B.38}$$

Substituting equation (B.37) in (B.36) $\tilde{\mathbf{a}}$ becomes:

$$\tilde{\mathbf{a}} = \tilde{\mathbf{D}}\tilde{\boldsymbol{\Omega}}\tilde{\mathbf{q}}, \tag{B.39}$$

where $\tilde{\mathbf{D}}$ is given by:

$$\tilde{\mathbf{D}} = \mathbf{I} - \tilde{\boldsymbol{\Omega}}\boldsymbol{\phi}_c^T\mathbf{G}\tilde{\mathbf{U}}. \tag{B.40}$$

The transverse velocity at a generic point of the structure $v(x, y, \omega)$ can be written as:

$$\tilde{v}(x, y, \omega) = \boldsymbol{\phi}_{xy}\tilde{\mathbf{a}} = \boldsymbol{\phi}_{xy}\tilde{\mathbf{D}}\tilde{\boldsymbol{\Omega}}\tilde{\mathbf{q}} \tag{B.41}$$

It can be demonstrated, that the power spectral density of a generic signal $x(t)$is given by:

$$S_{xx}(\omega) = \lim_{T\to\infty} E\left[\frac{1}{T}X^*(\omega)X(\omega)\right] \tag{B.42}$$

where $X(\omega)$ is the finite Fourier transform of $x(t)$ given by:

$$X(\omega) = \frac{1}{2\pi}\int_0^T x(t)e^{j\omega t}dt \tag{B.43}$$

and E[ ] denotes the expectation for an infinite sample length. Thus considering the general formulation for the instantaneous total kinetic energy in equation (B.24), the power spectral density of the total kinetic energy S_K, due to a time spatial stochastic disturbance over the structure surface, can be written as:

$$S_K(\omega) = \frac{1}{4}\rho h\int_S \lim_{T\to\infty} E\left[\frac{1}{T}\tilde{v}^*(x, y, \omega)\tilde{v}(x, y, \omega)\right]dS \tag{B.44}$$

Substituting (B.41) in (B.44) and taking in to account the orthogonality of the modes, the power spectral density of the kinetic energy of the structure becomes:

$$S_K(\omega) = \frac{1}{4}M\ \text{trace}\left(\tilde{\mathbf{D}}\tilde{\boldsymbol{\Omega}}\lim_{T\to\infty} E\left[\frac{1}{\mathrm{T}}\tilde{\mathbf{q}}\tilde{\mathbf{q}}^H\right]\tilde{\boldsymbol{\Omega}}^H\tilde{\mathbf{D}}^H\right) \tag{B.45}$$

Using equation (B.34), the *i*,*j* term of the matrix $\lim_{T\to\infty} E\left[\frac{1}{\mathrm{T}}\tilde{\mathbf{q}}\tilde{\mathbf{q}}^H\right]$ can be expressed as:

$$\lim_{T\to\infty} E\left[\frac{1}{\mathrm{T}}\tilde{q}_i\tilde{q}_j^H\right] = \int_{S'}\int_{S''}\phi_i(x',y')\phi_j(x'',y'')\lim_{T\to\infty} E\left[\frac{1}{T}\tilde{f}(x',y',\omega)\tilde{f}(x'',y'',\omega)\right]dS'dS''. \tag{B.46}$$

In case of 'rain-on-the-roof' excitation, the cross-expectation value of equation (B.46) is equal to one if $x' = x''$ and $y' = y''$ and zero otherwise. Thus, taking into account the orthogonality of the modes, the expectation value in equation (B.46) is equal to the identity matrix. Therefore equation (B.45) can be written as:

$$S_K(\omega) = \frac{1}{4}MS^2\,\mathrm{trace}\left(\tilde{\mathbf{D}}\tilde{\mathbf{\Omega}}\tilde{\mathbf{\Omega}}^H\tilde{\mathbf{D}}^H\right) \tag{B.47}$$

The power spectral density of total power absorbed by multiple decentralised control loops is given by:

$$S_P(\omega) = \frac{1}{4}\mathrm{trace}\left(\mathbf{G}\lim_{T\to\infty} E\left[\frac{1}{T}\tilde{\mathbf{v}}\tilde{\mathbf{v}}^{\mathrm{H}}\right]\right) \tag{B.48}$$

And thus substituting equation (B.37) in (B.48), $S_P(\omega)$ becomes:

$$S_P(\omega) = \frac{1}{4}S^2\,\mathrm{trace}\left(\mathbf{G}\tilde{\mathbf{U}}\tilde{\mathbf{\Omega}}\tilde{\mathbf{\Omega}}^H\tilde{\mathbf{U}}^H\right) \tag{B.49}$$

The individual power absorbed by the *r*-th control loop is given by the *r*-th diagonal term of the matrix $\mathbf{G}\tilde{\mathbf{U}}\tilde{\mathbf{\Omega}}\tilde{\mathbf{\Omega}}^H\tilde{\mathbf{U}}^H$.

Appendix C: Results for single channel systems

This appendix reports all the results, for each individual control channel, of the open loop frequency response function and simulated closed loop response. Figure C.1 shows the Bode diagram while Figure C.2 and Figure C.3 shows the Nyquist plot of the measured open loop FRF of the nine channels. Figure C.4 shows the simulated PSD of the kinetic energy of panel for different values of control gain obtained from measured responses. Finally, Figure C.5 shows the simulated frequency averaged kinetic energy and power absorbed by each single channel obtained from measured responses.

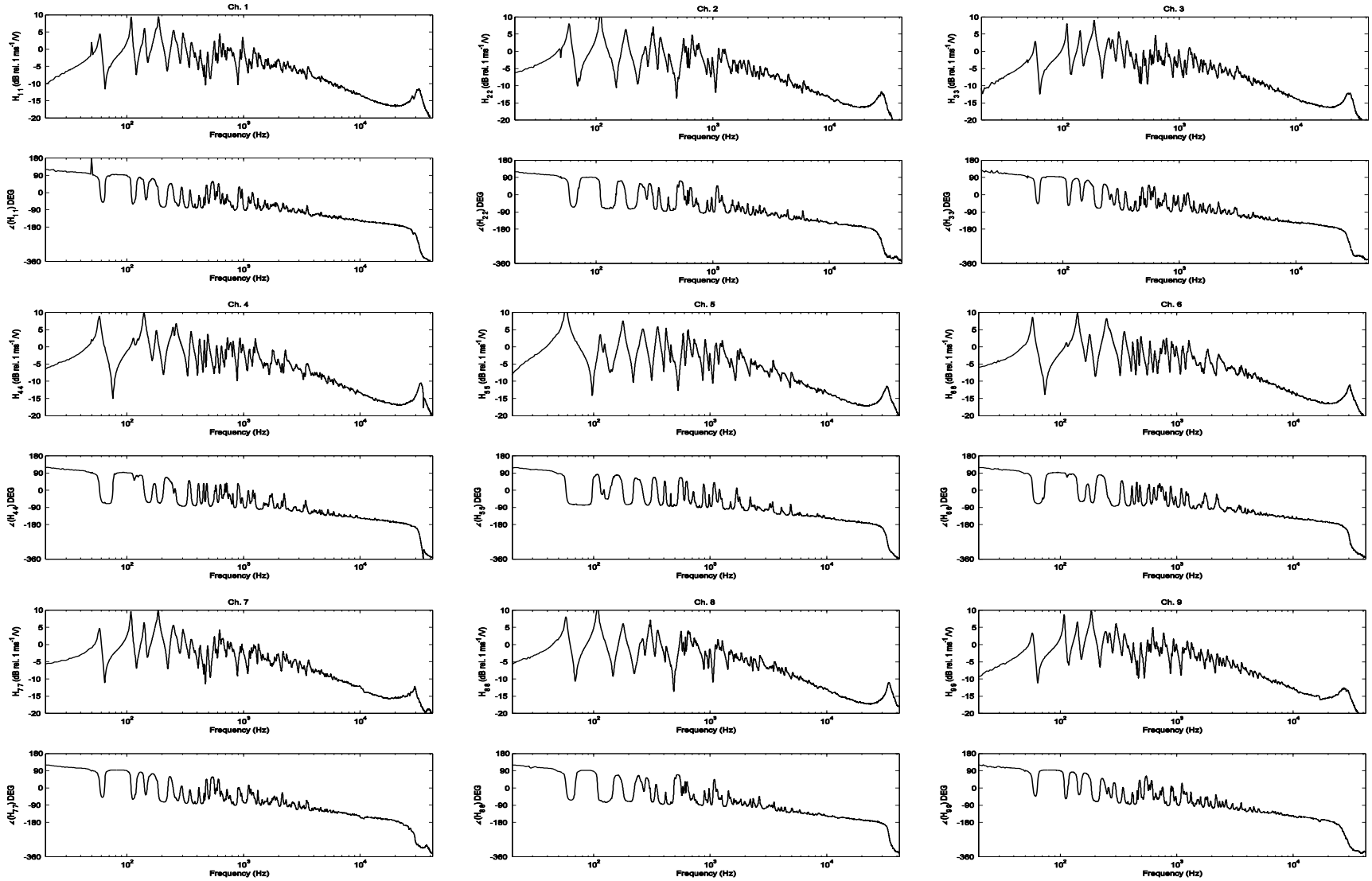

Figure C.1: Open loop FRFs using B&K accelerometers as feedback sensors

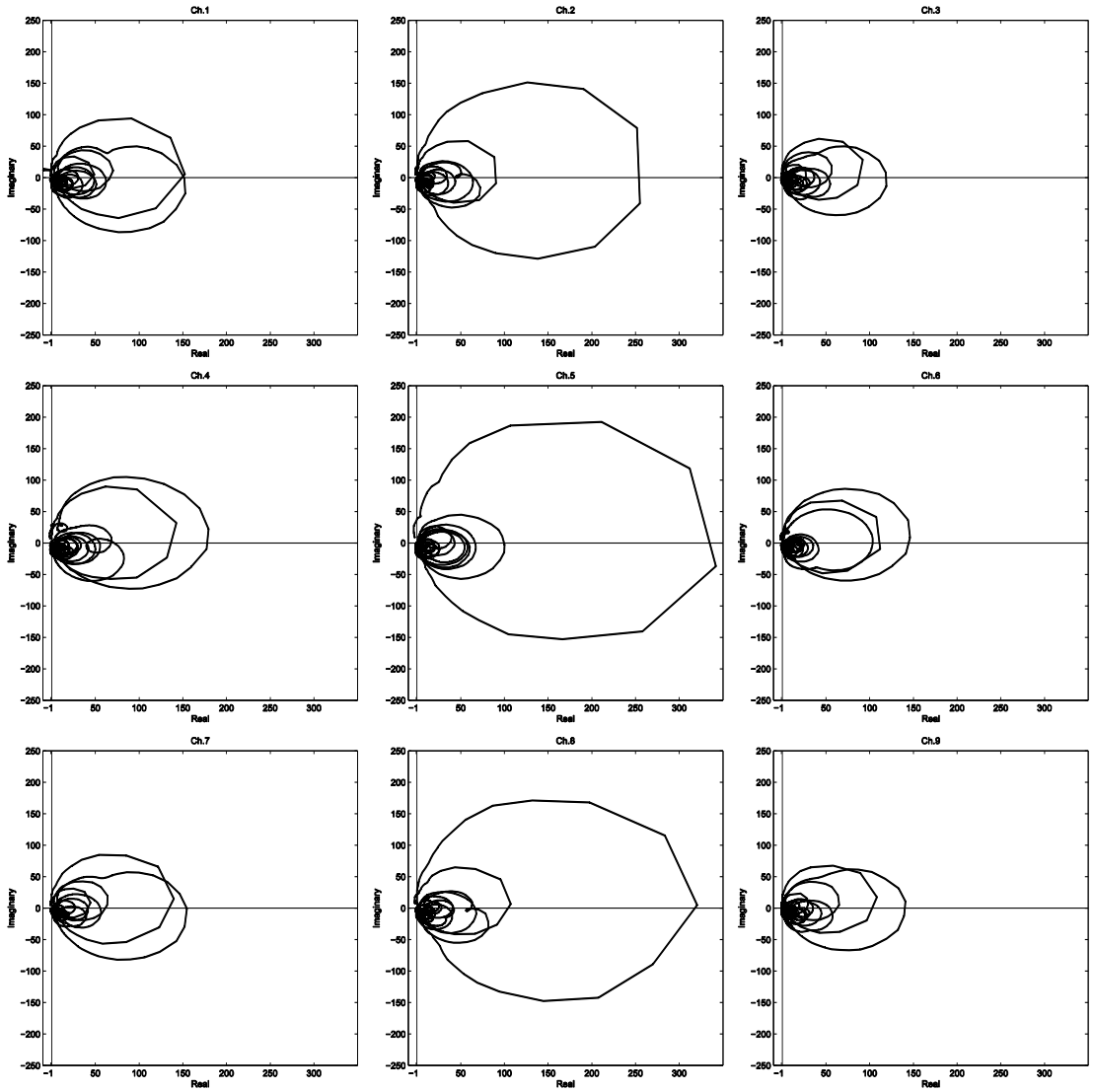

Figure C.2: Nyquist plots of the nine open loop sensor-actuator FRFs, acting alone, using B&K accelerometers

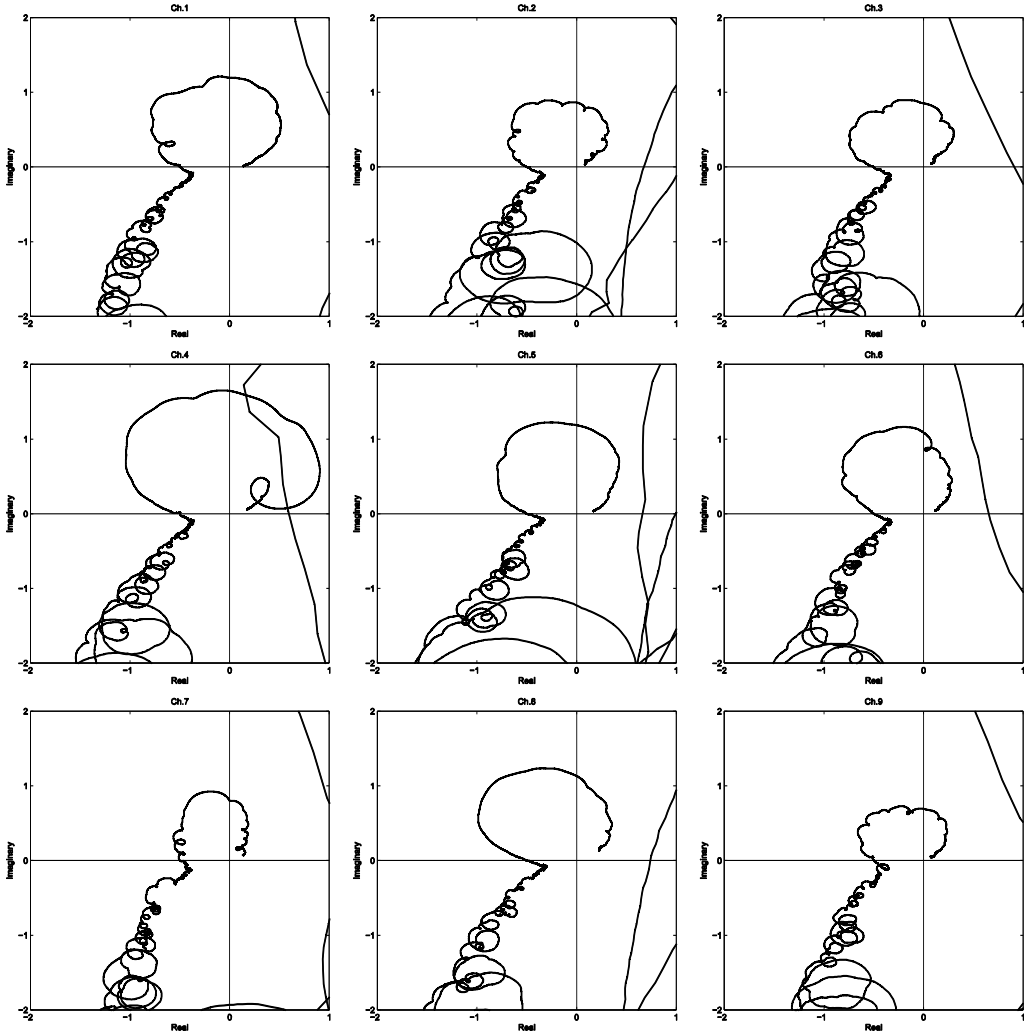

Figure C.3: Zoom at the origin of the Nyquist plots of nine open loop sensor-actuator FRFs, acting alone, using B&K accelerometers

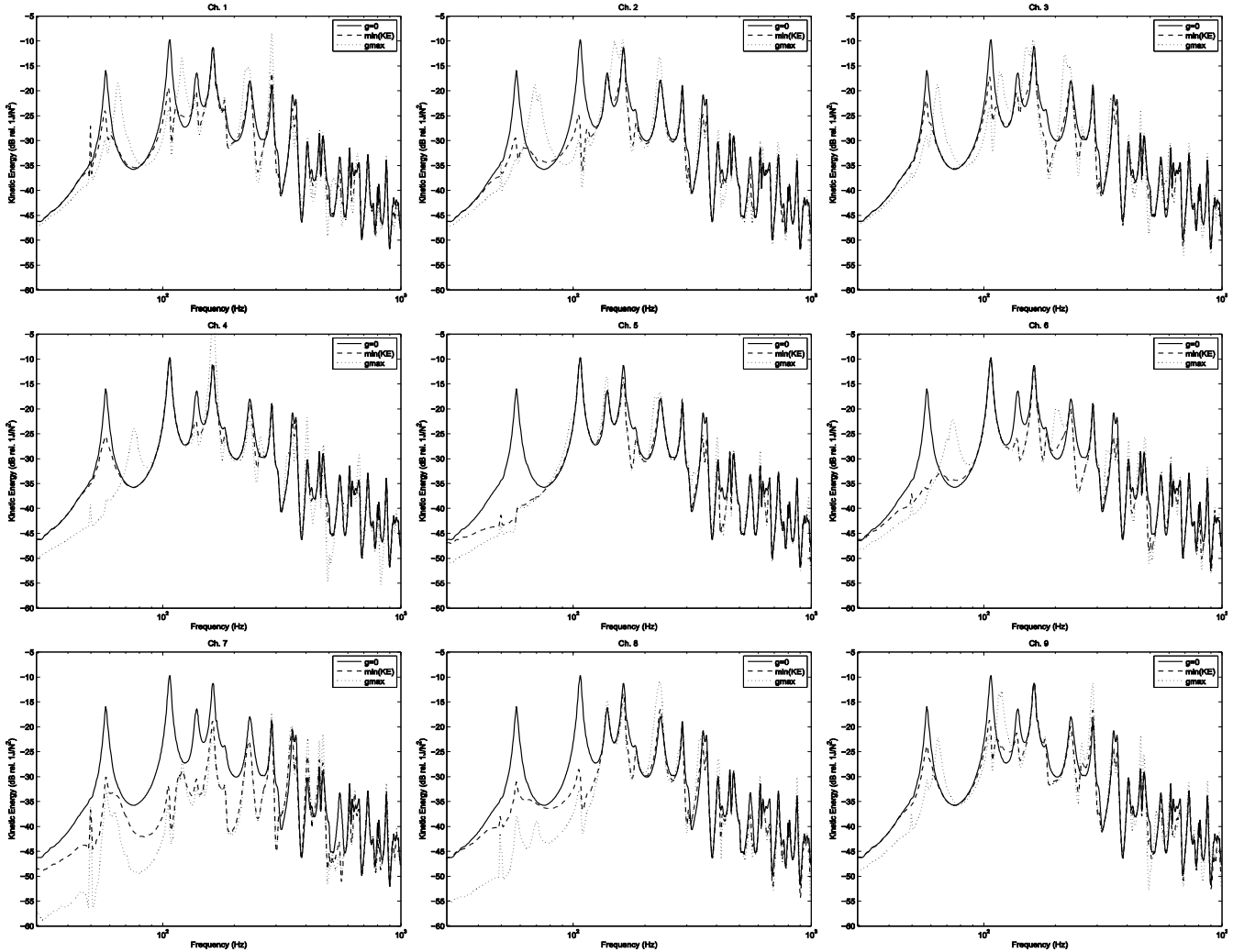

Figure C.4: Simulated of the kinetic energy of the panel without control (solid line), minimising the total kinetic energy (dashed-line) and implementing the gain that guarantees 6 dB gain margin from measured responses.

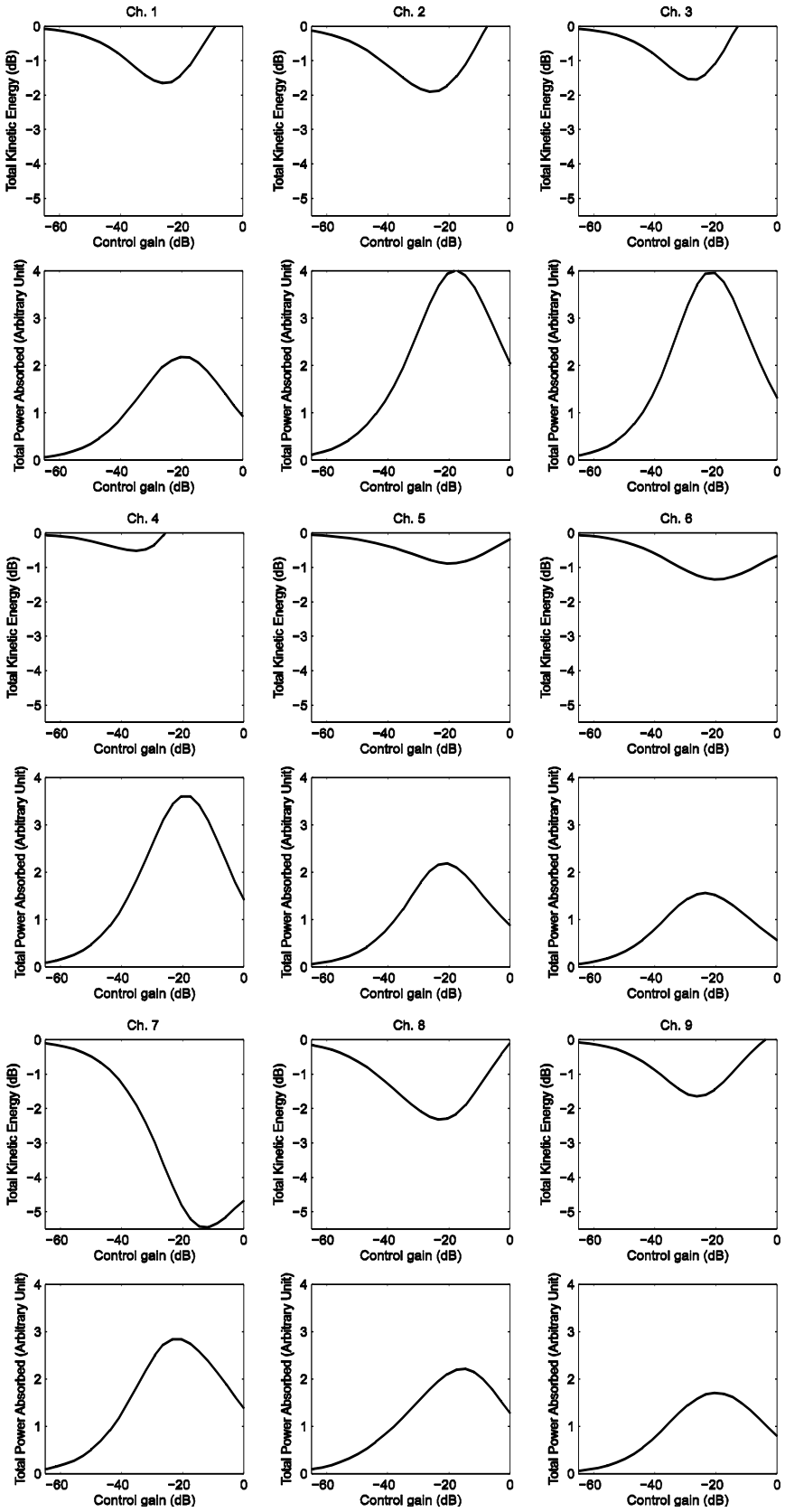

Figure C.5: Simulated from measured response of the total kinetic energy of the panel and total power absorbed a single channel control system.

Appendix D: Measured closed loop responses using control unit number 1

Experimental results for a single channel system using control unit number 1. The measured and simulated PSD of the estimated kinetic energy is shown in Figure D.1, for the same condition as in Figure 5.3 for control unit 1. Figure D.2 shows experimental and simulated total kinetic energy and power absorbed when control unit number 1 is used to control the response of the panel.

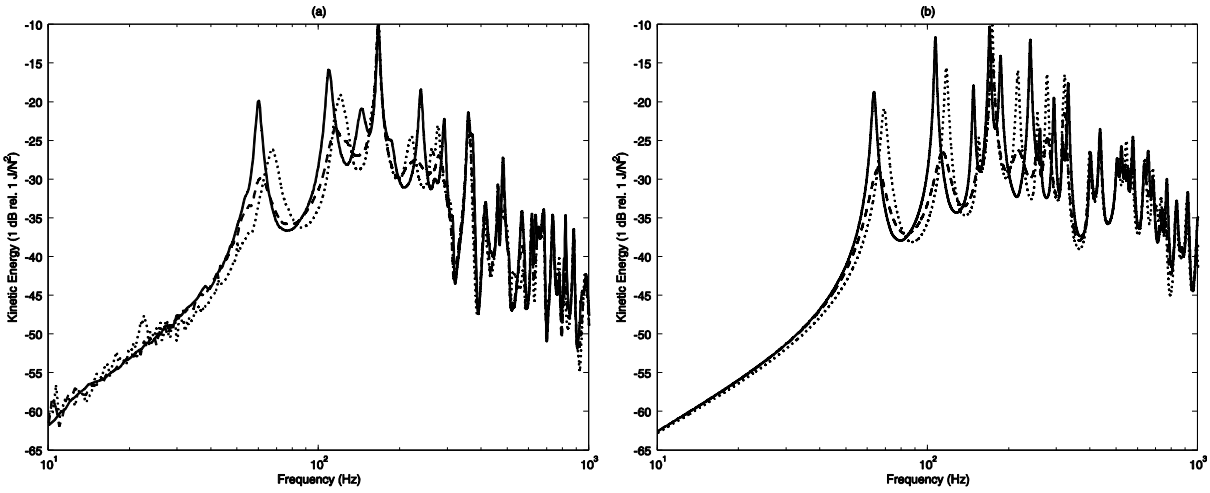

Figure D.1: PSD of the estimated kinetic energy of panel with no control (solid line), minimising the estimated frequency averaged kinetic energy of the panel (dashed line) and high control gain (dotted line) a) measured and b) simulated

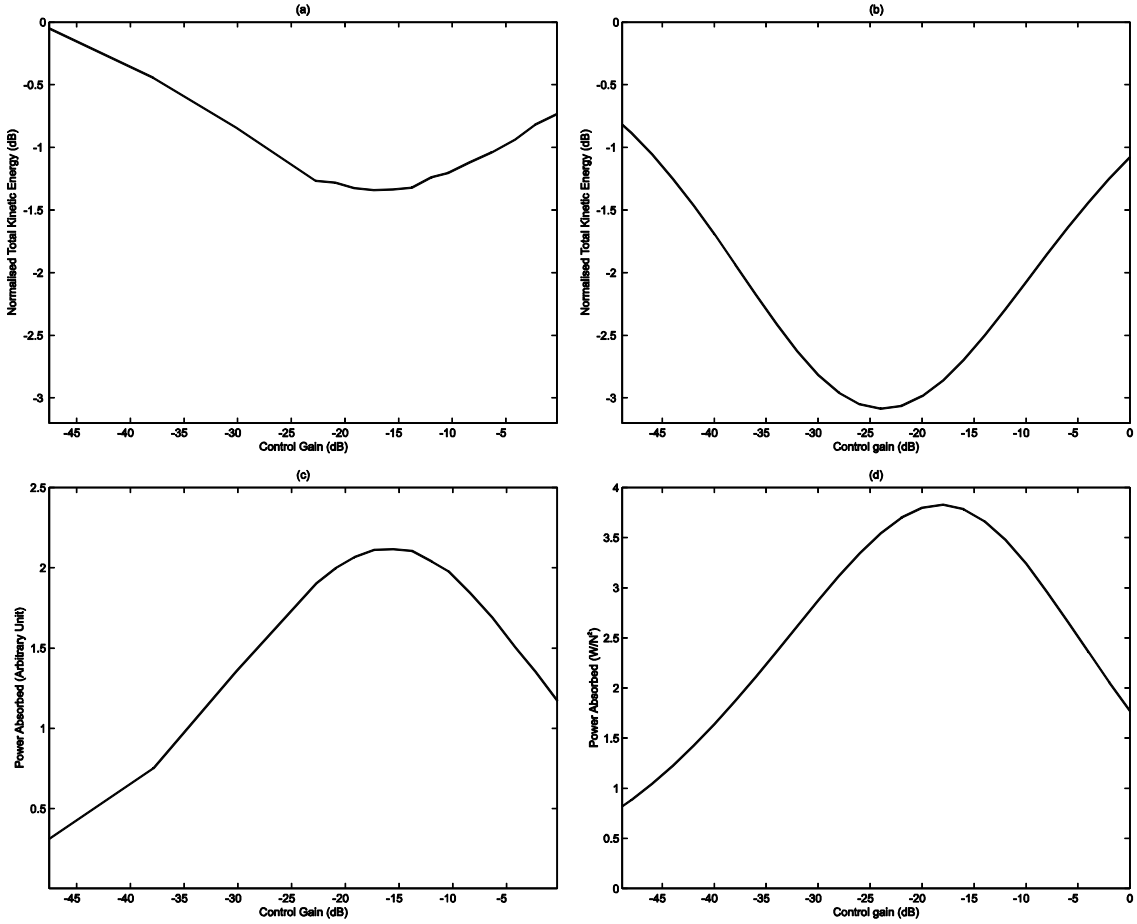

Figure D.2: a) experimental and b) simulated results of the normalised total kinetic energy of the panel and c) experimental and d) simulated results of the total power absorbed as function of the control gain 2

.

Appendix E: Impedances of an electromagnetic inertial actuator

In this appendix the analytical expression for the impedances used to describe the electromechanical behaviour of an electromagnetic inertial actuator are derived. In Figure E.1 a scheme of a one degree of freedom inertial actuator is shown.

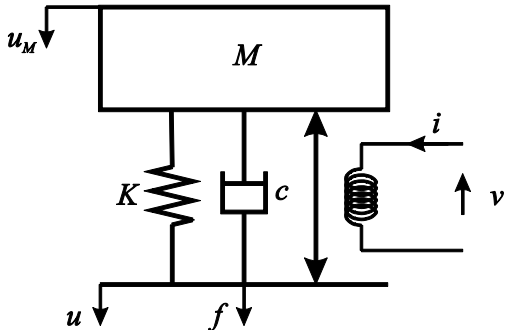

Figure E.1: Scheme of the electromagnetic inertial actuator

The open circuit mechanical impedance Z_{mo} is defined by:

$$Z_{\mathrm{mo}} = \left.\frac{f}{u}\right|_{i=0}. \tag{E.1}$$

and can be derived from the equilibrium of the forces in Figure E.1 as follow:

$$f = \frac{k + j\omega c(u - u_{\mathrm{M}})}{j\omega} \tag{E.2}$$

$$u_{\mathrm{M}} = f/j\omega \mathrm{M} \tag{E.3}$$

where k is the stiffness of the actuator suspension, c is the internal damping of the transducer, u is the velocity of the structure to which the actuator is attached, u_{M} is the velocity of the moving mass M. Substituting equation (E.3) in (E.2) Z_{mo} can be written as:

$$Z_{\mathrm{mo}} = \frac{f}{u} = \frac{j\omega M(k + j\omega c)}{j\omega c + k - \omega^2 M} \tag{E.4}$$

The transduction coefficient T_1 is defined as:

$$T_1 = \left.\frac{v}{u}\right|_{i=0}. \tag{E.5}$$

If the coil circuit is open the voltage *v* is produced by the electromagnetic coupling between the permanent magnet and the coil given by:

$$v = Bl(u - u_M) \tag{E.6}$$

where *B* is the magnetic flux density of the magnet and *l* is the length of the coil and $(u - u_M)$ is the relative velocity between the base of the actuator and the moving mass. Combining equations (E.2) and (E.4), the relative velocity between the moving mass and the structure is given by:

$$(u - u_M) = \frac{-\omega^2 M}{j\omega c + k - \omega^2 M} u. \tag{E.7}$$

Substituting equation (E.7) in (E.6) yields:

$$T_1 = Bl \frac{-\omega^2 M}{j\omega c + k - \omega^2 M} \tag{E.8}$$

However the two transduction coefficients have the same absolute value and their product is negative real so that $T_1 = -T_2$. Z_{eb} is the blocked electrical impedance defined as:

$$T_1 = \frac{v}{i}\Big|_{u=0}. \tag{E.9}$$

In this case the force generated by the actuator is given by the electromagnetic coupling coefficient *Bl* times the current *i* or by the velocity of the moving mass times the mechanical impedance of the actuator when *u*=0 and so:

$$f = Bli = (c + \frac{k}{j\omega} + j\omega M)u_{\mathrm{M}} \tag{E.10}$$

The voltage in the coil circuit is given by the current *i* times the electrical impedance of the circuit plus the voltage generated by the relative motion of the magnet-coil and thus:

$$v = (R + j\omega L)i + Blu_{\mathrm{M}} \tag{E.11}$$

where R is the electrical resistance and L the inductance of the coil. Combining Equation (E.10) and (E.11) the blocked electrical impedance is given by:

$$Z_{eb} = R + j\omega L + \frac{j\omega (Bl)^2}{j\omega c + k - \omega^2 M} \tag{E.12}$$

List of references

[1] Mead, D.J., *Passive vibration control*. 1998, Chichester: Johon Wiley & Sons Ltd.

[2] Griffin, M.J., *Handbook of human vibration*. 1990, London: Academic press limited.

[3] Brennan, M.J. and J. Dayou, *Global control of vibration using a tuneable vibration neutralizer.* Journal of Sound and Vibration, 2000. **232**(3): p. 585-600.

[4] Brennan, M.J., *Vibration control using a tunable vibration neutralizer*. Proceedings of the Institution of Mechanical Engineers, Part C: Journal of Mechanical Engineering Science, 1997. **211**(2): p. 91-108.

[5] Rustighi, E., M.J. Brennan, and B.R. Mace, *A shape memory alloy adaptive tuned vibration absorber: design and implementation.* Smart Materials and Structures, 2005. **14**(19).

[6] Bonello, P., M.J. Brennan, S.J. Elliott, J.F.V. Vincent, and G. Jeronimidis, *Designs for an adaptive tuned vibration absorber with variable shape stiffness element.* Proceedings of the Royal Society A: Mathematical, Physical and Engineering Science, 2005. **461**(2064): p. 3955-3976.

[7] Preumont, A., *Vibration Control of Active Structures*, ed. n. Edition. 2002, London: Kluwer Academic.

[8] Hagood, N.W. and A. von Flotow, *Damping of structural vibrations with piezoelectric materials and passive electrical networks.* Journal of Sound and Vibration, 1991. **146**(2): p. 243-268.

[9] Fleming, A.J. and S.O.R. Moheimani, *Inertial vibration control using a shunted electromagnetic transducer.* Mechatronics, IEEE/ASME Transactions on, 2006. **11**(1): p. 84-92.

[10] Niederberger, D., S. Behrens, A.J. Fleming, S.O.R. Moheimani, and M. Morari, *Adaptive electromagnetic shunt damping.* Mechatronics, IEEE/ASME Transactions on, 2006. **11**(1): p. 103-108.

[11] Fuller, C.R., S.J. Elliott, and P.A. Nelson, *Active Control of Vibration*. 1996, London: AcademicPress.

[12] Nelson, P.A. and S.J. Elliott, *Active control of sound*. 1992, London: Academic Press.

[13] Gardonio, P., *Review of active techniques for aerospace vibro-acoustic control.* Journal of aircraft, 2002. **39**(2): p. 206-214.

[14] Elliott, S.J., *Signal Processing for Active Control*. 2000, London: Academic Press.

[15] Clark, R.L., W.R. Saunders, and G.P. Gibbs, *Adaptive Structures*. 1sted ed. 1998, NewYork: JohnWiley&Sons.

[16] Fahy, F.J. and P. Gardonio, *Sound and Structural Vibration*. 2007, London: Elsevier.

[17] Elliott, S.J., *Global vibration control through local feedback*, in *Adaptive Structure: Engineering Applications*, D. Wagg, et al., Editors. 2007, Johon Wiley & Sons Ltd: Chichester. p. 59-87.

[18] Balas, M.J., *Direct Velocity Feedback Control of Large Space Structures* Journal of Guidance, Control, and Dynamics, 1979. **2**(3): p. 252-253.

[19] Frampton, K.D., O.N. Baumann, and P. Gardonio, *A comparison of decentralized, distributed, and centralized vibro-acoustic control.* The Journal of the Acoustical Society of America, 2010. **128**(5): p. 2798-2806.

[20] Wellstead, P.E. and M.B. Zarrop, *Self-tuning systems: control and signal processing*. 1991, Chichester: Johon Wiley & Sons Ltd.

[21] Liu, B., L. Feng, and A. Nilsson, *Influence of overpressure on sound transmission through curved panels.* Journal of Sound and Vibration, 2007. **302**(4-5): p. 760-776.

[22] Newland, D.E., *An Introduction to Random Vibrations, Spectral & Wavelet Analysis*. Third Edition ed. 1975, Mineola, New York: Dover Publications, Inc.

[23] Mace, B.R. and L. Ji, *Coupled Oscillators and Sets of Oscillators: Statistical Energy Analysis Revisited*. 2006, ISVR Technical Memorandum 961.

[24] Elliott, S.J., P. Gardonio, T.C. Sors, and M.J. Brennan, *Active vibroacoustic control with multiple local feedback loops.* The Journal of the Acoustical Society of America, 2002. **111**(2): p. 908-915.

[25] Gardonio, P. and M.J. Brennan, *F.J.Fahy J.Walker, Mobility and impedance methods in structural dynamics*, in *Advanced ApplicationsinAcoustics, Noise andVibration*, E.F. Spon, Editor. 2004: London. p. 387–388.

[26] Engels, W.P., *Decentralised velocity feedback control of structures*, in *Institute of Sound and Vibration Research*. 2006, University of Southampton: Southampton.

[27] Redman-White, W., P.A. Nelson, and A.R.D. Curtis, *Experiments on the active control of flexural wave power flow.* Journal of Sound and Vibration, 1987. **112**(1): p. 187-191.

[28] Guicking, D., J. Melcher, and R. Wimmel, *Active impedance control in mechanical structures.* Journal of acustica, 1989. **69**.

[29] Bardou, O., P. Gardonio, S.J. Elliott, and R.J. Pinnington, *Active power minimisation and power absorption in a plate with force and moment excitation.* Journal of Sound and Vibration, 1997. **208**(1): p. 111-151.

[30] Hirami, N., *Optimal energy absorption as an active noise and vibration control strategy.* Journal of Sound and Vibration, 1997. **200**(3): p. 243-259.

[31] Hirami, N., *An active maximum power absorber for the reduction of noise and vibration.* Journal of Sound and Vibration, 1997. **200**(3): p. 261-279.

[32] Sharp, S.J., P.A. Nelson, and G.H. Koopmann, *A theoretical investigation of optimal power absorptionas a noise control technique.* Journal of Sound and Vibration, 2002. **251**(5): p. 927-935.

[33] Gardonio, P. and S.J. Elliott, *Modal response of a beam with a sensor-actuator pair for the implementation of velocity feedback control.* Journal of Sound and Vibration, 2005. **284**(1-2): p. 1-22.

[34] Preumont, A., B.d. Marneffe, and S. Krenk, *Transmission Zeros in Structural Control with Collocated Multi-Input/Multi-Output Pairs.* Journal of guidance control and dynamics, 2008. **31**(2): p. 428-431.

[35] Williams, T., *Constrained modes in control theory: Transmission zeros of uniform beams.* Journal of Sound and Vibration, 1992. **156**(1): p. 170-177.

[36] Engelen, K., H. Ramon, W. Saeys, W. Franssens, and J. Anthonis, *Positioning and tuning of viscous damper on flexible structure.* Journal of Sound and Vibration, 2007. **304**(3-5): p. 845-862.

[37] Franklin, G.F., P.J. David, and A. Emami-Naeini, *Feedback control of dynamic system*. Sixth edition ed. 2010, New York: Pearson.

[38] Brennan, M.J., K.A. Ananthaganeshan, and S.J. Elliott, *Instabilities due to instrumentation phase-lead and phase-lag in the feedback control of a simple vibrating system.* Journal of Sound and Vibration, 2007. **304**(3-5): p. 466-478.

[39] Hunt, F.V., *Electroacoustics The Analysis of Transduction and Its Historical Background*. 1954, New York: Wiley and Sons.

[40] Diaz, C.G., C. Paulitsch, and P. Gardonio, *Active damping control unit using a small scale proof mass electrodynamic actuator.* The Journal of the Acoustical Society of America, 2008. **124**(2): p. 886-897.

[41] Rohlfing, J., *Decentralised velocity feedback control for thin homogeneous and lightweight sandwich panels*, in *Institute of Sound and Vibration Research*. 2009, University of Southampton, PhD Thesis.

[42] Baumann, O.N. and S.J. Elliott, *Destabilization of velocity feedback controllers with stroke limited inertial actuators.* The Journal of the Acoustical Society of America, 2007. **121**(5): p. EL211-EL217.

[43] Rohlfing, J., S.J. Elliott, and P. Gardonio, *Compensation filter for feedback control units with proof-mass electrodynamic actuators, simulations and experimental studies*. 2011, ISVR Technical Memorandum 991.

[44] Frahm, H., *Device for damping vibrations of bodies*, U. Patent, Editor. 1911.

[45] Sun, J.Q., M.R. Jolly, and M.A. Norris, *Passive, Adaptive and Active Tuned Vibration Absorbers---A Survey*. Journal of Vibration and Acoustics, 1995. **117**(B): p. 234-242.

[46] von Flotow, A.H., Beard, A., and Bailey, D. *Adaptive tuned vibration absorbers: tuning laws, tracking agility, sizing and physical implementations*. in *Noise-Con 94*. 1994. Fort Lauderdale, FL.

[47] Asami, T., O. Nishihara, and A.M. Baz, *Analytical solutions to H∞ and H2 optimization of dynamic vibration absorbers attached to damped linear systems.* Journal of vibration and acoustics 2002. **124**(2): p. 284-295.

[48] Cheung, Y.L. and W.O. Wong, *H2 optimization of a non-traditional dynamic vibration absorber for vibration control of structures under random force excitation.* Journal of Sound and Vibration, 2011. **330**(6): p. 1039-1044.

[49] Crandall, S.H. and W.D. Mark, *Random vibration in mechanical systems*. 1963: Academic Press.

[50] Den Hartog, J.P., *Mechanical Vibrations*. 4th ed. 1956, New York: McGraw-Hill.

[51] Millers, D.W., E.F. Crawleyss, and B.A. Wards, *Inertial actuator design for maximum passive and active energy dissipation in flexible space structures*, in *Structures, Structural Dynamics, and Materials Conference, 26th, April 15-17, 1985*, . 1985, American Institute of Aeronautics and Astronautics: Orlando FL. p. p. 536-544.

[52] Yamaguchi, H., *Damping of Transient vibration by a Dynamic Absorber.* Transactions of the Japan Society of Mechanical Engineers, Ser. C, 1988. **54**(499): p. 561-568.

[53] Krenk, S., *Frequency Analysis of the Tuned Mass Damper.* Journal of Applied Mechanics, 2005. **72**(6): p. 936-942.

[54] Warburton, G.B., *Optimum absorber parameters for various combinations of response and excitation parameters.* Journal of earthquake engineering and structural dynamics 1982. **10**: p. 381-401.

[55] Hart, J.D., *Pipeline vibration damper*, U.S. Patent, Editor. 1993: United State of Amrica.

[56] Zivanovic, S., A. Pavic, and P. Reynolds, *Vibration serviceability of footbridges under human-induced excitation: a literature review.* Journal of Sound and Vibration, 2005. **279**(1-2): p. 1-74.

[57] Dallard, P., T. Fitzpatrick, A. Flint, A. Low, R.R. Smith, M. Willford, and M. Roche, *London Millennium Bridge: Pedestrian-Induced Lateral Vibration.* Journal of Bridge Engineering, 2001. **6**(6): p. 412-417.

[58] Dallard, P., A.J. Fitzpatrick, A. Flint, S.L. Bourva, A. Low, R.M. Ridsdill-Smith, and M. Willford, *The London Millennium Footbridge.* Structural Engineer, 2001. **79**(22): p. 17-33.

[59] http://www.gerb.com. *London Millennium Bridge - Damper beneath deck, north side 2011*.

[60] Wärtsiliä, *Wärtsiliä Technical Journal.* 2008(2).

[61] von Flotow, A.H., M. Mercadal, K.B. Scribner, T. Mixon, and C. Roeseler, *Adaptively tuned vibration absorber for reduction of aircraft cabin noise*. 1999: US Patent 5,873,559.

[62] von Flotow, A.H. and T.S. Mixon, *Adaptively tuned vibration absorbers*. 1995: US Patent 5,695,027.

[63] Ormondroyd, J. and J.P. DenHartog, *The theory of the Dynamic Vbration Absorber.* Journal of Applied Mechanics, 1928. **50**(7): p. 9-22.

[64] Iwata, Y., *On the construction of the dynamic vibration absorber.* Japanese Society of Mechanical Engineering, 1982. **820**(8): p. 150-152.

[65] Jolly, M.R. and D.L. Margolis, *Regenerative Systems for Vibration Control.* Journal of Vibration and Acoustics, 1997. **119**(2): p. 208-215.

[66] Nakano, K., S.J. Elliott, and E. Rustighi, *A unified approach to optimal conditions of power harvesting using electromagnetic and piezoelectric transducers.* Smart Materials and Structures, 2007. **16**(4): p. 948.

[67] Paulitsch, C., Boonen, R., Gardonio, P., *Sas, P. and Elliott, S.J., *Design of an Inertial, Electrodynamic Actuator with Internal Velocity Sensor for Active Vibration Damping of Lightweight, Flexible Structures* 2004, ISVR Technical Memorandum No. 940: Southampton.

[68] Peirs, J., *Design of micromechatronic systems: scale laws, technologies and medical applications*. 2001, Katholieke Universiteit Lueven, Phd Thesis.

[69] Madou, M.J., *Fundamentals of Microfabrication: The Science of Miniaturization, Second Edition*. 1st Edition ed. 1997, Boca Raton: CRC Press.